

NAVAL POSTGRADUATE SCHOOL

Monterey, California



DISSERTATION

**SIMULATED ANNUAL AND SEASONAL ARCTIC OCEAN AND
SEA-ICE VARIABILITY FROM A HIGH RESOLUTION,
COUPLED ICE-OCEAN MODEL**

by

Douglas Craig Marble

September 2001

Dissertation Advisors:

Wieslaw Maslowski

Albert J. Semtner

Committee Members:

Robert H. Bourke

Roland W. Garwood, Jr.

Peter S. Guest

Approved for public release; distribution is unlimited

Report Documentation Page

Report Date 30 Sep 2001	Report Type N/A	Dates Covered (from... to) -
Title and Subtitle Simulated annual and seasonal Arctic Ocean and sea-ice variability from a high-resolution, coupled ice-ocean model		Contract Number
		Grant Number
		Program Element Number
Author(s) Douglas C. Marble		Project Number
		Task Number
		Work Unit Number
Performing Organization Name(s) and Address(es) Research Office Naval Postgraduate School Monterey, Ca 93943-5138		Performing Organization Report Number
Sponsoring/Monitoring Agency Name(s) and Address(es)		Sponsor/Monitor's Acronym(s)
		Sponsor/Monitor's Report Number(s)
Distribution/Availability Statement Approved for public release, distribution unlimited		
Supplementary Notes		
Abstract		
Subject Terms		
Report Classification unclassified		Classification of this page unclassified
Classification of Abstract unclassified		Limitation of Abstract UU
Number of Pages 208		

REPORT DOCUMENTATION PAGE			Form Approved OMB No. 0704-0188	
Public reporting burden for this collection of information is estimated to average 1 hour per response, including the time for reviewing instruction, searching existing data sources, gathering and maintaining the data needed, and completing and reviewing the collection of information. Send comments regarding this burden estimate or any other aspect of this collection of information, including suggestions for reducing this burden, to Washington headquarters Services, Directorate for Information Operations and Reports, 1215 Jefferson Davis Highway, Suite 1204, Arlington, VA 22202-4302, and to the Office of Management and Budget, Paperwork Reduction Project (0704-0188) Washington DC 20503.				
1. AGENCY USE ONLY (Leave blank)		2. REPORT DATE September 2001	3. REPORT TYPE AND DATES COVERED Dissertation	
4. TITLE AND SUBTITLE: Simulated annual and seasonal Arctic Ocean and sea-ice variability from a high-resolution, coupled ice-ocean model			5. FUNDING NUMBERS	
6. AUTHOR(S) Douglas C. Marble				
7. PERFORMING ORGANIZATION NAME(S) AND ADDRESS(ES) Naval Postgraduate School Monterey, CA 93943-5000			8. PERFORMING ORGANIZATION REPORT NUMBER	
9. SPONSORING / MONITORING AGENCY NAME(S) AND ADDRESS(ES) N/A			10. SPONSORING / MONITORING AGENCY REPORT NUMBER	
11. SUPPLEMENTARY NOTES The views expressed in this thesis are those of the author and do not reflect the official policy or position of the Department of Defense or the U.S. Government.				
12a. DISTRIBUTION / AVAILABILITY STATEMENT Approved for public release; distribution is unlimited			12b. DISTRIBUTION CODE A	
13. ABSTRACT (maximum 200 words) <p>The role of the Arctic Ocean in global thermohaline circulation and climate change is not well understood. High resolution, physically realistic simulations of the Arctic Ocean, calibrated and validated with observations and paleo-climate data, may provide the spatial and temporal coverage and resolution to more accurately characterize Arctic Ocean circulation, large-scale inter-ocean exchanges and allow future conditions to be projected correctly.</p> <p>A 1/12-degree (~9 km) resolution coupled ice-ocean model, optimized for massively parallel computers, was developed. The model employs the latest digital bathymetry and ocean climatology available. Decades of model integration using climatological and realistic daily varying atmospheric forcing were performed. Comparisons of model output with climatic atlases and observations indicate greatly improved representation of circulation, ocean and sea-ice characteristics, mass and property transports and water mass transformations. Areas where model physics and resolution improvements are needed are highlighted as well.</p> <p>Comparison with a 1/6 degree (~18 km) ice-ocean model quantifies improvements gained from doubling model resolution. A ten fold increase in eddy kinetic energy is seen in the 9 km model versus the 18 km model. Narrow shelf and slope boundary currents, absent in the latter, now appear and mass and property transports are closer to observed values.</p>				
14. SUBJECT TERMS Arctic Ocean, oceanography, modeling			15. NUMBER OF PAGES 181	
			16. PRICE CODE	
17. SECURITY CLASSIFICATION OF REPORT Unclassified	18. SECURITY CLASSIFICATION OF THIS PAGE Unclassified	19. SECURITY CLASSIFICATION OF ABSTRACT Unclassified	20. LIMITATION OF ABSTRACT UL	

THIS PAGE INTENTIONALLY LEFT BLANK

Approved for public release; distribution is unlimited

**SIMULATED ANNUAL AND SEASONAL ARCTIC OCEAN AND SEA-ICE
VARIABILITY FROM A HIGH RESOLUTION, COUPLED ICE-OCEAN
MODEL**

Douglas C. Marble
Lieutenant Commander, United States Navy
B.S., University of South Carolina, 1986
M.S., Naval Postgraduate School, 1993

Submitted in partial fulfillment of the
requirements for the degree of

DOCTOR OF PHILOSOPHY IN PHYSICAL OCEANOGRAPHY

from the


**NAVAL POSTGRADUATE SCHOOL
September 2001**

Author:

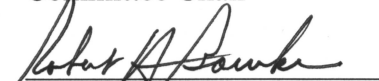


Douglas C. Marble

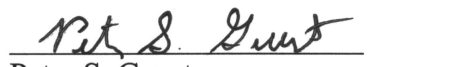
Approved by:



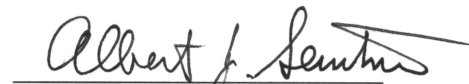
Wieslaw Maslowski
Associate Professor of Oceanography
Dissertation Advisor,
Committee Chair



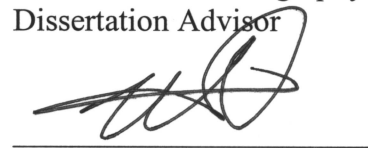
Robert H. Bourke
Professor of Oceanography



Peter S. Guest
Associate Professor of Meteorology



Albert J. Semtner
Professor of Oceanography
Dissertation Advisor



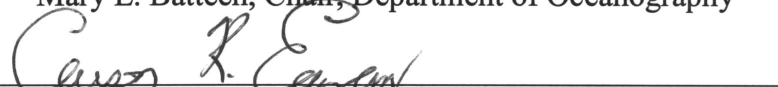
Roland W. Garwood
Professor of Oceanography

Approved by:



Mary L. Batteen, Chair, Department of Oceanography

Approved by:



Carson K. Eoyang, Associate Provost for Academic Affairs

THIS PAGE INTENTIONALLY LEFT BLANK

ABSTRACT

The role of the Arctic Ocean in global thermohaline circulation and climate change is not well understood. High resolution, physically realistic simulations of the Arctic Ocean, calibrated and validated with observations and paleo-climate data, may provide the spatial and temporal coverage and resolution to more accurately characterize Arctic Ocean circulation, large-scale inter-ocean exchanges and allow future conditions to be projected correctly.

A 1/12-degree (~ 9 km) resolution coupled ice-ocean model, optimized for massively parallel computers, was developed. The model employs the latest digital bathymetry and ocean climatology available. Decades of model integration using climatological and realistic daily varying atmospheric forcing were performed. Comparisons of model output with climatic atlases and observations indicate greatly improved representation of circulation, ocean and sea-ice characteristics, mass and property transports and water mass transformations. Areas where model physics and resolution improvements are needed are highlighted as well.

Comparison with a 1/6 degree (~ 18 km) ice-ocean model quantifies improvements gained from doubling model resolution. A ten fold increase in eddy kinetic energy is seen in the 9 km model versus the 18 km model. Narrow shelf and slope boundary currents, absent in the latter, now appear and mass and property transports are closer to observed values.

THIS PAGE INTENTIONALLY LEFT BLANK

TABLE OF CONTENTS

I.	OVERALL INTRODUCTION.....	1
A.	MODELING THE ARCTIC OCEAN	8
II.	MODEL DESCRIPTION AND METHODS	19
A.	INTRODUCTION.....	19
B.	THE OCEAN MODEL.....	19
	1. Physics.....	19
	2. Grid and bathymetry.....	24
	3. Forcing	30
	4. Experiment Design.....	33
C.	THE ICE MODEL.....	35
D.	ANALYSIS METHODS.....	36
III.	BARENTS SEA AND FRAM STRAIT	39
A.	OBSERVED PHYSICAL OCEANOGRAPHY	39
B.	MODEL PHYSICAL OCEANOGRAPHY	43
C.	MASS, HEAT AND SALT TRANSPORTS	52
	1. Mass Transport	52
	2. Heat and salt transports	55
D.	EDDY KINETIC ENERGY.....	61
E.	DISCUSSION	65
IV.	CANADIAN ARCTIC ARCHIPELAGO.....	67
A.	OBSERVED PHYSICAL OCEANOGRAPHY	67
B.	MODEL PHYSICAL OCEANOGRAPHY	70
	1. Canadian Arctic Archipelago Circulation.....	70
	2. Hudson Bay Circulation	76
	3. Baffin Bay Circulation.....	76
	4. Labrador Sea Circulation	78
C.	MASS, HEAT AND SALT TRANSPORTS	84
	1. Mass Transport	84
	2. Heat and Salt Transports	86
D.	EDDY KINETIC ENERGY.....	87
E.	DISCUSSION	91
V.	BERING STRAIT, CHUKCHI SEA	93
A.	OBSERVED PHYSICAL OCEANOGRAPHY	93
B.	MODEL PHYSICAL OCEANOGRAPHY	95
C.	MASS, HEAT AND SALT TRANSPORTS	104
	1. Mass Transport	105
	2. Heat and Salt Transports	106
D.	EDDY KINETIC ENERGY.....	107
E.	DISCUSSION	110
VI.	CENTRAL ARCTIC OCEAN.....	113
A.	OBSERVED PHYSICAL OCEANOGRAPHY	113
B.	MODEL PHYSICAL OCEANOGRAPHY	116

C.	EDDY KINETIC ENERGY	127
D.	DISCUSSION	133
VII.	9 KM MODEL VERSUS 18 KM MODEL	135
A.	18 KM MODEL DESCRIPTION	138
B.	BATHYMETRY IMPACTS	141
C.	BOUNDARY CURRENTS	144
D.	EDDIES AND EDDY KINETIC ENERGY	148
E.	DISCUSSION	151
VIII.	CONCLUSIONS AND RECOMMENDATIONS.....	153
	BIBLIOGRAPHY	163
	INITIAL DISTRIBUTION LIST	179

LIST OF FIGURES

Frontispiece:	Gerard Mercator's 1595 copper engraving of the Arctic. Elements from Medieval sources are combined with the latest explorations by the English and the Dutch. In this second state Barents' discoveries have been included. The magnetic Pole is depicted as a rock near the strait of Anian. Separate insets with the mythical island of Frysland, the Shetlands and the Faroer. The land of Gog is situated in North-East Tartaria. California is situated above the Arctic circle. 1633 edition available for purchase for US\$ 2,950.00, from Helmink Antique Maps (http://www.xs4all.nl/~helmink/gallery.html).	xxvi
Figure 1.1.	The Arctic Region including political boundaries and adjacent seas. Red line denotes the 10° C (50 ° F) contour in July, an accepted definition of the Arctic region. Map produced by the Central Intelligence Agency, provided courtesy of the General Libraries, University of Texas at Austin.	2
Figure 1.2.	a) SCICEX submarine science cruise tracks, 1993-1999, (Arctic Ocean science from submarines, a report based on the SCICEX 2000 Workshop, University of Washington, Applied Physics Laboratory, April 1999); b) Recent Oceanographic sections with a full sampling program for high quality hydrographic and tracer measurements. Arctic Climate System Study Implementation and Achievements Arctic Ocean Circulation Programme (http://acsys.npolar.no/impplan/ocean.htm). Note: The orientation of image b) is rotated approximately 180° with respect to image a).....	4
Figure 2.1.	Model domain and combined IBCAO and ETOPO5 based bathymetry (m).....	20
Figure 2.2.	Model bathymetry derived from the ~9 km resolution ETOPO5 database (top) and the 2.5 km resolution IBCAO database (bottom).....	27
Figure 2.3.	Hypothetical channel configuration on an Arakawa B grid. Circles indicate temperature and salinity grid points, stars = velocity grid points. Green circles = land points, blue circles = ocean points; red stars = zero velocity points; and yellow stars = non-zero velocity points, allowing flow through the channel. Gray shading represents land.....	28
Figure 2.4.	Model domain and ETOPO5 based bathymetry. Note the artificial "North American Channel" connecting the Atlantic Ocean and the Pacific Ocean along the bottom of the figure. Depth contours at 25, 50, 200, 500, 1000, 1500, 2000, 3000, 3500, 4000 and 5000 m in black.....	29
Figure 2.5.	Selected 16 year mean (1979-1984) fields from the ECMWF ERA-15 reanalysis products. (a) Sea Level Pressure, (b) 10 m wind velocity. From the ECMWF ERA-15 Picture Gallery (http://wms.ecmwf.int/research/era/Era-15_Composites_Surface.html).....	30
Figure 2.6.	365 day time series of daily average surface air temperature over the Arctic basin from ECMWF reanalysis products. For this illustration, the Arctic Basin is defined as the region enclosed by Fram Strait and the Bering Strait. Figure courtesy of Don Stark.	31
Figure 3.1.	Barents and Kara Seas bathymetry (m) and location of model sections and stations. Solid lines and letters denote sections. Hollow squares and	

numbers identify stations. Locations of observational data are indicated by red dots. d1 - Dalnye Zelintsi 1, July 1991. a12 = <i>Polarstern</i> ARKXII, August/September 1996. a94 = <i>Polarstern</i> ARKIX_4, August/September 1993.....	40
Figure 3.2. Two-year average 0-223m (model levels 1-16) velocity (cm s^{-1}). Velocity vectors are the average of spinup years 17 and 18 and are plotted every other grid point. Large gray arrows indicate interpreted pathways of mean currents.....	45
Figure 3.3. Vertical distribution of annual average potential temperature ($^{\circ}\text{C}$, a and d), salinity (psu, b and e), and velocity (cm s^{-1} , c and f) across the Norwegian Atlantic Current (model section A1, left) and the Bear Island Trough (model section A2, right). Note the differing vertical and horizontal scales. Negative velocity contours represent northward and eastward flows.....	46
Figure 3.4. Horizontal distribution of three year mean (1979-1981) average velocity (cm/s) in Fram Strait: (a) 0-226 m (model levels 1-16) mean; (b) 270-583 m (model levels 17-20). Background shading is 0-226 m (a) and 270-583 m (b) mean speed (scalar). Every second velocity vector is plotted. Note differing velocity vector scales.	48
Figure 3.5. Distribution of temperature and salinity in the upper 0-53 m (model levels 1-8) and sea ice concentration for various seasons. Winter average (Jan-Feb-Mar) potential temperature (a) and salinity (c). Summer average (Jul-Aug-Sep) potential temperature (b) and salinity (d). Maximum winter sea ice concentration (%), day 78 (mid-March) spinup year 18 (e). Minimum summer sea ice concentration (%), day 273 (early-September) spinup year 18 (f).....	50
Figure 3.6. Monthly mean volume transport (Sv), from the model and from observations, through the strait between Svalbard and Norway (a) and through the strait between Frans Josef Land and Novaya Zemlya (b). Observational data were taken from Ingvaldsen et al. (2000) for (a) and from Loeng et al. (1997) for (b).....	53
Figure 3.7. Vertical distribution of annual average potential temperature ($^{\circ}\text{C}$, a,d), salinity (psu, b,e), and velocity (cm s^{-1} , c,f) across the section north of Svalbard (model section B5, left) and the section north of Severnaya Zemlya (model section I, right). Note the differing horizontal scales. Negative velocity contours represent eastward flows.....	57
Figure 3.8. Summer average (Jul-Aug-Sep) potential temperature versus salinity (a), vertical distribution of potential temperature (b) and vertical distribution of salinity (c) for selected model stations in and around the Barents Sea. Each profile displayed represents an average over a 4x4 grid point region centered on the respective location given in Table 3.1.....	58
Figure 3.9. Potential temperature versus salinity, summer average (Jul-Aug-Sep) model output and observations in the western Barents Sea (a), in the St. Anna Trough (b), and north of Svalbard (c). dalzell = Dalnye Zelintsi, July 1991. a12-11 = <i>Polarstern</i> ARKXII, August/ September 1996. a94-10,12	

	= <i>Polarstern</i> ARKIX_4, August/September 1993. Note the differing temperature and salinity scales.	59
Figure 3.10:	Horizontal distribution of annual mean, 0-220 m (model levels 1-15) vertically averaged eddy kinetic energy ($\text{cm}^2 \text{s}^{-2}$), calculated from monthly mean model output. Area averaged monthly maximum – $363.22 \text{ cm}^2 \text{s}^{-2}$. Area averaged annual mean – $6.79 \text{ cm}^2 \text{s}^{-2}$. 400 m and 2750 m depth contours in white. EKE contours $5\text{-}25 \text{ cm}^2 \text{s}^{-2}$ by $5 \text{ cm}^2 \text{s}^{-2}$, $25\text{-}150 \text{ cm}^2 \text{s}^{-2}$ by $25 \text{ cm}^2 \text{s}^{-2}$ in black. Yellow lines indicate Norwegian Sea (NS) and Barents Sea (BS) sub-regions used in calculations for Figure 3.11.....	62
Figure 3.11.	Daily variability of area-averaged, surface, 0-5 m (model level 1), eddy kinetic energy ($\text{cm}^2 \text{s}^{-2}$) for the northern Norwegian and Barents Seas. Norwegian Sea and Barents Sea values were calculated in the sub-regions indicated by the yellow lines in Figure 3.10. The entire region average is for the region contained in Figure 3.10.....	63
Figure 3.12.	Distribution of the seasonal average of the eddy kinetic energy ($\text{cm}^2 \text{s}^{-2}$) at the surface, 0-5 m (model level 1), calculated from daily model output. Winter (Jan-Feb-Mar) (a); Spring (Apr-May-Jun) (b); Summer (Jul-Aug-Sep) (c); and Fall (Oct-Nov-Dec) (d). EKE contours 25, 50, 75, and $100 \text{ cm}^2 \text{s}^{-2}$ in black. 400 m depth contour in white.....	64
Figure 4.1.	Canadian Arctic Archipelago model geography and place names. PPI = Prince Patrick Isl. MI = Melville Isl. MKI = Mackenzie King Isl. BHI = Bathurst Isl. ERI/ARI = Ellef/Amund Ringness Isl. AHI = Axel Heiberg Isl. CI = Cornwallis Isl. PWI = Prince of Whales Isl. KWI = King William Isl. SI = Somerset Isl. BI = Bylot Isl.....	68
Figure 4.2(a).	Horizontal distribution of three year mean (1979-1981) 0-226 m (model levels 1-16) average velocity (cm/s) in the western Canadian Arctic Archipelago. Background shading is 0-226 m mean speed (scalar). Every other velocity vector is plotted. MKI = Mackenzie King Isl. ERI = Ellef Ringness Isl. ARI = Amund Ringness Isl. BI = Bathurst Isl. PWI = Prince William Isl. Note: vector length and shading scale differ from Figure 4.2(b)	71
Figure 4.2(b).	Horizontal distribution of three year mean (1979-1981) 0-226 m (model levels 1-16) average velocity (cm/s) in the eastern Canadian Arctic Archipelago. Background shading is 0-226 m mean speed (scalar). Every second velocity vector is plotted. BI = Bathurst Island. CI = Cornwallis Island. SI = Somerset Island. KWI = King William Island. Note: vector length and shading scale differ from Figure 4.2(a).....	72
Figure 4.3..	Horizontal distribution of three year mean (1979-1981) 0-226 m (model levels 1-16) average velocity (cm/s) in Hudson Bay. Background shading is 0-226 m mean speed (scalar). Every second velocity vector is plotted.	75
Figure 4.4.	Horizontal distribution of three year mean (1979-1981) 0-226 m (model levels 1-16) average velocity (cm/s) in Baffin Bay. Background shading is 0-226 m mean speed (scalar). Every second velocity vector is plotted.	77
Figure 4.5.	Horizontal distribution of three year mean (1979-1981) 0-226 m (model levels 1-16) mean velocity (cm/s) in the Labrador Sea. Background shading is 0-226 m mean current speed (scalar). Every third velocity vector is plotted.....	79

Figure 4.6. Horizontal distribution of 0-226 m (model levels 1-16) mean velocity (cm/s) in Amundsen Gulf for different seasons in 1980: (a) Winter Average (J-F-M); (b) Summer Average (J-A-S). Every velocity vector is plotted. Note the differing vector scales.	80
Figure 4.7. Horizontal distribution of 0-226 m (model levels 1-16) mean velocity (cm/s) in Coronation Gulf for different seasons in 1980: (a) Winter Average (J-F-M); (b) Summer Average (J-A-S). Every velocity vector is plotted. Note the differing vector scales.	81
Figure 4.8. Horizontal distribution of 0-226 m (model levels 1-16) mean velocity (cm/s) in Hudson Bay for different seasons in 1980: (a) Winter Average (J-F-M); (b) Summer Average (J-A-S). Background shading is seasonal average 0-226 m speed. Every other velocity vector is plotted. Note the differing vector and shading scales.	81
Figure 4.9. Distribution of temperature and salinity in the upper 0-53 m (model levels 1-8) and sea ice concentration for various seasons in 1980. Winter average (Jan-Feb-Mar) potential temperature (a) and salinity (c). Summer average (Jul-Aug-Sep) potential temperature (b) and salinity (d). Maximum winter sea ice concentration (%), day 72 (mid-March) 1980 (e). Minimum summer sea ice concentration (%), day 272 (early-September) 1980 (f). Note frames (e) and (f) cover a slightly larger region	83
Figure 4.10. Horizontal distribution of 1980 annual mean, 0-5 m (model level 1) eddy kinetic energy ($\text{cm}^2 \text{s}^{-2}$) in the Canadian Archipelago calculated from daily model output. EKE contours 4, 9, 16, 25, 50, 100, and 200 $\text{cm}^2 \text{s}^{-2}$	87
Figure 4.11. Horizontal distribution of eddy kinetic energy ($\text{cm}^2 \text{s}^{-2}$) in the Labrador Sea. (a) 1980 annual mean, 0-5 m (model level 1) calculated from daily model output. EKE contours 9, 16, 25, 50, 100, 200, 400, 600, and 800 $\text{cm}^2 \text{s}^{-2}$ in black; (b) Eddy kinetic energy deduced from surface drifter data. Drifters released in North Atlantic Ocean and Labrador Sea in the 1990s. Courtesy of J. Cuny, University of Washington.	88
Figure 4.12. Horizontal distribution of surface (0-5 m, model level 1) Eddy kinetic energy (cm^2/s^2) in Hudson Bay for different seasons: (a) Winter (J-F-M) average; (b) Summer (J-A-S) average. EKE contours: 4, 9, 16, 25, 36, 49, 100, and 200 cm^2/s^2	90
Figure 4.13. Horizontal distribution of surface (0-5 m, model level 1) Eddy kinetic energy (cm^2/s^2) in the Labrador Sea for different seasons: (a) Winter (J-F-M) average; (b) Summer (J-A-S) average. EKE contours: 4, 9, 16, 25, 36, 49, 100, 200, 400, 600 and 800 cm^2/s^2	91
Figure 5.1. Bering Strait geography, place names and model bathymetry (m). Depth contours correspond to model levels. The thick dashed line across Bering Strait indicates the section used for mass and property transport calculations. Red dots (E=East, W=West, N=North) indicate model stations chosen to match mooring locations in Roach et al., 1995.	94
Figure 5.2. Horizontal distribution of three year mean (1979-1981) 0-226 m (model levels 1-16) mean velocity (cm/s) in the Bering Strait. Background shading is 0-226 m mean current speed (scalar). Every other velocity vector is plotted.	97

Figure 5.3. Horizontal distribution of three year mean (1979-1981), 0-53 m (model levels 1-8) (a) Temperature ($^{\circ}$ C) and (b) Salinity (psu) in Bering Strait.....	98
Figure 5.4. Horizontal distribution of 0-53 m (model levels 1-8) velocity (cm/s) for different seasons: (a) Winter (J-F-M) average; (b) Summer (J-A-S) average.	99
Figure 5.5. Distribution of temperature and salinity in the upper 0-53 m (model levels 1-8) and sea ice concentration for various seasons. Winter average (J-F-M) potential temperature (a) and salinity (c). Summer average (J-A-S) potential temperature (b) and salinity (d). Maximum winter sea ice concentration (%), day 72 (mid-March) 1980 . (e). Minimum summer sea ice concentration (%), day 271 (early-September) 1980 (f)	101
Figure 5.6. Potential temperature versus salinity in Bering Strait: (a) Model 1980 January through December monthly mean values for (left) North, (middle) East and (right) West model stations, as indicated in Figure 5.1. Each profile displayed represents all data in a 2×2 grid point $(18 \text{ km})^2$ region; (b) Observed values from October 1990 through September 1991 (solid circles) and October 1993 through September 1994 (crosses) for (left) MA3, (middle) MA2, and (right) MA3 (Roach et al., 1995).....	102
Figure 5.7. 1979 monthly mean model volume transport through Bering Strait. Blue line is 1979 annual mean of 0.75 Sv.	105
Figure 5.8. 1979 cycle of monthly mean salt (10^6 kg/s , solid blue line) and heat (TW, dashed red line) transport through Bering Strait. Transports are calculated for the entire water column, across the section indicated in Figure 5.1. Heat transport referenced to -0.1° C , salt transport referenced to 34.4 psu. .	107
Figure 5.9. Horizontal distribution of 1980 annual mean, 0-5 m (model level 1) eddy kinetic energy ($\text{cm}^2 \text{ s}^{-2}$) in Bering Strait. EKE contours: 4, 9, 16, 25, 50, 100, $200 \text{ cm}^2 \text{ s}^{-2}$	108
Figure 5.9. Horizontal distribution of surface (0-5 m, model level 1) eddy kinetic energy (cm^2/s^2) in Bering Strait for different seasons: (a) Winter (J-F-M) average; (b) Summer (J-A-S) average. EKE contours: 2, 4, 9, 16, 25, 36, 49, 100, 200, 400 and $800 \text{ cm}^2/\text{s}^2$	110
Figure 6.1. Schematic diagram showing the inferred circulation in the Arctic Ocean of the Atlantic Layer and intermediate depth waters, between 200 m and 1700 m (Rudels et al., 1994).....	114
Figure 6.2. Central Arctic Ocean model bathymetry (m). Depth contours are every other model level. Dashed line in the Canadian Basin indicates the model section similar to repeated SCICEX trans-Arctic submarine sections.....	115
Figure 6.3. Horizontal distribution of three-year mean (1979-1981) 0-226 m (model levels 1-16) mean velocity (cm/s) in the Eurasian Basin. Background shading is 0-226 m mean current speed (scalar). Every third velocity vector is plotted.....	116
Figure 6.4. Horizontal distribution of three year mean (1979-1981) 0-226 m (model levels 1-16) mean velocity (cm/s) in the Laptev Sea. Background shading is 0-226 m mean current speed (scalar). Every other velocity vector is plotted.	118

Figure 6.5. Horizontal distribution of 1979-1981 three year mean, 0-226 m (model levels 1-16) mean velocity (cm/s) in the Canadian Basin. Background shading is 0-226 m mean current speed (scalar). Every third velocity vector is plotted.	119
Figure 6.6. Horizontal distribution of 1979-1981 three-year mean, 0-226 m (model levels 1-16) mean velocity (cm/s) in the Beaufort Sea. Background shading is 0-226 m mean current speed (scalar). Every other velocity vector is plotted.	120
Figure 6.7. Horizontal distribution of three-year mean (1979-1981) 0-226 m (model levels 1-16) mean velocity (cm/s) in the East Siberian Sea. Background shading is 0-226 m mean current speed (scalar). Every other velocity vector is plotted.	122
Figure 6.8. Horizontal distribution of 1980 annual mean 3250 m (model level 30) temperature ($^{\circ}\text{C}$) and salinity (psu-34): from (a) and (b) model output; (c) and (d) PHC 1.0 climatology mapped onto the model grid. Model depth contours 500 and 2200 m in black. Note: The 34 psu prefix is omitted from both salinity scales.	124
Figure 6.9. Vertical distribution of 1980 Summer (July-August-September) average properties for different seasons in the Canadian Basin: (a) potential temperature; (b) salinity. Note the x-axis is in units of delta-x, or grid spacing. The spacing between tick marks is 20 grid points or ~ 180 km.	125
Figure 6.10. Difference field between 1980 summer average (J-A-S) surface (0-5 m, model level 1) eddy kinetic energy (cm^2/s^2) minus winter average (J-F-M) surface EKE.	127
Figure 6.11. Snapshot of March 1980, 60-120 m (model levels 9-12) eddy kinetic energy (cm^2/s^2) in the Arctic Ocean.	129
Figure 6.12. Snapshot of August 1980, 60-120 m (model levels 9-12) eddy kinetic energy (cm^2/s^2) in the Arctic Ocean.	130
Figure 6.13. Snapshot of the August 1980 vertical distribution of EKE along the SCICEX transect in the Canadian Basin. Note the shading scale is adjusted to highlight lower values of EKE in the center of the basin. Bathymetry profile and x-axis distance scale as in Figure 6.9	132
Figure 7.1. 18 km PCAP58 model domain (a) and 9 km PIPS model domain (b). 18 km model image has been rotated 26° . Approximate distance scale is equivalent to 100-9 km model grid points and 50-18 km model grid points. 500 and 2500 m contours in black.	135
Figure 7.2. PCAP58 18 km coupled ice-ocean model domain and bathymetry (m). Contours are every other model level. Bathymetry north of 64° N derived from IBCAO 2.5 km resolution database. The black dot in the upper left corner denotes the location of the closed Bering Strait.	138
Figure 7.3. Distribution of 1980 annual mean velocity (cm/s) in the Barents Sea. (a) PCAP58, 0-225 m (model levels 1-7), every vector is plotted; (b) PIPS, 0-223 m (model levels 1-15), every other vector is plotted. Background shading is current speed (cm/s) and is the same for both model images. Note the differing vector scales.	141
Figure 7.4. Distribution of 1980 annual mean velocity in Hudson Strait. (a) PCAP58, 0-180 m (model levels 1-6), every vector is plotted; (b) PIPS, 0-183 m	

	(model levels 1-14), every other vector is plotted. Background shading as in Figure 7.3.....	142
Figure 7.5.	Distribution of 1980 annual mean velocity (cm/s) in the Labrador Sea. (a) PCAP58, 0-180 m (model levels 1-6); (b) PIPS, 0-183 m (model levels 1-14). Every other vector is plotted. Background shading as in Figure 7.3. Note the differing vector scales.	144
Figure 7.6.	Distribution of 1980 annual mean velocity (cm/s) in the surface layer of the Beaufort Sea. (a) PCAP58, 0-45 m (model levels 1-2), every vector is plotted; (b) PIPS, 0-43 m (model levels 1-7), every other vector is plotted. Background shading as in Figure 7.3. Note the differing vector scales.	146
Figure 7.7.	Distribution of 1980 annual mean velocity (cm/s) in the halocline of the Beaufort Sea. (a) PCAP58, 71-140 m (model levels 4-5), every vector is plotted; (b) PIPS, 66-120 m (model levels 10-12), every other vector is plotted. Background shading as in Figure 7.3. Note the differing vector scales.	147
Figure 7.8.	Distribution of 1980 annual mean velocity (cm/s) in the Atlantic Layer of the Beaufort Sea. (a) PCAP58, 360-565 m (model levels 10-11), every vector is plotted; (b) PIPS, 398-584 m (model levels 19-20), every other vector is plotted. Background shading as in Figure 7.3. Note the differing vector scales.	147
Figure 7.9.	August 1980 snapshot of surface layer eddy kinetic energy (cm^2/s^2) in the Labrador Sea: (a) PCAP58, 0-45 m (model levels 1-2); (b) PIPS, 0-43 m (model levels 1-7). Note different shading scales.....	149
Figure 7.10.	August 1980 snapshot of surface layer eddy kinetic energy (cm^2/s^2) in the Nordic (Greenland, Iceland and Norwegian) Seas: (a) PCAP58, 0-45 m (model levels 1-2); (b) PIPS, 0-43 m (model levels 1-7). Note the different shading scales.....	151
Figure 8.1.	1980 seasonal percent sea-ice concentration snapshots: (a) maximum extent, day 77 (mid March); (b) minimum extent, day 272 (mid September).....	155
Figure 8.2.	Tidal influences on the Arctic Ocean; (a) maximum shear of ice velocity due to M2, S2, K1 and O1 tidal species; (b) maximum tidal currents (cm/s) due to M2, S2, K1 and O1 tidal species (Kowalik and Proshutinsky, 1994).	156

THIS PAGE INTENTIONALLY LEFT BLANK

LIST OF TABLES

Table 2.1.	Vertical distribution of model levels. The fifth column, <i>dt_t</i> , indicates the multiplication factor that was applied to the temperature and salinity diffusion equations while deep acceleration was active.	25
Table 3.1.	Model sections and stations identified in Figure 3.1. Locations given for stations are center point of a (36 kilometer) ² (4x4 gridpoint) region. Profiles displayed for model stations are an average for that region.	44
Table 3.2.	Annual mean simulated volume transport (Vol, Sv), heat transport (Q _{heat} , TW) and total salt transport (Q _{salt} , 10 ⁶ kg s ⁻¹) through selected sections. In and out are defined as into and out of the Arctic Ocean, respectively, or following the path of Atlantic Water. Q _{heat} referenced to -0.1° C, Q _{salt} referenced to 0.0 psu. Calculations are for entire water column.	52
Table 4.1	1979-1981 three year mean simulated volume transport (Vol, Sv), net heat transport (Q _{heat} , TW) and net salt transport (Q _{salt} , 10 ⁶ kg s ⁻¹) through selected CAA sections. In/out are defined as into/out of the Arctic Ocean, respectively. Negative transports indicate transport out of the Arctic Ocean. Q _{heat} referenced to -0.1° C, Q _{salt} referenced to 34.4 psu. Calculations are for entire water column.	85
Table 5.1.	Three year mean (1979-1981) net transports through Bering Strait. Transports are calculated across the section in figure 5.1 and are for the entire water column.	106
Table 7.1.	18 km model (PCAP58) and 9 km model (PIPS) model configurations and key parameters.	136
Table 7.2.	Eddy kinetic energy (cm ² /s ²) statistics for the 0-45 m regional snapshots presented in Figures 7.9 and 7.10.	150

THIS PAGE INTENTIONALLY LEFT BLANK

ACKNOWLEDGMENTS

First and foremost, my thanks go to my wife, Claire, for her love, patience, support, understanding and motivation, and our six-month-old daughter, Elizabeth, for learning to sleep through the night early on.

I would like to thank the members of my dissertation committee for their valuable insights and assistance. Without the help of Drs. Don Stark, Waldemar Walczowski, Julie McClean, and Yuxia Zhang here at the Naval Postgraduate School, and Dr Ursula Schauer while at NPS as the ONR Arctic Chair, the quality of this work would have suffered tremendously. Other individuals who have provided crucial assistance are Tom Baring at the Arctic Region Supercomputer Center (ARSC), University of Alaska, Fairbanks; Bob Newton at Columbia University's Lamont Dougherty Earth Observatory; Mike Steele and Jerome Cuny, University of Washington; Harald Loeng, Institute of Marine Research, Bergen, Norway; Simon Prinsenbergh, Bedford Institute of Oceanography, Dartmouth, Nova Scotia; and Pete Braccio, Moss Landing Marine Laboratory. The list of the remaining people who have helped is long and I apologize for those not mentioned here by name.

Computer resources were provided by ARSC through the DoD Grand Challenge Program. Funding for development and integration of the 9 km ocean model was provided via grants from the Office of Naval Research and the National Science Foundation as part of the PIPS 3.0 development project.

I would like to dedicate this to my parents, Dr. Duane F. Marble and Jacquelynne H. Marble, who have been incredibly supportive of whatever I've chosen to do and an inspiration my entire life.

THIS PAGE INTENTIONALLY LEFT BLANK

EXECUTIVE SUMMARY

The focus on the Arctic Ocean as a key strategic region decreased considerably following the end of the cold war. However, interest in the region is once again on the rise due to concerns about climate change and the biological, commercial and military implications of a seasonally ice free Arctic Ocean (Smedsrud and Furevik, 2000; U.S. Arctic Research Commission, 2000; U.S Navy Symposium, 2001). The shipping route between Europe and Asia is approximately 7000 miles shorter via the Northwest Passage versus the Panama Canal route and 12,000 miles shorter than the route around Cape Horn (Falkingham, 2000). Commercial interests will move quickly to take advantage of a seasonally ice free Arctic Ocean if it occurs, therefore planning, policy making, and system design/procurement need to begin as soon as possible for government and military agencies to be able to operate successfully in such an environment. Additionally, the results of decades of industrial development, military activities, natural resource development and nuclear power operations have left a substantial, largely uncontrolled and generally unassessed legacy of contaminants in close proximity to the Arctic Ocean with the potential to be transported into the Arctic domain with very little warning or opportunity for remediation (U.S. Arctic Research Commission, 2001). Due to its remote location and the harsh operating environment, the Arctic remains one of the least well understood regions.

The Arctic Ocean's role in global climate change and thermohaline circulation is not well understood, yet it is felt to be significant (Aagaard et al., 1994, Maslanik and Dunn, 1997). Questions as to whether changes in the Arctic Ocean can be used as an early indicator of global warming or if the Arctic Ocean works to help regulate the global climate also remain unanswered. High resolution, physically realistic simulations of the Arctic Ocean, calibrated and evaluated with available observations and paleo-climate data, may provide the spatial and temporal coverage and resolution necessary to more accurately characterize the Arctic Ocean, narrow the gap between model output and observations and allow future conditions to be projected correctly. Under the broader scope of an Office of Naval Research (ONR) funded project to upgrade the U.S. Navy's Polar Ice Prediction System (PIPS) 2.0 to a state-of-the-art coupled ice-ocean model, the

work described here was undertaken in an attempt to narrow the gap between model output and observations and more accurately characterize annual and seasonal variability in the inflow and outflow regions of the Arctic Ocean.

A high resolution ($1/12^\circ$, or ~ 9.26 km) coupled ice-ocean model of the Arctic Ocean and adjacent seas was developed using the latest digital bathymetry and ocean climatology. The model was integrated with climatological atmospheric forcing, followed by daily varying realistic atmospheric forcing, in an effort to increase our understanding of Arctic Ocean circulation and variability and its response to changes in atmospheric forcing. An additional scientific goal of this project was to quantify gains realized from the increase in model resolution. To this end, results are compared with those from a similar yet coarser resolution, ~ 18 km, model.

Significant improvements are realized in the representation of ice and ocean circulation and characteristics. In the model sea ice, observed features such as the scalloped retreating ice edge in the Chukchi Sea (Paquette and Bourke, 1981; Martin and Drucker, 1997) and a feature similar to the ice Odden in the Greenland Sea (Wadhams and Comiso, 1999) are simulated. An increase in the number and complexity of leads is also noted. Seasonal growth and melt cycles are similar to those observed, however, under the atmospheric forcing applied to date, the summer ice edge remains too far south in the Chukchi and Beaufort Seas and Baffin Bay. As the ice edge is a strong function of sea surface temperature, it is felt this problem may be due to possible combinations of the climatological average atmospheric forcing and the quality of the ocean climatology used for restoring. Farther testing is needed to solve this discrepancy.

An increase of five to ten times in eddy kinetic energy is calculated when compared to a similar but coarser resolution ($1/6^\circ$ or ~ 18 km) model. However, the new model values are still two to four times less than that observed. In the 9-km simulation, the narrow boundary currents which dominate the observed basin scale circulation, but are poorly represented or entirely absent in coarser resolution models, now appear. Oceanic transports are also closer to those observed. Model results highlight a need for continued increases in resolution in Arctic Ocean models as well as improved

parameterizations of processes that impact mixing and water mass transformations, such as open ocean convection, mixed layer dynamics and bottom boundary flows.

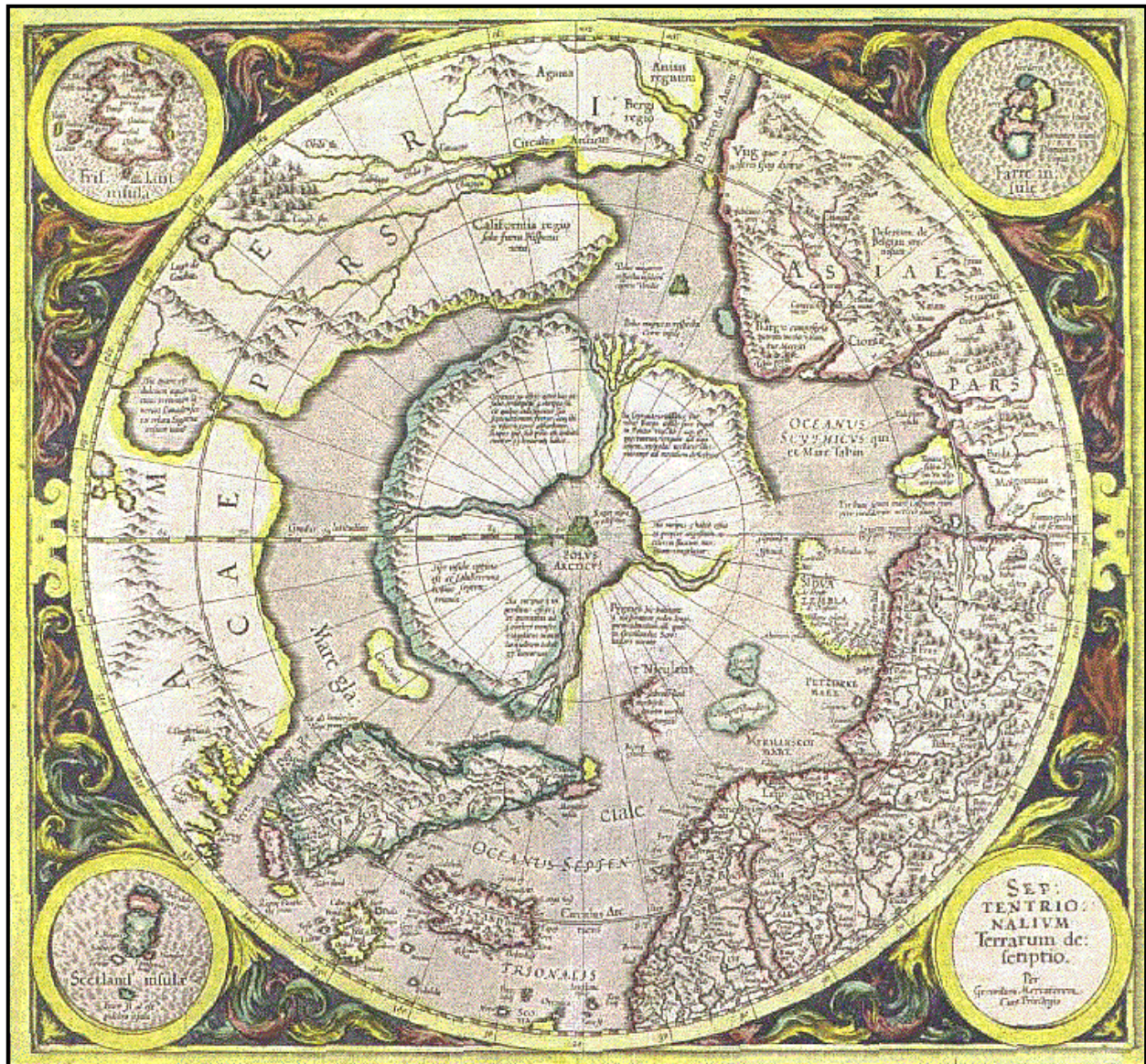
The coupled ice-ocean model described here is configured on a rotated spherical coordinate grid, having 1280x720 horizontal gridpoints and 45 fixed depth levels. The high resolution is an important asset as it allows realistic representation of the complex geography and bathymetry of the region and oceanic features greater than ~30 km in diameter. Significant physical features, which include the Bering Strait, the Canadian Arctic Archipelago, the vast coastal shelves and steep oceanic ridges, influence water mass circulation and modification and ice melt and formation. The model can be considered eddy-permitting, as the resolution captures eddies on the order of ~30 km or larger, but not eddy resolving. For an Arctic Ocean model to be considered eddy-resolving it would require a grid spacing of less than 2 km, as the deformation radius which governs many of the important physical processes in the Arctic is on the order of 10 km or less. A minimum of three points across a feature is required to resolve characteristics such as phase, amplitude and wavelength. 7-10 points across a feature would be optimal, which would require a resolution of ~1-1.5 km.

The ocean model code is a version of the Los Alamos National Laboratory (LANL) Parallel Ocean Program (POP) code (Dukowicz and Smith, 1994). The ice model is a version of the Zhang and Hibler (1997) viscous-plastic ice rheology with a surface heat budget after Parkinson and Washington (1979). The ocean model, an evolution of a previous ~18 km resolution model developed at the Naval Postgraduate School (Parsons et al., 1996; Zhang et al., 1999; Maslowski et al., 2000,2001) includes the capability to add passive and active tracers which will prove useful in tracing freshwater and contaminant pathways. Riverine temperature and salinity inputs and tides have not been implemented, but are planned for future inclusion. The ocean temperature and salinity climatology used for surface restoring will be upgraded from the University of Washington Polar Science Center Hydrographic Climatology (PHC, Steele et al., 2000) version 1.0 to PHC 2.0. Also planned for future inclusion is an improved energy conserving dynamic-thermodynamic ice model which will include a non-linear vertical temperature profile, vertically varying ice salinity, multiple ice thickness categories, a brine pocket parameterization, and a snow layer (Bitz, 1999).

The model was integrated in spinup mode for several decades using 365 days of 1979-1993 mean atmospheric forcing fields derived from the European Centre for Medium Range Weather Forecasts reanalysis data, followed by 6 years of daily varying 1979 forcing and then three cycles of repeated 1979-1981 forcing (9 years). The repeated 1979 and 1979-1981 forcing were applied to "baseline" the model towards conditions in the early 1980's prior to performing a "hindcast" simulation using 1979-2000 daily varying realistic forcing. Observations and climatological data are used for model verification. Using 128 processors of a Cray T3E-900 supercomputer, it takes approximately one week to integrate the model for 365 days. It is felt the sequential spinup, from 1979 to present, was needed in order to obtain realistic ocean circulation. The longer, sequential spinup was favored over other possible methods of starting the ocean from rest, such as a shorter spinup using observational data assimilation, as deep circulation is established on timescales of decades and centuries.

Decadal cycles are not examined here as the number of years of integration using realistic daily varying forcing is not sufficient. Monthly, seasonal and annual mean conditions and variability, based on the applied atmospheric forcing, are addressed.

THIS PAGE INTENTIONALLY LEFT BLANK



Gerard Mercator's 1595 copper engraving of the Arctic. Elements from Medieval sources are combined with the latest explorations by the English and the Dutch. In this second state Barents' discoveries have been included. The magnetic Pole is depicted as a rock near the strait of Anian. Separate insets with the mythical island of Friesland, the Shetlands and the Faroer. The land of Gog is situated in North-East Tartaria. California is situated above the Arctic circle. 1633 edition available for purchase for US\$ 2,950.00, from Helminck Antique Maps (<http://www.xs4all.nl/~helminck/gallery.html>).

I. OVERALL INTRODUCTION

From the explorations of Pytheas in 330 B.C, to the thirty plus years spent searching for the Franklin expedition (Mirsky, 1934), to the submarine science cruises of the 1990's, the Arctic Ocean has captivated explorers, scientists and merchants with its darkness and ice and the promise of a shorter sea route between the Atlantic and the Pacific Oceans. Today, there is little left in the way of geographic discovery in the Arctic, yet there are large gaps in our knowledge of the oceanography of the region. As the speed and capacity of supercomputers continues to increase, the goal of accurately simulating ocean circulation, from basin-scale gyres down to small-scale processes, appears more and more attainable. The Arctic Ocean (Figure 1.1) has been a particularly challenging area to model, due to its complex bathymetry, highly variable sea-ice cover, and physical processes that are significant at several length and depth scales. Also complicating the problem in this case are its intricate thermohaline structure and a deformation radius on the order of 10 km or less that governs important processes such as eddies and vertical and horizontal mixing. Representing any of these features requires a model with improved physics, improved parameterizations for those processes that cannot be simulated directly, and high spatial resolution, both horizontal and vertical.

Proper verification of Arctic Ocean modeling results has also proven challenging. The remoteness of the area and the expense involved in getting to and operating in such a harsh environment have limited the amount of observational data available for comparison. The use of U.S. Navy submarines as Arctic science platforms, during the Scientific Ice Experiments (SCICEX) program from 1993 through 1999, has significantly increased the amount of data available and resulted in over sixty presentations at international meetings and numerous publications in several different peer-reviewed scientific journals (<http://www.ldeo.columbia.edu/SCICEX/Pages/SCICEXpu.html>). The submarine science cruises and an increase in the number of surface ship scientific cruises in the 1990's (Figure 1.2) as well as advances in remote sensing technology have also added to the information available on the Arctic system. However, large gaps still remain in our knowledge of the oceanographic conditions of much of the Arctic Ocean. Due to



changes in the composition and missions of the U.S. submarine force, the future of this extremely valuable submarine science cruise program is uncertain. Prior to the 1990's, only limited attempts at basin-wide or synoptic interpretations of available data were possible (Aagaard and Greisman, 1975; Aagaard et al., 1981; Aagaard, 1989; Rudels, 1989). High resolution, physically realistic simulations of the Arctic Ocean, calibrated and evaluated with available observations and paleo-climate data, may provide the spatial and temporal coverage and resolution necessary to more accurately characterize Arctic Ocean circulation and large-scale inter-ocean interactions and narrow the gap between model output and observations.

The major scientific objective of this project is to work towards a better understanding of the Arctic Ocean circulation and its relation to the global climate through the use of a high resolution, coupled ice-ocean numerical model forced with multi-decadal, realistic atmospheric forcing. The primary focus of the model output analysis will be on the mean (annual and three year means) and seasonal variability of the oceanography in the major inflow and outflow regions of the Arctic Ocean -the Barents Sea/Fram Strait region, the Canadian Arctic Archipelago and Bering Strait.

Though our knowledge of the region has continued to improve, the role of the Arctic Ocean in global climate change is still uncertain but believed to be significant (Aagaard et al., 1994, Maslanik and Dunn, 1997). Climate simulations have shown that the Arctic region will be particularly sensitive to changes in the global climate (Semtner, 1984, 1987; Weatherly, 1997; Zhang et al., 1998a, Maslowski et al., 1998). However, it is not clear whether the Arctic Ocean is limited to responding passively to these changes or if feedback mechanisms exist that allow the Arctic to actively influence climate change. Observed seawater and air temperature increases, thinning ice cover and changes in Arctic Ocean circulation during the last decade or so (Carmack et al., 1995, 1997; Grotefendt et al., 1998; Melling, 1998; Steele and Boyd, 1998, Rothrock et al., 1999), are thought to be related to changes in large-scale atmospheric circulation (Chapman and Walsh, 1993, Morison et al., 1997; McPhee et al., 1998; Dickson, 1999, Maslowski et al.,

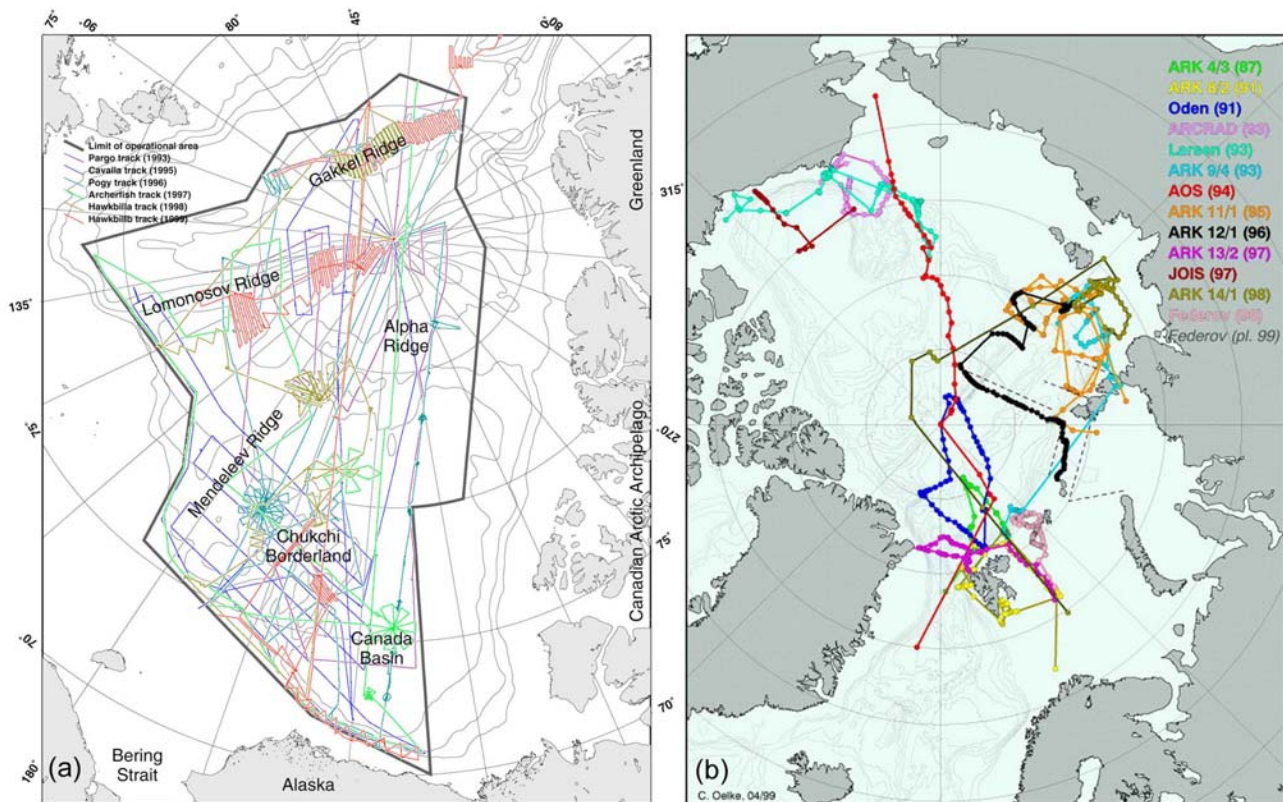


Figure 1.2. a) SCICEX submarine science cruise tracks, 1993-1999, (Arctic Ocean science from submarines, a report based on the SCICEX 2000 Workshop, University of Washington, Applied Physics Laboratory, April 1999); b) Recent Oceanographic sections with a full sampling program for high quality hydrographic and tracer measurements. Arctic Climate System Study Implementation and Achievements Arctic Ocean Circulation Programme (<http://acsys.npolar.no/impplan/ocean.htm>). Note: The orientation of image b) is rotated approximately 180° with respect to image a)

2000, 2001). Whether these oceanic and atmospheric changes are anthropogenic, permanent or temporary, or part of a natural oscillatory cycle has yet to be determined. If, or how, these changes will affect the large scale atmospheric circulation is another unknown. Some of the main deep-water formation areas in the world are fed by Arctic Ocean outflow. Studies have shown a relationship between the nature of Arctic Ocean outflow and the intensity of deep convection in these areas (Mysak et al., 1990; Skvillingstad et al., 1991; Visbeck et al., 1995; Dickson et al., 1988, 1996, 1998; Mauritzen and Hakkinen, 1997; and Belkin et al., 1998). There is little doubt the Arctic Ocean has significant potential to influence the global thermohaline circulation. However, determining the extent of the Arctic's influence on that circulation will be an important step in understanding the Arctic's role in the global climate. Results from two

high-resolution coupled ice-ocean models are used to present a better understanding of the Arctic Ocean's response to seasonal and interannual variability in atmospheric forcing and basin to basin interactions.

The second objective of this project was to advance the field of numerical modeling and quantify improvements realized from increases in model resolution. The 1/12 degree (~9 km) resolution model is based upon an existing 1/6 degree (~18 km) grid spacing coupled ice-model with 30 vertical levels (Parsons, 1995; Zhang et al., 1999; Maslowski et al., 2000, 2001). The first significant change to the model was decreasing the horizontal grid spacing to ~9 km and increasing the vertical resolution to 45 levels. An immediately noticeable improvement occurred in the representation of the complex bathymetry of the Arctic Ocean. Higher resolution permitted better representation of the flow through the Canadian Arctic Archipelago as well as the flow over the vast continental shelves surrounding the deep Arctic basins. Both of these regions and flow regimes play important roles in Arctic Ocean circulation, water mass formation, water mass modification and inter-ocean communications. Accurate representation of the Lomonosov Ridge and submarine canyons, using the latest submarine bathymetry data, improved simulation of the cross-basin intermediate and deep Arctic Ocean flow. A comparison of eddy, total kinetic and potential energy between the two model resolutions revealed improved simulation of the overall energy budget and better representation of physical processes, including mass transport, current velocity and structure, and dissipation scale eddy and meander motions. The investigation also addresses improving processing speed by streamlining the model code using massively parallel (MPP) and distributed shared memory (DSM) computers in collaboration with researchers from Los Alamos National Laboratory (LANL) and the National Center for Atmospheric Research (NCAR).

The principal approach for the proposed research included: 1) modification of an existing model to construct an eddy-permitting, coupled ice-ocean general circulation model of the pan-Arctic region with improved physics, extending into the North Pacific and the North Atlantic to allow inter-ocean, large-scale exchanges; 2) model integration; 3) model validation using observations and climatology; and 4) inter-comparison of the 9

km and 18 km model output. The ~9 km model is, to our knowledge, the highest resolution pan-Arctic model in the world. The domain includes much of the North Pacific from roughly 30° N, the Arctic Ocean and all adjacent seas, the Canadian Arctic Archipelago and the North Atlantic to 35°N. The model has 45 vertical levels to properly resolve the vast continental shelves, steep slopes and ridges, and improve representation of the important physical processes occurring there. Physical improvements included upgrading the model code to a free-surface formulation of LANL Parallel Ocean Program (POP, Dukowicz and Smith, 1994). Future versions of POP will include a switch to enable mixed layer K-profile parameterization (KPP, Large et al., 1994) for improved vertical mixing. The current ice model is based on a Hibler-style (1979) ice model optimized for multi-processor parallel computers. Planned upgrades to the sea-ice model include a much improved energy conserving dynamic/thermodynamic ice model, which will include multiple layers, multiple thickness categories, brine pocket parameterization and a snow layer (after Bitz and Lipscomb, 1999). Upgrading the model code and work toward inclusion of the new ice model were a community effort of the NPS Arctic Modeling group.

From the successes of the 18 km grid-spacing model (Zhang et al., 1999, Maslowski et al., 2000, 2001), it was anticipated the new model would more accurately represent the Arctic Ocean circulation and the observed climate shift in the Arctic. Due to time and resource constraints, this report primarily addresses how well the model represents known Arctic Ocean characteristics. The integration has not reached a point where there is enough interannual forcing output to be able to address how well the model captures the climatic shift observed in the late eighties and early nineties. The increase in resolution allows more accurate determination of simulated transports and fluxes through the Fram and Bering Straits and the Canadian Arctic Archipelago. Seasonal variability in the model results show a strong cause and effect relationship between warm Atlantic water inflow to the Arctic basin, Arctic Ocean surface and intermediate water circulation, Arctic Ocean freshwater (including sea ice) export through the Canadian Arctic Archipelago and Fram Strait and the large-scale atmospheric

circulation. Results also provide insights on potential Arctic Ocean feedbacks that may influence the North Atlantic thermohaline circulation.

A version of the completed coupled ice-ocean model has been provided to the Naval Research Laboratory, Stennis Space Center, Mississippi, for farther testing toward operational transition, to ultimately be included in the planned upgrade of the Navy's Polar Ice Prediction System (PIPS 2.0), to PIPS 3.0. The testing and operational transition of the model is a separate effort from this project. PIPS 2.0 (Cheng and Preller, 1996) currently provides operational output in the form of weekly ice drift, thickness and concentration hindcasts and forecasts to the National and Naval Ice Center (NIC) in Suitland, Maryland. It is anticipated that the greatly improved coupled ice-ocean model, which includes assimilation of sea ice drift velocity and ice edge data from buoys and satellites, will improve ice forecasts, including ice divergence/convergence and pressure ridge and lead orientation, throughout the basin and in the marginal ice zone, enhancing NIC capabilities to produce detailed and accurate operational ice analyses and forecasts for their Department of Defense, government, civilian and foreign users.

The remainder of Chapter I includes a review of regional and global Arctic Ocean modeling literature. Chapter II describes the ocean and ice models and the numerical experiments performed. Chapters III, IV and V are detailed discussions on long term mean and seasonally variable circulation and transports in the major inflow and outflow regions to the Arctic Ocean, the primary scientific focus of this report. The decision to focus on inflow and outflow regions of the Arctic Ocean was made to establish boundaries for the research, as the model covers a large geographic region and produces tremendous volumes of output. Chapter VI is an overview of model central Arctic Ocean, Laptev Sea and East Siberian Sea oceanography. Chapter VII discusses the differences in boundary currents, eddies and energetics between the earlier 18 km resolution model and the current 9 km model, the secondary scientific focus of this report. The final chapter, Chapter VIII, contains a summary of key findings and recommendations resulting from these findings.

A. MODELING THE ARCTIC OCEAN

Since scientific study of the Arctic region began, theories regarding the forces governing Arctic Ocean circulation have varied between thermohaline forcing versus wind driven forcing. Nansen's original assertion (Nansen, 1902) was that differences in water temperature and salinity between the Greenland and Norwegian Seas and the Arctic Ocean caused water exchange between these basins. Recently it has been demonstrated there are different Arctic climatic states (Mysak et al., 1990; Proshutinsky and Johnson, 1997; Mysak and Venegas, 1998; Thompson and Wallace, 1998; Maslowski et al., 2000, 2001) that are primarily dependent on the large-scale atmospheric circulation. The overall complexity of the Arctic atmosphere-ice-ocean system has made understanding the driving, let alone dominant, forces difficult. A delicate balance exists between Atlantic and Pacific Ocean inflow, Arctic Ocean outflow and the flux balances of salt, heat and momentum. The upper ocean structure is strongly tied to the freshwater budget, which is influenced by ice growth and melt, limited precipitation and significant, seasonally-variable river runoff. Water mass modification takes place on the vast continental shelves; and density driven plumes from the shelves and Arctic Ocean outflow can affect mid and possibly deep water properties in the Arctic Ocean (Schauer et al., 1997) and its adjacent seas (Bourke and Paquette, 1991).

In comparison with the rest of the world oceans, the Arctic Ocean is weakly stratified in temperature, yet there is a strong, shallow halocline and the question of halocline maintenance is not completely resolved. The thermocline is significantly deeper than the halocline, and indicates the upper limit of the warm Atlantic Water. However, in recent years the thermocline has apparently begun to shoal (Morison et al., 1998, Steele and Boyd, 1998), with potentially significant consequences for the heat budget and the stability of the Arctic sea-ice cover if it continues. The cause of the shoaling and its future trend are not fully determined, yet they are thought to be related to variability and long term trends in the atmospheric circulation (Chapman and Walsh, 1993; Proshutinsky and Johnson, 1997). Another complication is the combination of complex bottom topography and a relatively strong Coriolis effect creating a topographic waveguide, influencing the predominantly barotropic flow of the Arctic Ocean. It is

apparent that there is agreement within the Arctic science community that both thermohaline and wind-driven forcing play important roles in Arctic Ocean circulation, yet there is still a tremendous need for a better understanding of the balance between Arctic Ocean dynamics and thermodynamics.

In attempting to represent a continuous process with a discrete system of equations, it becomes important to consider how the discretization will affect the final goal of a consistent and accurate numerical solution that converges toward the continuous solution. The choice of vertical coordinates in the model can introduce truncation errors, so the choice between z -level coordinates, sigma coordinates and isopycnal coordinates must be made consciously with an understanding of the strengths and weaknesses of each type (Mellor et al., 1998).

The z -level coordinate system divides the vertical dimension based on geopotential surfaces, or more simply put, individual horizontal layers of predetermined depth or thickness. This method makes for relatively straightforward computer coding and implementation. A weakness of this method has been the staircase representation of bottom topography. Advances in computer technology have permitted increases in the number of vertical levels, making this less of an issue at present. The chosen depths of the coordinate surfaces remain fixed throughout model integration and the resolution of the topography and vertical processes are limited to that of the chosen coordinate surfaces. At lower vertical resolutions, this can present a problem in resolving narrow ridges and sills and the bottom boundary layer over shallow shelves. Another problem associated with z -level models occurs with regard to vertical mixing and down slope flows of dense waters formed on a shelf. Roberts et al. (1996) noted that in order for dense water formed on the shelf to flow off the shelf and into a deep basin in a z -level model, it must mix several times horizontally and vertically. This causes excessive mixing of the dense water and it cannot maintain the density necessary to reach the deep or abyssal ocean. Introducing a parameterization which simulates mixing along isopycnal surfaces (Gent and McWilliams, 1990, Gent et al., 1995) into the model may help overcome this limitation.

In sigma coordinate models, the vertical coordinate becomes terrain following, where the lowest layer is, in essence, the bathymetry profile. This approach retains the vertical resolution over shallow regions, which may be lost in z-level or isopycnal coordinate models. However, near steep topography, the pressure gradient computed along sigma surfaces is significantly contaminated by the overwhelmingly large and unwanted vertical pressure gradient contribution. Sigma coordinate models often require smoothing the topography to overcome this difficulty and it is believed that the simulated ocean circulation becomes fundamentally distorted in the process.

Both z-level and sigma coordinate models suffer from diapycnal diffusion due to diffusion along coordinate surfaces that do not align with isopycnals. To alleviate this shortcoming, isopycnal coordinate models have been designed that divide the water column into layers of constant density. An exception is the uppermost layer, which is designated as the mixed layer and has a density field that varies in the horizontal. This approach comes from the belief, that below the mixed layer, mixing and property distribution in the ocean are oriented preferentially along surfaces of constant density, vice along geopotential surfaces. Isopycnal coordinate models do not suffer from the staircase problems of the z-level models and generate smaller horizontal pressure gradient errors than sigma coordinate models. A significant weakness of isopycnal coordinate models is the possibility of disappearing layers. Prior to running a simulation, the vertical coordinates are predefined as density surfaces of fixed value. If the shelf or deep basin water evolves into a much lighter or denser class of water that lies outside the range initially specified, then only the mixed layer will exist on the shelf or in the basin and all other layers will have been mixed out of existence. The result is poor resolution over the shelf or basin. In addition, very deep mixed layers lead to poor representation of Ekman flows.

The model in this project is a z-level coordinate model with 45 levels extending over 6250 m, which provides rather high vertical resolution in the Arctic Ocean. The top five layers are each 5 m thick and over 20 layers represent the top 500 m. The selection of layer depths will be discussed in the model description section.

The earliest attempts at modeling the large-scale circulation of the Arctic Ocean include Galt's (1973) barotropic ocean model and Semtner's (1973, 1976a) fourteen z-level, three-dimensional model. Hakkinen (1990) provides a summary of Arctic Ocean model development up to 1990; some of the more important advances are reviewed here. Significant features demonstrated by the models of Galt and Semtner include topography influencing the location of the Beaufort Gyre and limiting it to the Canadian Basin, wind forcing dominating flow in the Canadian Basin, thermohaline flow dominating circulation in the Eurasian Basin, and an Atlantic connection to the Arctic through the Barents Sea. The Galt (1973) model was forced using surface stress predicted from an ice model using annual mean winds. The Semtner (1976a) model was forced with wind stress computed from geostrophic velocities based on mean annual atmospheric pressure and an estimated drag coefficient. As both models were forced using annual means, the seasonal variations in ice cover and salt fluxes were not simulated.

Hibler and Bryan (1984, 1987) and Semtner (1987) presented the next step in model evolution with their coupled ice-ocean models using seasonal forcing. Hibler and Bryan (1984) coupled a fully dynamic-thermodynamic ice model with the Bryan-Cox 14 level ocean model (Bryan, 1969), using a derived geostrophic wind field from the First Global GARP Experiment, daily varying sea level pressures, monthly climatological air temperatures and humidities and seasonally varying river runoff. Climatological salinity and temperature data were used to relax the model ocean climatology towards the observed climatology. Semtner's (1987) model was similarly a multi-level ocean model coupled to an ice model, with a few important differences. The model used simplified ice dynamics by using bulk viscosity as the only internal sink for ice energy, a three level thermodynamic model of snow covered ice (Semtner 1976b), long-term monthly mean atmospheric forcing fields and most importantly, removed the relaxation of oceanic temperature and salinity values to climatology. Hibler and Bryan (1987) simulated the Barents and Greenland Sea ice edges reasonably well and demonstrated that oceanic currents greatly increase the ice drift in the East Greenland Current. Important results from Semtner (1987) include demonstrating that the Greenland Sea ice edge is controlled by upwelled heat from deep ocean convection, that the coastal shelves are the major ice

growth areas in the Arctic, and that river runoff has only localized effects on the ice cover. Additionally, from one of the Semtner (1987) case studies, it was shown that a 2° C increase in surface air temperature would result in the complete melting of the Arctic ice pack by the end of the melt season.

Preller and Posey (1989) formulated an ice-ocean model, based on Hibler's (1979) dynamic-thermodynamic ice model and Cox's (1984) z-level ocean model, that is currently used in ice edge and thickness forecasting for the United States Navy as the Polar Ice Prediction System (PIPS) 2.0. Initially, the PIPS methodology consisted of developing several regional high-resolution sea ice forecast models in areas of Navy interest. The current version of the PIPS 2.0 model (Cheng and Preller, 1996) includes all of the seasonally-ice-covered Northern Hemisphere seas and uses a grid resolution of 0.28 degrees (approximately 27 km) and 15 levels in the vertical. The development and implementation of the 1/12°, 45 level ocean model described in this project will be a component of the ice-ocean model system that will replace PIPS 2.0.

Hakinnen and Mellor (1992) adapted the Princeton Ocean Model (POM) to the Arctic and North Atlantic Oceans in the form of a 20 sigma level, approximately 8/10 degree (~85-km) resolution model. Their domain extends from a closed Bering Strait to roughly 15° S in the Atlantic Ocean. The smoothed bathymetry is derived from the National Geophysical Data Center (NGDC) TerrainBase database. The ocean depths in TerrainBase are essentially those of the NGDC ETOPO5, 5 minute resolution elevation/bathymetry dataset (TerrainBase summary documentation). Recent use of their sigma coordinate model is reported in Mauritzen and Hakinnen (1997), where they present a reasonably realistic representation of large-scale features. Yao et al. (2000) coupled a multi-category, variable thickness sea ice model to a 16-sigma level, 1/6° (~18-km) version of POM for their study of sea ice in the Labrador Sea. Their model is forced using monthly climatological atmospheric forcing. Initial conditions are derived from a gridded, objectively analyzed temperature and salinity dataset, which is used in order to improve the resolution of gradients near the shelf break. Their results show good agreement with the main features of the observed ice concentration and seasonal growth and retreat, although ice decay in the model is too rapid compared to observations. They

recommend an appropriate treatment of the atmospheric boundary layer over the ice to remedy this.

Initial efforts in isopycnal ocean modeling include Oberhuber (1993) and Aukrust and Oberhuber (1995). Currently, there are numerous isopycnal models in use, from the Navy Layered Ocean Model (NLOM), the Hallberg isopycnal model which is being run at the Geophysical Fluid Dynamics Laboratory (GFDL), and probably the most widely used isopycnal model, the Miami Isopycnal Coordinate Model (MICOM). A variation of MICOM adapted for Arctic studies is the Courant Institute of Mathematical Sciences Arctic Ocean Model (Holland et al., 1996). This model has 21 isopycnal layers, 1/4 degree (27-km) resolution, a modified mixed layer parameterization, two ice thickness categories, and viscous-plastic ice dynamics. A recent and unique modification is the introduction of a hybrid vertical coordinate system. The vertical coordinates in the model switch from isopycnal to fixed level surfaces for turbulent near surface waters, maintaining high resolution where it is needed most.

The Nansen Environmental and Remote Sensing Center (NERSC) uses a modified version of MICOM as well (Drange and Simonsen, 1997). This 23-layer version has coupled snow and ice modules, a bulk type mixed layer, and uses a general curvilinear, orthogonal coordinate system in the horizontal, giving it approximately 50-km resolution in the Nordic Seas. The domain includes the Arctic Ocean and the Atlantic Ocean south to the subtropics. Additional applications of isopycnal coordinate models are described in Mellor et al. (1999).

Kowalik and Proshutinsky (1994) conducted a modeling study to determine the importance of semidiurnal tides in the Arctic. They used a 14-km grid, 2-dimensional (vertically integrated) primitive equation model, with a domain including the Arctic Ocean, all of the Nordic Seas, and Baffin Bay. Their results compared favorably to tidal observations and showed how tidal current velocities in certain regions can greatly affect ice convergence and divergence and cause mixing over steep topographic features. This mixing can influence heat transfer to the surface, impacting polynya formation, ice melt, and ice growth.

Wang et al. (1994) presented results from a sigma level model, regarding three-dimensional circulation in Hudson Bay. The current version being run at the International Arctic Research Center at the University of Alaska, Fairbanks, is a variation of the Princeton Ocean Model (POM) sigma coordinate model, including the entire Arctic and North Atlantic. The coupled ice-ocean model has 27.5-km resolution, 16 vertical sigma levels, and prescribed salt and heat fluxes and wind stress. It is forced with NCAR/NCEP reanalysis daily atmospheric forcing, climatological freshwater runoff, and oceanic lateral boundary forcing. The ice model is a seven category, dynamic-thermodynamic model

A 30 z-level, 18km model of the Arctic Ocean and Nordic Seas was developed by researchers at the Naval Postgraduate School, Monterey (Parsons, 1995; Maslowski, 1996; Zhang et al., 1999). The model has a closed Bering Strait and specified river runoff in the form of temperature and salinity values (no mass inflow is specified), based on an annual climatological cycle. The regional model was developed to avoid the problem of specified transports at boundaries. One of the interesting aspects of their work was an independent experiment to find the most computationally efficient equation of state which also performed well in the extremely cold waters of the Arctic. A full description of the experiment is included in Parsons (1995), who found that the Bryan and Cox equation of state (Bryan and Cox, 1972) sacrificed the least accuracy and was the most computationally efficient. Among the ocean modeling case studies performed with their model was an inclusion of tides, resulting in stronger and more variable surface currents in shallow waters. At the time, it was the highest resolution three-dimensional model of the Arctic Ocean. The ~9 km ice-ocean model discussed in this project can be considered the third generation of this original model.

Nazarenko et al. (1997) and Eby and Holloway (1994) reported a 29 z-level, 55-km resolution model, based on the GFDL Modular Ocean Model (MOM). Their model has a rigid lid, and an internal stream function. Unique to their application, horizontal viscosity is replaced by eddy-topography rectification (called the Neptune effect) which simulates the dynamic and mixing effects of eddies without the resolution requirements. This parameterization allows for coarser grids and faster long-term integration, which is

useful for conducting multiple model runs, while varying certain conditions or parameters to test their relative importance. Case study comparisons of model runs with and without the Neptune effect show that some form of eddy parameterization is required at larger grid sizes in order to reasonably simulate the Arctic Ocean circulation.

Gerdes et al. (1997), from the Alfred Wegener Institute, Bremerhaven, Germany, are running a 1° (~110-km) resolution, 19 z-level version of the GFDL MOM-2 with a domain covering the entire North Atlantic north of 20° S. They are developing a 0.25° (28-km) resolution, 60 z-level model that will cover the North Atlantic north of 50° N. Boundary values for their higher resolution model will come from their 1° model. Other features of the new model will include a convective adjustment scheme that ensures homogenization of an unstable region within a finite number of steps, a rigid lid, quadratic bottom friction, viscous-plastic sea ice rheology volume (Gerdes et al., 1999). They will use the new model to simulate the propagation of Atlantic Water northward.

At the University of Washington, Zhang et al. (1998a and 1998b) are running a 21 z-level, 40-km resolution version of the GFDL MOM. Their model includes a rigid lid, coupled ice and snow model, and an embedded mixed layer. They present results from several case studies with weak restoring to climatological values and no restoring. They demonstrate the potential impact of no restoring and how it can prevent realistic representation of surface fluxes.

Maslowski et al. (2000, 2001) present results from the Naval Postgraduate School 18 km, 30 z-level primitive equation model, a farther evolution of their earlier project. Improvements include the use of the LANL POP code to run the model on massively parallel computers, inclusion of a coupled viscous-plastic rheology (Hibler, 1979), a dynamic-thermodynamic sea ice model adapted for parallel code, and inclusion of passive and active tracers. Surface temperature and salinity are restored toward the Levitus (Levitus et al., 1994; Levitus and Boyer, 1994) monthly climatology on a time scale of 1 year and 4 months, respectively. Fresh water inputs from the nine major Arctic rivers and the Bering Strait are prescribed. No mass is exchanged, but salinity and temperature are recalculated in their source regions, acting as a form of freshwater input. Initially, twenty years of model spin-up were forced with repeated 1979 ECMWF annual

atmospheric cycle and climatological freshwater data, initialized from an earlier 200-year integration using 1990-1994 ECMWF forcing. After spin-up, the model was driven by 1979-1993 ECMWF daily atmospheric forcing, simulating seasonal and inter-annual variability. In a separate experiment, 15 more years of repeated 1979 forcing were performed after the initial 20-year spin up. Limited change in model results indicated an approach toward equilibrium, with negligible drift. The addition of passive and active tracers has allowed more detailed analysis of transport pathways and the effects of different atmospheric regimes on circulation. During the interannual forcing experiment, recently observed changes in Arctic Ocean circulation and temperature structure were reasonably simulated, indicating that regional atmospheric forcing appears to be sufficient to drive changes in the ice-ocean system.

A follow on experiment included continued integration using 1994-1998 ECMWF daily atmospheric forcing and a multi-decade integration using repeated 1997/1998 atmospheric forcing (Maslowski et al., 2001). Results from this experiment show that a possible shift back toward the ‘traditional’ anticyclonic sea ice circulation regime may be occurring in the late 1990s. Ice motion difference fields comparing the early 80s and the early 90s illustrate a cyclonic shift in sea ice motion, or weakening of the Beaufort Gyre. Ice motion difference fields comparing the early 90s and the late 90s illustrate an anticyclonic shift, or strengthening of the Beaufort Gyre. Two-year average ice motion fields from 1981/82 show many similarities to those from 1997/98, especially when contrasted with the 1991/92 fields. The $1/12^\circ$ (9-km), 45 z-level model discussed here is a farther evolution of this model.

As computer speed and model resolution have increased, the representation of the Arctic Ocean in global models has improved as well. Initially, coarse resolution global models eliminated the Arctic Ocean. As resolution increased, models simulated the Arctic Ocean outflow with specified fluxes along a northern boundary from Greenland to Norway (Semtner and Chervin, 1992). Farther resolution increases and changes in model grids have resulted in more realistic representations of the Arctic in global models (Maslowski et al., 1998; McClean et al., 1998; Washington et al., 1998, 2000).

Maslowski et al. (1998) and McClean et al. (1998) presented results using a fully global, $1/3^\circ$ (~ 36 -km) version of the LANL POP forced with 1979-1993 ECMWF reanalysis products and 1994-1997 ECMWF operational data. The variability of the large-scale upper ocean circulation was analyzed and the observed shift in Arctic Ocean circulation was realistically simulated. Goosse et al. (1999) describe the flow through the Canadian Archipelago using a global ice-ocean model and Miller and Russell (1997) describe the interactions among river runoff, salinity, and sea ice using a global atmosphere-ice-ocean model.

The Parallel Climate Model (PCM) Effort has coupled the NCAR Community Climate Model (CCM) version 3, the LANL POP, a University of Texas river transport model and a sea ice model from the Naval Postgraduate School together in a massively parallel computer environment (Washington et al., 1998, 2000). The PCM has an average resolution of $2/3$ -degree latitude and longitude with increased latitudinal resolution near the equator of approximately $1/2$ -degree, 32 z-levels, and a rotated grid, eliminating the convergence at the poles. The sea ice model coupled to the PCM has a resolution of about 27 km, which provides a realistic Arctic simulation of eddy-permitting ocean and sea ice motion (Weatherly and Zhang, 2000.) The above review illustrates that dramatic improvements have been made in global climate modeling, yet concern still exists over misinterpretation of results or suspect results from improper representation of the Arctic (Battisti et al., 1997).

Regional and global Arctic Ocean modeling has been evolving towards models of increased physical complexity and higher resolution. The model developed here takes the field one step closer to the goal of a physically realistic, eddy resolving simulation. As the local radius of deformation in the Arctic is at or below 10 km, this model cannot be called eddy resolving. Due to its ability to resolve features on the order of ~ 30 km or greater, it is considered eddy-permitting. The high resolution enlarged domain, featuring an open Bering Strait and more accurate representation of the complex geometry of the vast Arctic shelves and the CAA, will assist in determining the importance of inter-basin and inter-ocean exchanges in Arctic Ocean circulation.

THIS PAGE INTENTIONALLY LEFT BLANK

II. MODEL DESCRIPTION AND METHODS

A. INTRODUCTION

The model domain (Figure 2.1), which includes the Sea of Japan, the Sea of Okhotsk, the sub-polar North Pacific and North Atlantic Oceans, the Arctic Ocean, the Canadian Arctic Archipelago (CAA), the Bering Sea and the Nordic Seas, was chosen to include all of the Northern Hemisphere seas that experience seasonal ice formation, in response to National Ice Center requirements. An added benefit of this chosen region is the inclusion of all major inflow and outflow areas of the Arctic Ocean. Additional benefits and drawbacks of the chosen region will be discussed in the grid and bathymetry section.

B. THE OCEAN MODEL

1. Physics

The ocean model is based on the Los Alamos National Laboratory (LANL) Parallel Ocean Program (POP) model (Dukowicz and Smith, 1994), which evolved from the Semtner and Chervin (1992) global ocean model with an added free surface (Killworth et al., 1991; Semtner, 1995). A benefit of using the POP code is that as the LANL team of researchers adds improvements to model physics and increases the numerical efficiency of the code, new versions can be readily implemented. The free surface allows for the incorporation of unsmoothed, high-resolution bathymetry. Due to computational constraints, many earlier ocean models were formulated using a rigid-lid assumption. To avoid numerical instability in rigid lid models, it was often necessary to smooth the bathymetry to eliminate excessively steep depth gradients, which had the potential to over-accelerate the flow along the bottom. The model assumes hydrostatic balance and makes the Boussinesq approximation. The finite difference scheme uses an Arakawa B-grid (Mesinger and Arakawa, 1976) and integrates the primitive equations in spherical coordinates. To eliminate the convergence of meridians at the North Pole inherent in spherical coordinates, the model grid was rotated off the pole, placing the model equator along the meridians 26° W and 164° E.

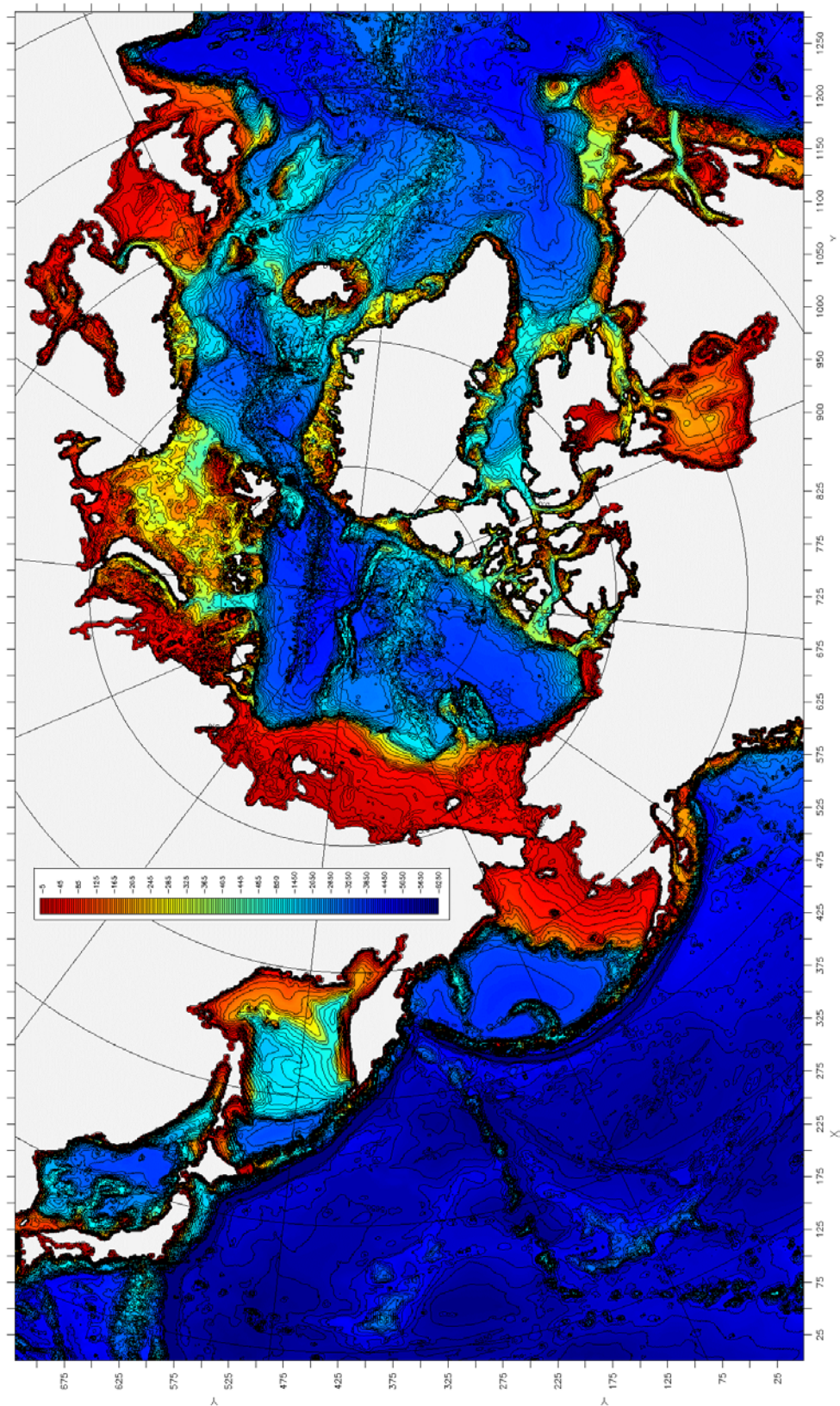


Figure 2.1. Model domain and combined IBCAO and ETOPO5 based bathymetry (m)

As in the 18-km model, the model includes the capability to add passive and active tracers which will prove useful in determining pathways of riverine outflow and contaminants. The model's prognostic variables and equations to solve for them are:

u and v in the horizontal momentum equations

$$\frac{\partial u}{\partial t} + L(u) - fv = -\frac{1}{\rho_o a \cos \varphi} \frac{\partial p}{\partial \lambda} + \frac{\partial}{\partial z} \left(K_M \frac{\partial u}{\partial z} \right) + B_M \nabla_H^4(u) \quad (1)$$

$$\frac{\partial v}{\partial t} + L(v) + fu = -\frac{1}{\rho_o a} \frac{\partial p}{\partial \varphi} + \frac{\partial}{\partial z} \left(K_M \frac{\partial v}{\partial z} \right) + B_M \nabla_H^4(v) \quad (2)$$

pressure (p) in the hydrostatic equation

$$\frac{\partial p}{\partial z} = -\rho g \quad (3)$$

vertical velocity (w) in the continuity equation

$$\frac{1}{a \cos \varphi} \frac{\partial u}{\partial \lambda} + \frac{1}{a \cos \varphi} \frac{\partial (v \cos \varphi)}{\partial \varphi} + \frac{\partial w}{\partial z} = 0 \quad (4)$$

potential temperature (T) and salinity (S) in the advection-diffusion equations

$$\frac{\partial T}{\partial t} + L(T) = \frac{\partial}{\partial z} \left(K_D \frac{\partial T}{\partial z} \right) + B_D \nabla_H^4(T) \quad (5)$$

$$\frac{\partial S}{\partial t} + L(S) = \frac{\partial}{\partial z} \left(K_D \frac{\partial S}{\partial z} \right) + B_D \nabla_H^4(S) \quad (6)$$

density (ρ) in the equation of state

$$\rho = \rho(S, T, p) \quad (7)$$

The subscripts M and D denote momentum and diffusion, respectively.

In order to maintain computational efficiency and accuracy, a modified version of the Bryan and Cox (1972) equation of state was used to compute density. Bryan and Cox use a polynomial fit to the Knudsen equation (Foffonof, 1962). Their approach was farther modified to best fit the full UNESCO Equation of State for Seawater (1981). Details of that approach can be found in Parsons (1995).

The variables contained in the above equations are defined as: model longitude λ , model latitude φ , depth z , time t , Earth's radius a , gravity acceleration g , mean density ρ_o , Coriolis parameter $f = 2\Omega \sin \Phi$ where Ω is the Earth's angular rotation speed and Φ is the true geographical latitude, biharmonic horizontal eddy viscosity $B_M = -1.25 \times 10^{18} \text{ cm}^4 \text{ s}^{-1}$ and diffusivity $B_D = -5 \times 10^{17} \text{ cm}^4 \text{ s}^{-1}$ coefficients, and vertical eddy viscosity K_M and diffusivity K_D coefficients. The values of the coefficients do not vary horizontally. The coefficients for vertical mixing are calculated as a function of Richardson number using a modified Munk and Anderson (1948) approach with guidance adopted from Brooks (1994) and Endoh et al. (1981). The advection operator is defined as:

$$L(\sigma) = \frac{1}{a \cos \varphi} \frac{\partial}{\partial \lambda} (u\sigma) + \frac{1}{a \cos \varphi} \frac{\partial}{\partial \varphi} (v\sigma \cos \varphi) + \frac{\partial}{\partial z} (w\sigma) \quad (8)$$

The horizontal Laplacian operator is:

$$\nabla_H^2 \sigma = \frac{1}{a^2 \cos^2 \varphi} \frac{\partial^2 \sigma}{\partial \lambda^2} + \frac{1}{a^2 \cos \varphi} \frac{\partial}{\partial \varphi} \left(\cos \varphi \frac{\partial \sigma}{\partial \varphi} \right) \quad (9)$$

and the horizontal biharmonic operator is:

$$\nabla_H^4 \sigma = \frac{1}{a^2 \cos^2 \varphi} \frac{\partial^2}{\partial \lambda^2} (\nabla_H^2 \sigma) + \frac{1}{a^2 \cos \varphi} \frac{\partial}{\partial \varphi} \left(\cos \varphi \frac{\partial}{\partial \varphi} (\nabla_H^2 \sigma) \right) \quad (10)$$

where σ is a dummy variable.

A no-slip boundary condition is imposed at the lateral walls, such that $u=v=0$. No flux of heat or salt is allowed through the boundary. The impact of this boundary condition will become more apparent during the discussion of flow through the narrow Canadian Arctic Archipelago channels. At the bottom, flow is required to follow the slope of the bathymetry and no fluxes are allowed through the bottom. Bottom stress (τ_b) is a quadratic approximation using the bottom total velocity vector (\vec{U}), a bottom drag coefficient (C_d) and the thickness of the bottom layer (d) in the form:

$$\frac{\tau_b}{\rho} = \frac{C_d \overline{U} |\vec{U}|}{d^2} \quad (11)$$

The vertical velocity at the surface is allowed to be a function of the sea surface height η (free surface):

$$w = \frac{\partial \eta}{\partial z} \text{ at } z = 0 \quad (12)$$

By allowing a free surface, the model is required to explicitly solve both the barotropic and baroclinic components of the motion. The barotropic motions are defined through the shallow water equations:

Barotropic momentum (U, V)

$$\frac{\partial U}{\partial t} - fV = -\frac{1}{a \cos \phi} gH \frac{\partial \eta}{\partial \lambda} + \nabla_H^4 U + X \quad (13)$$

$$\frac{\partial V}{\partial t} + fU = -\frac{1}{a} gH \frac{\partial \eta}{\partial \phi} + \nabla_H^4 V + Y \quad (14)$$

Free surface hydrostatic relationship:

$$\frac{P_{surf}}{\rho_o} = g\eta(\lambda, \phi, t) \quad (15)$$

Continuity in terms of sea surface height:

$$\frac{\partial \eta}{\partial t} + \frac{1}{a \cos \phi} \frac{\partial U}{\partial \lambda} + \frac{1}{a \cos \phi} \frac{\partial}{\partial \phi} (v \cos \phi) = 0 \quad (16)$$

where $-H$ is the depth of the water column and the vertically integrated (barotropic) mass flux is defined as:

$$U = \int_{-H}^{\eta} u dz \quad (17)$$

$$V = \int_{-H}^{\eta} v dz. \quad (18)$$

The forcing terms for the barotropic field are defined as follows where F^u and F^v are the turbulent friction terms in the u and v horizontal momentum equations:

$$X = -\frac{1}{a \cos \phi} \frac{\partial}{\partial \lambda} \left[\int_{-H}^{\eta} u^2 dz \right] - \frac{1}{a} \frac{\partial}{\partial \phi} \left[\int_{-H}^{\eta} uv dz \right] - \frac{1}{a \cos \phi} \left[\int_{-H}^{\eta} dz \int_z^0 g \frac{\partial \rho}{\partial \lambda} dz \right] + \int_{-H}^{\eta} F^u dz \quad (19)$$

$$Y = -\frac{1}{a \cos \phi} \frac{\partial}{\partial \lambda} \left[\int_{-H}^{\eta} uv dz \right] - \frac{1}{a} \frac{\partial}{\partial \phi} \left[\int_{-H}^{\eta} v^2 dz \right] - \frac{1}{a} \left[\int_{-H}^{\eta} dz \int_z^0 g \frac{\partial \rho}{\partial \phi} dz \right] + \int_{-H}^{\eta} F^v dz. \quad (20)$$

2. Grid and bathymetry

The model horizontal grid contains 1280x720 points. The high resolution, equivalent to $1/12^\circ$ or approximately 9.26 kilometers, and the large domain will properly include most of the important processes in the Arctic Ocean and allow more realistic exchanges between the Pacific Ocean, the Arctic Ocean, the CAA and the North Atlantic Ocean. Realistically simulating these exchanges is important as the inflow of Pacific and Atlantic water into the Arctic provides thermohaline forcing in the Arctic Ocean. Additionally, the outflow from the Arctic Ocean, through the CAA and Fram Strait, influence deep-water formation in the North Atlantic and ultimately the global thermohaline circulation as described by Broecker (1991). At this resolution, the model is not yet eddy resolving, but it can be considered eddy permitting, as it will resolve features with a diameter on the order of ~ 30 km or larger. Vertically, the model is divided into 45 z-coordinate levels (Table 1). The choice of z-levels over other vertical coordinates was made primarily as the existing code is written for a z-level model, plus it was felt this larger number of levels will overcome some of the staircase bathymetry problems inherent in z-level models. The eleven layers in the first 100 m and nineteen layers in the first 500 m are chosen to provide accurate representation of the vast Arctic continental shelves and slopes. The complex bathymetry of the deep basins and steep submarine ridges are well represented by twenty-two 200-300 m thick layers from 1000 to 6250 m deep.

The maximum depth in the model is set to 6250 m. This precludes modeling the deep ocean trenches in the Pacific Ocean, but it is felt this will not adversely impact the

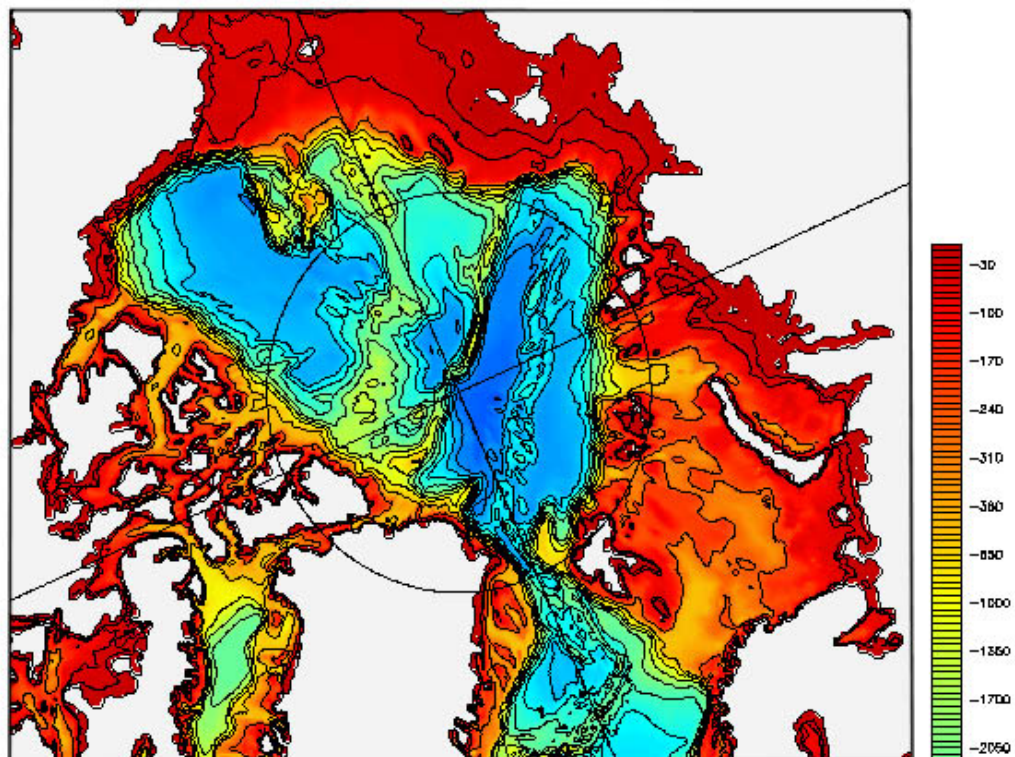
Layer	Thickness	Lower depth	Midpoint	dtl
1	5.0	5.0	2.5	1.0
2	5.0	10.0	7.5	1.0
3	5.0	15.0	12.5	1.0
4	5.0	20.0	17.5	1.0
5	6.0	26.0	23.0	1.0
6	7.3	33.3	29.7	1.0
7	8.8	42.1	37.7	1.0
8	10.6	52.7	47.4	1.0
9	12.8	65.4	59.1	1.0
10	15.4	80.8	73.1	1.0
11	18.6	99.4	90.1	1.0
12	22.4	121.8	110.6	1.0
13	27.0	148.9	135.4	1.0
14	32.6	181.5	165.2	1.0
15	39.3	220.8	201.2	1.0
16	47.5	268.3	244.6	1.1
17	57.3	325.5	296.9	1.3
18	69.1	394.6	360.1	1.6
19	83.3	477.9	436.3	2.0
20	100.5	578.4	528.2	2.6
21	121.6	700.0	639.2	3.3
22	150.0	850.0	775.0	4.0
23	200.0	1050.0	950.0	4.7
24	200.0	1250.0	1150.0	5.4
25	200.0	1450.0	1350.0	6.1
26	200.0	1650.0	1550.0	6.8
27	200.0	1850.0	1750.0	7.5
28	200.0	2050.0	1950.0	8.2
29	200.0	2250.0	2150.0	8.9
30	200.0	2450.0	2350.0	9.4
31	200.0	2650.0	2550.0	9.7
32	200.0	2850.0	2750.0	9.9
33	200.0	3050.0	2950.0	10.0
34	200.0	3250.0	3150.0	10.0
35	250.0	3500.0	3375.0	10.0
36	250.0	3750.0	3625.0	10.0
37	250.0	4000.0	3875.0	10.0
38	250.0	4250.0	4125.0	10.0
39	250.0	4500.0	4375.0	10.0
40	250.0	4750.0	4625.0	10.0
41	300.0	5050.0	4900.0	10.0
42	300.0	5350.0	5200.0	10.0
43	300.0	5650.0	5500.0	10.0
44	300.0	5950.0	5800.0	10.0
45	300.0	6250.0	6100.0	10.0

Table 2.1. Vertical distribution of model levels. The fifth column, *dtl*, indicates the multiplication factor that was applied to the temperature and salinity diffusion equations while deep acceleration was active.

goals of the simulation. The improved vertical resolution will result in improved representation of vital shelf processes, such as water mass formation and modification (Munchow and Carmack, 1997), intermediate and deep-water flow along the submarine ridges, and transports into and out of the Arctic Ocean. Better simulation of transports through the CAA may improve understanding of the relationships between atmospheric forcing, preferred Arctic freshwater outflow paths and convection in the Greenland and Labrador Sea (Rudels, 1986; Dickson et al., 1996.)

The 2.5 km resolution digital Arctic bathymetry database, developed by the IOC/IASC/IHO Editorial Board for the International Bathymetric Chart of the Arctic Ocean (IBCAO, Jakobsson et al., 2000), has been interpolated onto the model grid. See Figure 2.2 for a comparison of central Arctic Ocean bathymetry between the two model bathymetry fields. This high-resolution digital bathymetry dataset, which contains all available bathymetric data north of 64° N, was compiled by the IBCAO editorial board, an international organization partially funded by the Office of Naval Research. Participating countries include the United States, Russia, Iceland, Norway, Denmark, Germany and Canada. However, integration with the improved bathymetry has not begun. Due to significant differences in some regions, such as the Lomonosov Ridge where ocean points in the ETOPO5 based bathymetry are now land points in the IBCAO based bathymetry, the existing restart files cannot be used to continue the integration from its current point. Based on available computer resources and integration time (one year of model time requires over a week of integration on 128 processors of the Cray T3E-900 at the Arctic Region Supercomputer Center, Fairbanks, Alaska), the decision was made to continue integration using the modified ETOPO5-based bathymetry vice restarting the model from a cold start, losing the 15 years of spinup already completed. An effort is underway to interpolate the old restart files (upwards of ~3.5 Gb of data) onto the IBCAO grid. The model bathymetry for all of the data presented here is based primarily on the ETOPO5, 5-minute resolution global elevation database from the NOAA

ETOPO5 bathymetry database mapped to model grid (with modifications)



IBCAO bathymetry database mapped to model grid

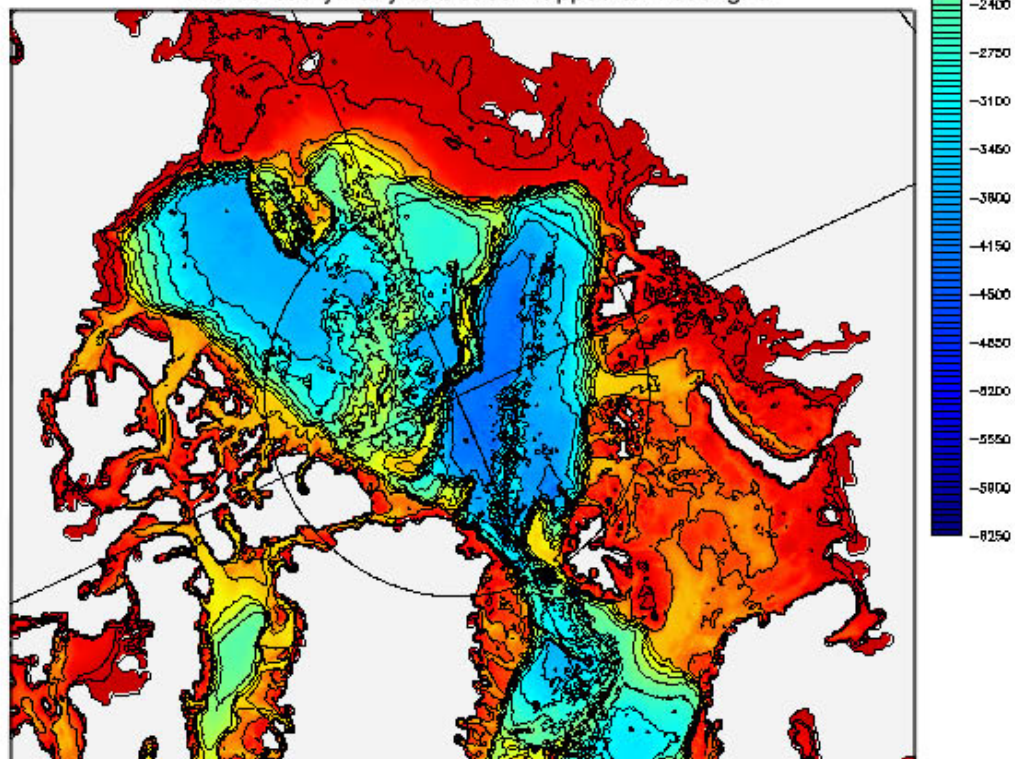


Figure 2.2. Model bathymetry derived from the ~9 km resolution ETOPO5 database (top) and the 2.5 km resolution IBCAO database (bottom).

National Geophysical Data Center, mapped onto model coordinates. Additional bathymetry data from recently declassified U. S. and Royal Navy submarine tracks, as well as Navy Research Lab, Canadian Hydrographic Service and Russian hydrographic service charts were used to correct known ETOPO5 deficiencies in the Canadian Arctic Archipelago, the central Lomonosov Ridge, the Siberian Shelf Seas and off the east coast of Greenland.

A significant amount of time was spent manually checking narrow passages, deep ridges and all coastline points to ensure key channels were kept open and to remove one-to-three grid-point-wide coastal features. Channels, bays, ridges and sills were examined in order to maintain a minimum of two velocity points across their narrowest area. The model uses the surrounding temperature and salinity (T/S) points in the calculation of velocity and the bathymetry is defined on the T/S grid as well. If any of the four points surrounding a velocity point is land, where T/S values are set to zero, the corresponding velocity point is then set to zero as well due to the no-slip boundary condition imposed in the model, in which velocity at the coastline must equal zero. In order for there to be flow through a narrow opening, the channel must be defined by at least four grid points. This minimum-opening configuration would allow velocity at only the center velocity point in the channel (Figure 2.3). Coastal features less than three grid points wide were either enlarged to four grid points or removed to increase the efficiency of the model.

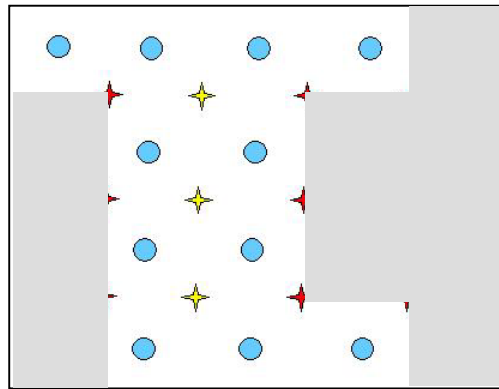


Figure 2.3. Hypothetical channel configuration on an Arakawa B grid. Circles indicate temperature and salinity grid points, stars = velocity grid points. Green circles = land points, blue circles = ocean points; red stars = zero velocity points; and yellow stars = non-zero velocity points, allowing flow through the channel. Gray shading represents land.

There is a routine that runs during the initial setup of the integration, which checks the grid for small features and removes them. Smoothing the coastline prior to running the mode increases the efficiency of the integration.

An additional modification to the bathymetry was the creation of an 18 grid point wide (~162 km), 500 m deep U-shaped channel through North America, south of Hudson Bay, connecting the Atlantic Ocean to the Pacific Ocean (Figure 2.4). The bathymetry at each of the ends was modified to facilitate smooth flow into and out of the channel. The channel was added to provide a return path for the flow of water from the Pacific Ocean, through the Arctic Ocean, to the Atlantic Ocean. A westward wind forcing of 1.2 dyne

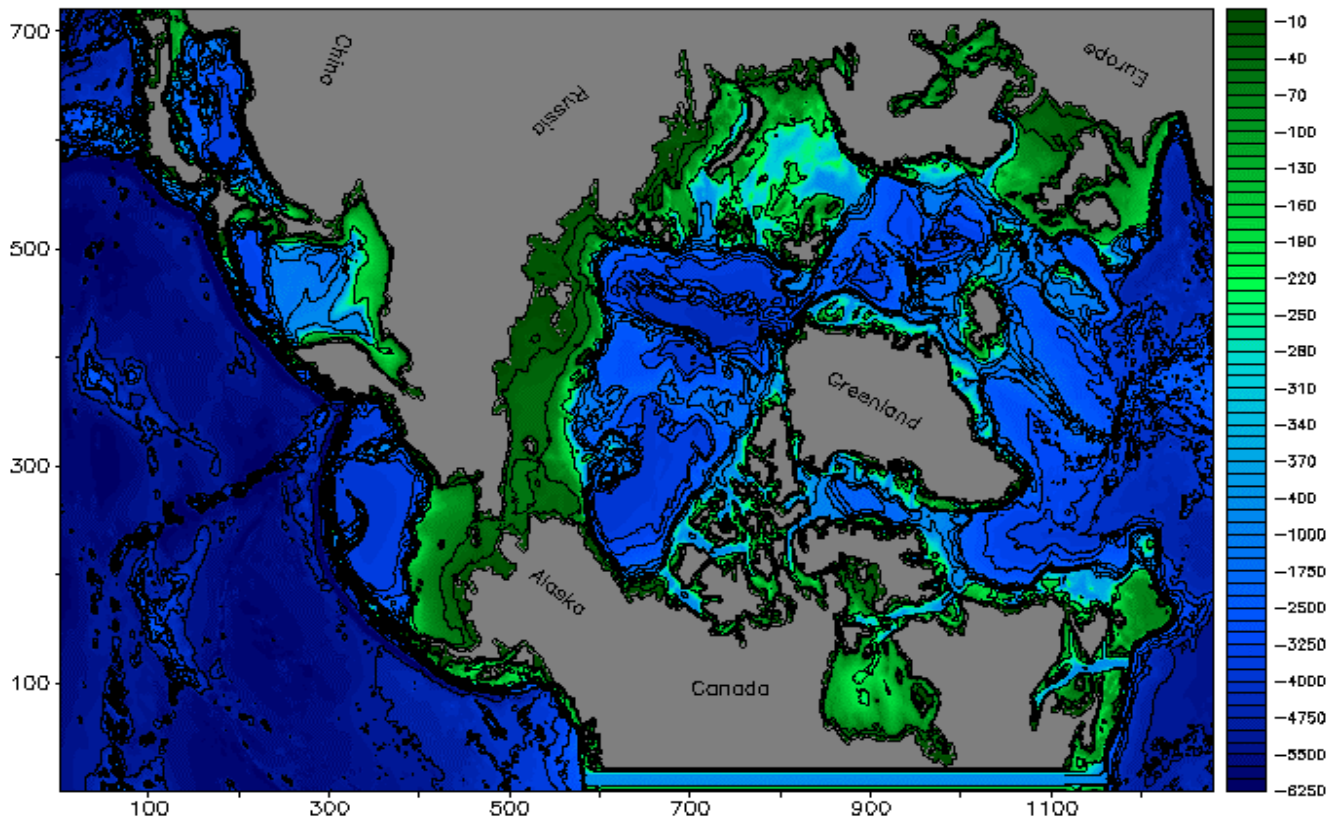


Figure 2.4. Model domain and ETOPO5 based bathymetry. Note the artificial "North American Channel" connecting the Atlantic Ocean and the Pacific Ocean along the bottom of the figure. Depth contours at 25, 50, 200, 500, 1000, 1500, 2000, 3000, 3500, 4000 and 5000 m in black.

cm^{-2} is prescribed along the channel, which appears to help maintain an average northward volume transport varying between 0.5 and 0.8 Sv into the Arctic Ocean. Bering Strait circulation and transports will be discussed in more detail in Chapter V.

3. Forcing

During spin-up, the model was forced using a 15-year mean, annual cycle of daily averaged atmospheric forcing derived from the European Center for Medium Range Weather Forecasting 1979-1993 reanalyzed data (ERA-15, Gibson et al., 1999, Figure 2.5). Forcing fields include 10 m elevation east-west and north-south (u and v) wind velocity components, surface pressure, temperature and dewpoint, and long-wave and short wave radiation. The $\sim 1.125^\circ$ resolution forcing data were first averaged over 15 years and then interpolated onto the model grid. The atmospheric forcing is an average from years dominated by both anticyclonic and cyclonic regimes, with a slight bias toward the anticyclonic or "traditional" regime. Comparison of the two-year mean 0-50 m Arctic Ocean circulation pattern with representative ocean surface circulation patterns

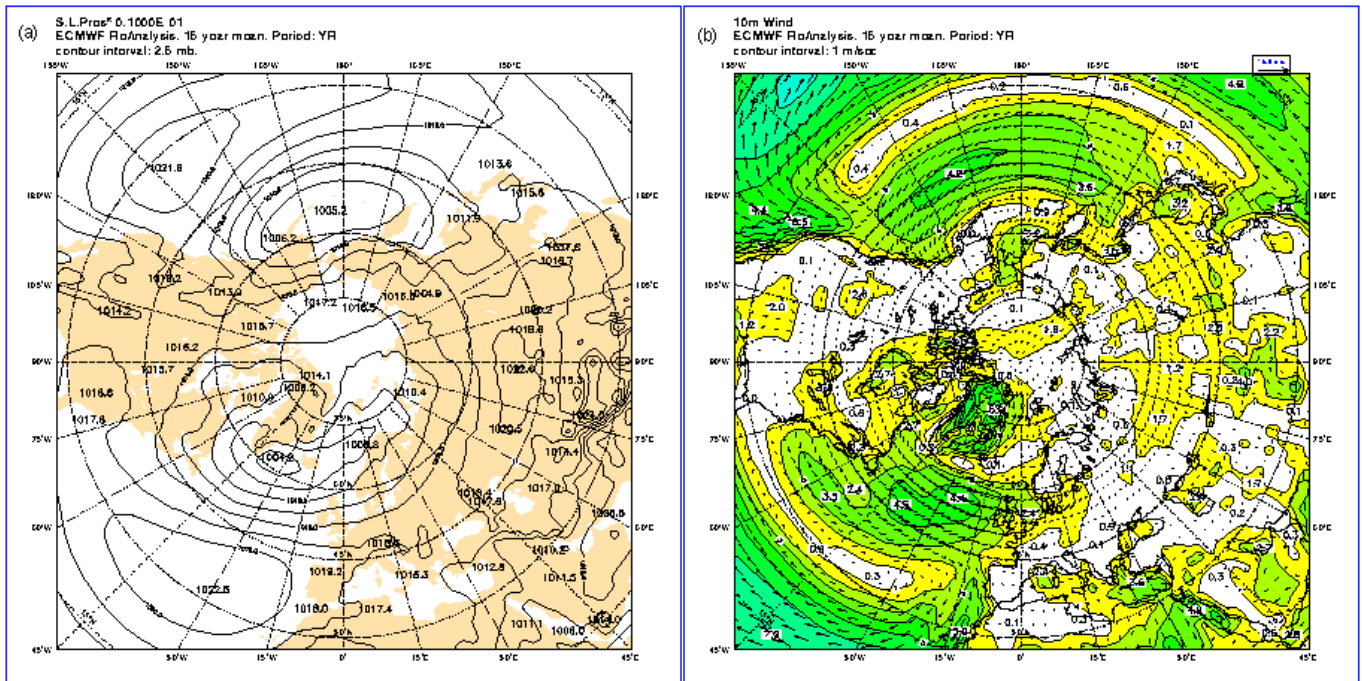


Figure 2.5. Selected 16 year mean (1979-1984) fields from the ECMWF ERA-15 reanalysis products. (a) Sea Level Pressure, (b) 10 m wind velocity. From the ECMWF ERA-15 Picture Gallery (http://wms.ecmwf.int/research/era/Era-15_Composites_Surface.html).

for each regime (Proshutinsky and Johnson, 1997; Maslowski et al., 2000; Maslowski et al., 2001) shows a flow in between the two extremes, with a medium-sized Beaufort Gyre and a Transpolar Drift Stream aligned along the Mendeleyev Ridge. However, calculation of a five-year average of net ice growth in a region bounded by Bering Strait and Fram Strait revealed a net annual ice growth of approximately 7.1 cm per year. This net ice growth suggests that over long periods of integration, the slight bias toward the anticyclonic atmospheric regime in this particular choice of forcing can have a significant impact on sea ice and ocean properties. During the planned 1979-2000 “hindcast” integration the model will be forced using daily varying atmospheric forcing from ECMWF reanalyses and operational data, for the period 1979-2000. In its operational forecast mode the model will be run at the Fleet Numerical Meteorology and Oceanography Center, Monterey and forced with NOGAPS forecast products.

At this point, the model has been integrated for 27 years using the repeated 15-year average climatology, followed by 6 years of repeated 1979 forcing and three repeats of 1979-1981 forcing (9 years). The repeated 1979 forcing was used in an effort to baseline the model towards conditions of the late 1970’s prior to beginning the 1979-2000 integration. However, after several years of repeated 1979 forcing, increases in ice concentration and thickness were noted and the repeated 1979-1981 cycle of forcing was started in an attempt to avoid continually forcing the model with a “cold” year.

From a time series of the daily mean air temperature over the central Arctic (Figure 2.6), 1979 is, on the average, colder than the 1979-1993, 15 year mean forcing,

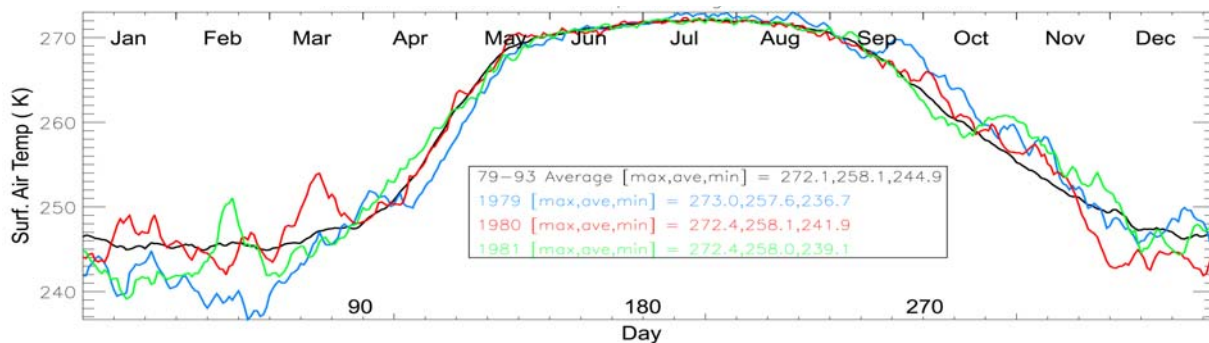


Figure 2.6. 365 day time series of daily average surface air temperature over the Arctic basin from ECMWF reanalysis products. For this illustration, the Arctic Basin is defined as the region enclosed by Fram Strait and the Bering Strait. Figure courtesy of Don Stark.

and 1981 is warmer. Comparison of annual mean ice thickness data near the end of the repeated 1979 forcing and following two cycles of 1979-1981 forcing (not shown) indicates a decrease in the central Arctic Ocean ice thickness after the application of the repeated 1979-1981 forcing cycle.

The ocean was started from rest and initialized using 3-dimensional temperature and salinity fields from the University of Washington Polar Science Center Hydrographic Climatology 1.0 (PHC, Steele et al., 2000) interpolated on to the model grid. The PHC is a combination of the 1998 version of the World Ocean Atlas (Antonov et al., 1998; Boyer et al., 1998) with the regional Arctic Ocean Atlas (EWG, 1997; 1998). The ocean surface level, 5 m thick, is restored on a monthly timescale to the monthly average PHC climatology, as a correction term to the explicitly calculated fluxes between the ocean and overlying atmosphere or sea ice. The restoring terms for temperature and salinity are applied to the right hand side of equations (5) and (6) and are of the form $-R_t(T-T_o)$ and $-R_s(S-S_o)$, respectively. R_t and R_s are the restoring constants and are set to $1/(30 \text{ days})$ for the surface level and $1/(10 \text{ days})$ at the domain boundaries, for both temperature and salinity. T and S are the calculated temperature salinity values and T_o and S_o are the PHC climatological temperature and salinity values at that grid point.

A 4° wide, or 48 grid point thick, curtain along the model's southern ocean boundary points ($x=1:48$ and $x=1232:1280$, $y=1:720$) is restored on a ten day timescale to the annual average PHC temperature and salinity climatology. A 2° wide, or 24 grid point thick, curtain along the model's western and eastern ocean boundary points ($y=1:24$ and $y=696:720$, $x=1:1280$) is restored on a ten day timescale to the annual average PHC temperature and salinity climatology. The restoring timescale increases linearly by a factor of ten, from 10 days to 240 days, over the next 24 grid points toward the center of the model domain (i.e. along the Pacific Ocean boundary, the restoring timescale at $x=71$ is 230 days, $x=72$ is 240 days. For $x=73$ or greater, until $x=1208$ at the opposite boundary, there is no deep ocean restoring). The curtain restoring at the model boundaries partially compensates for the effects of strong mid-latitude currents in the vicinity of the domain boundaries. The boundaries are far enough away from the primary region of interest so that the influence of the curtain restoring on the central Arctic Ocean

ice and circulation was felt to be minimal. However the impact of the boundary is seen in the western North Atlantic, as ice flow out of the Labrador Sea turns east vice following the coast to the south, due to the strong eastward flowing model North Atlantic Current. Additionally, the impact of the nature of the restoring climatology (annual mean vice monthly mean) will be seen later.

In considering ocean climatology bias, the time span of the merged ocean climatology datasets (Steele et al., 2000, Table 1) shows the 1946 to 1994 data were collected during periods of anticyclonic and cyclonic atmospheric forcing regimes (Proshutinsky and Johnson, 1997; Johnson et al., 1999). Thus, it is felt there is no strong ocean climatology bias toward either regime. The combination of the EWG Arctic Ocean Atlas with the World Ocean Atlas (WOA) has helped remove much of the strong summer bias in the WOA Arctic Ocean climatology. A planned improvement in oceanic restoring is modification of the temperature and salinity restoring fields to monthly mean values from PHC 2.0, vice annual mean PHC 1.0 values. Improvements in PHC 2.0 include a modification of the interpolation scheme used to merge the two data sets that has resulted in larger and more realistic temperature variability in the Nordic Seas.

4. Experiment Design

The project includes three main phases: 1) Model development, implementation and integration; 2) Model verification; and 3) Data analysis. Phases 2 and 3 began following several decades of spin up.

Model development and implementation included modifying the existing code, building the new model domain, and preparing the initial and restoring ocean temperature and salinity fields and the atmospheric forcing fields. Model integration included the spin up phase simulations. A team of researchers was involved with the development of the coupled ice-ocean model to meet the Navy's PIPS upgrade contract requirements. This team included Dr. Wieslaw Maslowski, Dr. Bert Semtner, Dr. Don Stark, Dr. Yuxia Zhang, and Dr. Waldemar Walczowski along with myself and collaborators from other institutions. The research presented here is primarily focused on the ocean model. This report includes a description of the ice model, and where applicable, comparisons of modeled and observed ice characteristics in the major inflow and outflow regions to the

Arctic Ocean. Ice data assimilation has not been incorporated into the model yet and is outside the scope of this project.

The model code has been modified for the new domain. Changes included decreasing the model timestep to 8 minutes to maintain computational stability (CFL criteria) and decreasing the horizontal mixing coefficients (the momentum horizontal mixing coefficient is approximately eight times smaller than in the 18-km version). The final modification to model bathymetry, mapping the 2.5 km IBCAO dataset to the model grid, has been completed but has not been fully implemented as described above. The initial and restoring ocean temperature and salinity fields have been mapped on to the model grid from the merged Environmental Working Group/Levitus climatology. The 15-year-average daily atmospheric forcing fields have been mapped onto the model grid from 1979-1993 ECMWF reanalysis products. Spin up is nearing completion and we so far have completed over four decades of integration.

The verification phase will determine the success of the new model in simulating observed Arctic Ocean means, climatology and observed seasonal variability. Due to the nature of the spin up to date (repeat forcing of 365 days of 15 year mean, repeated 1979 forcing and repeated 1979-1981 forcing), interannual variability will not be addressed in this report. It is anticipated that the 9 km model will accurately represent the Arctic Ocean response to differing atmospheric forcing regimes as the 18 km model, driven by daily varying realistic atmospheric forcing, has been shown to accurately represent the decadal water mass shift in the central Arctic Ocean (Maslowski et al., 2000). The differences between the two models will be discussed in more detail in Chapter VII.

The starting point of the verification phase will be the verification of model spin up output in contrast with climatology. This will involve calculating three year means and generating selected fields of ocean velocity, temperature and salinity at several depths and comparing their seasonal and spatial variability with similar fields from the merged National Snow and Ice Data Center (NSIDC) Environmental Working Group (EWG) -Levitus climatology, the EWG Summer and Winter Climatological atlases and other available data sets.

One of the primary scientific focuses of this project will be a comparison of observed and modeled fluxes of mass, heat and salt into and out of the Arctic Ocean through the Barents Seas, the Canadian Arctic Archipelago, and the Bering Strait/Chukchi Sea region. The magnitude and variability of energy and mass transfers into and out of the Arctic Ocean has not been well determined. This comparison of observed and modeled fluxes will be performed in an attempt to clarify the role of inter-ocean exchanges and thermohaline forcing versus large scale atmospheric forcing in driving changes in the modeled circulation and Arctic Ocean variability. Questions to be considered include: Is atmospheric forcing alone sufficient to drive the majority of the observed Arctic Ocean variability?; How much of the variability is controlled by the thermohaline circulation?

The other main scientific focus of this project will be a quantitative analysis of the importance of the resolution change from 18 km to 9 km, involving model energetics, the representation of eddies, currents, and resolution of the complex bathymetry, islands and inlets. This study will include a statistical comparison of eddy kinetic energy between the 18 km model and the 9 km model within a similar sized region. Comparison plots of sea surface height, temperature, salinity and velocity fields will also be used. With the greater density of oceanographic observations in the Labrador and Nordic Seas, it will also be possible to compare fields such as eddy kinetic energy and mass transport/stream function between the 9 km model, the 18 km model and observations.

C. THE ICE MODEL

The Hibler (1979) style sea ice model, optimized for massively parallel architectures, uses a viscous-plastic ice rheology (Zhang et al., 1999) and the zero-layer approximation for heat conduction through ice (Semtner, 1976). The surface heat budget follows Parkinson and Washington (1979). The ice model time step is 48 minutes. The ice model was initialized with a uniform 2 m thick layer of ice over water areas having a temperature less than 0.0° C. This method, a departure from a common approach in regional models which places a uniform layer of ice over the entire domain, was chosen to avoid the shock to the surface freshwater budgets of the North Atlantic and North

Pacific Oceans which would result from melting a slab of ice in regions where sea ice is not normally present.

The improved ice model, which is currently being implemented, consists of the energy-conserving thermodynamic model of Bitz and Lipscomb (1999), and the Zhang and Hibler (1997) viscous-plastic ice dynamics model. Improvements over previous ice models include a non-linear vertical temperature profile in the ice, vertically varying ice salinity, a snow layer, an explicit brine pocket parameterization, and a multi category (in this case five categories) ice thickness distribution. The improved energy conserving, dynamic-thermodynamic ice model will have a Lagrangian ice thickness distribution, i.e., the ice within a single category can vary in thickness with time, simplifying heat and mass transfer among categories. All model ice data presented here is from the earlier version Hibler/Zhang ice model.

D. ANALYSIS METHODS

The model results used in this analysis consist of 24 monthly averaged ocean data sets from spinup years 17 and 18, plus 365 daily ocean and ice files from year 18 for the Barents Sea analysis, 36 monthly averaged ocean data sets from years 1979-1981 of the first application of this three year repeated forcing, 365 daily ocean data sets from 1980 and 365 daily ice data sets from 1980 for the remaining regional analyses. The analyses were performed as the output files became available.

At this time in the spinup, the 365 days of atmospheric forcing, each day an average of 15 years, has been applied 27 times, repeated 1979 forcing has been applied for 6 years and the repeated 1979-1981 forcing has been applied three times. At the beginning of the second decade, deep-acceleration was turned on. This is a numerical method used to save computational time, which increases the timestep applied to temperature and salinity diffusion calculations at depth. The timestep in the top sixteen layers (0-220 m) remains 8 min (Table 2.1). Below 220 m, the timestep applied to the temperature and salinity diffusion equations increases smoothly by a factor from one to ten, through level 33 (3050 m). Below 3050 m in the model, the deep ocean evolves ten times faster than the upper 220 m. Using this method, through the second decade of

model integration, the deep ocean has been effectively integrated for 100 years. Deep-acceleration was turned off in the third decade of spinup. Farther analysis of the impact of this numerical method on the vertical distribution of temperature and salinity in the Arctic Ocean, a region particularly sensitive to large changes in salinity is presented in Chapters 5 and 6..

The model verification portion of this report is divided into geographic sub-regions, with the primary focus on regions of inflow and outflow to the Arctic Ocean. A brief description of the general circulation of the central Arctic Ocean and the Siberian shelf seas is included, following the discussions on the three major inflow/outflow regions, for completeness. The progression within each section is 1) a discussion of the observed physical oceanography based on published literature or available data; 2) a discussion of model physical oceanography, covering first the long term mean circulation and then seasonal variability; followed by a discussion of 3), mass, heat and salt transports and 4) eddy kinetic energy. The discussion section following the regional analyses serves to tie together the significant model strengths and weaknesses in certain regions or common to all regions. Following the verification portion, is a section on comparison of two similar models of different resolution and a discussion of the gains realized due to increasing the resolution.

THIS PAGE INTENTIONALLY LEFT BLANK

III. BARENTS SEA AND FRAM STRAIT

A. OBSERVED PHYSICAL OCEANOGRAPHY

Our understanding of the importance of the water mass transformations that occur in the Barents Sea has continued to evolve since it was first recognized that there were two possible paths for Atlantic water to enter the Arctic Ocean (Nansen, 1906). Many processes, such as the overall mass and property budgets of the Barents Sea and the monthly, seasonal and annual current variability, are still undetermined and the subject of much discussion. A factor contributing to the limited understanding of the Barents Sea is that many of the theories and conclusions are necessarily drawn from summer data, due to inaccessibility brought about by harsh wintertime conditions in the region. Efforts are underway, such as the European Union funded program “Variability of Exchanges in the Northern Seas” (VEINS), to obtain much needed long-term time series. Several recent studies (Harms, 1997; Loeng et al., 1997; Ozhigin et al., 2000; Ingvaldsen et al., 2000) have used a combination of observations and modeling and some of the few available long-term time series to update long-standing theories on Barents Sea circulation and variability of the Atlantic inflow to the Barents Sea.

The warm, salty northward flowing Norwegian Atlantic Current splits in the vicinity of 70° N, with a portion of the flow entering the Barents Sea through the Barents Sea Opening (BSO) as the North Cape Current, and the remainder continuing north along the Norwegian Sea/Barents Sea shelf break toward Svalbard, becoming the West Spitsbergen Current (Aagaard, 1989). See Figure 3.1 for a map of the region and locations of key features. For the purposes of this discussion, the two main paths of flow into the Barents Sea from the Norwegian Sea are the Norwegian Coastal Current and the North Cape Current. The Norwegian Coastal Current is the fresher of the two being derived from the outflow of the brackish Baltic Sea, and travels closest to the Norwegian coast. The North Cape Current is defined as that branch entering the Barents Sea primarily via the Bear Island Trough, and is predominantly comprised of warm, salty waters of Atlantic origin.

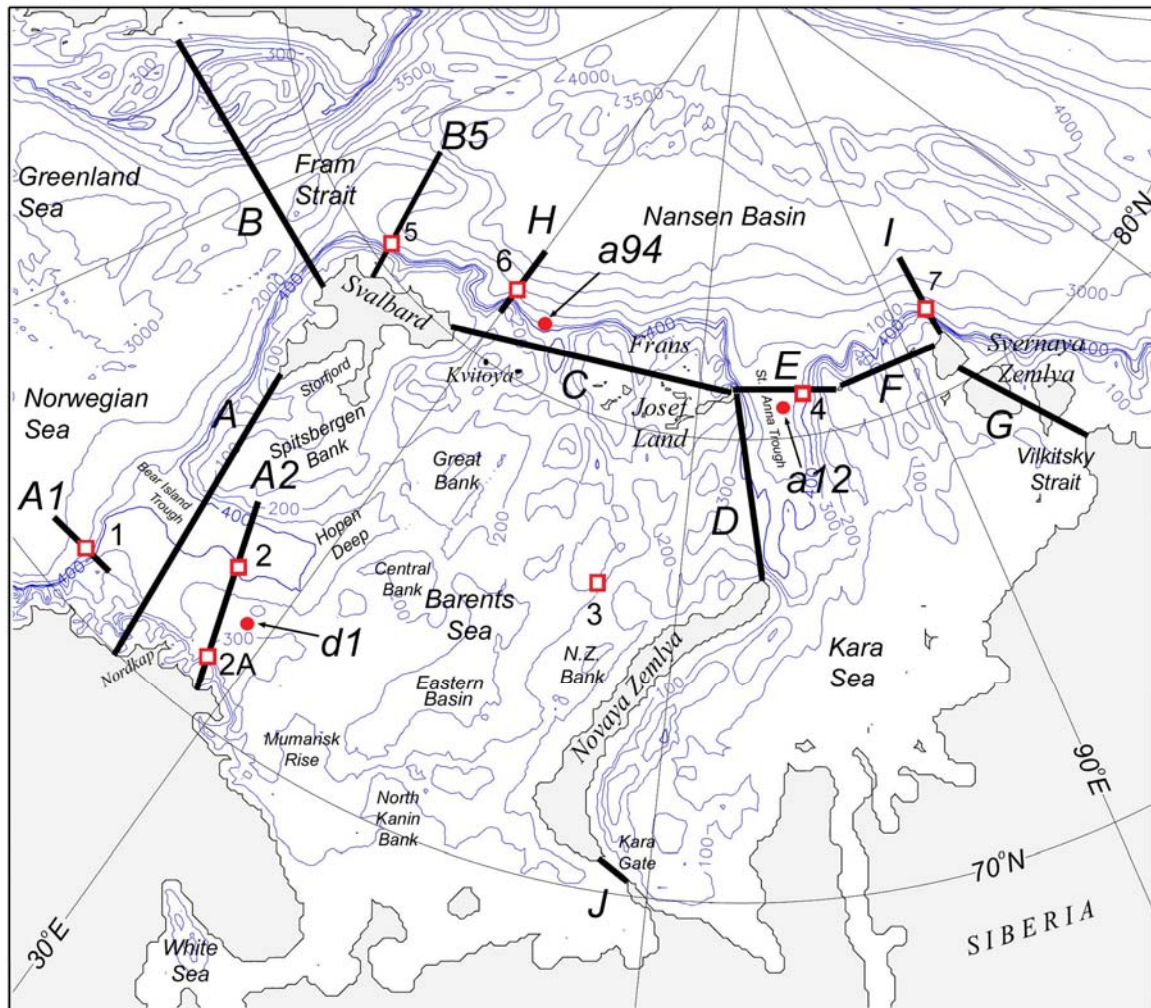


Figure 3.1. Barents and Kara Seas bathymetry (m) and location of model sections and stations. Solid lines and letters denote sections. Hollow squares and numbers identify stations. Locations of observational data are indicated by red dots. d1 - Dalnye Zelintsi 1, July 1991. a12 = *Polarstern* ARKXII, August/September 1996. a94 = *Polarstern* ARKIX_4, August/September 1993.

The flow through the BSO, as implied by the hydrographic conditions, was thought to be relatively stable with seasonally variable inflow in the southern two-thirds and outflow in the northern third (Blindheim, 1989, Pfirman et al., 1994, Parsons et al., 1996). Results from one year of measurements obtained from several moorings across a section from Bear Island to Fugloya, north of Norway, (Ingvaldsen et al., 2000) indicate the predominantly barotropic flow may vary between a broad Atlantic inflow or outflow all the way south to 72° N, or inflow and recirculation in nearby cells. Ingvaldsen et al.

(2000) did not observe a seasonal signal in the inflow. However, their measurements did indicate current intensification, strong lateral velocity gradients and a distinct surface-intensified relatively high-velocity core of inflow caused by the frequent passing of atmospheric lows in the winter. During the summer, the inflow area was seen to be wider with two, lower velocity, cores of inflow.

During certain periods, the net flow was observed to be an outflow from the Barents Sea to the Norwegian Sea (Ingvaldsen et al., 2000). This reversal of the flow was interpreted to be due primarily to variations in the atmospheric pressure. Some of the high net outflow was attributed to the presence of transient mesoscale eddies in the ocean. The monthly mean volume transport across the section covered by moorings, which did not represent the full section between Bear Island and Fugloya, fluctuated over a range of 11 Sv ($1 \text{ Sv} = 10^6 \text{ m}^3 \text{ s}^{-1}$) between 5.5 Sv into or out of the Barents Sea (Ingvaldsen et al., 2000).

Another source of water to the Barents Sea is the colder and fresher Norwegian Coastal Current, which carries waters originating from the Baltic Sea and Scandinavian terrestrial runoff, eastward along the Norwegian and Russian coasts. Due to the relatively small river input into the Barents Sea, the Norwegian Coastal Current is considered the main freshwater source, in addition to ice melt, for the region. An updated schematic of the Barents Sea circulation (Ozhigin et al., 2000) shows this current hugging the coast and following the 100 m contour. Farther east and north, a portion of the coastal current joins the Bear Island Trough inflow at the southern edge of the Eastern Basin. The Norwegian (now Murmansk) Coastal Current continues to the east and it is not clear how much of it mixes with White Sea and Pechora River outflow prior to entering the Kara Sea via the Kara Gate. Values between 0.05 to 0.7 Sv (Loeng et al., 1997), up to 1 Sv (Aagaard and Greisman, 1975) have been estimated for the flow south of Novaya Zemlya into the Kara Sea.

A portion of the North Cape Current recirculates within the Bear Island Trough, flowing westward, parallel to the cold Bear Island Current, and then exiting the Barents Sea (Pfirman et al., 1994; Parsons et al., 1996). This recirculation within the Bear Island Trough was seen to be relatively stable at approximately 1.0 Sv, but with higher outflow

episodes occurring during winter and early spring (Ingvaldsen et al., 2000). The remainder of the North Cape Current continues its eastward flow passing south of the Central Bank, following the bathymetry, to the Eastern Basin. Ozhigin et al. (2000) demonstrate that Eastern Basin Deep Water is local in origin, formed by significant modification of Atlantic Water, rather than Arctic Water carried southwest by the Central Current. Their results show a dome shaped structure of waters in the Eastern Basin, resulting in well pronounced cyclonic circulation in that area and no indication of Arctic Water transport into the Eastern Basin from the northeast.

The now significantly modified Atlantic Water travels north-northeast from the Eastern Basin as the Novaya Zemlya Current, staying west of the Novaya Zemlya Bank and exiting the Barents Sea between Frans Josef Land and Novaya Zemlya (Ozhigin et al., 2000). This is the main outflow region of the Barents Sea. Estimates of average mass transport leaving the Barents Sea are on the order of 2 Sv (Loeng et al., 1993; Rudels and Friedrich, 2000), varying between 1 to 3 Sv with a distinct maximum during the cold season and a minimum during summer (Loeng et al., 1997).

The modified Atlantic water then transits the northern Kara Sea where the majority enters the Nansen Basin via the St. Anna Trough (Rudels, 1987, Harms, 1997) and then moves eastward along the slope, displacing the Fram Strait branch of Atlantic Water (FSBW) away from the slope (Schauer et al., 1997; 2001). During summer, a portion of the Novaya Zemlya Current may be diverted to flow southward along the east coast of Novaya Zemlya (Harms and Karcher, 1999). Johnson et al. (1997) were not able to corroborate this warm flow from the Barents Sea around the northern end of Novaya Zemlya based on a series of moorings in the Kara Sea. The focus of their efforts was farther to the south and they do acknowledge the density of their observation network may not have been sufficient to resolve this particular feature.

A portion of the West Spitsbergen Current recirculates within the Storfjord Trough, while the majority continues north along the shelf break (Pfirman et al., 1994). West of Svalbard, the West Spitsbergen Current splits, with the Return Atlantic Current heading west and eventually south in the Greenland Sea, while the remainder enters the Arctic Ocean via Fram Strait (Bourke et al., 1988). This branch upon entering Fram

Strait splits again, one branch traveling north along the western edge of the Yermak Plateau and the remainder continuing to the east along the shelf break north of Svalbard (Manley et al., 1992; Rudels et al., 1997). Due to interaction with the ice encountered in Fram Strait and north of Svalbard, the surface signature of the Atlantic Water is obscured as it loses its warm and saline characteristics. The Atlantic Water core, consisting of water greater than 2 or 3° C, becomes an intermediate water mass and is denoted as the Atlantic Layer (Rudels and Friedrich, 2000). Limited amounts of Atlantic Water are thought to enter the Barents Sea from the north via Frans Josef - Victoria Trough as a near-bottom water mass (Pfirman et al., 1994). Loeng et al. (1997) use values obtained from Russian literature of 0.4 Sv entering the Barents Sea from the Arctic Ocean and 0.1 Sv exiting the Barents Sea to the Arctic Ocean between Svalbard and Frans Josef Land. The East Spitsbergen Current and the Persey Current, west of Frans Josef Land, bring cold, fresh Arctic Water from the north into the Barents Sea. Its extension, the cold, high-velocity Hopen-Bjornoya Current, travels south and west along the eastern edge of the Spitsbergen Bank. Its interaction with the recirculating North Cape Current is marked by the Arctic Polar Front (Loeng, 1991; Pfirman et al., 1994; Parsons et al., 1996).

B. MODEL PHYSICAL OCEANOGRAPHY

Since the output used in this analysis is from integration performed with 15-year average atmospheric forcing data, we do not expect to recreate specific conditions related to specific cruises or years. Nevertheless, the model is able to simulate climatological features, such as the summer freshening of surface waters in the Barents Sea, and important processes, such as mass and property transports and water mass transformations, which are known to occur in the Arctic Ocean and its adjacent seas, at the highest resolution to date for a large-domain coupled ice-ocean model. The names and locations of sections and stations discussed in the text are given in Table 3.1.

The two-year average velocity in the top 16 levels (0-223 m) in the Barents Sea (Figure 3.2) is predominantly west-to-northeast and constrained by bathymetry. It shows a broad, meandering Norwegian Atlantic Current along the west coast of Svalbard, a strong, narrow Norwegian Coastal Current and Atlantic Water inflow and recirculation in

Bear Island Trough. The Norwegian Atlantic Current, measured just north of the northern tip of Norway, is represented as a broad (100-130 km) flow with an annual mean salinity of 35.2 psu, temperature of 6.5° C and velocity of 4-5 cm s⁻¹ (Figure 3.3(a-c)) averaged over the 300 m thick core.

Section	Name
<i>A</i>	Svalbard - Norway
<i>A1</i>	Norwegian Atlantic Current
<i>A2</i>	Bear Island Trough
<i>B</i>	Fram Strait
<i>B5</i>	North of Svalbard
<i>C</i>	Svalbard - Frans Josef Land
<i>D</i>	Frans Josef Land - Novaya Zemlya
<i>E</i>	St. Anna Trough
<i>F</i>	Voronin Trough
<i>G</i>	Severnaya Zemlya
<i>H</i>	30° E
<i>I</i>	95° E
<i>J</i>	Kara Gate

Station	Name	Location
1	Norwegian Atlantic Current	71° 36' N, 16° 45' E
2	Bear Island Trough	73° 36' N, 25° 12' E
2A	Norwegian Coastal Current	71° 00' N, 27° 30' E
3	Novaya Zemlya Current	77° 06' N, 52° 18' E
4	St. Anna Trough	81° 18' N, 73° 12' E
5	North of Svalbard	80° 54' N, 13° 00' E
6	NE of Svalbard	82° 09' N, 30° 00' E
7	North of Severnaya Zemlya	82° 18' N, 95° 00' E

Table 3.1. Model sections and stations identified in Figure 3.1. Locations given for stations are center point of a (36 kilometer)² (4x4 gridpoint) region. Profiles displayed for model stations are an average for that region.

The North Cape Current flows into the Bear Island Trough (Figure 3.2) along its southern edge and a portion turns north and then recirculates along the 400 m isobath back out to the Norwegian Sea and the West Spitsbergen Current. A smaller fraction follows the 300 m contour clockwise around the Hopen Deep. The majority of the North Cape Current continues east along the southern flank of Central Bank (Figure 3.2) into the Eastern Basin.

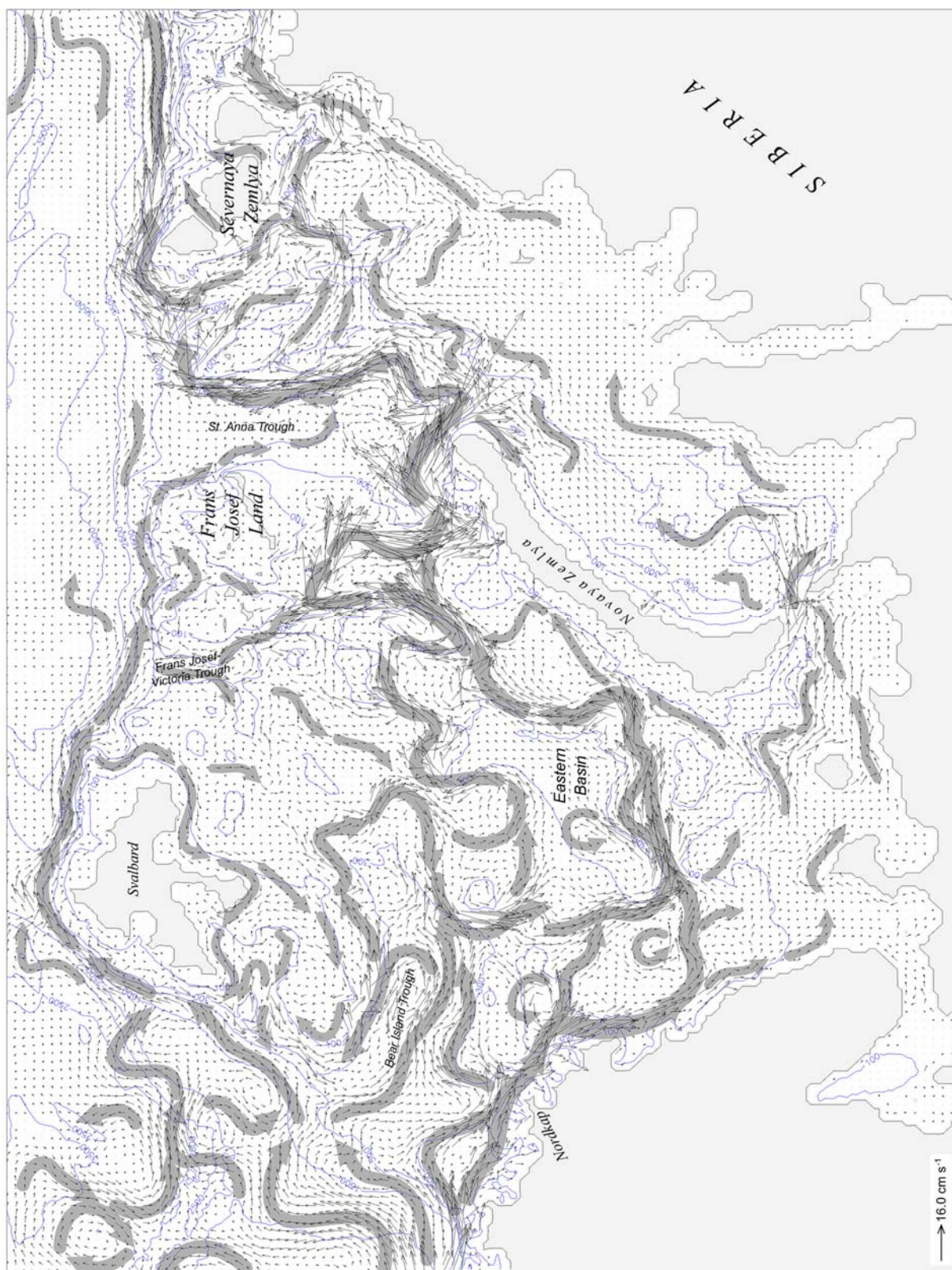


Figure 3.2. Two-year average 0-223m (model levels 1-16) velocity (cm s^{-1}). Velocity vectors are the average of spinup years 17 and 18 and are plotted every other grid point. Large gray arrows indicate interpreted pathways of mean currents.

In Model Section A2, from the Norwegian Coast east of Nordkap toward Bear Island (Figure 3.1, Figure 3.3(d-f)), the Norwegian Coastal Current is narrower (~ 55 km versus ~ 130 km based on the velocity distribution), colder (5.4°C versus 6.5°C), fresher (34.2 psu versus 35.16 psu), and considerably faster (36 cm s^{-1} versus 9 cm s^{-1}) than the North Cape Current in Bear Island Trough. There are bands of recirculation between the North Cape Current and the Norwegian Coastal Current and bands of inflow and outflow, along the southern flank of Spitsbergen Bank. In monthly averaged sections across Bear Island Trough (not shown) the inflow in wintertime is narrower and stronger, with a maximum in January, and it is weakest in summer, features similar to those reported by Ingvaldsen et al. (2000). In general, the model distribution of temperature, salinity and velocity in Bear Island Trough is similar to the observed distribution (Parsons et al., 1996; Loeng et al., 1997) with outflow constrained to the northern one-third (Figure 3.3(f)).

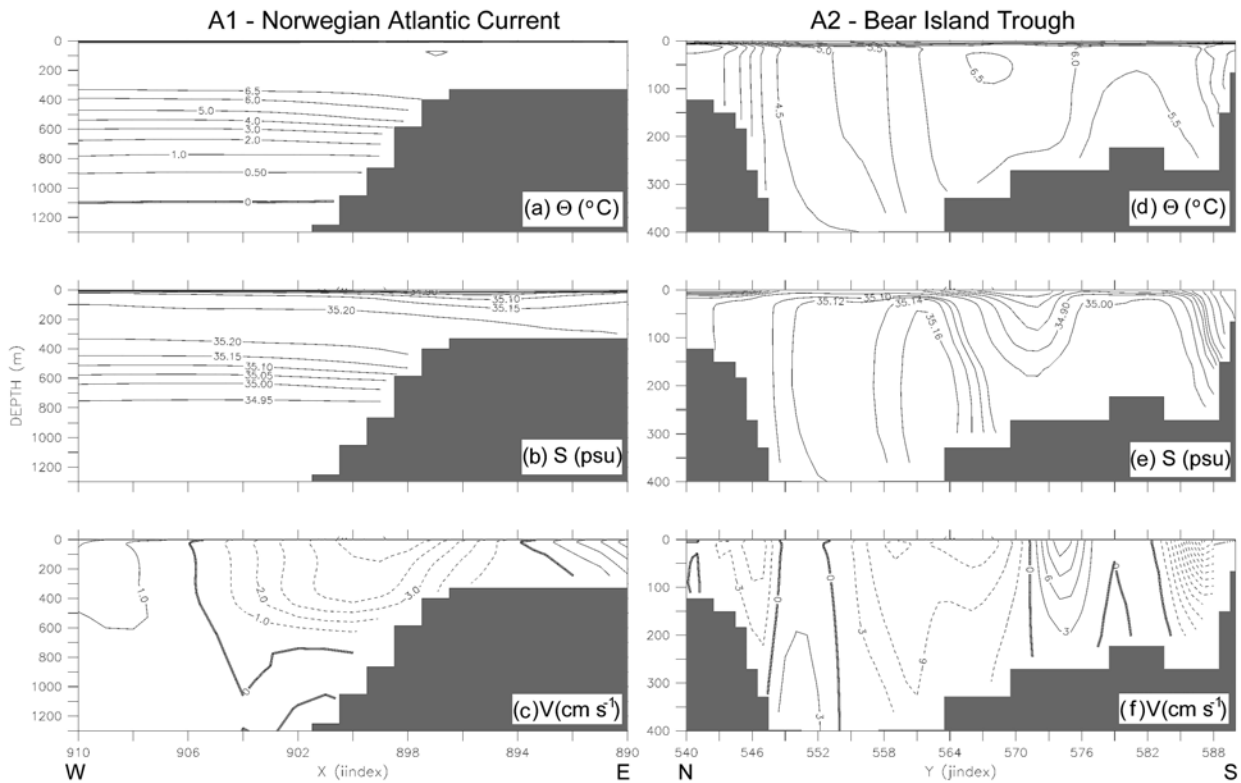


Figure 3.3. Vertical distribution of annual average potential temperature ($^\circ\text{C}$, a and d), salinity (psu, b and e), and velocity (cm s^{-1} , c and f) across the Norwegian Atlantic Current (model section A1, left) and the Bear Island Trough (model section A2, right). Note the differing vertical and horizontal scales. Negative velocity contours represent northward and eastward flows.

In the northwestern corner of the region, the cold, narrow East Spitsbergen Current entering the Barents Sea between Svalbard and Kvitoya, is well represented in the two-year average velocity field. The Persey Current is a broad southward flow between Svalbard and Frans Josef Land and across the Great Bank. The Hopen-Bjornoya Current travels along the southern flank of Spitsbergen Bank. The polar front associated with the Hopen-Bjornoya Current, which is stronger in winter, is clearly discernible in the winter and summer 0-50 m ocean temperature and salinity fields (Figure 3.5 (a-d)). The general path of the warm, salty Atlantic Water, entering the Barents Sea via Bear Island Trough, traveling east, south of the Central Bank, and then north-northeast along the west side of Novaya Zemlya Bank, rounding the northern tip and exiting the Kara Sea via St. Anna Trough, can also be seen in the seasonal temperature and salinity fields. Several quasi-permanent cyclonic eddies can be identified in the southeastern Barents Sea, associated with distinct bathymetric features like the Nordkap, the Central Bank, Murmansk Rise, North Kanin Bank, and the southern end of the Eastern Basin (Figure 3.2).

The three year mean (1979-1981) 0-583 m (model levels 1-20) flow through Fram Strait (Figure 3.4) indicates a significant portion of the West Spitsbergen Current recirculates to the Greenland Sea just north of the Fram Strait sill (as observed, Bourke et al., 1988). The main branch of Arctic Ocean outflow, between the 500m and 2500 m contours, flows around Moris Jesup Plateau and out Fram Strait. The broad southerly flow from the Eurasian Basin may serve to limit the northward penetration of Atlantic Water away from the shelf break. There is also indication of Northerly flow between the Greenland coast and the 1000 m contour (Figure 3.4(a)), originating as a branching of the southward flowing shelf slope current exiting the Arctic Ocean. The long term mean flow around Yermak Plateau shows little indication of a percentage of the Fram Strait Branch of Atlantic Water flowing clockwise around it. Instead, there is a relatively steady, cyclonic eddy of warm Atlantic origin water in-between the Plateau and the Svalbard shelf. A steady anticyclonic eddy of cold Arctic water is located southeast of Moris Jesup Plateau and a warm cyclonic eddy is located just north of the Fram Strait sill, centered over the Molloy Deep (as observed, Bourke et al., 1987). Based on the long

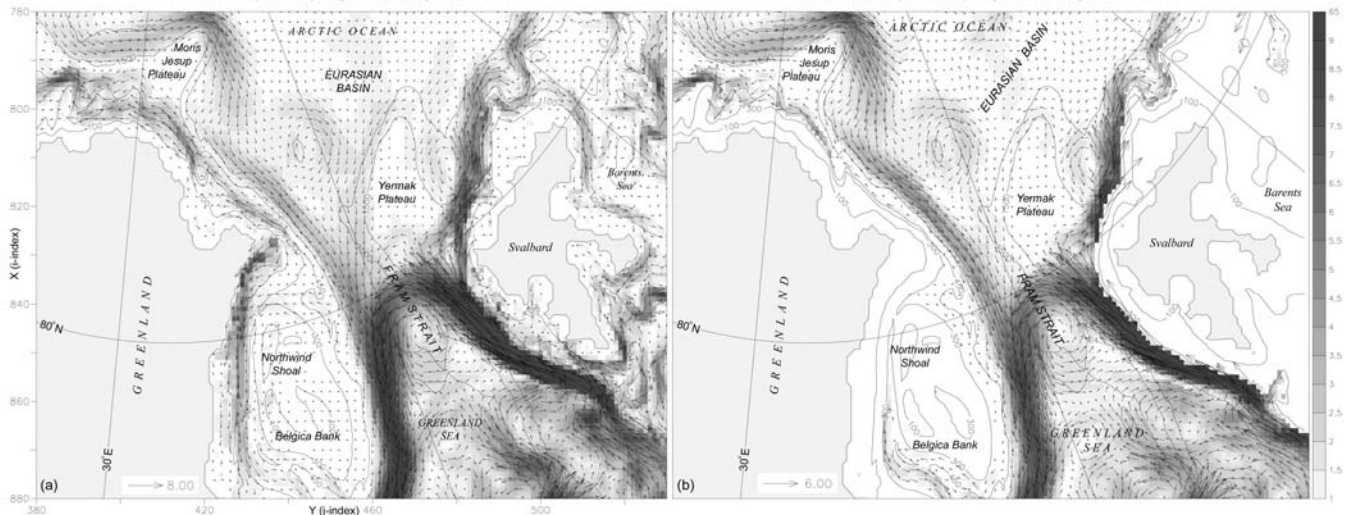


Figure 3.4. Horizontal distribution of three year mean (1979-1981) average velocity (cm/s) in Fram Strait: (a) 0-226 m (model levels 1-16) mean; (b) 270-583 m (model levels 17-20). Background shading is 0-226 m (a) and 270-583 m (b) mean speed (scalar). Every second velocity vector is plotted. Note differing velocity vector scales.

term mean circulation, attempting to characterize the flow through Fram Strait by using data gathered from a single transect would probably not adequately resolve the complex flow. Resources permitting, data gathered from sections/moorings due north of the western tip of Svalbard, east from Greenland along 81° N and across Fram Strait along 78° N may provide a means of separating inflow, outflow and recirculation.

On both sides of the Eastern Basin, the mean deep flow is northward, with the main branch of warm Atlantic water following the eastern side, toward Novaya Zemlya Bank (Figure 3.2). A distinct cyclonic circulation in the Eastern Basin is not readily visible in the two-year average velocity field. However, examination of winter and summer mean velocity fields (not shown) show a distinct cyclonic circulation around the Eastern Basin and a general intensification of currents in winter. In agreement with Ozhigin et al. (2000), the model results show no evidence of Arctic Water transport into the Eastern Basin from the northeast. The predominantly barotropic, northward flows of Atlantic Water on either side of the Eastern Basin merge at the northern end, isolating the Eastern Basin from advection of Arctic water from the north.

Prior to exiting the Barents Sea, the Novaya Zemlya Current splits, with one part traveling north, toward the southern coast of Frans Josef Land. A portion of the

northward flow exits the Barents Sea via the Frans Josef - Victoria Trough, west of Frans Josef Land. Atlantic Water exiting the Barents Sea via the eastern edge of this trough is readily visible in animations of 100-200 m and 200-300 m monthly-average temperature and salinity. Atlantic origin water, which has entered the Arctic Ocean via Fram Strait, enters the Barents Sea via the western side of the Frans Josef - Victoria Trough. Both of these exchanges occur primarily during the summer. The majority of the modified Atlantic Water flow headed toward Frans Josef Land turns east and then back to the south, guided by bathymetry, to meet the remainder of the north-eastward flowing Novaya Zemlya Current, west of the northern tip of Novaya Zemlya.

The Novaya Zemlya Current in the vicinity of Station 3, Figure 3.1, has an annual average core velocity of approximately 30 cm s^{-1} , a salinity of 34.99 psu and a temperature of 3.8°C . The Novaya Zemlya Current flows through a narrow, 200-220 m deep gap in the sill between Frans Josef Land and Novaya Zemlya (Jakobsson et al., 2000) and enters the southern reaches of the Santa Anna Trough. Here the majority of the flow follows the bathymetry between the 200 and 300 m isobaths and travels toward the Nansen Basin along the eastern edge of Santa Anna Trough. The flow then travels east along the shelf break, with some water recirculating through Voronin Trough.

A portion of the Novaya Zemlya Current continues south around the NE tip of Novaya Zemlya into the Kara Sea. Both branches of the warm flow are visible in the summer and winter average ice cover (Figures 3.5(e) and 3.5(f)), as a decrease in concentration along their path. The thermodynamically driven thinning of the ice cover along the path of the warm flow is clearly visible in animations of daily ice concentration and thickness. This thermodynamic effect is strong enough to be distinguished from the wind driven flow of ice in the northern Kara Sea, even in mid-winter.

Comparison of matching 0 m, 30 m, 50 m, 100 m and 200 m monthly average temperature and salinity fields (not shown) with the 1998 NOAA Barents Sea Climatic Atlas (Matishov et al., 1998) reveal that the North Cape Current in the model Barents Sea is roughly 1°C warmer and 0.1 - 0.2 psu saltier than climatology. Additionally, the

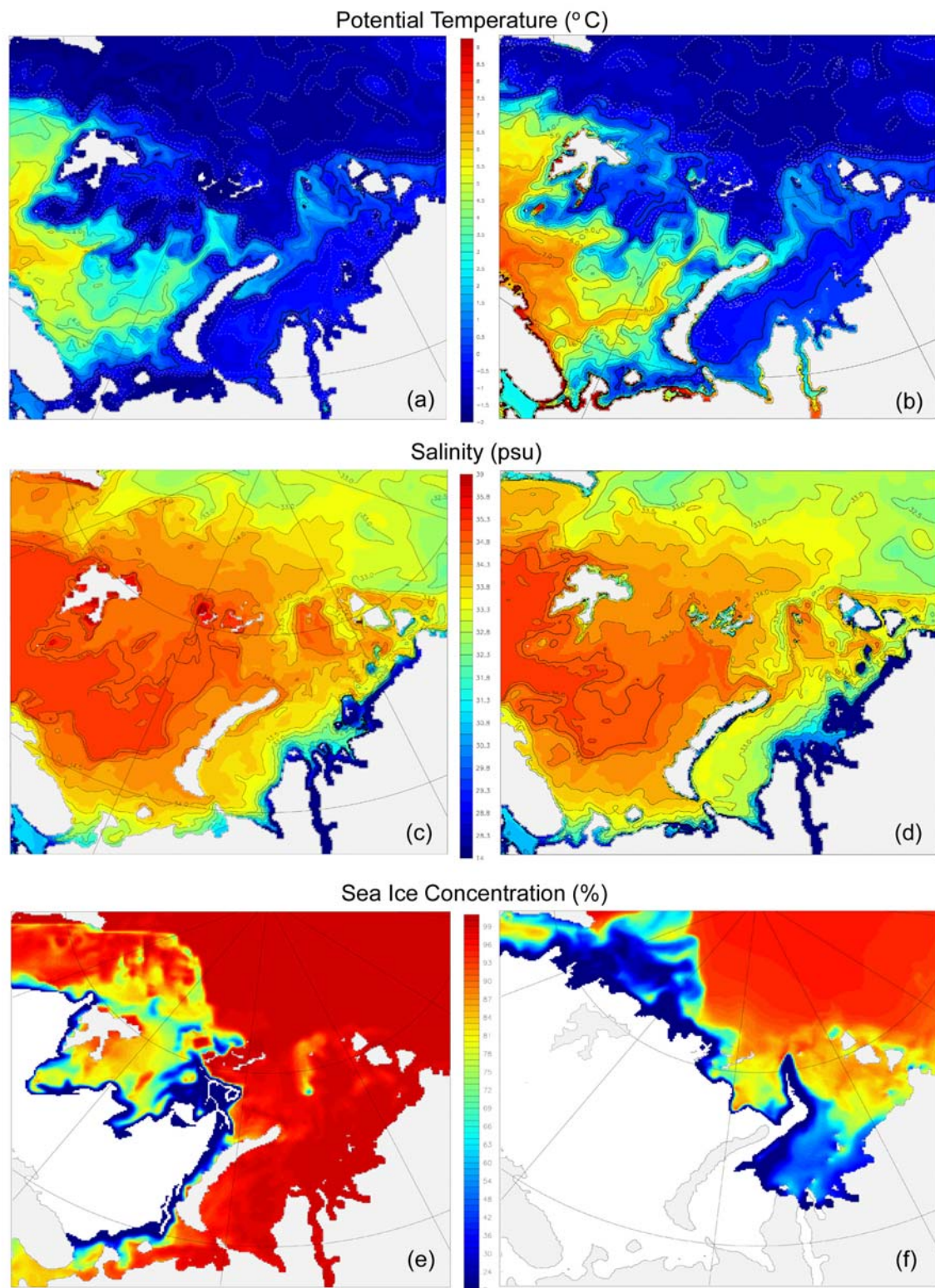


Figure 3.5. Distribution of temperature and salinity in the upper 0-53 m (model levels 1-8) and sea ice concentration for various seasons. Winter average (Jan-Feb-Mar) potential temperature (a) and salinity (c). Summer average (Jul-Aug-Sep) potential temperature (b) and salinity (d). Maximum winter sea ice concentration (%), day 78 (mid-March) spinup year 18 (e). Minimum summer sea ice concentration (%), day 273 (early-September) spinup year 18 (f).

warmer and saltier waters reach farther north, along the northwest coast of Novaya Zemlya.

A possible solution to narrowing the temperature and salinity differences is the planned modification of the restoring curtain along the model ocean boundaries to monthly average temperature and salinity climatology vice the annual average climatology currently being applied. The monthly average climatology will create greater seasonal variability in the water column along the model boundaries, which will propagate throughout the domain. Another factor that may help align model salinities with those observed is the planned inclusion of the annual cycle of river runoff in the simulation. Accurately representing the seasonal salinity maxima and minima will influence the preconditioning of the model Barents Sea for ice formation and convection. The application of realistic daily varying forcing, vice the 15 year mean used during spinup, will introduce greater variability into all aspects of the atmospheric forcing and may also improve model representation of the northward extent of warmer and saltier waters.

The location of the Barents Sea Polar Front (BSPF), the seasonal summer northward pulse of warmer water and the summer freshening along the Russian coast in the model agree well with the climatology. In September, the BSPF is not readily discernible in the surface temperature field. Otherwise, throughout the year it is well defined by the gradient between the 34.6-34.9 psu isopleths and the 2-4 °C isotherms. Parsons et al. (1996) found the 34.6 psu isohaline to be a good indicator of the frontal position and below a shallow mixed layer (~20 m), the front was defined by a moderate temperature gradient coincident with the 2°C isotherm. As in the climatology, the seasonal signal in temperature and salinity variability decreases with depth. In the summer at 200 m depth, the small northward pulse of warmer and saltier water reaches just north of the Eastern Basin. In contrast, the summer northward pulse of warmer water at the surface can be seen entering the St. Anna Trough, most likely due to increased wind influence in the upper layers.

C. MASS, HEAT AND SALT TRANSPORTS

1. Mass Transport

Mass, heat and salt transports were calculated at the various boundaries of the Barents Sea indicated in Figure 3.1. Ice-ocean freshwater fluxes are not addressed directly in this paper. However, the influence of ice growth and melt can be seen in changes in the seasonal distribution of 0-50 m temperature and salinity (Figure 3.5). The alignment of each section in Figure 3.1 was chosen to ensure positive values of volume transport into the Arctic Ocean. For north-south aligned sections (sections A, A2, B5, D, H and I in Figure 3.1) positive values of volume transport indicate transport to the east or along the path of Atlantic Water inflow to the Arctic Ocean.

An annual-average volume transport of 3.97 Sv enters the Barents Sea between Norway and Svalbard, and approximately 0.9 Sv exits through the same section, yielding a net annual average transport of 3.06 Sv (Table 3.2). The magnitudes of the transports are somewhat larger than those obtained from observations (3.1 Sv in, 1.2 Sv out, 1.9 net - Loeng et al., 1997; 2 Sv net - Ingvaldsen et al., 2000).

	Section	Net Vol	Vol in	Vol out	Net QHeat	Qheat in	Qheat out	Net QSalt	Qsalt in	Qsalt out
A	Svalbard - Norway	3.06	3.97	-0.91	79.46	95.01	-15.54	109.98	142.60	-32.63
B	Fram Strait	-2.12	4.73	-6.85	9.31	45.06	-35.75	-75.58	169.79	-245.37
C	Svalbard - Frans Josef Land	-0.22	0.55	-0.77	-2.78	-0.59	-2.20	-7.69	19.78	-27.47
D	Frans Josef Land - Novaya Zem.	2.76	3.18	-0.42	15.95	16.63	-0.67	98.58	113.46	-14.88
E	St. Anna Trough	2.52	3.22	-0.70	14.15	17.18	-3.04	89.76	114.87	-25.11
F	Voronin Trough	0.31	0.65	-0.35	1.18	3.39	-2.21	10.69	23.04	-12.35
G	Severnaya Zemlya	0.18	0.18	0.00	0.03	0.03	0.00	6.01	6.01	0.00
H	East of Yermak Plateau	2.58	2.76	-0.19	20.27	21.19	-0.93	92.38	99.08	-6.70
I	North of Severnaya Zemlya	5.57	5.79	-0.22	29.32	28.75	0.57	198.80	206.79	-7.99
J	Kara Gate	0.22	0.22	0.00	0.12	0.16	-0.04	7.55	7.65	-0.10

Table 3.2. Annual mean simulated volume transport (Vol, Sv), heat transport (Qheat, TW) and total salt transport (Qsalt, 10^6 kg s^{-1}) through selected sections. In and out are defined as into and out of the Arctic Ocean, respectively, or following the path of Atlantic Water. Qheat referenced to -0.1°C , Qsalt referenced to 0.0 psu. Calculations are for entire water column.

An explanation for the difference may lie in the method of calculation. For the model results, transport is calculated across the entire section, coastline to coastline, whereas the boundaries of transports calculated from observations are determined by the mooring locations and exclude flow shoreward of the moorings. A comparison of model monthly-averaged volume transport through the Svalbard-Norway section with values from a year-long time series obtained by current meter moorings between Bear Island and Fugloya (Ingvaldsen et al., 2000) (Figure 3.6a) shows considerably less variability in the model output, no clear seasonal signal and no indication of periods of net outflow, which are most likely due to the averaged atmospheric forcing.

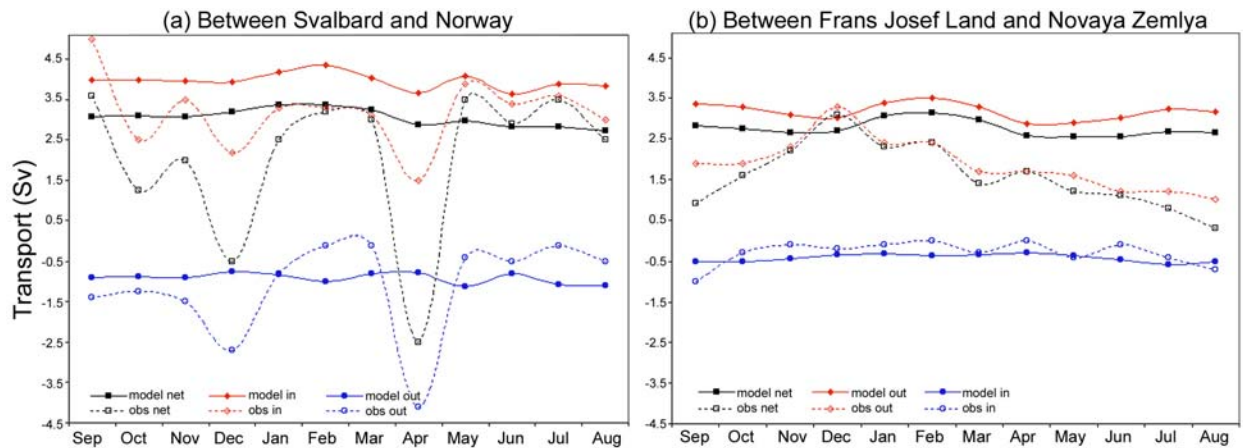


Figure 3.6. Monthly mean volume transport (Sv), from the model and from observations, through the strait between Svalbard and Norway (a) and through the strait between Frans Josef Land and Novaya Zemlya (b). Observational data were taken from Ingvaldsen et al. (2000) for (a) and from Loeng et al. (1997) for (b)

Between Svalbard and Frans Josef Land, (section C) a net 0.22 Sv enters the Barents Sea from the Arctic Ocean. From reviewing animations of the monthly-mean vertical distribution of temperature, salinity and velocity across this section, the flow into the Barents Sea (0.77 Sv) is a mixture of Polar Surface Water and warm Fram Strait Branch Atlantic Water. The outflow to the Arctic Ocean (0.55 Sv) is cold, Barents Sea-modified Atlantic water. A weak seasonal signal in the transport, with an increase in both inflow and outflow in the winter, is observed. The net transport into the Barents Sea between Svalbard-Norway (section A) and Svalbard – Frans Josef Land (Section C) is

balanced by net flow out of the Barents Sea between Frans Josef Land and Novaya Zemlya (Section D) and Kara Gate (Section J), within a $\pm 5\%$ margin of error.

The outflow between Frans Josef Land and Novaya Zemlya (Section D) is concentrated in an approximately 90 km wide band in the southern one-quarter of the section, and it reaches speeds of up to 30 cm s^{-1} in the wintertime. Comparing the model transport between Frans Josef Land and Novaya Zemlya (Figure 3.6b) with that obtained from one year of current meter measurements (Loeng et al., 1997), the mean magnitudes of the transports agree, yet the observed seasonal signal is not visible in the one year of model results. This may again be attributed to dampening the seasonal cycle in the atmospheric forcing by using a 15-year average.

South of Novaya Zemlya, the predominantly eastward flow through Kara Gate has a winter maximum of 0.34 Sv and a summer minimum of 0.14 Sv, and a net annual average transport from the Barents Sea to the Kara Sea of 0.22 Sv. The only periods of weak westward flow through Kara Gate, approximately 0.01 Sv, are in August and September. The majority of the Barents and Kara Seas outflow to the Arctic Ocean occurs via the St. Anna Trough (Section E), approximately 2.5 Sv versus approximately 0.3 Sv via Voronin Trough (Section F) and 0.2 Sv via Vilkitsky Strait (Section G).

The magnitude of the net volume transport out of the Arctic Ocean through Fram Strait under the applied climatological forcing, 2.12 Sv, is similar to the multi-year mean of 1.6 ± 1.1 Sv observed through direct measurements in the late 1990's (Fahrback et al., 2001). However, the magnitudes of the separate modeled volume transports into and out of the Arctic are approximately half those observed, 4.73 Sv modeled versus 9.5 ± 0.7 Sv observed transport to the north and 6.85 Sv modeled versus 11.1 ± 0.9 Sv observed transport to the south (Fahrback et al., 2001). Comparison of model mean northward and southward velocities with those observed by Fahrback et al. (2001) indicates model velocities under climatological forcing are 25-50% smaller than those observed in the late 1990's.

2. Heat and salt transports

To compare the flow into the Arctic Ocean via Fram Strait with that through the Barents Sea, mass, heat and salt transports were calculated through Fram Strait and along the northern Barents Sea shelf slope (Table 3.2, sections *B*, *H* and *I*).

The amount of heat flowing into the Barents Sea, between Svalbard and Norway, (Section A) is about double that of the amount of heat entering the Arctic Ocean via Fram Strait (Section B), i.e., 95TW compared to 45TW. However, the Barents Sea branch loses about 80% of its heat prior to exiting the Barents Sea. The net amount of heat entering the Barents Sea between Svalbard and Norway, 79 TW, is towards the high end of estimates from observations (Simonsen and Haugan, 1996). The mean heat loss from the Barents Sea, the difference in heat transport between Section A and Section D, is about 64TW. This estimate is in the upper range of the published heat loss between 28 and 80 TW (Simonsen and Haugan, 1996) and it is in the lower range of 42-162 TW, estimated by Simonsen and Haugan (1996) using different parameterizations of the sea surface heat budget. In the model, 14 TW enters the Arctic Ocean via the St. Anna Trough and additional ~ 1 TW via the Voronin Trough. This is about 75% of the heat transported via the Fram Strait branch of Atlantic Water across section H, east of the Yermak Plateau and about 800 km upstream of the St. Anna Trough.

The amount of net heat entering the Arctic Ocean from the Barents Sea, via St. Anna and Voronin troughs (~ 15 TW) is roughly half of the net heat transport across section I, north of Severnaya Zemlya (~ 29 TW). Under the atmospheric forcing conditions during model spinup, the Barents Sea branch and the Fram Strait branch of Atlantic Water supply equal sources of heat to the boundary current along the shelf slope, north of Severnaya Zemlya.

The salt transport into the Barents Sea (across section A) and through Fram Strait are of similar magnitude, $\sim 143 \times 10^6 \text{ kg s}^{-1}$ compared to $170 \times 10^6 \text{ kg s}^{-1}$, respectively. The salt export from the Barents Sea into the Arctic Ocean via St. Anna and Voronin Troughs is $\sim 138 \times 10^6 \text{ kg s}^{-1}$, indicating that the contributions due to ice melt and formation roughly cancel out within the Barents Sea. This export is larger than the $99 \times 10^6 \text{ kg s}^{-1}$ of eastward

salt transport of the Fram Strait branch across section H, east of Yermak Plateau and it constitutes $\sim 67\%$ of the total of $207 \times 10^6 \text{ kg s}^{-1}$ salt transport across section I, north of Severnaya Zemlya. This indicates that under the applied atmospheric forcing, the Barents Sea Branch of Atlantic Water contributes a larger amount of salt to the boundary current north of Severnaya Zemlya than the Fram Strait Branch. The planned addition of river inputs may decrease this percentage.

A comparison of the mean net volume transports via the two pathways helps to farther evaluate the relative importance of each branch on the central Arctic Ocean circulation and water mass properties. The mean net volume transport through the Svalbard-Norway section is 3.06 Sv, with 3.97 Sv entering the Barents Sea and 0.91 Sv recirculating back to the Greenland Sea. The respective transports through Fram Strait (from the surface to the bottom) are: 2.12 Sv (net southward), 4.73 Sv in and 6.85 Sv out of the Arctic Ocean. The northward volume transport in the boundary current north of Svalbard is reduced from 4.73 Sv entering Fram Strait to 2.76 Sv across section H, east of the Yermak Plateau, suggesting that approximately half of this water recirculates within Fram Strait or enters the central Nansen Basin. The long term mean velocity in Fram Strait (Figure 3.4) indicates significant recirculation rather than flow into the central Nansen Basin. The net volume transport through the St. Anna and Voronin troughs is 2.83 Sv (2.52 Sv and 0.31 Sv, respectively), slightly larger than that across section H, east of the Yermak Plateau. Similarly as in the case of heat and salt contributions, the net volume input from the Barents Sea accounts for roughly $\sim 50\%$ of the net volume transport of 5.57 Sv along the boundary current across section I, north of Severnaya Zemlya.

The above discussion is provided to argue that the two branches are about equally important sources of mass, heat and salt to the central Arctic under the given atmospheric forcing. Model results are in support of earlier observations by Rudels (1994) and the heat budget analysis by Simonsen and Haugan (1996). Those studies suggest that the Barents Sea branch plays a crucial and equal role to the Fram Strait branch in the renewal of the intermediate and deep waters and the thermohaline circulation of the Arctic Ocean. It is also felt that during periods of strong positive North Atlantic Oscillation (NAO),

when the predominant atmospheric forcing over the North Atlantic Ocean, the Norwegian Sea and the Barents Sea changes, the increased frequency of storms reaching higher latitudes will in turn increase the inflow of Atlantic Water to the Barents Sea (Dickson et al., 2000). This may then cause the contribution of the Barents Sea branch of Atlantic Water to the boundary current along the shelf slope north of Severnaya Zemlya to increase significantly, predominantly through increased St. Anna Trough outflow. As it is discussed below, the Fram Strait Branch is displaced seaward, off the shelf, by the Barents Sea Branch. A percentage of the deeper Fram Strait Branch turns north and follows the Lomonosov Ridge, through conservation of vorticity. Therefore the role of the Barents Sea Branch in the distribution of heat and salt in the Canadian Basin may be qualitatively more important than the Fram Strait Branch under certain atmospheric conditions.

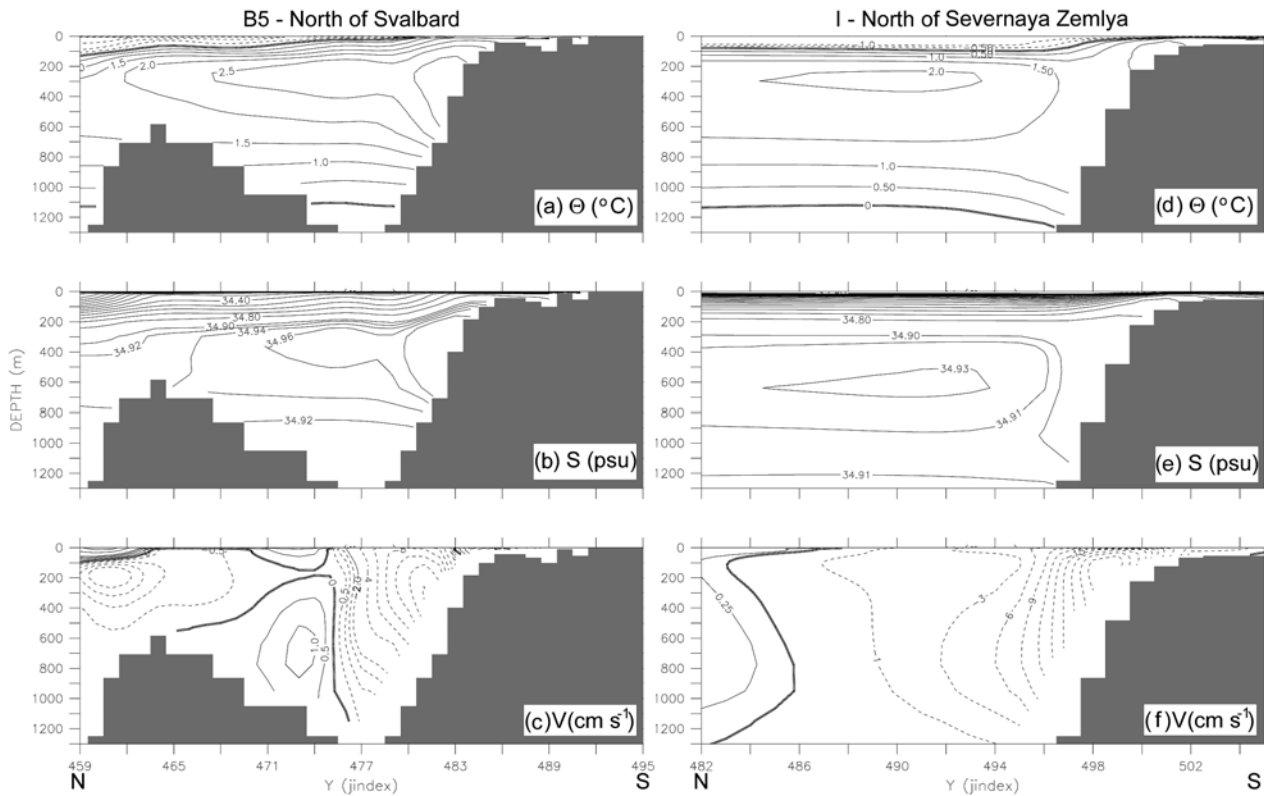


Figure 3.7. Vertical distribution of annual average potential temperature ($^{\circ}\text{C}$, a,d), salinity (psu, b,e), and velocity (cm s^{-1} , c,f) across the section north of Svalbard (model section B5, left) and the section north of Severnaya Zemlya (model section I, right). Note the differing horizontal scales. Negative velocity contours represent eastward flows.

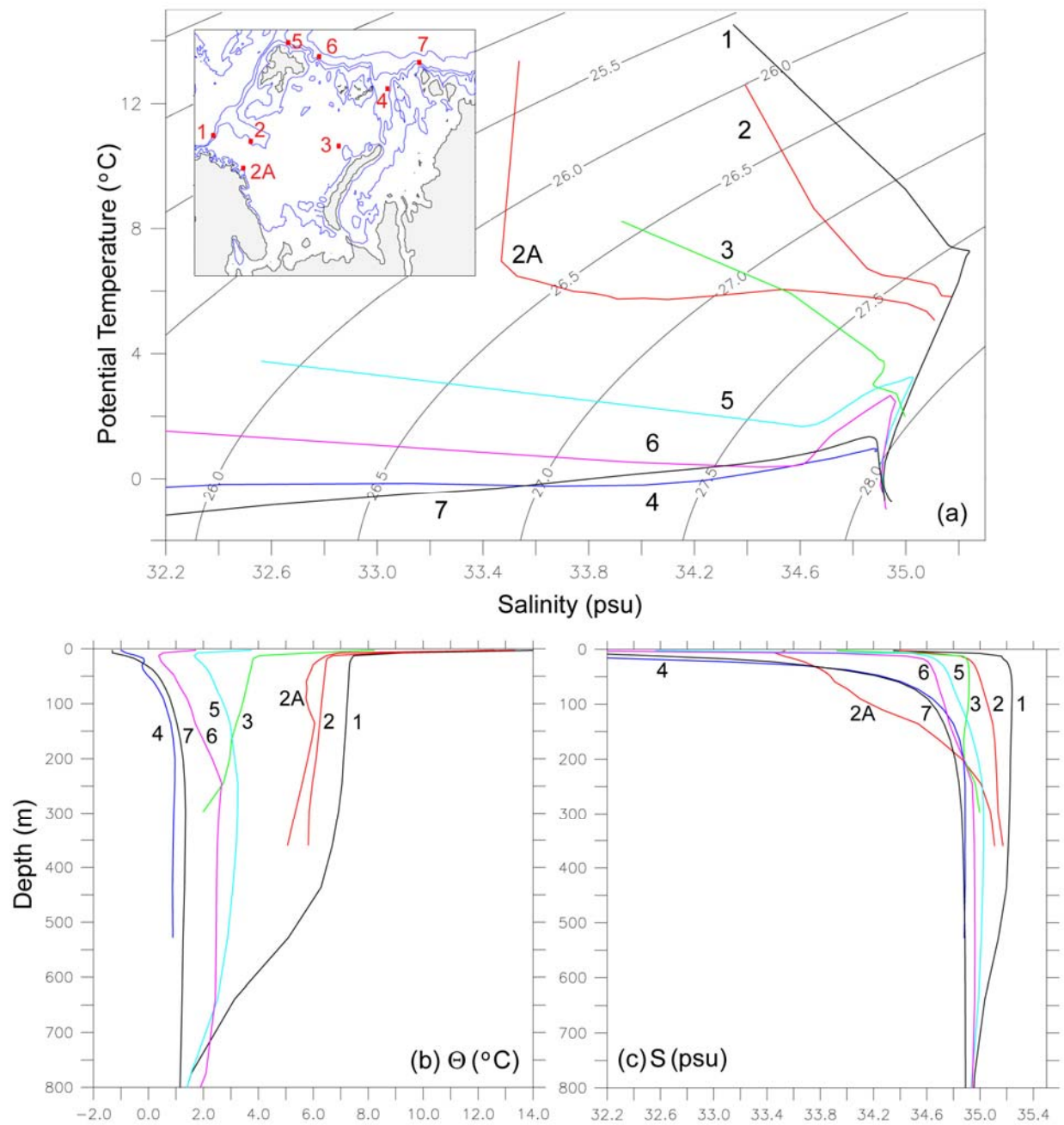


Figure 3.8. Summer average (Jul-Aug-Sep) potential temperature versus salinity (a), vertical distribution of potential temperature (b) and vertical distribution of salinity (c) for selected model stations in and around the Barents Sea. Each profile displayed represents an average over a 4x4 grid point region centered on the respective location given in Table 3.1.

The model realistically simulates the observed (Schauer et al., 1997; Schauer et al., 2000) northward displacement of the Fram Strait Branch of Atlantic Water inflow by the St. Anna Trough outflow (Figure 3.7 (a-f)). Temperature and salinity maxima are

displaced seaward of the continental slope; and the area of eastward flow (negative velocity values) is broadened. In an effort to display the evolution of temperature and salinity along the flow of the two branches of Atlantic water through the Barents Sea and the Kara Sea in the model, eight stations were chosen representing entry, mid, and exit points (Figure 3.8.). The station locations are based on the current distribution given by the 0-223 m July-August-September summer average current speed ($spd = \sqrt{u^2 + v^2}$, not shown). Across the major currents, the maxima of temperature and salinity were chosen for the station center (a luxury unique to analysis of high resolution model output.) In order to better represent the significant water masses in that part of the flow, the profiles are averages over a 4x4 grid point region (1296 km²).

The temperature versus salinity diagrams and their vertical profiles (Figure 3.8) show warm, salty Atlantic Water entering the Barents Sea (Stations 1, 2, 2A), which is cooled and freshened before it reaches the Eastern Basin (Station 3) and which finally exits via the St. Anna Trough (Station 4) after more cooling. Stations 1, 5 and 6 show the evolution of the Fram Strait branch of Atlantic Water as it enters the Arctic Ocean and is cooled and freshened as it travels east along the northern slope of the Barents Sea. The vertical distribution of temperature, salinity and velocity for these stations are visible in

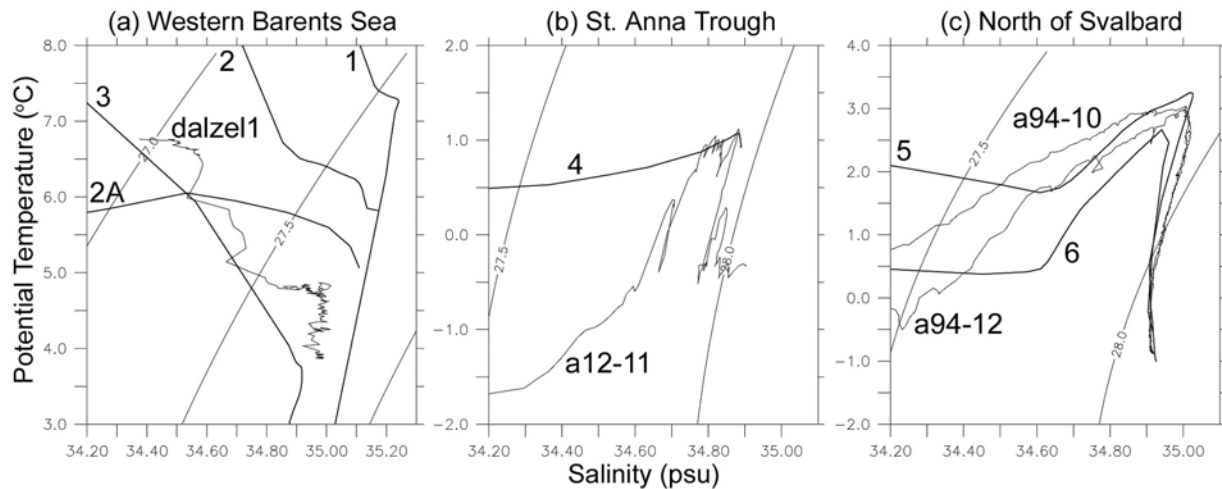


Figure 3.9. Potential temperature versus salinity, summer average (Jul-Aug-Sep) model output and observations in the western Barents Sea (a), in the St. Anna Trough (b), and north of Svalbard (c). dalzel1 = Dalnye Zelintsi, July 1991. a12-11 = *Polarstern* ARKXII, August/ September 1996. a94-10,12 = *Polarstern* ARKIX_4, August/September 1993. Note the differing temperature and salinity scales.

Figure 3.3 (a-c) and Figure 3.7 (a-f). The colder, fresher St. Anna Trough outflow (Station 4) combines with the Fram Strait branch (Station 6) and the end result in temperature and salinity properties is shown at station 7.

Model stations compare well with selected observations (Figure 3.9.) It must be kept in mind that these are comparisons between the average of 3 months of model output, using an average, climatological forcing and snapshot observations at a specific point. Within these constraints, the agreement is good and thus we might be confident that the model simulates important characteristics of the water masses entering, transiting and exiting the Barents Sea reasonably well. The summer averaged model inflow is warmer than observations (Figure 3.9(a)). However, this may be a function of the model stations being west of the observed station (Figure 3.1). The coincidence of the modeled and observed temperature and salinity distribution in St. Anna Trough (Figure 3.9(b)) indicates appropriate cooling of the water in the model Barents Sea. Comparison of model Station 3 with Norwegian observations taken west of Novaya Zemlya (courtesy of H. Loeng, not shown) shows the majority of the cooling in the model takes place farther east than observed, between model stations 3 and 4. The model captures the characteristics of the Fram Strait branch quite well when compared with observed data from August/September 1993 (Figure 3.9(c)). Due to its larger width (approximately 50 km based on the velocity distribution in Figure 3.7(c)), the Fram Strait Branch is well represented in the model while the eastward shift in water mass transformation in the Barents Sea highlights a need for better parameterization of sub grid-scale mixing and/or an increase in resolution. Improved parameterizations would avoid the additional computational expense of increased resolution, yet features smaller than four grid points (~36 km) across would still not be resolved. The addition of tidal effects to the model may also improve the agreement between observed and modeled T/S distribution in the central Barents Sea. Parsons (1995) found the net residual tidal currents due to the M2 tidal species generally opposed the inflow. In the model, this would result in slower eastward velocities and potentially more cooling in the central Barents Sea.

D. EDDY KINETIC ENERGY

Since the high spatial resolution of the model allows analysis of eddies down to a scale of ~ 30 km, we investigate the distribution of eddy kinetic energy ($EKE = (u'^2 + v'^2)/2$). These calculations are done for monthly and daily fluctuations, referred to the annual mean. The monthly average data sets used in EKE calculations represent the average of all timesteps in that month (roughly 5,400 timesteps), while a daily snapshot represents the last timestep out of the approximately 180 timesteps during one day. Additionally, due to storage and integration time considerations, the daily snapshots contain only surface velocity components among other limited variables.

The annual mean velocity components, \bar{u} and \bar{v} , were subtracted from the daily velocity values or monthly average velocity values to obtain u' and v' . EKE was calculated for the region including the northern Norwegian, Greenland and Barents Seas. The annual mean surface EKE, calculated from monthly average output, was found to represent approximately 15 percent of the annual mean surface EKE calculated from daily snapshots ($8.40 \text{ cm}^2 \text{ s}^{-2}$ versus $54.53 \text{ cm}^2 \text{ s}^{-2}$; with standard deviations about the means of $12.6 \text{ cm}^2 \text{ s}^{-2}$ versus $70.2 \text{ cm}^2 \text{ s}^{-2}$, respectively).

A comparison of the EKE calculated in a similar region using output from an earlier, 18 km resolution model (Maslowski et al., 2000) shows an increase in the area-averaged monthly-mean EKE in the 9 km model over that in the 18 km model by a factor of five.

A dramatic difference is noted between the 0-220 m (model levels 1-15) annual average EKE in the northern Norwegian Sea and the Barents Sea (Figure 3.10). The northern Norwegian Sea is dominated by vigorous eddy activity including a region of Atlantic Water inflow at the entrance to the Bear Island Trough. Additionally, a distinct concentration of EKE, just north of Norway in the western Barents Sea associated with the Norwegian Coastal Current, is observed as well as a separate region of eddy activity at the eastern end of Bear Island Trough, associated with the warmer and saltier North Cape Current. These two currents meet farther to the east and a zone of increased eddy activity denotes their confluence, just southwest of the Central Bank, which would tend

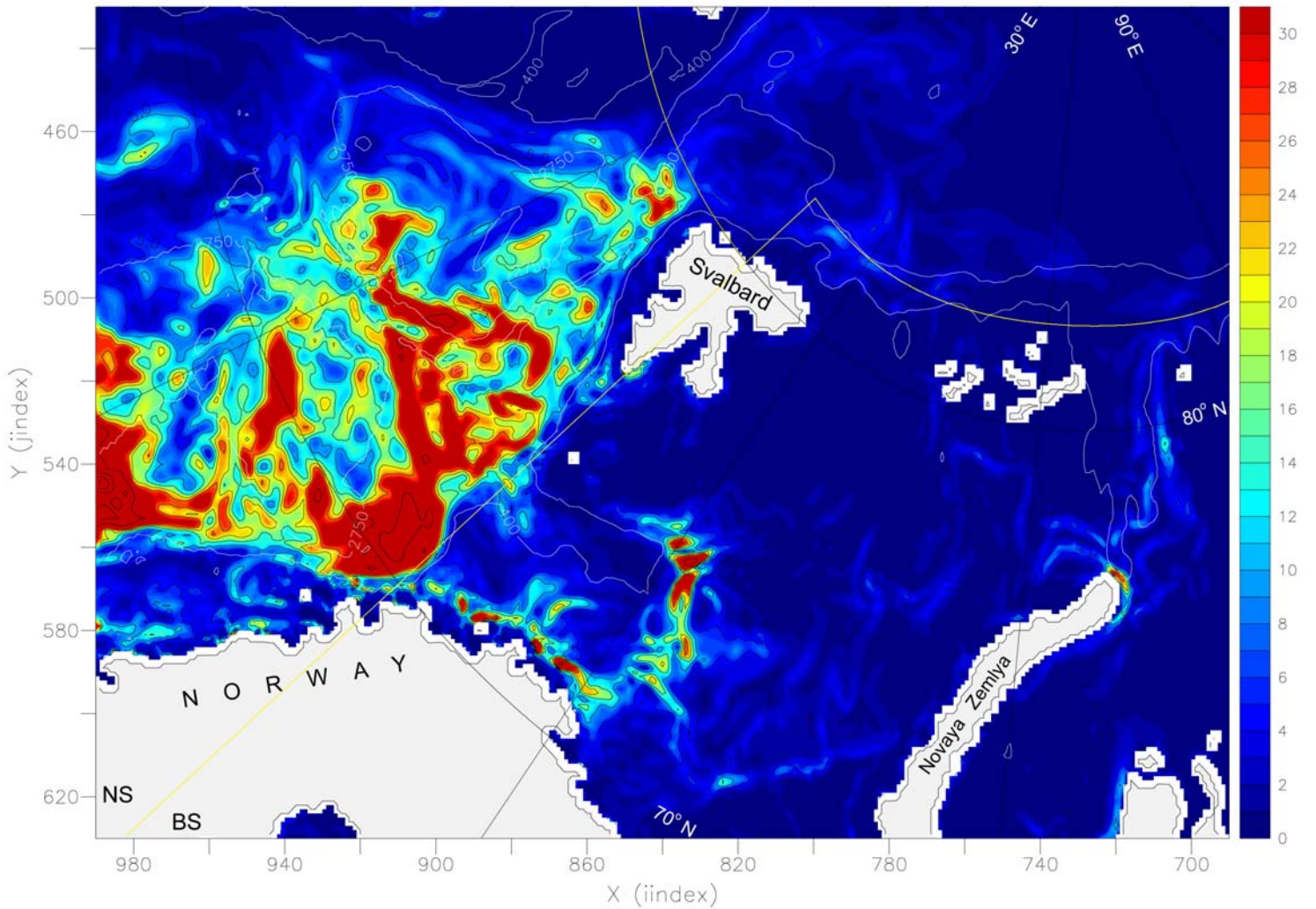


Figure 3.10: Horizontal distribution of annual mean, 0-220 m (model levels 1-15) vertically averaged eddy kinetic energy ($\text{cm}^2 \text{s}^{-2}$), calculated from monthly mean model output. Area averaged monthly maximum – $363.22 \text{ cm}^2 \text{s}^{-2}$. Area averaged annual mean – $6.79 \text{ cm}^2 \text{s}^{-2}$. 400 m and 2750 m depth contours in white. EKE contours $5\text{-}25 \text{ cm}^2 \text{s}^{-2}$ by $5 \text{ cm}^2 \text{s}^{-2}$, $25\text{-}150 \text{ cm}^2 \text{s}^{-2}$ by $25 \text{ cm}^2 \text{s}^{-2}$ in black. Yellow lines indicate Norwegian Sea (NS) and Barents Sea (BS) sub-regions used in calculations for Figure 3.11.

to mix their properties. There are several areas of eddy activity associated with bathymetric features, along 30° E in the southwestern Barents Sea and adjacent to the sharp northward turn in the shelf slope near 15° E , where the Norwegian Sea meets the Barents Sea.

In stark contrast to the annual mean eddy activity in the southern half of the Barents Sea is an area of almost no eddy activity in the predominantly cold Arctic Ocean origin water south and east of Svalbard. It is suspected that the seasonal ice cover in this region tends to decrease the annual mean EKE by damping the effect of stronger surface

winds during periods of increased atmospheric low activity. Slightly higher levels of EKE ($0-5 \text{ cm}^2/\text{s}^2$) are observed west of Novaya Zemlya, along the path of the Atlantic Water flow, indicating continued mixing and modification as it transits the Barents Sea. Eddy activity increases north of Novaya Zemlya and along the eastern side of St. Anna Trough, increasing the mixing occurring between the Barents modified Atlantic Water and Kara Sea origin water, flowing into to the Eurasian Basin. A steady decrease of EKE with depth occurs in the Norwegian and Barents Seas, with the area-averaged EKE between 0 and 500 m being 65% of the annual mean value between 0 and 50 m ($7.54 \text{ cm}^2 \text{ s}^{-2}$ versus $11.49 \text{ cm}^2 \text{ s}^{-2}$ respectively). Based on comparison of annual mean surface EKE calculated from monthly means with that calculated from daily snapshots, one can expect the 0-500 m annual mean EKE based on daily values to be on the order of $45 \text{ cm}^2 \text{ s}^{-2}$.

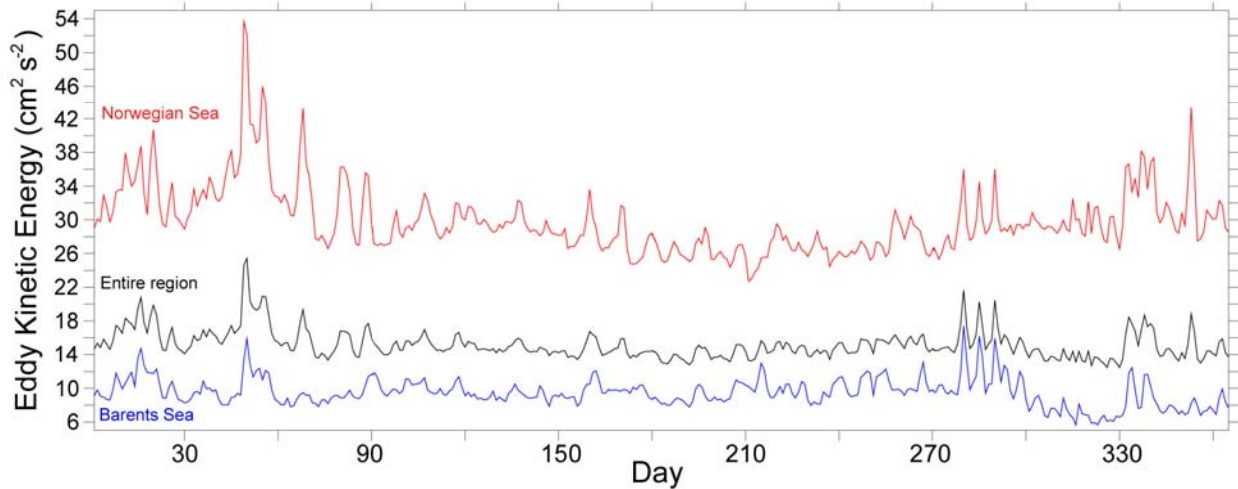


Figure 3.11. Daily variability of area-averaged, surface, 0-5 m (model level 1), eddy kinetic energy ($\text{cm}^2 \text{ s}^{-2}$) for the northern Norwegian and Barents Seas. Norwegian Sea and Barents Sea values were calculated in the sub-regions indicated by the yellow lines in Figure 3.10. The entire region average is for the region contained in Figure 3.10.

Surface (0-5 m, model level 1) EKE, calculated from daily output, varies seasonally and with what appears to be atmospherically induced variability, indicated by distinct 5-7 day peaks in a one year times series (Figure 3.11). Fall and winter are the periods of maximum surface eddy activity in the northern Norwegian Sea, due to an increase in frequency and intensity of atmospheric lows transiting the region. However, winter and summer are the periods of maximum eddy activity in the Barents Sea. This

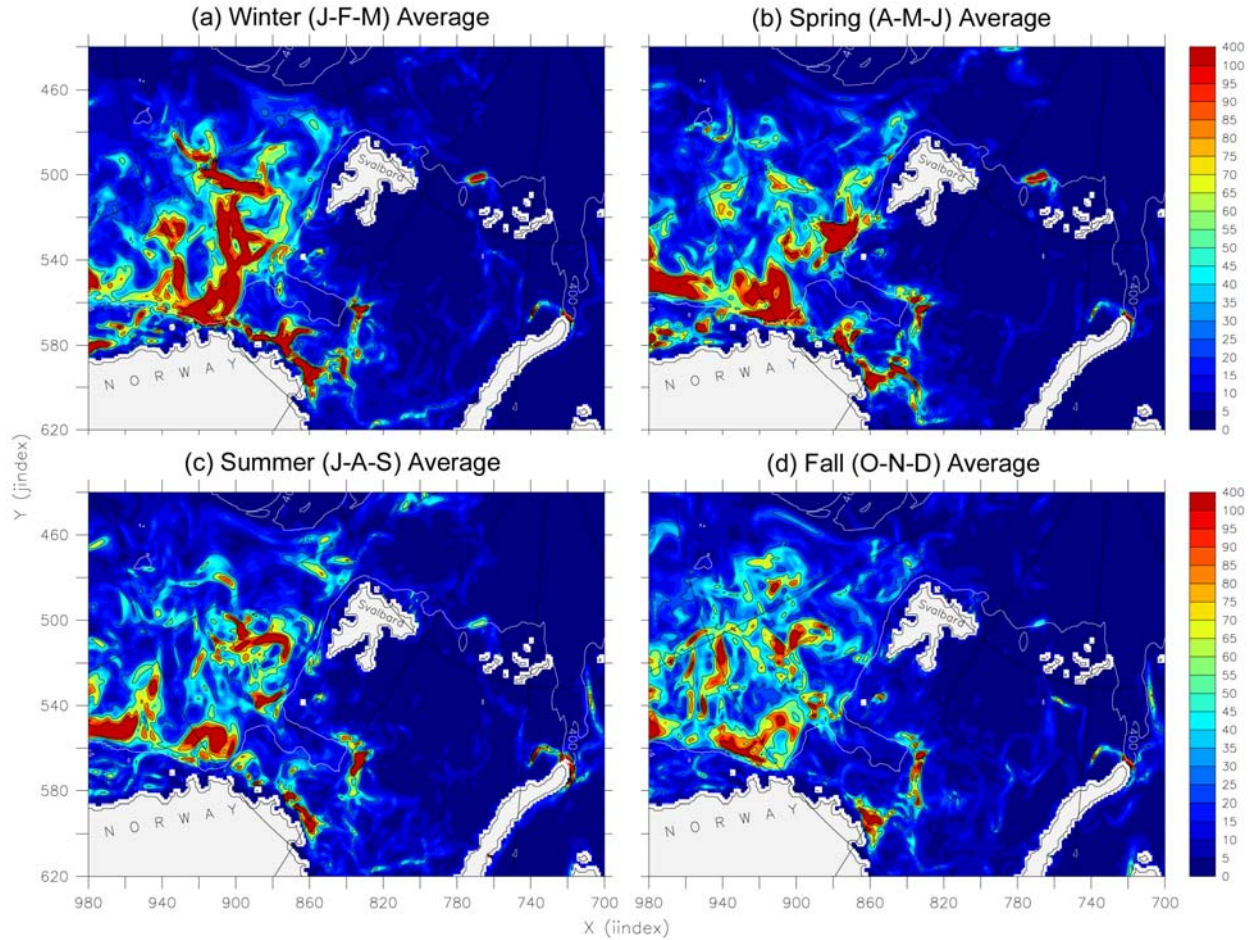


Figure 3.12. Distribution of the seasonal average of the eddy kinetic energy ($\text{cm}^2 \text{s}^{-2}$) at the surface, 0-5 m (model level 1), calculated from daily model output. Winter (Jan-Feb-Mar) (a); Spring (Apr-May-Jun) (b); Summer (Jul-Aug-Sep) (c); and Fall (Oct-Nov-Dec) (d). EKE contours 25, 50, 75, and $100 \text{ cm}^2 \text{s}^{-2}$ in black. 400 m depth contour in white

difference in periods of maximum eddy activity is most likely a result of the growth and retreat of the sea ice cover in the Barents Sea directly affecting the transfer of momentum between the atmosphere and the ocean in the fall. The winter maximum in EKE in the Barents Sea may be a result of a lag in the energy propagating from the Norwegian Sea. Atlantic Water flow through the Barents Sea intensifies in summertime, particularly north of Novaya Zemlya and along the eastern edge of St. Anna Trough (Figure 3.12). There is a small increase in EKE in the fall in the northwestern quarter of the Barents Sea, east and south of Svalbard, and northeast of Bear Island. In fall and winter, periodic increases in eddy activity occur every three to five days, on the order of $20\text{-}30 \text{ cm}^2 \text{s}^{-2}$ in one day.

These propagate rapidly from west to east in response to atmospheric lows transiting the region.

The EKE in the model is still under-represented due to inadequate resolution, the use of mean atmospheric forcing to drive the model during spinup and the monthly mean output used in many of these calculations. The internal Rossby radius of deformation is about 6 km in the St. Anna Trough (U. Schauer, personal communication) and a model would need a grid cell spacing on the order of 1 km to be able to properly resolve features of that scale.

E. DISCUSSION

Comparison of monthly averaged and daily-snapshot model output with observations shows the high-resolution coupled-ice ocean model captures many of the important processes and water masses in the Barents Sea reasonably well. However, due in part to model resolution and the small internal Rossby radius at high latitudes, some processes are not as well resolved.

The free surface and high vertical resolution allow application of realistic bathymetry in the Barents Sea, which is the primary controlling factor for much of the circulation. As a result, the long-term circulation patterns agree well with published maps (Ozhigin et al., 2000). The Atlantic Water flow through the Barents Sea, from the merging of portions of the North Cape Current and the Norwegian Coastal Current south of the Central Bank to the St Anna Trough outflow, is well defined. There is seasonal variability in the intensity of the flow, yet limited variability in the overall path. Comparison of model stations with selected observations indicates sub-grid-scale-mixing processes may be under-represented. Mass and property transport magnitudes agree reasonably well with those calculated from observations. However, monthly and seasonal variability is smaller than some published observations. The application of realistic daily varying atmospheric forcing and the inclusion of river inputs and tidal effects in the model are expected to improve modeled seasonal variability and possibly the representation of water mass transformations in the Barents Sea.

Under the prescribed atmospheric forcing, the mass, heat and salt contributions of the Fram Strait and the Barents Sea branches of Atlantic Water, extending eastward to the shelf break boundary current north of Severnaya Zemlya, are nearly equal. It is hypothesized that during periods of strong positive NAO, when Atlantic Water inflow to the Barents Sea increases, the BSBW will displace the FSBW farther north, causing a greater amount of the FSBW to follow the Lomonosov Ridge to the north and recirculate within the Eurasian Basin.

Calculations of EKE indicate a response to seasonal variability as well as areas of increased activity apparently associated with bathymetric features. Reducing the model grid spacing, from 18 km to 9 km, has resulted in an increase in EKE by a factor of five in this region. It is expected that further increases in resolution will increase model EKE levels in the Barents Sea. Five numerical simulations using a closed basin quasi-geostrophic ocean model, varying only in horizontal resolution (from 25 km to 1.56 km) and viscosity coefficients, and therefore Reynolds number (Re), indicated a continual increase in EKE with increased resolution (Siegel et al., 2001). Siegel et al. (2001) also found that the rate of increase slows somewhat at the highest Re , indicating the possibility of a regime where eddy variability becomes insensitive to further increases in Re .

IV. CANADIAN ARCTIC ARCHIPELAGO

A. OBSERVED PHYSICAL OCEANOGRAPHY

The Canadian Arctic Archipelago (CAA), a complex collection of islands and channels (Figure 4.1) that has lured explorers and merchants for centuries with the promise of riches and a shorter passage from the Atlantic Ocean to the Pacific Ocean, is one of the four pathways of communication between the Arctic Ocean and the world oceans. Along with the Barents Sea and Fram Strait, the CAA influences exchanges with the Atlantic Ocean (Rudels, 1986). However, unlike the Barents Sea and Fram Strait with two way exchanges, flow through the Archipelago is essentially unidirectional, from the Arctic Ocean toward the south/southeast. Arctic surface waters are modified as they pass through the CAA by the addition of buoyancy fluxes from ice growth and melt and from land drainage (Melling et al., 1984; Prinsenber and Bennett, 1987). The modified Arctic waters emerging from Baffin Bay and Hudson Bay contribute greatly to the oceanography along the southern part of the Canadian east coast (Ingram and Prinsenber, 1998).

The shallow sills are the primary factor that limit Arctic outflow through the region to the upper water layers. In the western and northern Archipelago, 350-450 m sills limit inflow from the Beaufort and Lincoln Seas. A 250 m sill north of Kane Basin limits flow through Smith Sound into Baffin Bay. In the center of the Archipelago, Barrow Strait is the shallowest section of the Northwest Passage at approximately 125 m (Prinsenber, 1997). Southeast of Barrow Strait, a 150 m sill in Fury and Hecla Strait controls communication from the northern Archipelago to Foxe Basin and then Hudson Bay. Davis Strait, a 300 km wide opening located between Baffin Bay and the Labrador Sea, is 640 m at its shallowest and a 250 m deep sill at the western end of Hudson Strait limits flow between the Labrador Sea, Foxe Basin and Hudson Bay.

Fissel et al. (1988) provide an excellent overview of non-tidal, residual currents observed in many of the channels of the Archipelago during an extensive Institute of Ocean Sciences observation program from 1981 through 1985. They discuss the history



Figure 4.1. Canadian Arctic Archipelago model geography and place names. PPI = Prince Patrick Isl. MI = Melville Isl. MKI = Mackenzie King Isl. BHI = Bathurst Isl. ERI/ARI = Ellef/Amund Ringness Isl. AHI = Axel Heiberg Isl. CI = Cornwallis Isl. PWI = Prince of Whales Isl. KWI = King William Isl. SI = Somerset Isl. BI = Bylot Isl.

of data collection in the Archipelago and include data collected from ice beset ships, drifting buoys and other sources as well, where appropriate. The key points of their compilation regarding circulation in the CAA are provided here.

Mean flows vary from 0.2 to 19 cm/s over the area, and the maximum non-tidal current observed in 1981-1985 was 37 cm/s; the strongest flows were concentrated near the shore (Fissel et al., 1988). They report the larger values are found in the shallower central waterways: Byam Martin Channel, Barrow Strait, Penny Strait and Wellington Channel. The smallest currents are found in the broad, deep, ice-bound western channels: western Parry Channel, McClintock Channel and the waterways of the Queen Elizabeth Islands; narrow, stronger coastal currents up to 10 km in width do, however, exist in these areas. Flow fluctuations of significant amplitude occur over periods up to several tens of days in duration, with the largest variance at periods between 10 and 25 days. As with mean values, the fluctuations are generally larger in the central waterways and larger variances occur in fall and early winter. In the summer, current fluctuations increase noticeably in the near surface zone (but not at depth), presumably due to more effective wind forcing in the open-water season (Fissel et al., 1988).

The overall circulation suggested first by ice beset vessels and then confirmed by drifting buoy observations is a net drift south and east towards Baffin Bay. Currents were usually strongest along the sides of the channels, often being weak and directionally variable in mid-channel (Fissel et al., 1988). The currents on opposite sides of the channels are often opposite in direction, a combination which is possible in terms of geostrophic dynamics if the width of the channel is large compared to the local internal Rossby radius of deformation (LeBlonde, 1980). LeBlonde (1980) discusses generalized geostrophic dynamics in channels with different shapes as well as counter currents in several of the wider channels in the Archipelago (Hudson Strait, Lancaster Sound and Prince Regent Inlet). He calculates the governing radii for the southern and northern sides of the mouth of Hudson Strait as 13.5 km and 4.7 km, respectively, clearly allowing the two opposing currents in the approximately 40 km wide channel. Drifter tracks serve to illustrate the interaction between the opposing currents at the mouth of Hudson Strait and it is postulated that the interaction may be due to non-geostrophic effects such as

friction, causing flow down the pressure gradient, or inertia, which leads to overshooting in corners (LeBlonde, 1980). Fissel et al. (1988) discuss the preference for eastward flow along the southern side of eastern Parry Channel and the coastal currents flowing in opposing directions on either side of Wellington Channel, Prince Regent Inlet, Admiralty Inlet, McDougal Sound and Peel Sound. Fissel et al. (1988, Chapter IV) provide a detailed description of the variable and intricate annual mean and seasonal residual circulation in the many channels of the Archipelago. Model similarities and differences relative to observed characteristics will be discussed in the next section. Due to the geographic complexity of the region the discussion will focus on the main pathways of flow of Arctic origin water through the Archipelago.

B. MODEL PHYSICAL OCEANOGRAPHY

A three year mean of 0-226 m (model levels 1 through 16) velocity (Figures 4.2(a, b)) indicates model flow through the CAA follows the observed south and eastward pattern. This chapter is organized geographically, first discussing the circulation of Arctic surface water entering the Archipelago through the northern channels, circulation in the central channels of the Archipelago, Hudson Bay circulation, Baffin Bay circulation and finally Labrador Sea circulation. The discussion of seasonal variability will follow a similar geographic sequence but will be limited to regions with significant seasonal variability or differences from observed circulation.

1. Canadian Arctic Archipelago Circulation

Arctic surface water enters the CAA primarily through Nares Strait north of Smith Sound; Peary Channel between Axel Heiberg Island and the Ringness Islands; Prince Gustav Adolf Sea between Ellef Ringness Island and Mackenzie King Island; McClure Strait between Prince Patrick and Banks Islands; and Amundsen Gulf between Banks Island and the Canadian mainland. The steady flow through McClure Strait does not concur with the “generally weak and variable in direction residual flow” described in Fissel et al. (1988), however, observed circulation patterns in this region remain poorly resolved due to the small number of direct measurement sites and the spatial complexity

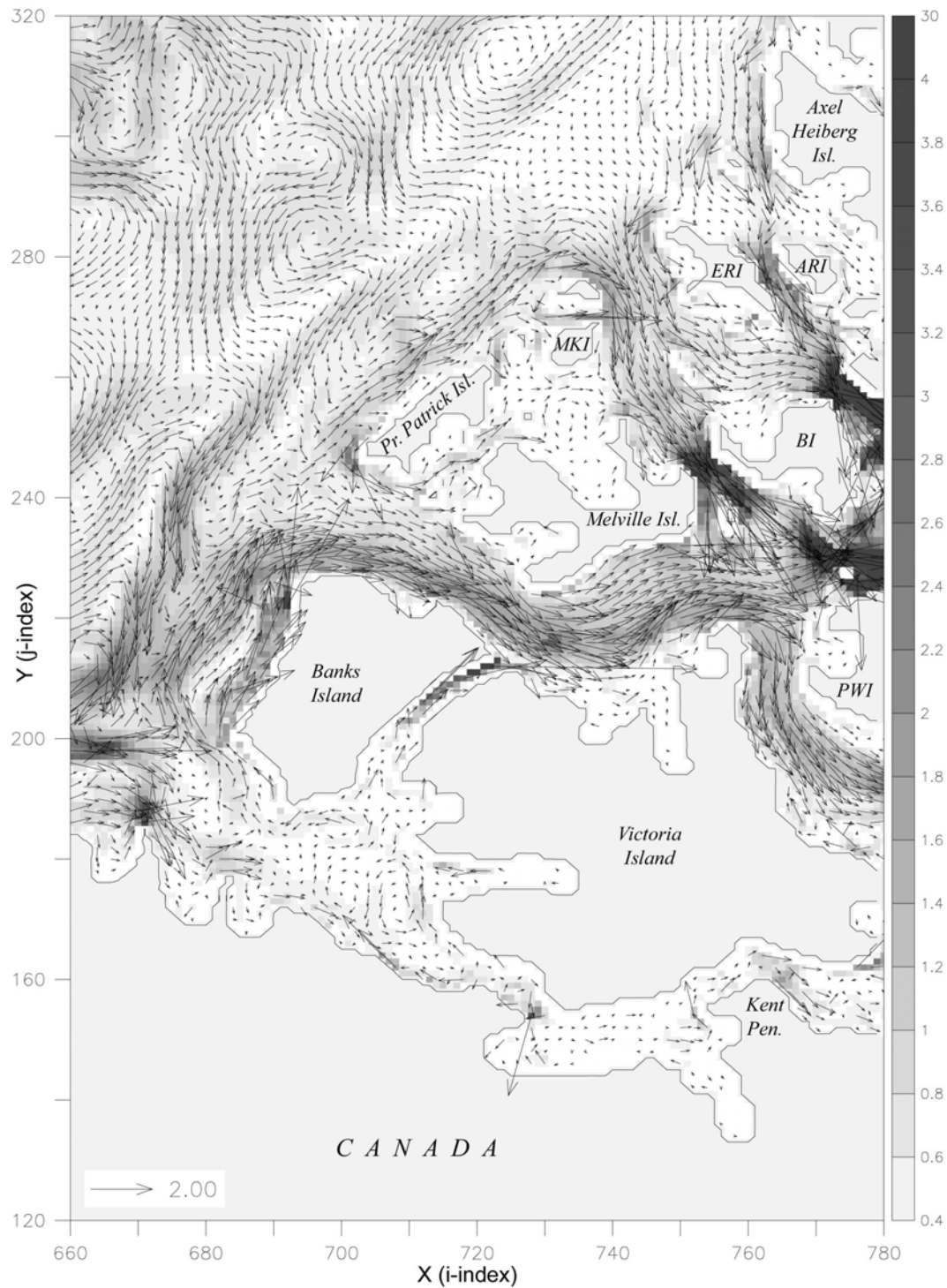


Figure 4.2(a). Horizontal distribution of three year mean (1979-1981) 0-226 m (model levels 1-16) average velocity (cm/s) in the western Canadian Arctic Archipelago. Background shading is 0-226 m mean speed (scalar). Every other velocity vector is plotted. MKI = Mackenzie King Isl. ERI = Ellef Ringness Isl. ARI = Amund Ringness Isl. BI = Bathurst Isl. PWI = Prince William Isl. Note: vector length and shading scale differ from Figure 4.2(b)

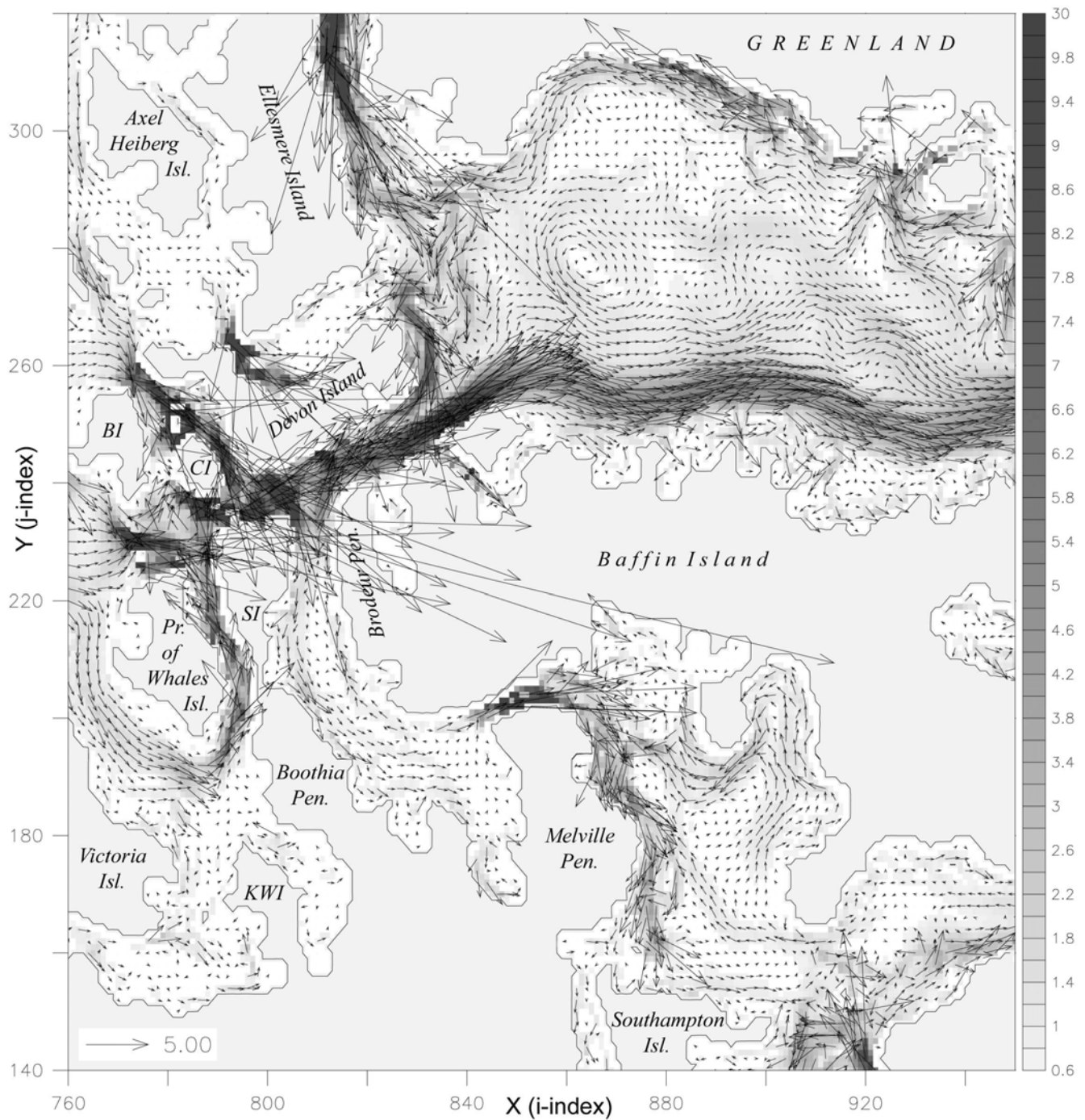


Figure 4.2(b). Horizontal distribution of three year mean (1979-1981) 0-226 m (model levels 1-16) average velocity (cm/s) in the eastern Canadian Arctic Archipelago. Background shading is 0-226 m mean speed (scalar). Every second velocity vector is plotted. BI = Bathurst Island. CI = Cornwallis Island. SI = Somerset Island. KWI = King William Island. Note: vector length and shading scale differ from Figure 4.2(a).

of the measured flow (Fissel et al., 1988). The steady model flow may be in part due to the absence of tidal effects in this model. Tidal forces may induce flow reversals and thus reduce the mean velocity through McClure Strait. Fissel et al. (1988) found reversing tidal currents of up to 10 cm/s in many of the northern channels connecting the CAA to the Arctic Ocean.

Arctic surface water enters the western side of Amundsen Gulf (Figure 4.2(a)). The majority of this flow recirculates out of Amundsen Gulf along the west coast of Banks Island, but a portion continues south along the coast of the Northwest Territories. Most of this branch then recirculates back to the north before it reaches Dolphin and Union Strait, between Amundsen Gulf and Coronation Gulf. There is a weak eastward flow indicated through Prince of Whales Strait between Banks and Victoria Islands. This is most likely overestimated in the model as the ~20 km wide channel was artificially widened to ~36 km (four grid points) to maintain flow through the channel due to model resolution and velocity point calculation requirements as described in Chapter II.

There are additional locations within the Archipelago where modifications were made to the geography and bathymetry due to model resolution. Consideration was given to the dynamical importance of the feature and the pros and cons involved in either widening, deepening, or closing narrow channels. King William Island, at the eastern end of Queen Maud Gulf, is connected to mainland Canada. Additionally, Belot Strait, between the Boothia Peninsula and Somerset Island is closed. It was felt both channels were too narrow to be properly represented at this resolution. In contrast, Fury and Hecla Strait, between the Melville Peninsula and Baffin Island was widened to 36 km in order to maintain flow through it (Figure 4.2(b)). These modifications highlight the need for further increases in resolution, to be able to properly represent the bathymetry as well as exchanges through smaller channels within the CAA.

The mean flow in Coronation Gulf and Queen Maud Gulf is weak and variable, indicating considerable seasonal variability, which will be discussed below. There is a weak (less than 0.5 cm/s) mean northward flow along the eastern tip of Victoria Island from Queen Maud Gulf into McClintock Channel (Figure 4.2(b)). There is a broad eastward flow throughout McClure Strait into Viscount Melville Sound, with an average

speed of 1-2 cm/s. A portion of this flow turns south in McClintock Channel and travels counter-clockwise around Prince of Whales Island, passing through Larsen Sound, the Franklin Channel and Peel Sound, to re-enter the main flow through Parry Channel, just to the west of Barrow Strait.

The southerly flow from the Arctic Ocean enters Prince Gustav Adolf Sea, passing between Ellef Ringness and Mackenzie King Islands. This flow splits north of Bathurst Island. The westerly branch enters Byam-Martin Channel and splits again to flow around Byam Martin Island (represented in the model by one grid point) and travels through Byam Channel to the west and Austin Channel to the east. Both of these branches flow into Parry Channel. The eastward branch of flow out of the Prince Gustav Adolf Sea, along with Arctic surface water entering the Archipelago via Peary Channel, between Ellef Ringness Island and Axel Heiberg Island, travels south through Penny Strait. The majority of the flow through Penny Strait continues through the Wellington Channel, driven to the east of Cornwallis Island by bathymetry, and then into the eastern end of Parry Channel, east of Barrow Strait.

The mean Arctic surface water flow from Norwegian Bay into Jones Sound is relatively fast, with a maximum near 50 cm/s, however it is severely limited by bathymetry and the narrowness of the passage between Devon Island and Ellesmere Island. The mean flow through Barrow Strait also has maxima on the order of 50-60 cm/s, due to a venturi effect as the bathymetry shoals and narrows between Cornwallis Island and Somerset Island. Some of the largest long term mean current velocities, 50-60 cm/s, occur in Nares Strait, as Arctic Water travels from the Lincoln Sea, through Kane Basin, into Smith Sound. Generally, the mean velocities in the eastern portion of the Archipelago, east of 95° W, are the fastest.

There is southward flow into the western side of Prince Regent Inlet, south of Devon Island. This flow continues south along the east coast of Somerset Island and the Boothia Peninsula. Recirculation occurs to the north within the Gulf of Boothia and a weak northward current along the west coast of the Brodeur Peninsula on Baffin Island. Flow accelerates through the chokepoint of Fury and Hecla Strait and enters Foxe Basin.

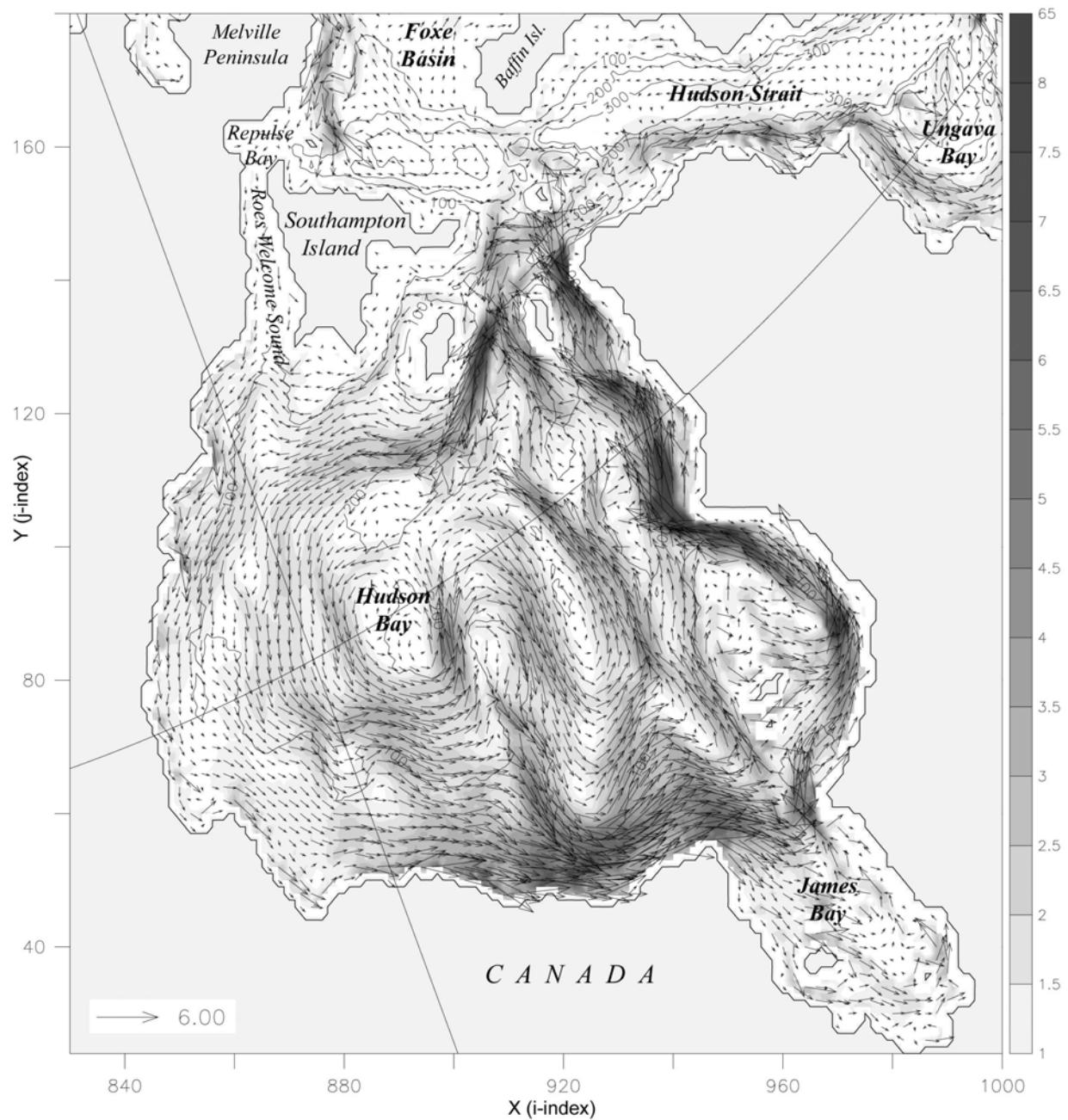


Figure 4.3.. Horizontal distribution of three year mean (1979-1981) 0-226 m (model levels 1-16) average velocity (cm/s) in Hudson Bay. Background shading is 0-226 m mean speed (scalar). Every second velocity vector is plotted.

There is steady southward flow along the east coast of the Melville Peninsula which continues to the north coast of Southampton Island and into Hudson Bay. The mean flow in Foxe Basin is to the north, with separate currents identifiable along the 50 m contour and closely following the coast of Baffin Island as well.

2. Hudson Bay Circulation

Due to resolution, Repulse Bay and Roes Welcome Sound are not well represented in the model, yet there is indication of weak southward flow into Hudson Bay via this route (Figure 4.3). This flow, along with westward Hudson Strait flow entering Hudson Bay along the south coast of Southampton Island, travels cyclonically around Hudson Bay. This cyclonic boundary current intensifies along the southern and eastern coasts. Long term mean circulation within central Hudson Bay is essentially cyclonic as well, following the bathymetry (Figure 4.3). A portion of the Hudson Bay coastal circulation travels cyclonically around James Bay, rejoining the main coastal flow as it heads north toward Hudson Strait.

The model captures the observed westward inflow on the northern side and eastward outflow on the southern side of Hudson Strait (LeBlonde, 1980; Fissel et al., 1988). The mean outflow to the Labrador Sea is generally wider (50-60 km versus 20-30 km) and more intense (3-4 cm/s versus 1-2 cm/s) than the inflow. These model widths are roughly four to five times those calculated by LeBlonde (1980) and this is most likely a result of model resolution not being fine enough to accurately represent these narrow opposing flows. There is indication of recirculation of Baffin Bay water in Hudson Strait and interaction between the opposing flows in the center of Hudson Strait. The majority of the eastward flowing Hudson Strait outflow follows the coastline around Ungava Bay prior to continuing south along the Labrador coast (Figure 4.3).

3. Baffin Bay Circulation

The three year mean circulation in Baffin Bay is predominantly cyclonic (Figure 4.4) and agrees reasonably well with that observed (Bourke et al., 1989). Arctic Water enters Baffin Bay from the south along the west coast of Greenland as the West Greenland Current. Flow from the north enters Baffin Bay through Smith, Jones and Lancaster Sounds. Mean flow within central Baffin Bay is cyclonic as well. Lancaster Sound is the main source of Arctic water to northern Baffin Bay and Smith Sound provides the next largest contribution. The weak outflow from Jones Sound joins the Smith Sound outflow, these combine with the West Greenland Current and then merge with Lancaster Sound outflow. The Baffin Current, ~70-80 km wide, flows south along the northeast coast of Baffin Island with a mean velocity of 3-5 cm/s. There is a broad

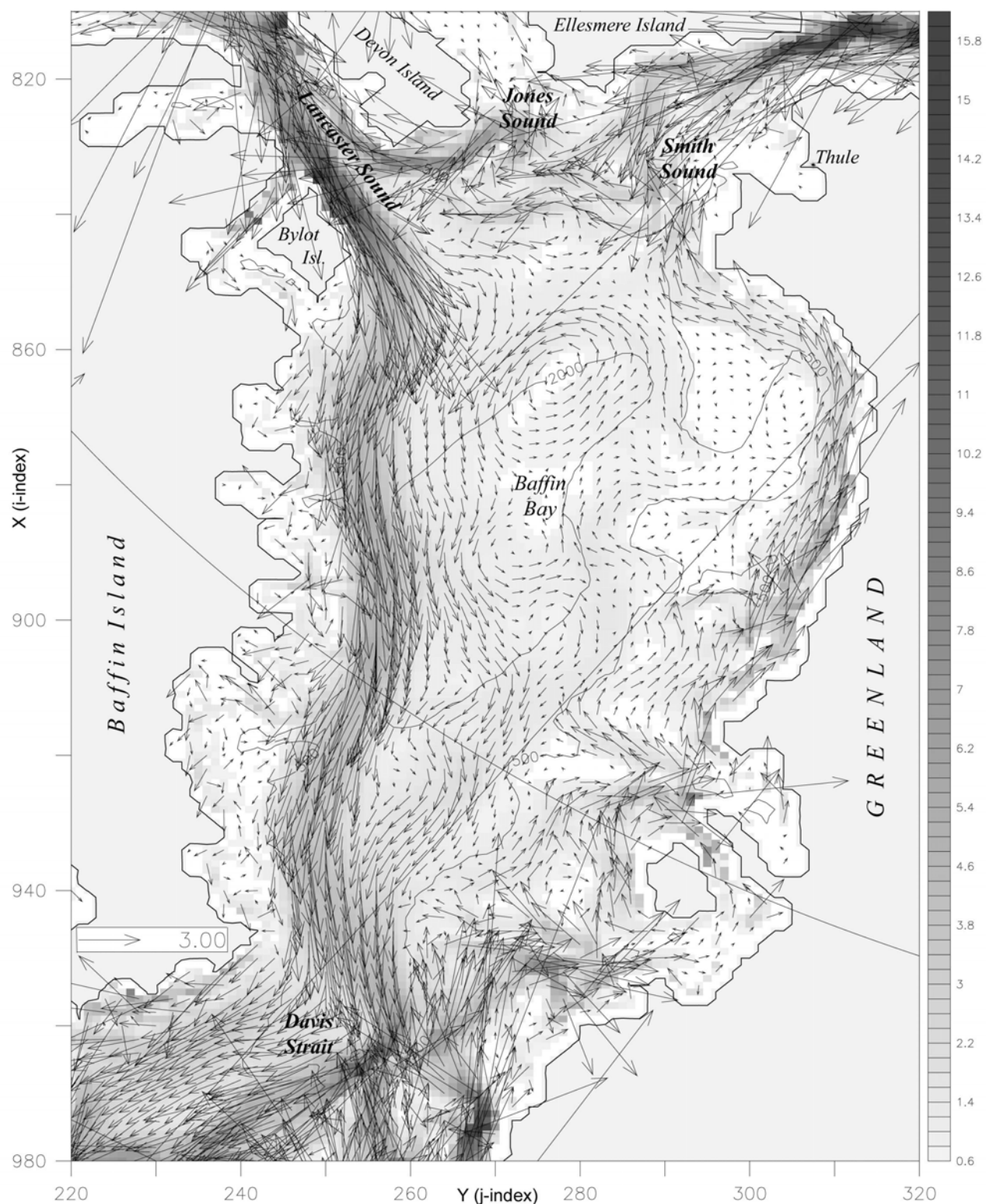


Figure 4.4. Horizontal distribution of three year mean (1979-1981) 0-226 m (model levels 1-16) average velocity (cm/s) in Baffin Bay. Background shading is 0-226 m mean speed (scalar). Every second velocity vector is plotted.

southward flow through the western two-thirds of Davis Strait and a weaker, less organized, northward flow through the eastern one-third.

4. Labrador Sea Circulation

The three year mean flow in the Labrador Sea is predominantly east to west, with Arctic water from the East Greenland Current rounding Cape Farewell, turning north along the southwestern coast of Greenland and departing the coast of Greenland in several distinct paths, predominantly following the 1000, 2000 and 3000 m isobaths toward the Labrador coast (Figure 4.5). Two separate branches of the West Greenland Current are discernable, one following the 500 m curve north through Davis Strait and the other hugging the Greenland coast as it travels north. The Baffin Land Current is represented as a broad southward flow through Davis Strait, from the southeast coast of Baffin Island to the 500 m isobath with intensification along the shelf break. The southward flow following the 500 m curve bifurcates to travel around a depression in the bathymetry near the mouth of Hudson Strait. A portion of the western branch enters Hudson Strait to flow west along the south coast of Baffin Island while the majority continues around the bathymetric depression to rejoin the eastern branch (Figure 4.5).

South of 60° N, the multiple bands of flow crossing the Labrador Sea from the east join with the flow along the 500 m isobath to form an approximately 90 km wide, 8-12 cm/s, southerly flowing Labrador Current. This current flows primarily between the 500 and 2000 m isobaths. Closer to the Labrador Shore, a narrow coastal current is observed, which appears to be predominantly Hudson Strait outflow. Limited bathymetry driven interaction between the coastal current and the current along the shelf break is noted. This would indicate that the fresher Hudson Bay outflow stays on the shelf and is not a significant source of freshwater to the central Labrador Sea. The northward flow east of the Labrador Current is warm North Atlantic Current water. The mean northward extent of this flow is between 57 and 58° N and after entering the Labrador Sea, it turns and meanders east, flowing toward Europe.

Considerable seasonal variability is present in the flow through the CAA (not shown), primarily in the form of a summer intensification of existing currents due to increased wind influence as the ice cover decreases. For the purposes of this discussion,

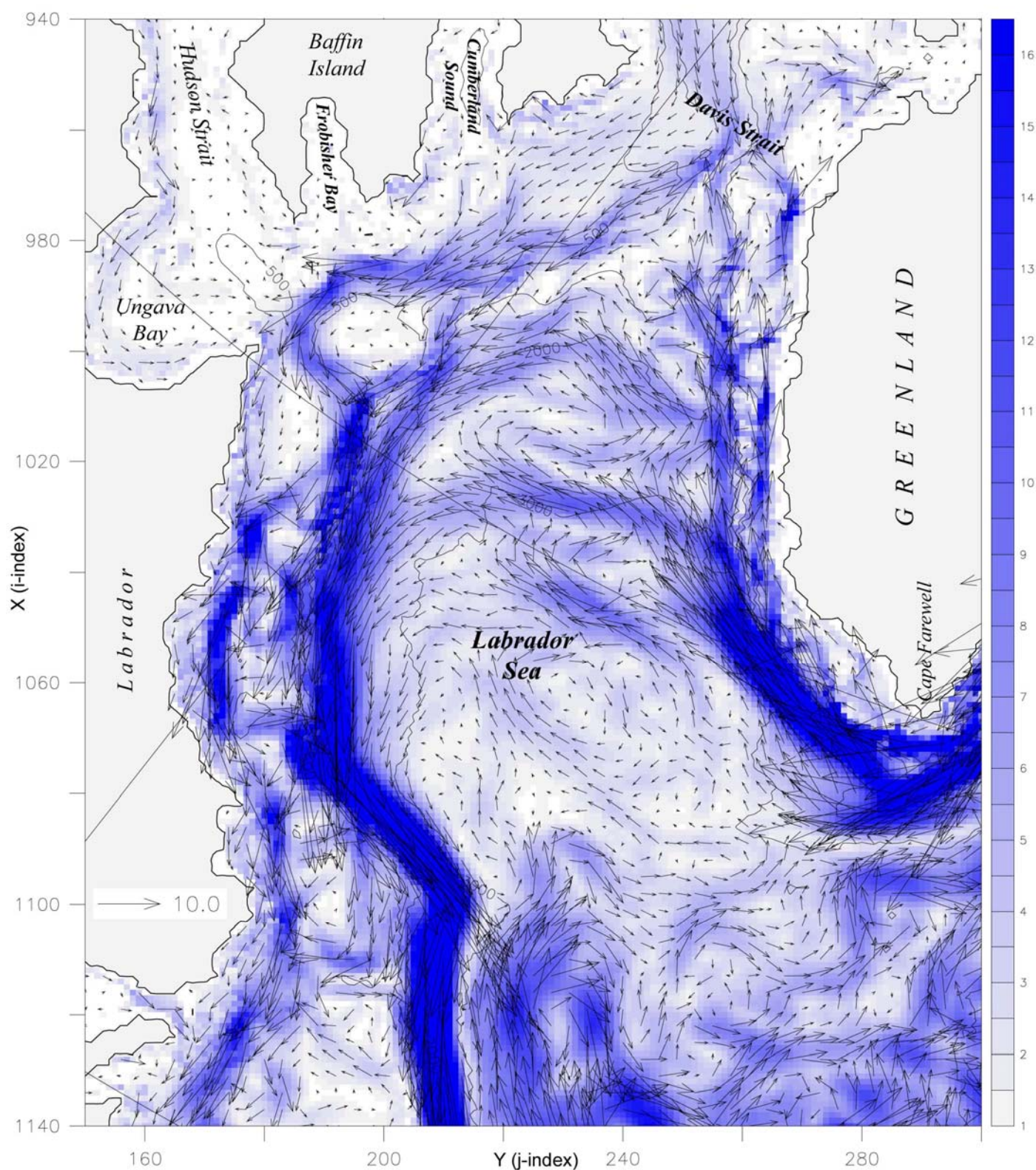


Figure 4.5. Horizontal distribution of three year mean (1979-1981) 0-226 m (model levels 1-16) mean velocity (cm/s) in the Labrador Sea. Background shading is 0-226 m mean current speed (scalar). Every third velocity vector is plotted.

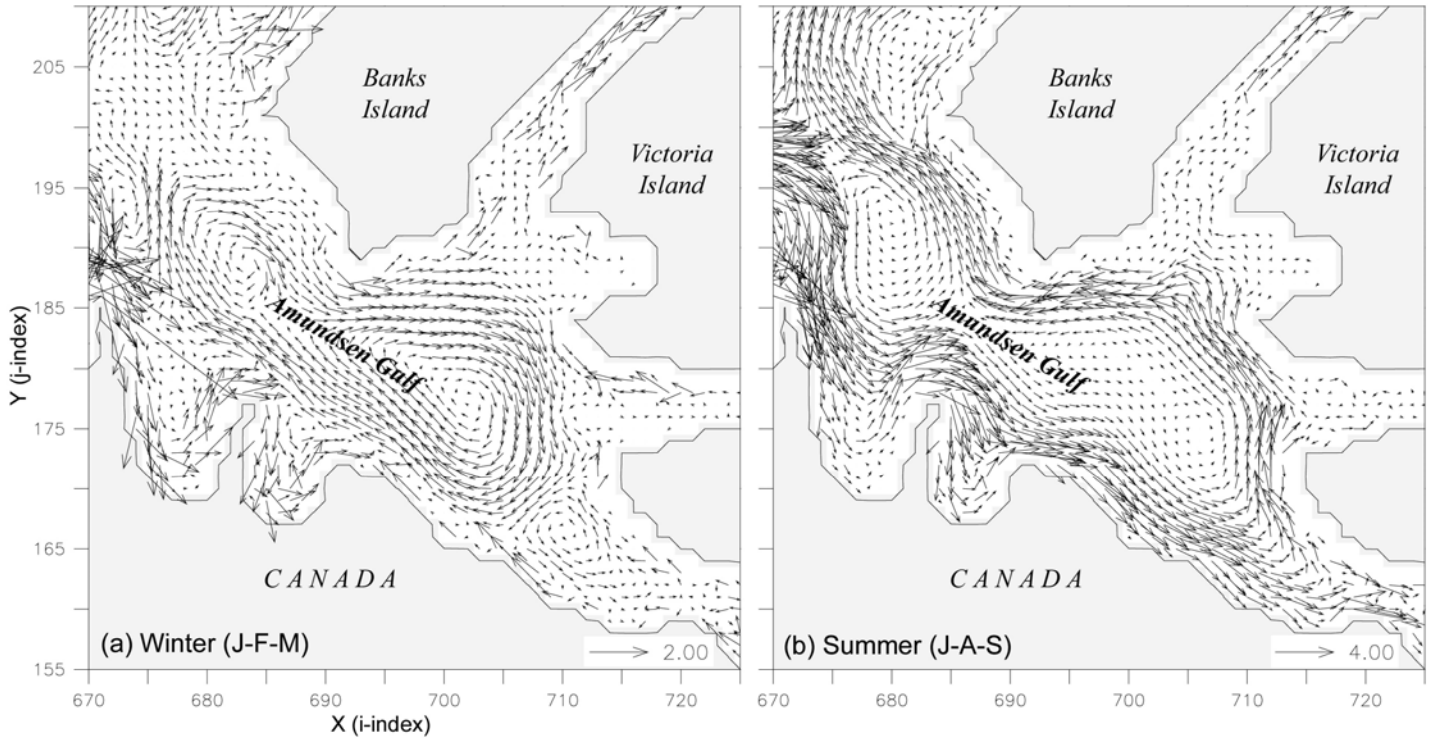


Figure 4.6. Horizontal distribution of 0-226 m (model levels 1-16) mean velocity (cm/s) in Amundsen Gulf for different seasons in 1980: (a) Winter Average (J-F-M); (b) Summer Average (J-A-S). Every velocity vector is plotted. Note the differing vector scales.

summer is defined as July, August and September, while winter is defined as January, February and March. The model output used in this analysis consists of seasonal means created from January, February and March, and July, August and September 1980 monthly means.

Flow reversals occur in Amundsen Gulf (Figure 4.6), Coronation Gulf (Figure 4.7), and Queen Maud Gulf (not shown). The predominantly cyclonic flow in the summer reverses to become a weak anticyclonic flow in the winter months. A combination of land-fast and sea-ice completely covers these regions in the winter, severely limiting wind influence and allowing the thermohaline circulation to dominate. No seasonal reversal in circulation is seen in McClure Strait. Instead, a summer intensification of the southeastward flow helps to maintain the ice cover through increased advection of cold Arctic surface water and sea-ice.

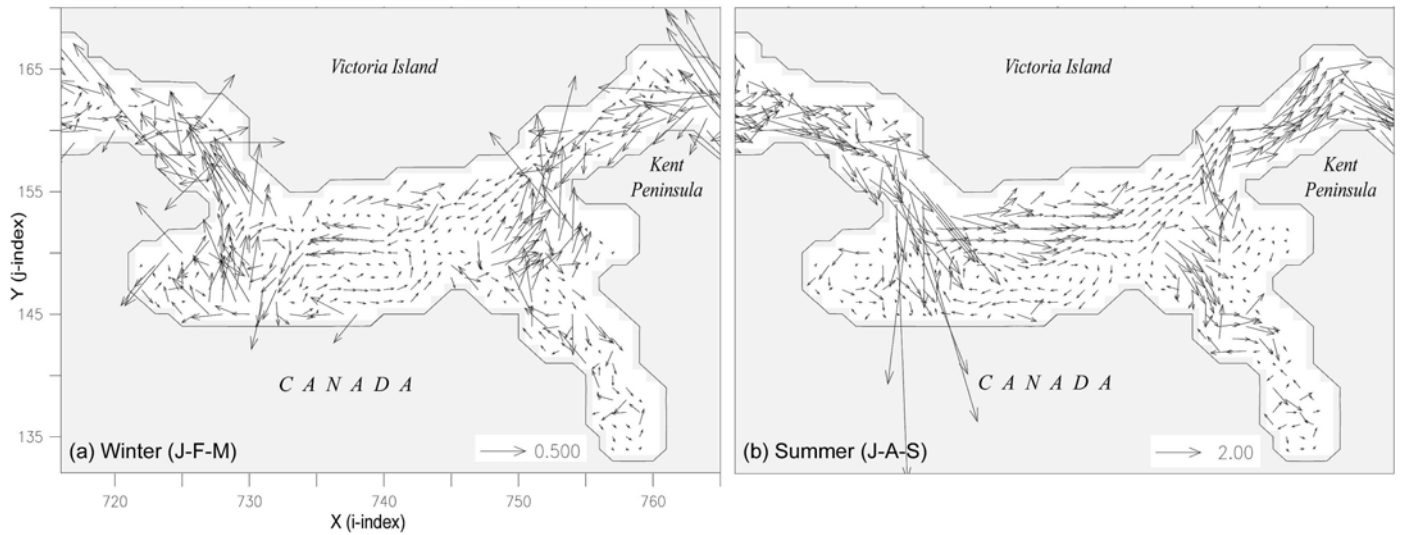


Figure 4.7. Horizontal distribution of 0-226 m (model levels 1-16) mean velocity (cm/s) in Coronation Gulf for different seasons in 1980: (a) Winter Average (J-F-M); (b) Summer Average (J-A-S). Every velocity vector is plotted. Note the differing vector scales.

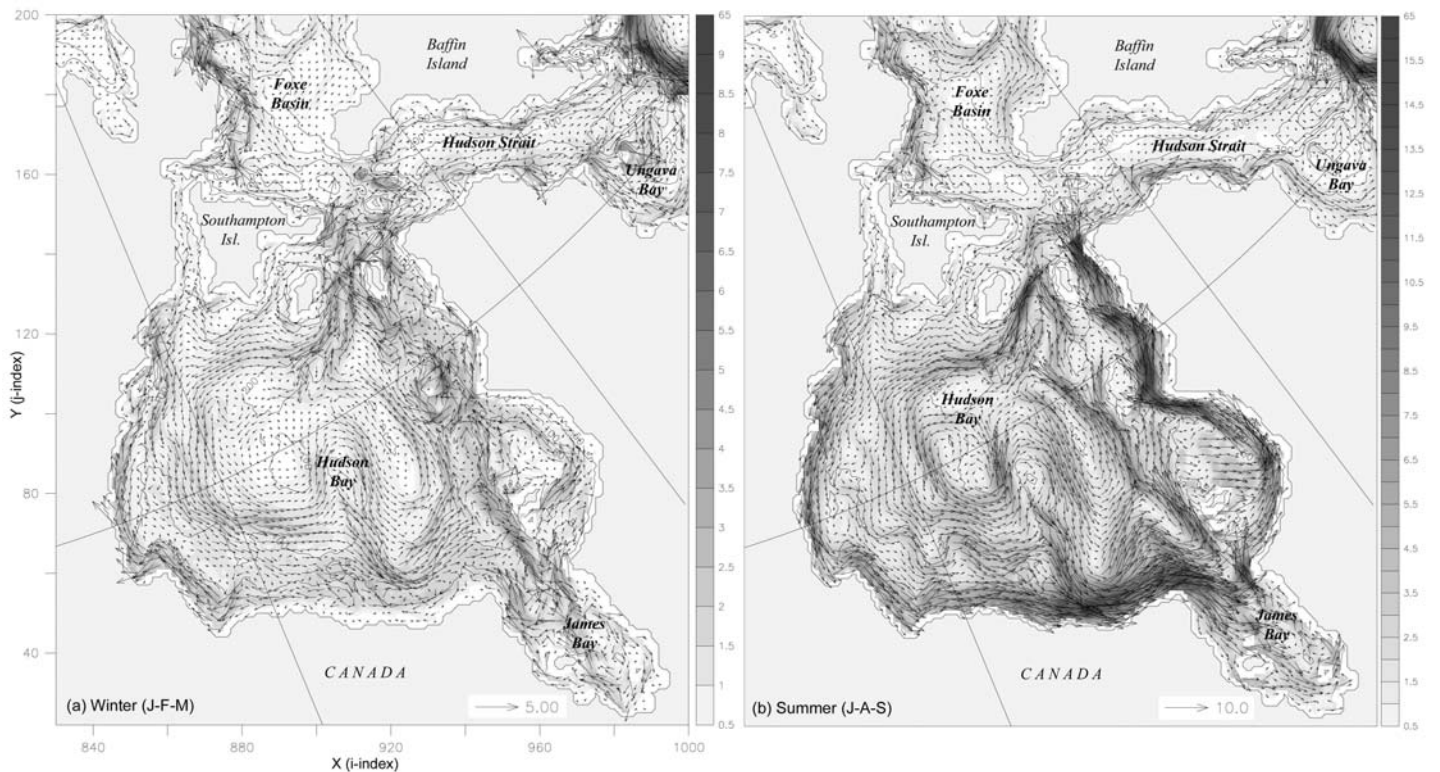


Figure 4.8. Horizontal distribution of 0-226 m (model levels 1-16) mean velocity (cm/s) in Hudson Bay for different seasons in 1980: (a) Winter Average (J-F-M); (b) Summer Average (J-A-S). Background shading is seasonal average 0-226 m speed. Every other velocity vector is plotted. Note the differing vector and shading scales.

A seasonal reversal is also seen in a portion of the coastal current in Hudson Bay (Figure 4.8) in contradiction to the observed year round circulation, which is described as continually cyclonic, with stronger flow in the summer (Prinsenbergh, 1987). The steady cyclonic flow along the west and south coasts, between the coast and the 50 m isobath, gives way in winter to a weak anticyclonic flow. Weak northward flow is observed through Roes Welcome Sound, west of Southampton Island, as well. Wintertime currents in James Bay and eastern Hudson Bay are predominantly cyclonic, as in summer, yet significantly weaker and much less organized. The lack of tides and river inputs to Hudson Bay in the model may explain the seasonal reversal along the coast, above the 50 m curve. Prinsenbergh (1987) found barotropic semidiurnal tidal currents of up to 28 cm/s in amplitude dominating the hourly observed currents. He also discusses how density driven circulation, enhanced by river runoff, contributes to the cyclonic flow in Hudson Bay.

The opposing flows on the north and south side of Hudson Strait are less evident in the summer, with eastward Hudson Bay outflow covering the southern two thirds of the channel in the summer months (Figure 4.8). Circulation within Foxe Basin remains to the north in the eastern part and to the south along the coast of the Melville Peninsula throughout the year, although the northward flow is considerably weaker in the winter. Generally throughout the Archipelago, flow reversals do not occur below 100 m, however, summer intensification of existing currents is evident. Also of note, the majority of the flow below 100 m in Hudson Strait is to the west, towards Hudson Bay, in both summer and winter. This indicates the model is able to capture a degree of vertical shear between the baroclinic, or wind driven flow in the upper layers and the predominantly barotropic deep flow.

A pronounced seasonal variability in the distribution of temperature and salinity is strongly evident in the top 50 m of the Canadian Archipelago (Figure 4.9 a-d). The change from nearly complete sea-ice coverage in the winter to primarily open water in nearly all of the channels south of 75° N (Figure 4.9 e, f) is a key factor in causing this variability. Warmer water penetrates farther north into eastern Baffin Bay in the summer and significant summer freshening of the top 50 m is evident in Coronation Gulf, Foxe

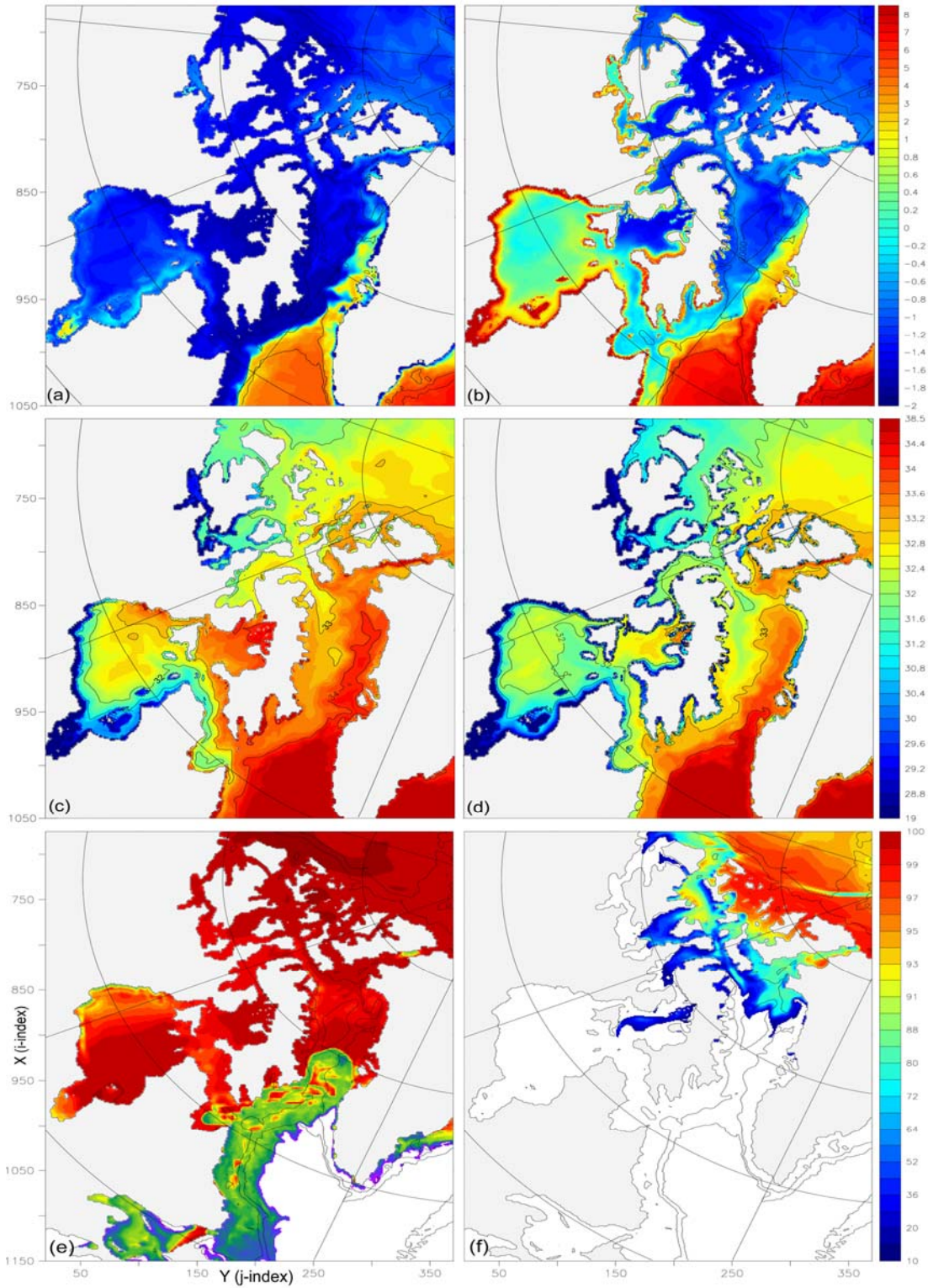


Figure 4.9. Distribution of temperature and salinity in the upper 0-53 m (model levels 1-8) and sea ice concentration for various seasons in 1980. Winter average (Jan-Feb-Mar) potential temperature (a) and salinity (c). Summer average (Jul-Aug-Sep) potential temperature (b) and salinity (d). Maximum winter sea ice concentration (%), day 72 (mid-March) 1980 (e). Minimum summer sea ice concentration (%), day 272 (early-September) 1980 (f). Note frames (e) and (f) cover a slightly larger region

Basin, western Hudson Bay and the central passages of the Archipelago. The model Hudson Bay is saltier in summer than observed with a maximum central salinity approaching 32.4 psu and a large area of salinities greater than 31 psu. Ingram and Prinsenberg (1998) report an average salinity near 29 psu with a small region of salinities greater than 30 psu in southwestern Hudson Bay. Inclusion of Hudson Bay river runoff in the model will most likely go a long way toward aligning the model salinity with that observed. Summer average model temperatures in Hudson Bay are colder than observed as well. The addition of river inputs, along with improved ocean climatology in this region (M. Steele, personal communication), are potential solutions.

Comparison of model monthly mean ice concentrations with satellite observed monthly mean concentration values (Gloersen et al., 1992) indicates a tendency towards under-predicting the amount of summer sea-ice melt in northern Baffin Bay and Hudson Bay. It is felt this may be due to the 'cold-bias' in the repeated climatological atmospheric forcing and the repeated 1979 forcing. With the application of the 1979-1981 cycle of forcing, a slight increase in summer sea-ice melt has been observed. It is hoped that with continued application of realistic daily forcing, and the associated increase in variability, the trend will continue toward a more realistic summer ice edge in northern Baffin Bay.

C. MASS, HEAT AND SALT TRANSPORTS

1. Mass Transport

Model volume transport results reflect the net flow from the Arctic Ocean into Baffin Bay and the Labrador Sea through the Archipelago. A net three year mean (1979-1981) Canadian Arctic Archipelago volume transport of approximately 1.01 Sv (1 Sv = 10^6 m³/s) is obtained by combining the calculated net volume transports through Lancaster, Jones and Smith Sounds with the net Hudson Strait transport (Table 4.1). This value is approximately half of that estimated by Aagaard and Greisman (1975) and Prinsenberg (1997). Although the reported values are derived from what are essentially snapshots or time series of limited duration. Model horizontal resolution may provide a partial explanation for this in that the width of some of the channels may be.

Section	Net Volume Transport	Vol In	Vol Out	Net Heat Transport	Net Salt Transport
Amundsen Gulf	-0.0034	0.0344	-0.0378	-0.1359	-0.1038
McClure Strait	-0.2861	0.0014	-0.2875	-1.2019	-0.8534
Barrow Strait	-0.1795	0.00	-0.1795	-0.8458	-5.9587
Fury and Hecla Str.	-0.0260	0.00	-0.0260	-0.1089	-0.8534
Lancaster Sound	-0.6133	0.0388	-0.6522	-2.3022	-20.6131
Jones Sound	-0.0194	0.0064	-0.0257	-0.1412	-0.6379
Smith Sound	-0.3544	0.0717	-0.4261	-0.5994	-12.4600
Hudson Strait	-0.0254	0.1155	-0.1409	-0.8526	-0.5143
Davis Strait	-1.1971	0.4456	-1.6427	5.8549	-41.2592

Table 4.1 1979-1981 three year mean simulated volume transport (Vol, Sv), net heat transport (Qheat, TW) and net salt transport (Qsalt, 10^6 kg s^{-1}) through selected CAA sections. In/out are defined as into/out of the Arctic Ocean, respectively. Negative transports indicate transport out of the Arctic Ocean. Qheat referenced to -0.1° C , Qsalt referenced to 34.4 psu. Calculations are for entire water column.

underestimated by between 1 and 4 km (alternatively, some channels may also be too wide by the same amounts). Channel widths in the model are limited to no narrower than 36 km (4 grid points across) and widths increase in increments of 9 km above that

Vertical resolution may play a role as well, as layer thickness between 100 and 300 m vary from 20 m thick to 50 m thick and depths shallower than the layer midpoints (Table 2.1) were rounded up. More importantly, due to the nature of how velocity is calculated in the model (described in Chapter II), a model channel that is four grid points across will only have flow in the center two velocity points, as the two coastal velocity points will be set to zero. The end result would be a significant under-representation of transport through this channel. One very labor intensive solution for this includes modifying the model bathymetry at the existing model resolution by adding an extra grid point on either side of the channel to ensure the velocity cross sectional area matches the physical cross section of the actual channel. This may result in more realistic mean transports, however, processes governed by the small radius of deformation at high latitudes would still not be well represented. Continued increases in model resolution, particularly in the Canadian Arctic Archipelago, may provide a better solution to both problems.

The model transport values through Smith Sound and Fury and Hecla Strait are roughly half of those reported by Fissel et al.(1988). Some of the difference here may be due to temporal differences between the modeled and observed data as well as how the model resolves the Canadian Archipelago bathymetry. Another possible source of disagreement is that the values reported in Fissel et al. (1988) were measured predominantly in the spring and summer, when eastward flow through the Archipelago is at a maximum. The larger percentage of the flow through the model Archipelago appears to be through Lancaster Sound, vice divided nearly equally between Smith and Lancaster Sounds (Fissel et al., 1988). This may be due to the steady southeasterly flow through McClure Strait in the model, where in reality, tidal effects may cause flow reversals and decrease the mean flow.

2. Heat and Salt Transports

Three year mean net heat and salt transports for the entire Archipelago are calculated as -3.89 TW and -34.23×10^6 kg/s, respectively. These values are approximately one-third to one-half of the -9.6 TW and 63×10^6 kg/s reported by Prinsenberg (1997) based on a compilation of available observed data. The under-representation of fluxes through the Archipelago is thought primarily to be a function of model resolution. Decreased skill in this region will then affect the mass, heat and salt budgets of the central Arctic Ocean, which may impact the primary goal of the simulation, the ice forecasting capability. If the difference between modeled and observed transports is due to resolution, the inability of a 9 km grid spacing model to accurately represent mass and property transports through the CAA has significant implications for the ability of course resolution climate simulations to accurately simulate the Arctic Ocean mass, heat and salt balance, thus affecting the global thermohaline circulation.

There is a three year mean (1979-1981) northward heat transport through Davis Strait of ~ 6.72 TW and a southward heat transport of ~ 0.86 TW, resulting in a net northward heat transport (Table 4.1). This small southward heat transport, when compared to the ~ 3.0 TW entering Baffin Bay through Lancaster, Jones and Smith Sounds, indicates significant cooling occurs in Baffin Bay. Considerable mixing of cold Arctic origin water, modified in the CAA, with the relatively warmer water of the West

Greenland Current occurs in regions of relatively high eddy kinetic energy in Smith Sound and the south-western half of Baffin Bay (Figure 4.10).

D. EDDY KINETIC ENERGY

Regions of high annual mean eddy kinetic energy in the Canadian Archipelago are limited to chokepoints, such as Barrow Strait ($\sim 25 \text{ cm}^2/\text{s}^2$) and Fury and Hecla Strait ($\sim 16 \text{ cm}^2/\text{s}^2$), and Lancaster Sound ($\sim 16 \text{ cm}^2/\text{s}^2$, Figure 4.10). The increase in energy in these regions is most likely a result of changes in bathymetry accelerating the flow through narrow openings. High eddy kinetic energy in Lancaster Sound will result in considerable mixing of outflow from the western part of the Archipelago with Smith

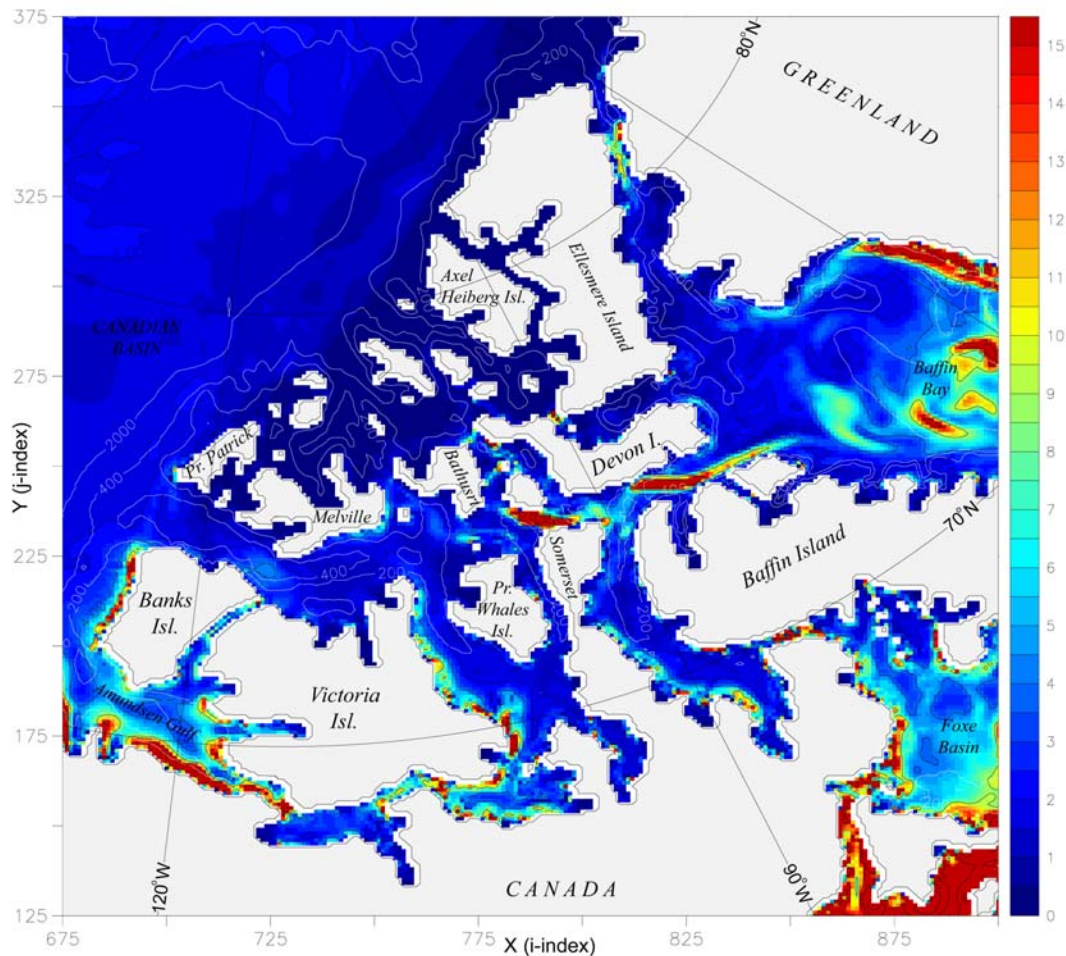


Figure 4.10. Horizontal distribution of 1980 annual mean, 0-5 m (model level 1) eddy kinetic energy ($\text{cm}^2 \text{s}^{-2}$) in the Canadian Archipelago calculated from daily model output. EKE contours 4, 9, 16, 25, 50, 100, and $200 \text{ cm}^2 \text{s}^{-2}$.

Sound outflow and water from the West Greenland Current. The recirculation within Amundsen Gulf contains comparatively high EKE values as well, with an annual mean EKE of $\sim 16 \text{ cm}^2/\text{s}^2$. This increase in EKE, as well as those observed in Queen Maud Gulf, McClintock Channel, the Gulf of Boothia and Foxe Basin, are most likely due to the summer retreat of the ice edge and a resultant increase in wind influence.

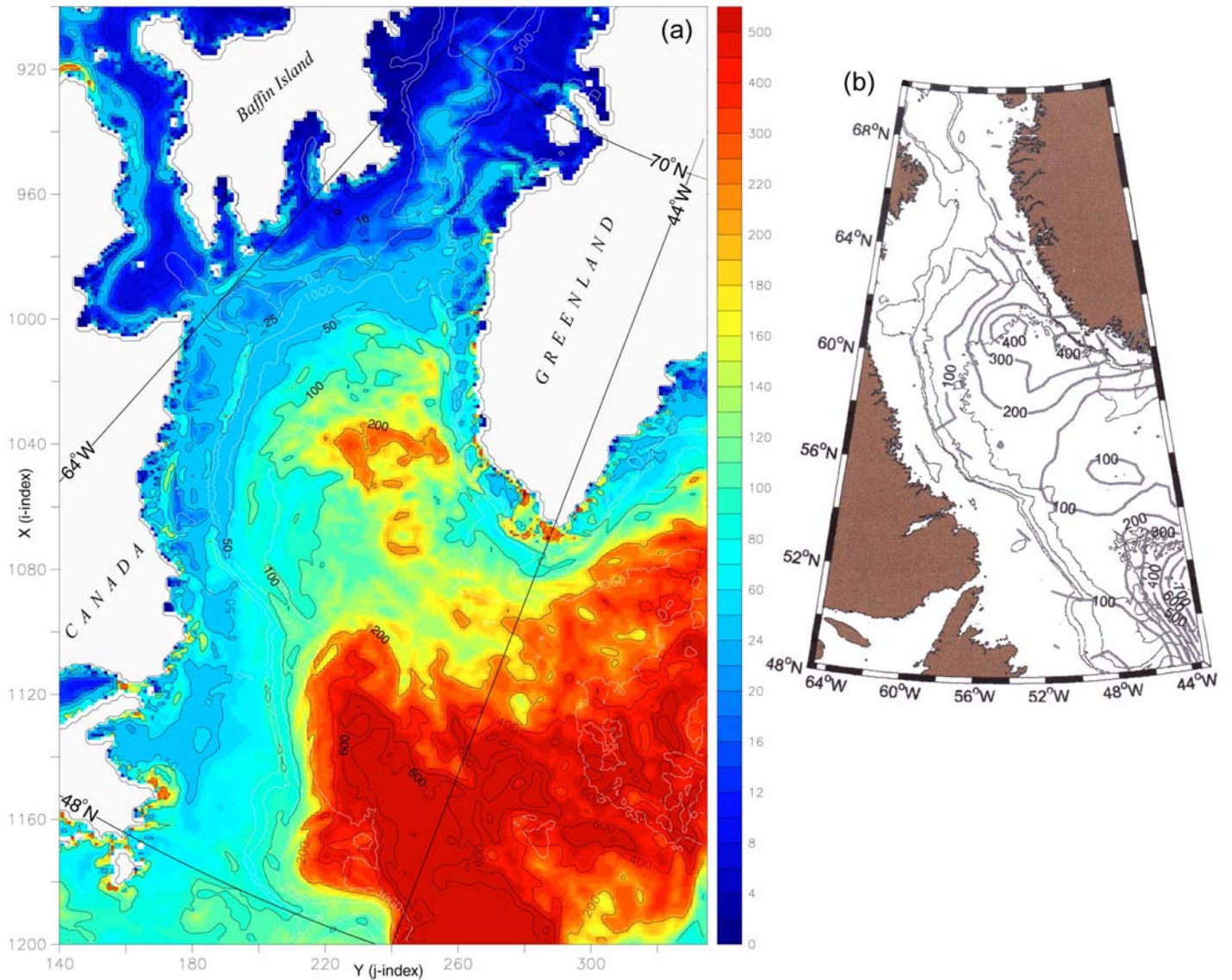


Figure 4.11. Horizontal distribution of eddy kinetic energy ($\text{cm}^2 \text{s}^{-2}$) in the Labrador Sea. (a) 1980 annual mean, 0-5 m (model level 1) calculated from daily model output. EKE contours 9, 16, 25, 50, 100, 200, 400, 600, and 800 $\text{cm}^2 \text{s}^{-2}$ in black; (b) Eddy kinetic energy deduced from surface drifter data. Drifters released in North Atlantic Ocean and Labrador Sea in the 1990s. Courtesy of J. Cuny, University of Washington.

The eddy kinetic energy in the islands of the northeastern Archipelago, between Axel Heiberg Island and Prince Patrick Island, approaches zero as this region is covered with ice year round and currents are relatively weak

A comparison of model 1980 annual mean surface EKE with multi-year mean EKE values deduced from observed surface drifter data indicates the model is able to reproduce the geographic distribution of EKE maxima similar to that observed (Figure 4.11). Model EKE values match those observed in a northern extension of the North Atlantic Current, the lower right corner of Images 4.11(a) and 4.11(b). Farther north, however, the model EKE values are roughly half of the observed values. The maximum daily surface EKE in the region in Figure 4.11(a) is $\sim 1542 \text{ cm}^2/\text{s}^2$, the annual mean $\sim 113 \text{ cm}^2/\text{s}^2$ with a standard deviation about the mean of $168 \text{ cm}^2/\text{s}^2$.

It must be noted that the drifter data were obtained from drifters released into the North Atlantic Ocean and Labrador Sea in the 1990s. Thus the comparison is of a 1980 model mean with an early 1990s observed mean. The difference in EKE in the northern Labrador Sea may be due to differences in the predominant atmospheric forcing regime which was anticyclonic, or low NAO during the early 80's versus cyclonic, or high NAO during the early 90's. An aspect of the high positive NAO years is increased cyclone activity farther north. Another potential cause of the difference may be due to model resolution. As latitude increases and vertical density stratification decreases, the internal Rossby radius decreases. The North Atlantic Current is well stratified in comparison to the nearly vertically homogeneous waters of the northern Labrador Sea, thus the Rossby radius within the North Atlantic Current is larger and the model is able to reproduce the observed eddy kinetic energy. That the 9 km model is able to reproduce observed values of EKE is quite significant, especially when compared to EKE values calculated in a similar region using output from a coarser resolution $\sim 18 \text{ km}$ model. The 9 km model values are ten times larger than the 18 km model values. Chapter VII contains further discussion of EKE differences between the two models.

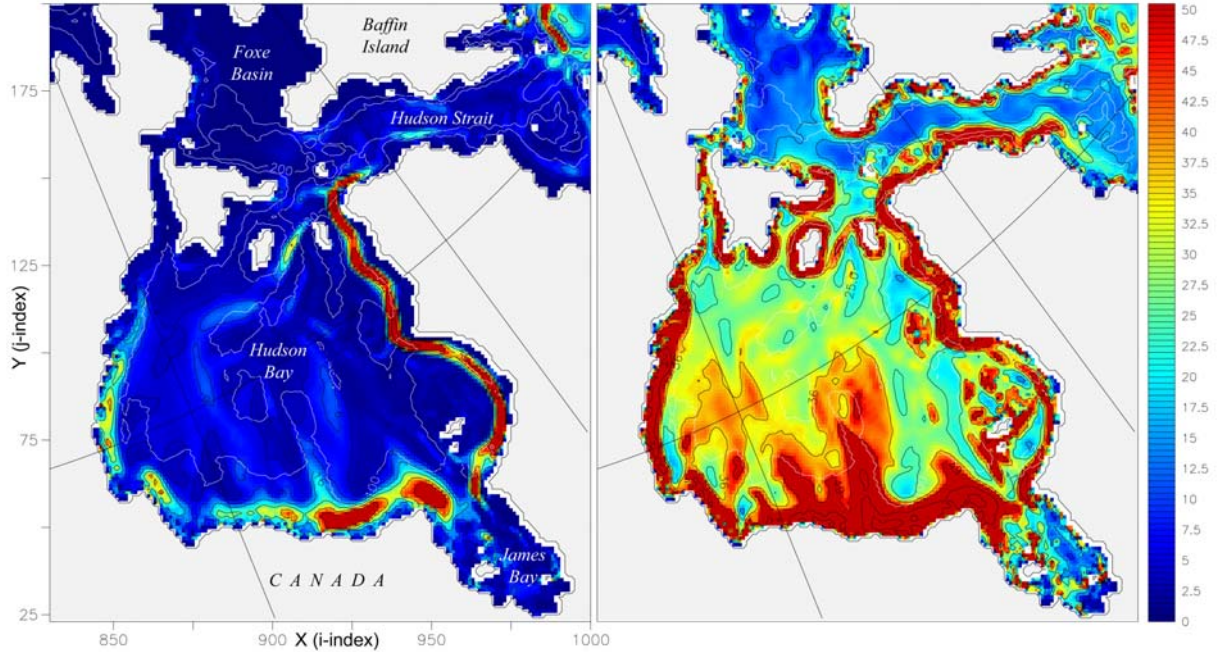


Figure 4.12. Horizontal distribution of surface (0-5 m, model level 1) Eddy kinetic energy (cm^2/s^2) in Hudson Bay for different seasons: (a) Winter (J-F-M) average; (b) Summer (J-A-S) average. EKE contours: 4, 9, 16, 25, 36, 49, 100, and $200 \text{ cm}^2/\text{s}^2$.

Considerable seasonal variability is noted in the EKE distribution in Hudson Bay (Figure 4.12), Baffin Bay and the Labrador Sea (Figure 4.13). There is a summer increase in energy in Hudson Strait and along the Newfoundland coast as well. The winter EKE minima in Hudson Bay and Baffin Bay are due to the winter growth of the sea ice cover, diminishing the wind influence on the surface layer. The winter EKE maximum in the Labrador Sea, the majority of which remains ice-free year round, is due to an increase in storm activity during the winter months. The daily EKE maximum in the Labrador Sea in wintertime is roughly 25% larger than the summer maximum, $2400.1 \text{ cm}^2/\text{s}^2$ versus $1919.8 \text{ cm}^2/\text{s}^2$, respectively. The Labrador Sea winter mean EKE, $135.6 \text{ cm}^2/\text{s}^2$, is ~ 1.7 times the summer mean of $80.2 \text{ cm}^2/\text{s}^2$ and there is more variability in the values in the wintertime, with winter standard deviation about the mean $\sim 205 \text{ cm}^2/\text{s}^2$ and summer standard deviation about the mean $\sim 150 \text{ cm}^2/\text{s}^2$.

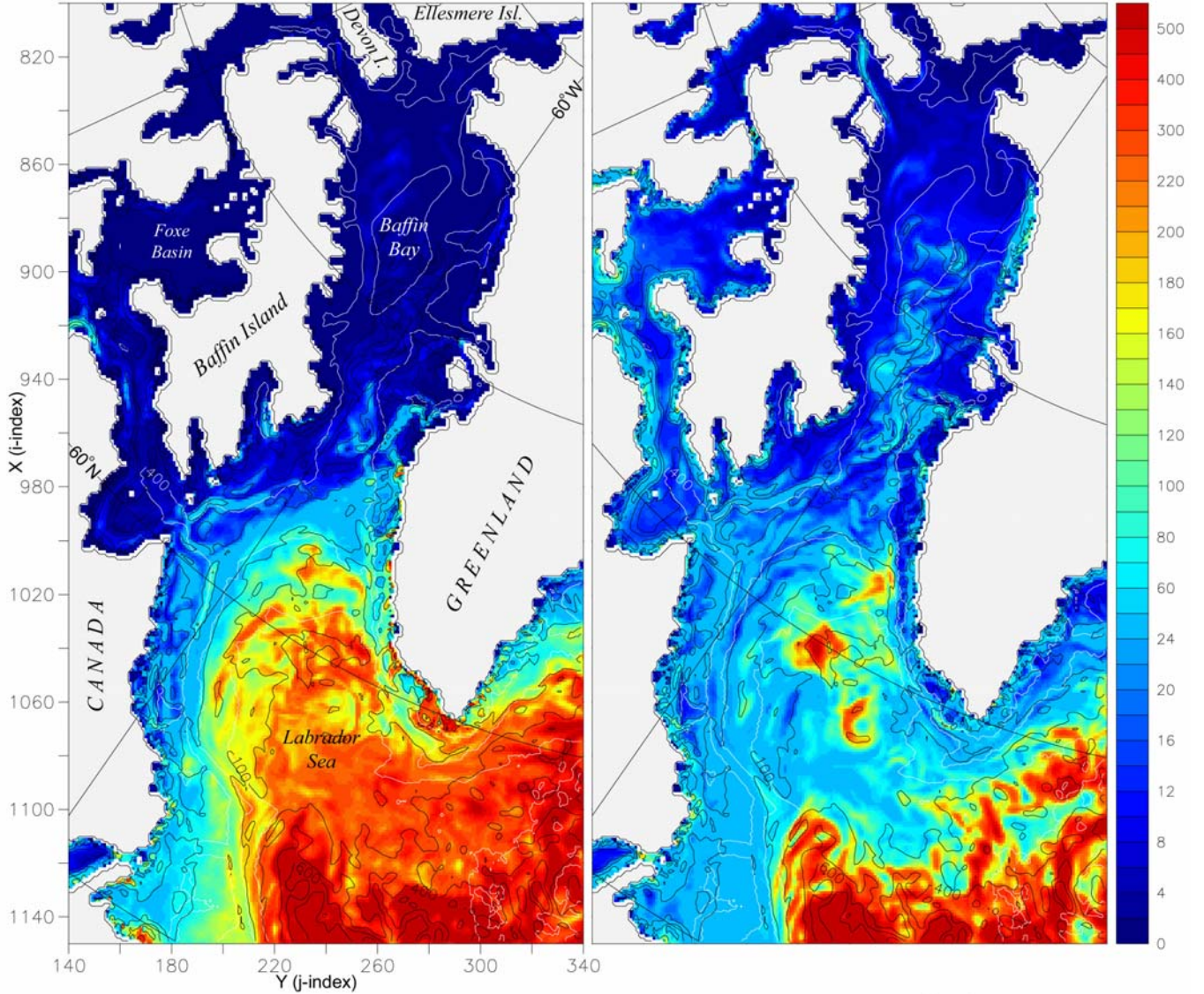


Figure 4.13. Horizontal distribution of surface (0-5 m, model level 1) Eddy kinetic energy (cm^2/s^2) in the Labrador Sea for different seasons: (a) Winter (J-F-M) average; (b) Summer (J-A-S) average. EKE contours: 4, 9, 16, 25, 36, 49, 100, 200, 400, 600 and 800 cm^2/s^2 .

E. DISCUSSION

Analysis of the 9 km model's representation of Canadian Archipelago circulation and transports has highlighted strengths and weaknesses in the simulation. As one of the highest resolution regional models of its type, it represents the complex geography and bathymetry quite well. The ability of the model to capture the opposing flows on opposite sides of Hudson Strait, let alone resolve many of the other channels within the

Archipelago, is an excellent example of gains realized through resolution increases. However, the anomalous winter reversal of coastal circulation in Hudson Bay and the steady flow through McClure Strait emphasize the need to include tides in the model. Inclusion of river inputs to Hudson Bay, which was not considered necessary or feasible at lower resolutions, may improve the representation of winter circulation in Hudson Bay.

Long term mean volume and property transports calculated through the Archipelago are approximately half of those observed. This may be due to temporal differences between the annual mean model values and the observed data, representing snapshots or shorter duration time series. Model resolution and the no-slip boundary condition may also be significant contributing factors to the under-representation of transport through the CAA. The no-slip boundary condition requires flow at the velocity grid point nearest shore to equal zero. Possible solutions for narrow channels are an increase in resolution, which will be computationally expensive, or modification or relaxation of the no slip condition, to allow flow through the entire channel, thus increasing transports.

The model is able to simulate observed eddy kinetic energy levels in the southern Labrador Sea. However, 10° to the north, modeled values are approximately one-half of those observed. A definitive judgement on model skill in representing EKE in this region is difficult to make due to the significant differences in the predominant atmospheric forcing between 1980 and the early 1990's. Another factor may be model resolution being just at the threshold of capturing features of a size on the order of the internal Rossby radius of deformation in the southern Labrador Sea and too coarse farther north. Unfortunately, observed values of 1980 surface eddy kinetic energy in the Labrador Sea were not available. If the end goal is accurate simulation of mass and property transports through the Archipelago, this can be achieved at this, or even lower resolutions, by careful modification of the main pathways to ensure proper velocity cross-sections. This will not, however, accurately represent circulation in the Archipelago or eddy kinetic energy in the northern Labrador Sea. To achieve these ends, additional resolution increases are needed.

V. BERING STRAIT, CHUKCHI SEA

A. OBSERVED PHYSICAL OCEANOGRAPHY

The exchange between the Arctic and Pacific Oceans through the Bering Strait (Figure 1) has increasingly been recognized not only as important to the Arctic Ocean and its adjoining shelf seas, but also as a matter of global interest (Roach et al., 1995) as the strait represents an essential link in the global freshwater cycle. Biologically, Bering Strait is the key connection within the Bering Sea-Western Arctic Ocean ecosystem. It is a major migratory pathway and it incorporates the time-dependent integrated output of the northern Bering Sea. The region immediately north of Bering Strait is both the primary Western Arctic production zone and a downstream deposition region for Bering Sea production. As such, it also delivers a burden of anthropogenic contaminants to the Western Arctic (Aagaard et al., 2001a). Additionally, the Pacific throughflow conditions the density structure of a major portion of the Arctic Ocean.

A pronounced annual cycle in both the transport and water properties of the Bering Strait flow has long been observed. Based on four years of measurements, the annual mean volume transport is 0.83 Sv northward with a weekly standard deviation of 0.66 Sv. The annual transport through Bering Strait averaged over the past decade has varied by over 50% of the long-term mean (Roach et al., 1995). The average annual peak-to-peak amplitude of the salinity variation is approximately 2 psu, with salinity reaching a maximum in early April, the period of maximum ice extent in the Bering Sea (Roach et al., 1995). The salinity variation is driven primarily by freezing, which expels salt into the water. Average ice growth rates of 5 cm/day, with maxima near 17 cm/day and corresponding increases in salinity of the northward flow (Roach et al., 1995), are attributed to polynyas in Anadyr Gulf and south of St Lawrence Island. The salinity memory of the water on the shelf is quite long, exceeding six months, so that the effects of freezing persist through the following summer and fall (Aagaard et al., 2001a). The interannual variability in monthly mean maximum salinity in Bering Strait during late winter corresponds to a difference in injection depth into the Arctic Ocean halocline of 60 m or more (Aagaard et al., 2001b). A steric height difference of about 0.5 m (relative to a

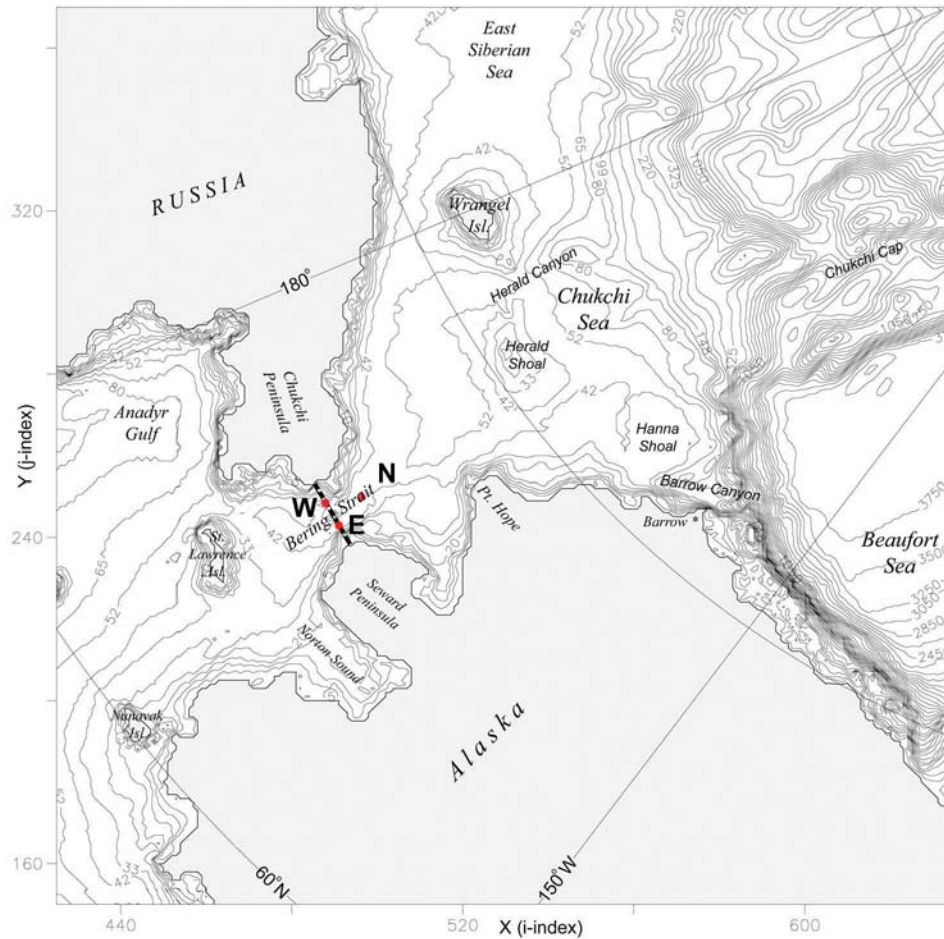


Figure 5.1. Bering Strait geography, place names and model bathymetry (m). Depth contours correspond to model levels. The thick dashed line across Bering Strait indicates the section used for mass and property transport calculations. Red dots (E=East, W=West, N=North) indicate model stations chosen to match mooring locations in Roach et al., 1995.

reference level of 1000m) between the North Pacific and Arctic Oceans drives a mean northward flow through the Bering Strait (Stigebrandt, 1984). The current field in the strait is constrained by local topography and tends to be directed north-south, with over 75% of the recorded variance aligned along that axis (Roach et al., 1995). Much of the variability in the flow is wind-forced, with up to two thirds of the variance accounted for by the surface geostrophic wind (Aagaard et al., 1985). The precipitation-evaporation balance over the shelf and Yukon River runoff appear to be the largest sources of freshwater, followed by the advective import of freshwater from the Gulf of Alaska.

Three water masses, primarily differentiated by their salinity, are representative of waters flowing through the Bering Strait in summer (Coachman et al., 1975). Alaskan Coastal Water is relatively warm and the freshest of the three, with salinities less than 32.1 (Roach et al., 1995). Bering Shelf Water is of higher salinity (about 32.5) but north of the strait it rapidly loses its identity by mixing with the third water mass, Anadyr Water, which has salinities near 33 and is typically quite cold, generally near 0° C (Roach et al., 1995). In winter, the T-S properties collapse to the freezing line and over time increase in salinity along that line (Roach et al., 1995) due to ice formation.

In addition to the annual cycle of temperature and salinity, there are important longer-term variations occurring in Bering Strait. In particular, the record of salinity through the past decade shows that the Bering Strait inflow to the Arctic has freshened about 1 psu during 1991-92 and then remained relatively fresh until 1999-2000, when about one-half of the earlier freshening effect was reversed (Aagaard et al., 2001b). The temperature of the inflow has also changed significantly during the past decade, with a dramatic long-term warming that peaked during 1996-97, followed by rapid cooling, so that water as cold as observed in summer 2000 was last seen in 1990-91 (Aagaard et al., 2001b). It appears the primary cause of this decadal cycle is a shift of the predominant atmospheric forcing regime from the 'traditional' strong Beaufort high pressure system, anticyclonic regime of the '70s and '80s to a cyclonic forcing regime which began in 1989/1990 (Chapman and Walsh, 1993; Dickson et al., 2000). Atmospheric conditions in the late 1990s appear to be trending toward the more traditional, colder cycle (Johnson and Proshutinsky, 1999). The freshening of the Bering Strait flow during this past decade is associated with a decrease in dissolved nitrate concentrations. Possible consequences of a sustained freshening therefore include a reduction in biological production in the Western Arctic (Aagaard et al., 2001b).

B. MODEL PHYSICAL OCEANOGRAPHY

A feature that makes this model unique among regional Arctic Ocean models is an open Bering Strait. Water is allowed to circulate freely through the Strait without any imposed constraints such as a net volume transport or prescribed currents. This was done in an

effort to simulate circulation through the Strait as realistically as possible. An earlier coarser resolution model, developed at NPS, was configured with a closed Bering Strait and a prescribed annual cycle of climatological temperature and salinity inputs (Maslowski, et al., 1999; 2000). Several other regional models (Zhang et al., 2000; Hakinnen, 1999; and Nazarenko et al., 1998 for example) have been configured with the 0.8 Sv northward flow through the Bering Strait as a prescribed boundary condition. The addition of the "North American channel" and the prescribed wind forcing over this channel, as described in Chapter II, are the only numerical methods introduced in this model to sustain a net circulation through Bering Strait. Therefore, circulation, water properties and variability in and around Bering Strait are driven solely by the steric height difference between the Pacific Ocean and the Arctic Ocean created by the applied daily varying atmospheric forcing and thermohaline circulation in the region. The significant differences in circulation between the 18 km and 9 km NPS models will be addressed in Chapter VII.

The 1979-1981 three year mean circulation in the vicinity of Bering Strait is net northward, with accelerated flow through Bering Strait, ~35 cm/s, slowing down and following depressions in the bathymetry in the Chukchi Sea to the north, across the broad continental shelf and traveling primarily through Herald and Barrow Canyons to the shelf break (Figure 5.2). The northward flowing Anadyr Current is well represented in the model. In agreement with published theories (Roach et al., 1995), there is eastward flow north of St Lawrence Island and a portion of the Anadyr Current enters the eastern channel. Weak circulation of Alaskan Coastal Water is also visible in Norton Sound. There is no evidence, in the long term mean circulation, of the eastward flowing East Siberian Current. There is flow to the north and west along the Siberian coast, across the entire passage between Wrangel Island and the Siberian mainland. Once west of Wrangel Island, this circulation turns north, slows, and broadens, spreading out over the eastern third of the East Siberian Sea. This circulation continues east above the north coast of Wrangel Island and then flows north through Herald Canyon. A small portion of the Herald Canyon outflow heads west and then north onto Chukchi Cap where it mixes

with the strong cyclonic boundary current traveling through Chukchi Cap along the shelf break.

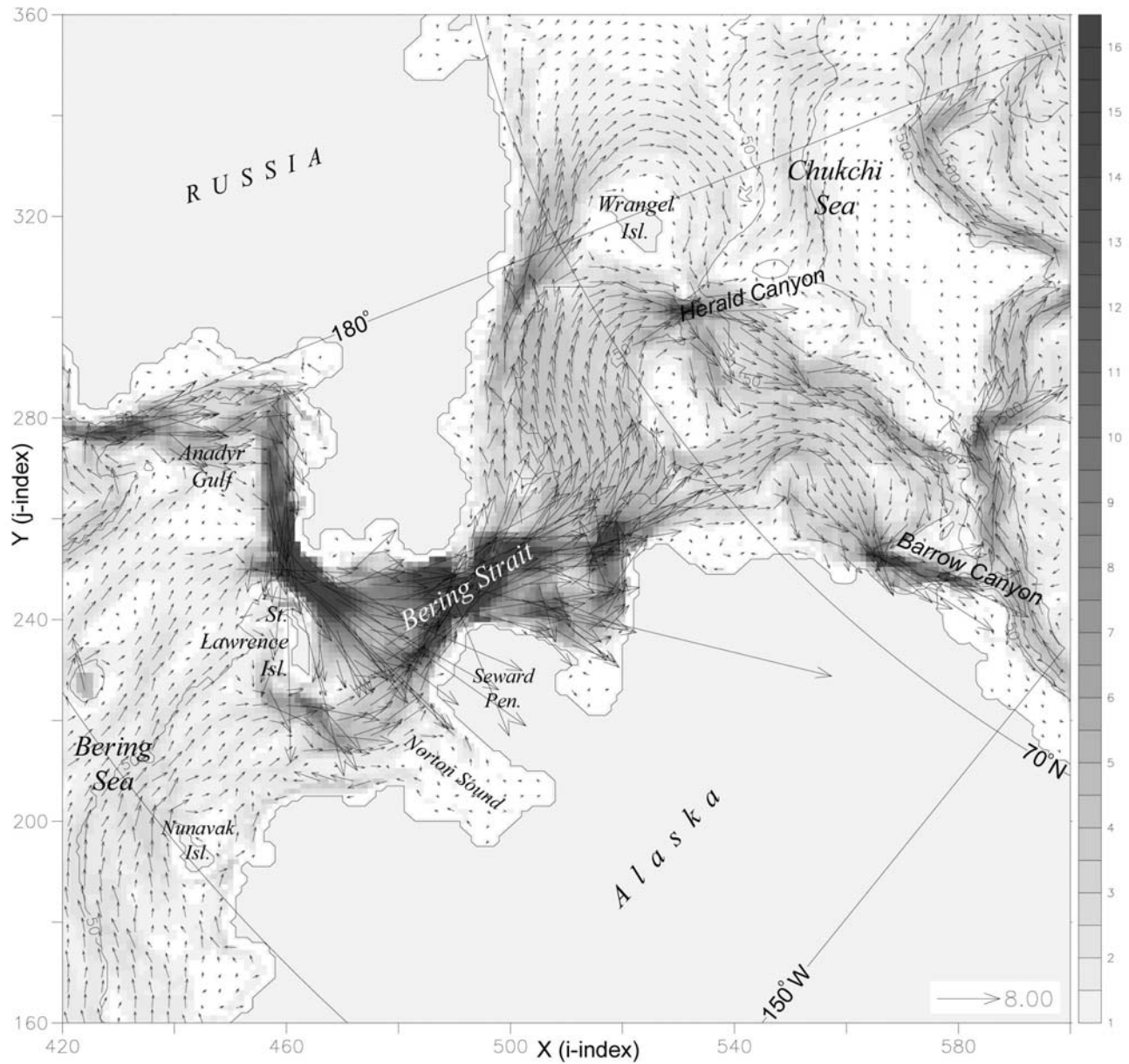


Figure 5.2. Horizontal distribution of three year mean (1979-1981) 0-226 m (model levels 1-16) mean velocity (cm/s) in the Bering Strait. Background shading is 0-226 m mean current speed (scalar). Every other velocity vector is plotted.

Due to its shallower minimum depth, Herald Shoal is relatively well represented in the model while Hanna Shoal is not (Figure 5.1), thus the impact of Herald Shoal on the northward circulation in the Chukchi Sea is more pronounced. The divergence of the

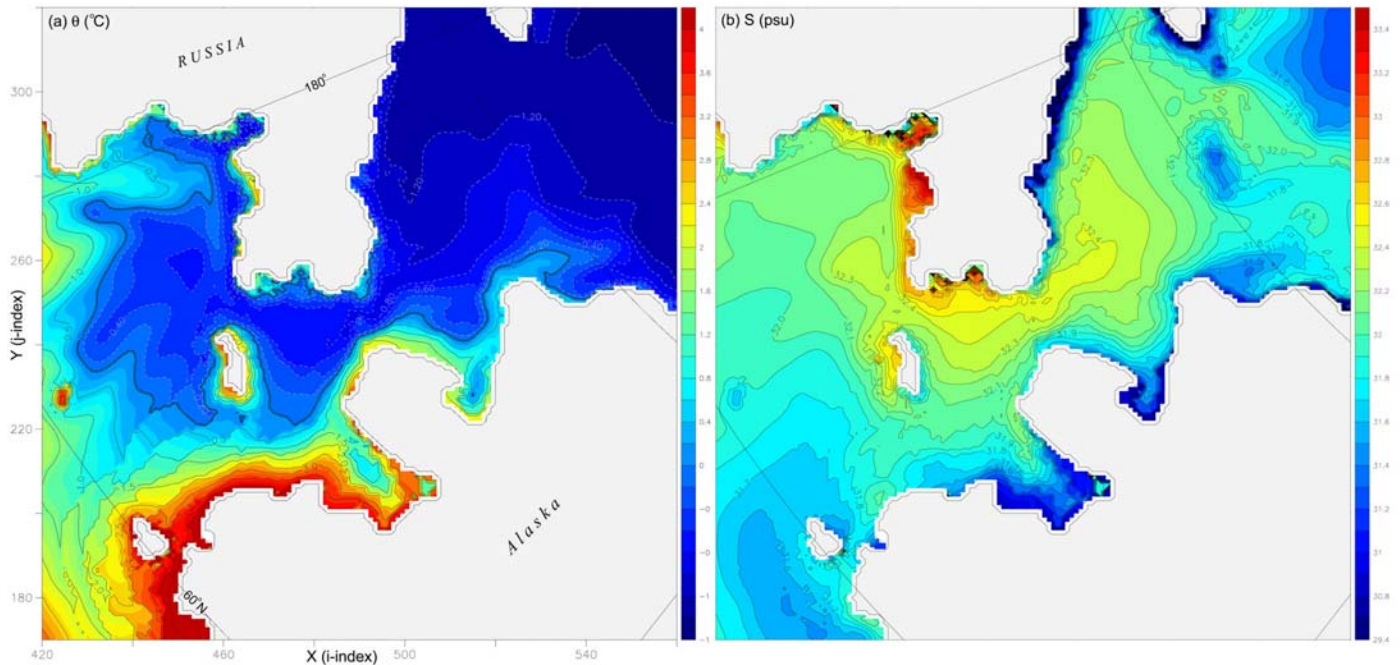


Figure 5.3. Horizontal distribution of three year mean (1979-1981), 0-53 m (model levels 1-8) (a) Temperature ($^{\circ}$ C) and (b) Salinity (psu) in Bering Strait.

northward flow around Herald Shoal is seen to the east of Wrangel Island. Flow accelerates through Herald Canyon and the majority of it turns northeast, traveling between the 50 and 100 m contours. The circulation east of Herald Shoal is driven by the bathymetry towards Barrow Canyon and then off the shelf. Hanna Shoal, west of Barrow Canyon, diverts the circulation to the north and then east, toward Barrow Canyon. As the flow leaves the shelf, much of it joins the strong cyclonic boundary current, while another portion continues east along the north coast of Alaska.

Identification of the three main water masses flowing through Bering Strait, i.e., Alaskan Coastal Water, Bering Shelf Water and Anadyr Water, is possible based on the horizontal distribution of long-term mean temperature and salinity in the top 50 m (Figure 5.3). However, it appears the long-term mean salinity values are 0.5-0.7 psu fresher than the summer classifications used by Roach et al. (1995), yet they do fall within their interannual variation in salinity of ~ 1 . Large salinity variations are more common in winter (Roach et al., 1995). Model Anadyr Water can be identified as water with $T < 0^{\circ}$ C and salinity > 32.3 . Model Bering Shelf Water has salinities on the order of

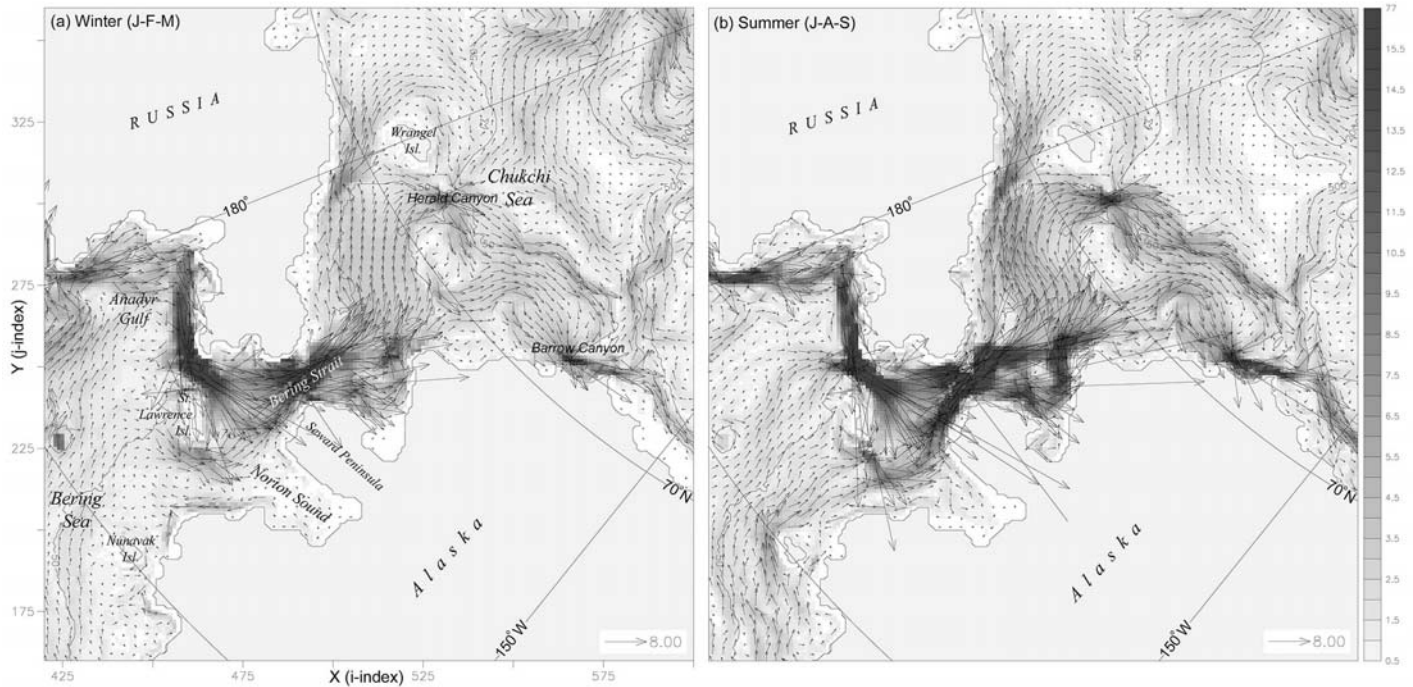


Figure 5.4. Horizontal distribution of 0-53 m (model levels 1-8) velocity (cm/s) for different seasons: (a) Winter (J-F-M) average; (b) Summer (J-A-S) average.

32.1 and Alaskan Coastal Water has a salinity of ~ 31.8 . Significant mixing occurs in and north of the Strait, and the predominant salinity is on the order of $\sim 32-32.3$.

A possible cause of these depressed salinity values may be the build up of too much ice, during decades of spin-up using ‘cold-biased’ climatological forcing followed by rapid melting and flushing out of much of the excess ice after the application of the 1979-1981 cycle of daily varying realistic forcing. The average thickness of ice in the central Arctic Ocean reached $\sim 4-5$ m under the 15 year mean forcing. Ice thickness exhibits a downward trend toward an average thickness of 3-4 m under the 1979-1981 cycle of forcing. Adjusting the model ice cover can be accomplished by modifying an ice restart file, consisting of one, 1280×720 2-D array, to equate to the desired thickness distribution or mean thickness. Adjusting the distribution of ocean temperature and salinity is more difficult in that it would involve modifying 90 1280×720 arrays (two variables, 45 vertical levels). This emphasizes an important modeling consideration that must be addressed before beginning any model integration, in that the choices made while determining the method of spinup can have far reaching consequences, which may

not be easily corrected. Other than re-mapping ocean T/S properties in a restart file to, perhaps, the PHC 2.0 ocean climatology (Steele et al., 2000), other methods of adjusting T/S include restarting the model from rest, using a different set of atmospheric forcing during spinup, or inclusion of an ocean data assimilation scheme. However, ocean data assimilation at high latitudes may be of limited value to the paucity of data.

Model currents through Bering Strait are generally slower during the winter months than in the summer (Figure 5.4) primarily due to winter ice cover diminishing the wind influence. Maximum summer current speeds of 64 cm/s are nearly double the wintertime speed maxima of ~33 cm/s, while the mean summer current speed over the entire region in Figure 5.4, ~3 cm/s, is only 20% larger than the mean winter current speed, ~2.5 cm/s. Within Bering Strait and the Chukchi Sea, summer current velocities are mainly higher than winter values due to the absence of sea-ice in summer. Acceleration of the flow between Wrangel Island and the Siberian coast and in the flow through Herald and Barrow Canyons occurs in summer. An increase in the velocity of the flow exiting Herald Canyon and travelling east between the 50 and 100m isobaths in the Chukchi Sea is observed as well. In contrast, velocities in the northwestern Bering Sea and the Anadyr Current are stronger in winter, as the ice cover permits thermohaline influences to dominate over the wind driven flow. Additionally, the portion of the flow that exits Herald Canyon and travels west is faster in winter than in summer.

Significant seasonal variations in the distribution of temperature and salinity are observed in the top 50 m in the northern Bering Sea, Bering Strait and the Chukchi Sea (Figure 5.5 (a-d)). Winter conditions are dominated by lower temperatures and increased salinities, in a large part due to the effects of the winter ice cover (Figure 5.5(e)). Elevated winter salinities south of St Lawrence Island, along the northern Anadyr Gulf coast, and the Alaskan coast in the vicinity of 60° N correspond with variations in the ice concentration fields and are likely regions of increased ice production due to polynyas. The winter maximum ice extent (Figure 5.5(e)) approaches the Bering Sea shelf break in the west, yet does not extend far enough south along the Aleutian Island chain in the east due to thermal effects from advection of warm water from the Alaska Stream through a false channel in the islands. In subsequent model bathymetry grids this channel has been

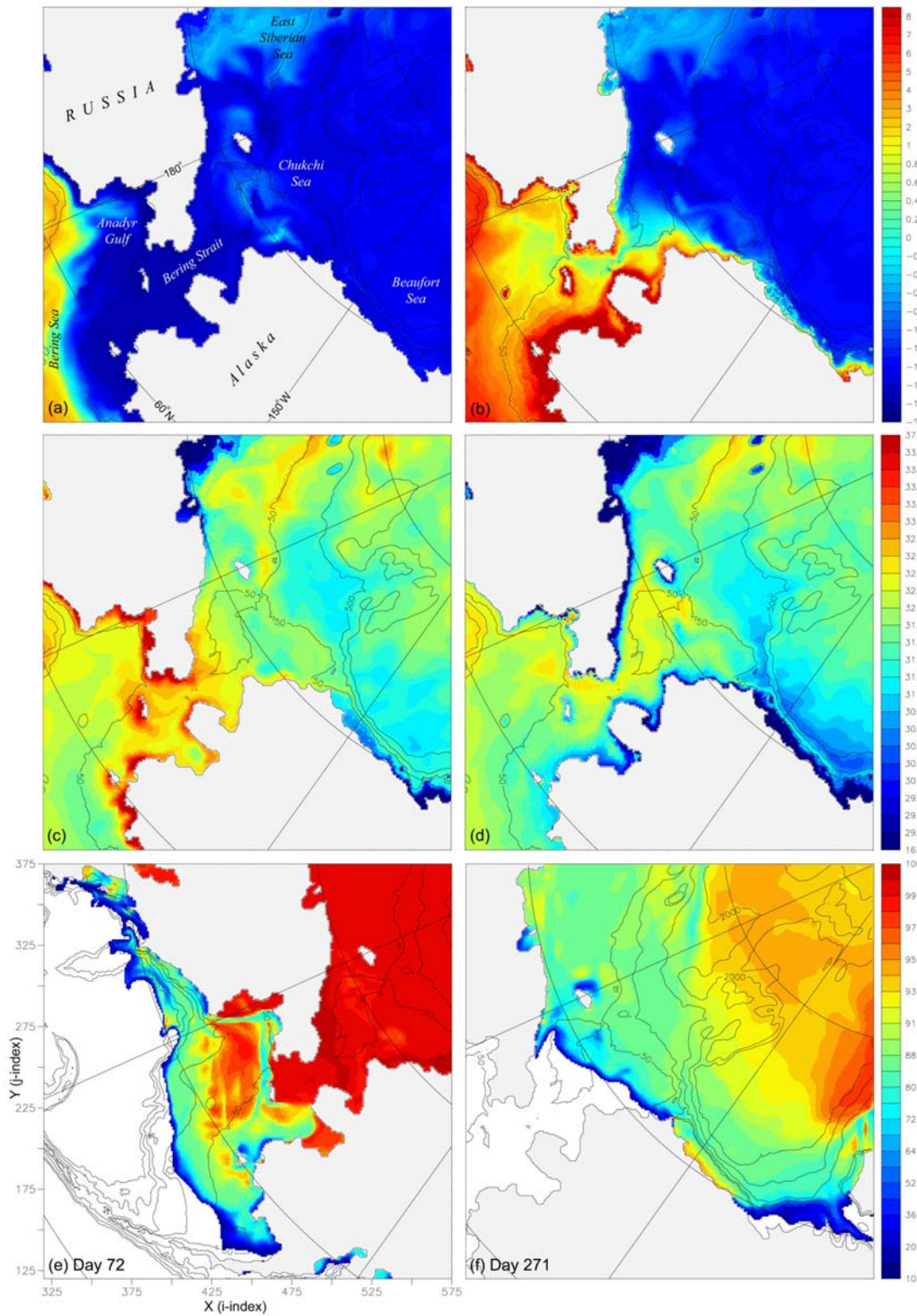


Figure 5.5. Distribution of temperature and salinity in the upper 0-53 m (model levels 1-8) and sea ice concentration for various seasons. Winter average (J-F-M) potential temperature (a) and salinity (c). Summer average (J-A-S) potential temperature (b) and salinity (d). Maximum winter sea ice concentration (%), day 72 (mid-March) 1980 . (e). Minimum summer sea ice concentration (%), day 271 (early-September) 1980 (f)

closed and it is anticipated the representation of the ice edge in the southeastern Bering Sea, and quite possibly the salinity in the Bering Strait, will improve as a result.

An attempt to identify the three primary Bering Strait water masses using the 1980 summer average salinity distribution (Figure 5.5(d)) once again indicates that the model salinities are too fresh by ~ 0.5 when compared to observed values (Roach et al., 1995). The Alaskan Coastal Current is identified by salinities less than 31.8, and the maximum salinities in the Anadyr Water do not exceed 32.8. The planned inclusion of Yukon River temperature and salinity inputs will impact the distribution of these

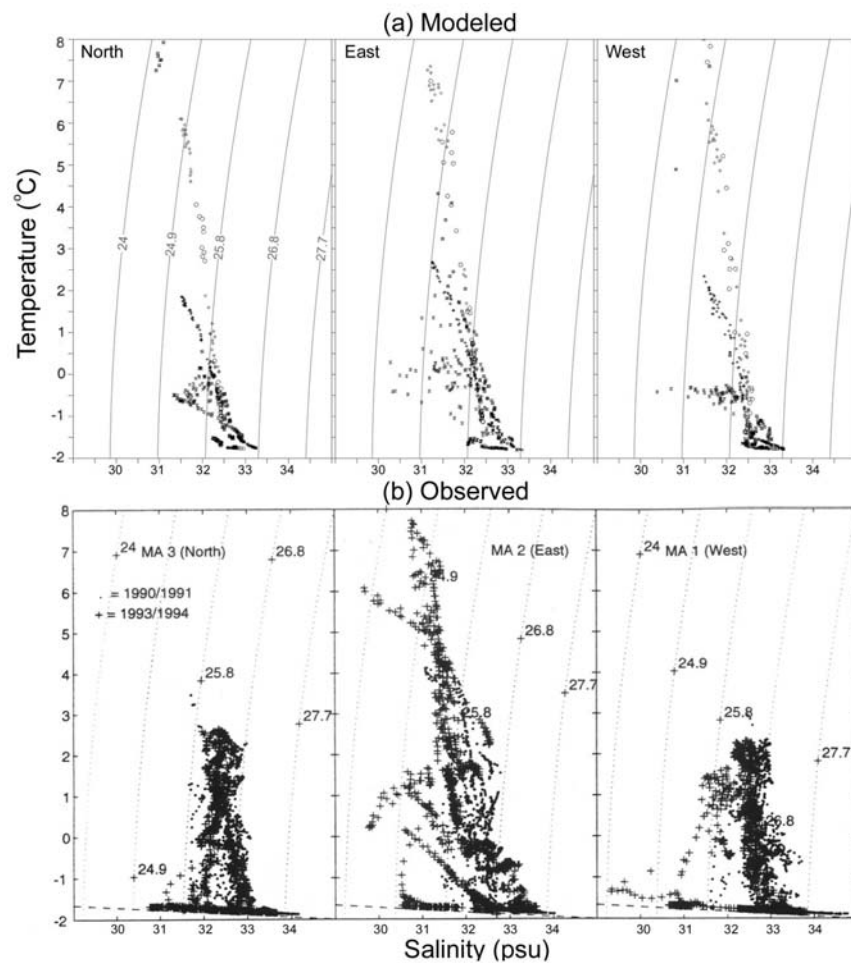


Figure 5.6. Potential temperature versus salinity in Bering Strait: (a) Model 1980 January through December monthly mean values for (left) North, (middle) East and (right) West model stations, as indicated in Figure 5.1. Each profile displayed represents all data in a 2×2 grid point $(18 \text{ km})^2$ region; (b) Observed values from October 1990 through September 1991 (solid circles) and October 1993 through September 1994 (crosses) for (left) MA3, (middle) MA2, and (right) MA3 (Roach et al., 1995).

properties in Bering Strait. However, they most likely will not work toward increasing the overall salinity in the region.

The influence of the warm, fresh Alaskan Coastal Water is responsible for the warmer temperatures and lower salinities along the north coast of Alaska (Figure 5.5(b,d)). The temperature increase is not sufficient to melt back the ice from the Alaskan coast in summer (Figure 5.5(f)). The 1980 summer minimum sea ice extent in the Chukchi Sea (Figure 5.5(f)), as well as monthly mean sea ice concentration fields (not shown), have features similar to those observed, yet the ice edge extends too far south when compared to monthly mean images from a NASA satellite ice atlas (Gloersen et al., 1992). The scalloped shape of the ice edge, along with the temperature and salinity minima visible over Herald Shoal, and less distinct in the vicinity of Hanna Shoal, indicate bathymetric steering of the warm Bering Strait flow and possibly the formation of Taylor columns, which impact summer ice retreat (Paquette and Bourke, 1974; Martin and Drucker, 1997). It is expected that the depressed salinities and the choice of spinup methods may account for the excess summer ice in the Chukchi Sea.

Comparison of temperature versus salinity plots of selected model stations with data from several years of nearly continuous observations in and north of Bering Strait (Roach et al., 1995) indicate the model is able to capture the general characteristics of the primary water masses seen in the Bering Strait, but with some differences (Figure 5.6). It must be emphasized that the comparison is of 1980 monthly-average model output with data collected in the early 1990s from three specific moorings. This comparison is made primarily as the early eighties are as far as the integration has proceeded with realistic daily varying forcing and second, due to a lack of comparable long-duration observational data sets from the early 1980s (Aagaard, personal communication).

The most readily noticeable difference between the modeled and observed plots is the warm, comparatively fresh water seen in the West and North model stations. Closer examination of model output reveals these values are all summer (July through September) values in the top 10 m (model levels 1 and 2). The observed data were recorded with sensors moored 1 m below the current meters, or 9 m above the bottom of the Strait (Aagaard, personal communication). Thus the difference may be due to the

deeper sensors not recording the warm surface values. Examination of plots of T/S data from sections taken in the late 1960's and early 1970's (Coachman et al., 1975) indicate surface temperatures of up to 10° C were measured in Bering Strait, although primarily in the eastern channel of Bering Strait.

Warmer surface waters aside, the upper limits of the main concentrations of model 1980 temperature and salinity values are cooler on the order of 0.5° C and fresher by ~0.5 psu than those observed in the early 90's (Figure 5.6). The temperature difference may be attributable to the observed warming trend seen throughout the Arctic Ocean (Morison et al., 1997) and in the Bering Strait (Aagaard et al., 2001b) which began in 1989. The 1979-1981 three year mean salinity in Bering Strait of 32.2 does fall at the lower end of the range of values reported by Coachman et al. (1975). That the model salinities are fresher than those observed in the early 90's, which was the beginning of an observed freshening trend in Bering Strait waters (Aagaard et al., 2001b) may be indicative of the model salinity issues discussed previously.

Due to the significant differences in the nature of the plots in Figure 5.6, i.e., 1980 monthly and area averaged means versus early 1990s point observations, it is difficult to draw any definitive conclusions as to model performance. However, greater similarity of the model values with station data from the late 60's and early 70's, which is again comparing monthly mean output with observed snapshots, may be more useful in that the atmospheric/climatic regimes were more similar. Continued integration into the 1990s and comparison of that output with the long-term time series data still being collected in the Bering Strait will provide more definitive results.

C. MASS, HEAT AND SALT TRANSPORTS

There is substantial variability in the simulated 1979 monthly mean volume transport through Bering Strait (Figure 5.7). Periods of increased northward transport as well as occasional periods of southward transport highlight the natural variability in the circulation. Bering Strait net transport has been monitored as a diagnostic output variable for the duration of the integration and an approximately 0.25 Sv increase in net northward

transport occurred with the application of realistic daily varying 1979 atmospheric forcing, vice the 1979-1993 15 year mean forcing. Net southward transport, for periods of one to three days, began to occur as well, which were not seen during the application of 15-year mean forcing.

1. Mass Transport

The 1979 monthly mean modeled transports (Figure 5.7) compare quite well with those calculated using the northward component of the geostrophic wind (Coachman and Aagaard, 1988) with a maximum in summer (1.2 Sv in August) and a minimum in early winter (0.32 Sv in November). An increase in monthly mean transport is noted in January yet it is not clearly a secondary maximum. In seven of the twelve months, the differences between the model monthly means and the wind-based monthly means are less than 0.05 Sv and all values fall within one standard deviation of the Coachman and Aagaard (1998) monthly estimates based on their 36 year time series. The 1979-1981 three-year mean model volume transport through Bering Strait of 0.664 Sv (Table 5.1) is within 5% of a 1979-1981 three year mean volume transport (~ 0.68 Sv) calculated from the Coachman and Aagaard (1988) 1946-1982 annual mean transport time series.

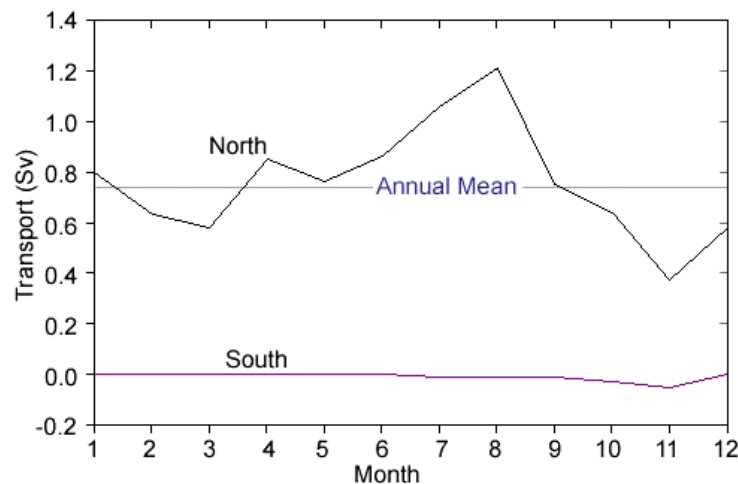


Figure 5.7. 1979 monthly mean model volume transport through Bering Strait. Blue line is 1979 annual mean of 0.75 Sv.

Model trends in Bering Strait volume transport will continue to be monitored as the integration using 1979-2000 daily varying atmospheric forcing continues and, if necessary, the prescribed wind forcing over the "North American Channel" will be tuned.

The true measure of how well the model represents Bering Strait transport will come from comparison of 1990s model output with the only available extended time series.

1979-1981 Mean Transports	
Volume (Sv)	0.664
Heat (TW)	-0.965
Salt (10^6 kg/s)	22.032

Table 5.1. Three year mean (1979-1981) net transports through Bering Strait. Transports are calculated across the section in figure 5.1 and are for the entire water column.

A significant difference exists in the width of Bering Strait between the ETOPO5-based and the IBCAO-based model bathymetry datasets. The Bering Strait in the ETOPO5-based bathymetry is 14 grid points wide giving the Strait a width of ~126 km, which is ~30 km wider than reality. This is a result of mapping a comparatively coarse database onto a similar resolution grid, possibly compounding position errors, and, admittedly, failure to verify the exact dimensions of Bering Strait while preparing the ETOPO5-based model grid. After careful checking, it has been verified that the Bering Strait in the IBCAO-based bathymetry dataset is 9 grid points across, or approximately 90 km wide. Shifting to the improved bathymetry may cause a decrease in the mean volume transport through Bering Strait, due to the differing geometries, and require additional modification of the prescribed channel forcing.

2. Heat and Salt Transports

Simonsen and Haugan (1996) recalculated earlier published values of heat transport through the Arctic Ocean and Bering Strait, relative to -0.1° C to aid in their comparison of the various estimates. The Bering Strait heat transport values they report vary from a low of 3.8 TW (Aagaard and Greisman, 1975) to a high of 11.4 TW (Rudels, 1987). The 1979-1981 three-year mean of -0.96 TW (Table 5.1) falls well below this range. A separate calculation of 1979 annual mean heat transport from monthly mean values yields 1.08 TW.

As anticipated, a large seasonal cycle in the heat and salt transport is present associated with the flow through Bering Strait (Figure 5.8). During July through October

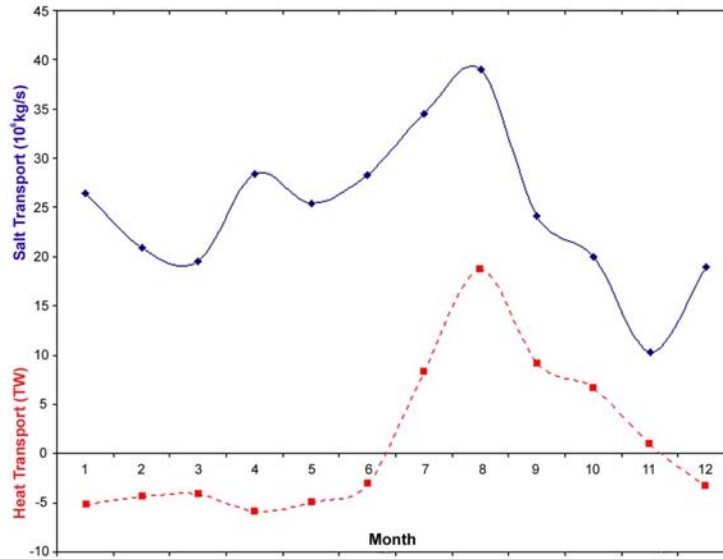


Figure 5.8. 1979 cycle of monthly mean salt (10^6 kg/s, solid blue line) and heat (TW, dashed red line) transport through Bering Strait. Transports are calculated for the entire water column, across the section indicated in Figure 5.1. Heat transport referenced to -0.1°C , salt transport referenced to 34.4 psu.

the net heat transport is northward, with a peak in August. The annual cycle of salt transport is to the north with a minimum in November, a secondary minimum in March and a peak in August. It takes approximately 4-6 months for the warm, salty Pacific waters to advect northward, melting the sea-ice along the way, before it gets to Bering Strait. The observed sea-ice edge passes through Bering Strait ~ 15 June each year, so there is a 2 month lag before peak temperature and salinity values are realized (R. Bourke, personal communication). This six-month lag between the period of maximum ice production in the Bering Sea and when this salt signal is seen in the Bering Strait is similar to the long-term salinity memory discussed by Aagaard et al. (2001a).

D. EDDY KINETIC ENERGY

Several distinct areas of increased energy, associated primarily with bathymetric features that guide the flow, characterize the annual mean surface eddy kinetic energy in the Bering Strait (Figure 5.9). There are concentrated areas of increased EKE at the southern entrance and eastern exit of the Anadyr Gulf, along the path of the Anadyr Current, yet comparatively little activity in the central Anadyr Gulf. The southern region

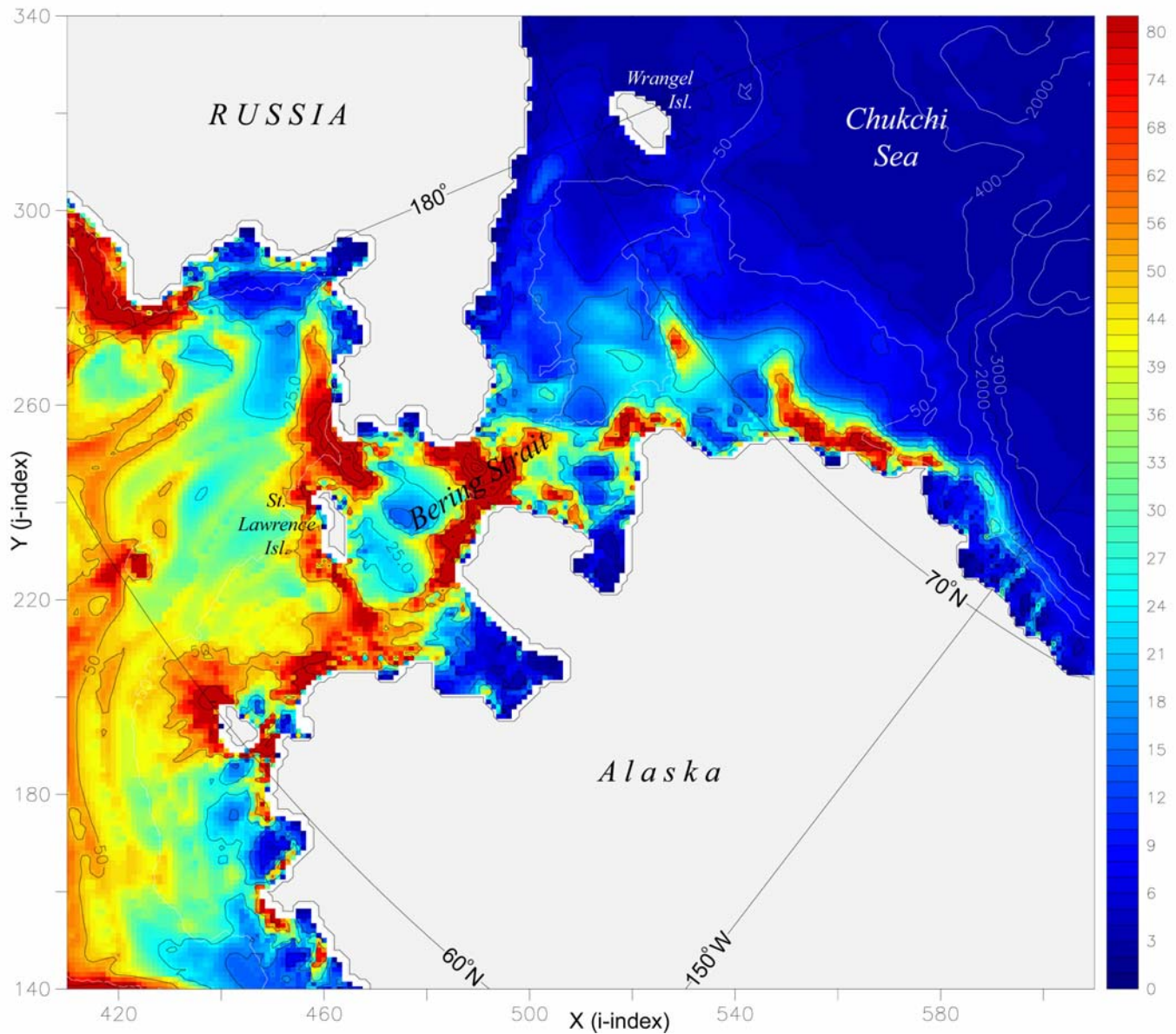


Figure 5.9. Horizontal distribution of 1980 annual mean, 0-5 m (model level 1) eddy kinetic energy ($\text{cm}^2 \text{s}^{-2}$) in Bering Strait. EKE contours: 4, 9, 16, 25, 50, 100, 200 $\text{cm}^2 \text{s}^{-2}$.

of increased Anadyr Gulf EKE is where the westerly shelf break current meets a sharp southerly turn in the continental shelf and a portion turns north onto the shelf and travels up-slope, along the coast. The bathymetry contours in Anadyr Gulf broaden (Figure 5.1) and the flow slows and spreads out as it follows the coastline north and then east. The Anadyr Current is constricted and accelerated while passing through Anadyr Strait, between the Chukchi Peninsula and St Lawrence Island, accounting for the increased EKE in that region.

The diversion of the generally northward Bering Sea flow around Nunavak Island and the confluence of the Alaskan Coastal Current with Anadyr Water flowing south and then east of St Lawrence Island may cause the increased eddy activity in these areas. The banded features south of Nunavak Island, also seen in the three year mean and summer average temperature fields (Figures 5.3 and 5.5, respectively), may be indications that the model is capturing some aspect of the multiple temperature fronts aligned along the bathymetry in the Bering Sea and their interactions. The flow through Bering Strait is constricted by bathymetry that shoals and narrows, causing considerable mixing in and just north of the Strait, accounting for the difficulty in separately identifying Anadyr and Alaskan Coastal water masses north of the strait. Point Hope impedes the flow north of Bering Strait and the region of increased EKE south of Herald Shoal is where the flow splits around the shoal. Eddy activity remains high along the length of Barrow Canyon, indicating significant mixing of surface waters in the canyon. Higher levels of surface EKE are seen east of Barrow, Alaska, as well. This is manifested in the observed highly fractured sea-ice cover which is a consistent feature there (R. Bourke, personal communication).

Seasonal eddy kinetic energy variability in Bering Strait appears to be dominated by seasonal changes in atmospheric forcing, modulated by the sea-ice cover (Figure 5.10). Winter maxima of EKE are seen in the Bering Sea along the shelf break and to the south, where the effects of increased winter storm activity are not damped by the sea ice cover (Figure 5.10(a)). Northward, under the winter sea-ice cover, EKE values remain high in bathymetric chokepoints such as Anadyr Strait and Bering Strait, with maximum values of $\sim 200 \text{ cm}^2/\text{s}^2$. In the Chukchi Sea, there are generally higher levels of EKE ($\sim 4 \text{ cm}^2/\text{s}^2$) along the northerly path of Bering Strait outflow, indicating continued mixing of these waters as they cross the Chukchi Sea. Concentrations of energy are seen in Herald Canyon and on the south side of Herald Shoal (maximum values of $\sim 9 \text{ cm}^2/\text{s}^2$) and in Barrow Canyon as well ($\sim 25 \text{ cm}^2/\text{s}^2$).

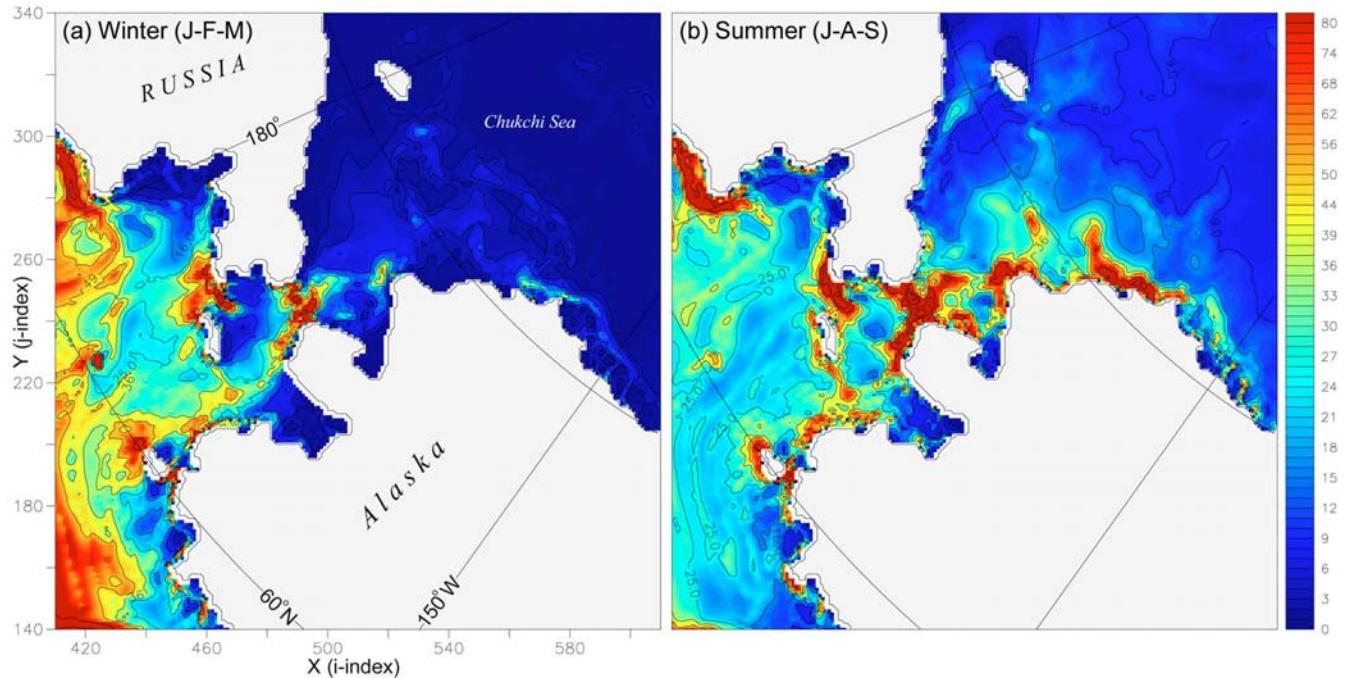


Figure 5.9. Horizontal distribution of surface (0-5 m, model level 1) eddy kinetic energy (cm^2/s^2) in Bering Strait for different seasons: (a) Winter (J-F-M) average; (b) Summer (J-A-S) average. EKE contours: 2, 4, 9, 16, 25, 36, 49, 100, 200, 400 and $800 \text{ cm}^2/\text{s}^2$

In the summer months, maximum values of EKE have decreased in the Bering Sea and at the western entrance to Anadyr Gulf (from a concentrated maximum of $\sim 200 \text{ cm}^2/\text{s}^2$ to an elongated region of values $\sim 100 \text{ cm}^2/\text{s}^2$.) EKE values have increased in Anadyr and Bering Straits to $\sim 400 \text{ cm}^2/\text{s}^2$ and $\sim 800 \text{ cm}^2/\text{s}^2$ respectively (Figure 5.10(b)). The background level of EKE in the Chukchi Sea has increased to $\sim 9 \text{ cm}^2/\text{s}^2$ and EKE values at the southern edge of Herald Shoal are now greater than $36 \text{ cm}^2/\text{s}^2$. Values in Barrow Canyon have reached $100 \text{ cm}^2/\text{s}^2$.

E. DISCUSSION

Analysis of model output in the Bering Strait has revealed strength in its representation of the overall seasonal variability in the region, weakness in the representation of some water mass characteristics, which may impact the sea-ice field, and how decisions made during the preparation phase of a model integration regarding forcing and model bathymetry can have far reaching effects.

Similarities between modeled and observed volume transports, both in magnitude and annual variability, indicate that at this resolution, the model is skillful in this area. The depressed model salinities in the Chukchi Sea and Bering Strait and the insufficient summer retreat of the sea-ice edge in the Chukchi Sea, which are related, indicate care must be taken in the choice of spinup forcing. Ideally, one would spend the time analyzing multiple years of atmospheric forcing to find the proper neutral combination that would not induce significant drift to any model variable. This is much easier said than done, particularly in the Arctic region where the interrelations and feedbacks between the atmosphere, ocean and ice are complex and not well understood. The question becomes what is appropriate atmospheric forcing for spinup? Perhaps application of daily varying realistic 1979-2000 forcing followed by application of that same forcing, progressing backward from 2000 to 1979 would avoid bias toward anticyclonic or cyclonic atmospheric regimes and maintain the variability needed in winds and temperatures to avoid unnatural buildup of sea ice cover.

We have learned that extended application of the same year of forcing may not be an optimum spinup method as it is likely to induce significant drift. This may be the cause for the excessive ice buildup in the Siberian shelf seas seen in the NPS 18 km model where 1979 forcing was repeated for several decades as part of the spinup (Zhang et al., 1999; Maslowski et al., 2000). The selection of forcing during spinup will be addressed in more detail in the final chapter. As the model resolution increases, the potential for errors in the bathymetry grid becomes larger and lacking specific regional knowledge of key channels and features, the potential for not catching these errors increases as well. This is the case in the overly wide ETOPO5-based bathymetry Bering Strait and the flow of warmer water from the Alaska Stream through a false channel in the Aleutian Islands impacting the winter ice edge in the southeastern Bering Sea

In all, the unforced and unconstrained natural variability of circulation in Bering Strait can be viewed as a significant achievement in regional Arctic Ocean modeling. However, additional effort remains to fine tune some water mass characteristics in the region. The inclusion of Yukon river inputs and a tidal model will influence the modeled salinity and circulation in the region through increased concentrations of freshwater in

primarily the Alaskan Coastal Current and the possibility of tidally induced flows damping or enhancing the wind driven and thermohaline circulation. The significant measured and unconstrained modeled variability makes the choice of a steady, prescribed 0.8 Sv northward transport through the Strait, as in many regional models, suspect. This constant northward flow will have a significant impact on Chukchi Sea and Canadian Basin circulation and water mass characteristics. Lacking the resolution and domain size to allow natural flow through Bering Strait, a more realistic boundary condition might be an annual cycle derived from the available extended time series of Aagaard et al. (2001a,b).

VI. CENTRAL ARCTIC OCEAN

A. OBSERVED PHYSICAL OCEANOGRAPHY

This section provides a brief analysis of model oceanography in the central Arctic Ocean (Figure 6.1) and the adjacent shelf seas not previously discussed, specifically the Laptev, East Siberian, Beaufort and Lincoln Seas. Due to the tremendous volume of data produced by the model, the decision was made to limit the focus of this report primarily to a detailed analysis of the inflow and outflow regions of the Arctic Ocean. This chapter is included in the interests of completeness and for the purpose of assessing model skill in simulating features in the central Arctic Ocean. Also included in this chapter are comparisons of selected horizontal and vertical sections with observations and climatology and a discussion of surface and subsurface eddy kinetic energy.

Climate related processes and contaminant disposition are central issues driving research on circulation and mixing in the Arctic Ocean (Carmack et al., 1997). As the volume of literature grows, so do the number of unanswered questions it seems. Prior to 1987, almost all of the data for the Arctic Ocean available to western scientists came from a few scattered ice camps and from cruises to marginal seas (Swift et al., 1997). The Arctic Ocean was generally viewed as a horizontally nearly uniform, and not especially dynamic, body of water. With results from recent section-oriented icebreaker expeditions to central regions of the Arctic Ocean, as well as scientific submarine cruises (Figure 1.2), a picture of a much more structured Arctic Ocean is emerging (Swift et al., 1997). The circulation of the deep and intermediate waters in the Arctic Ocean was not well known until these cruises successfully sampled the water column from the shelf seas to the interior at high spatial resolution (Anderson et al., 1994; Smethie et al., 2000). The voluminous data gathered during the SCICEX series of cruises has only just begun to be analyzed and results published.

Aagaard et al. (1981, 1985a), Melling et al. (1984), Rudels (1987, 1989), Aagaard (1989) are a few examples of initial works on explaining the large scale circulation of the Arctic Ocean. Rudels et al. (1994) remains a defining work on an updated understanding of the circulation of intermediate depth waters in the Arctic Ocean. Figure 6.1 depicts

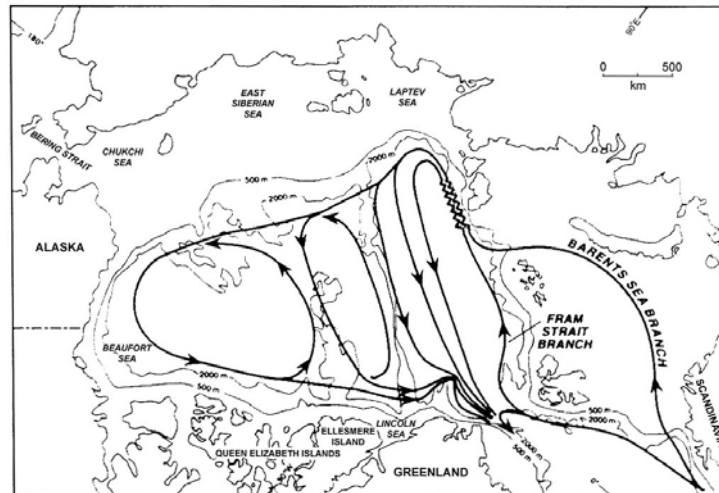


Figure 6.1. Schematic diagram showing the inferred circulation in the Arctic Ocean of the Atlantic Layer and intermediate depth waters, between 200 m and 1700 m (Rudels et al., 1994)

the generally accepted view of intermediate water circulation in the Arctic Ocean and has been reproduced in several papers. It shows the primary paths of the relatively well sampled warm Atlantic Water inflow to the Arctic Ocean via the Fram Strait Branch of Atlantic Water (FSBW) and the Barents Sea Branch of Atlantic Water (BSBW). These two branches meet east of St. Anna Trough, where the BSBW displaces the FSBW seaward. The cyclonic boundary current follows the Laptev Sea shelf break and is thought to take two separate paths upon reaching the Lomonosov Ridge. A percentage turns north and follows the Lomonosov Ridge while the remainder continues east, along the East Siberian Sea shelf Break.

The specifics of the circulation from this point on and around the each of the Arctic Basins are not well understood. Even less well understood are the dynamics and hydrography in the interior of each of these basins. However, it is felt that the intermediate water circulation is comprised of multiple, topographically steered cyclonic gyres. What little is actually known about the dynamics and large scale hydrography of the Central Arctic Ocean is based on a limited number of cruises, spread over the period of several decades and until recently, the majority of the cruises were in the Eurasian Basin (Figure 1.2).

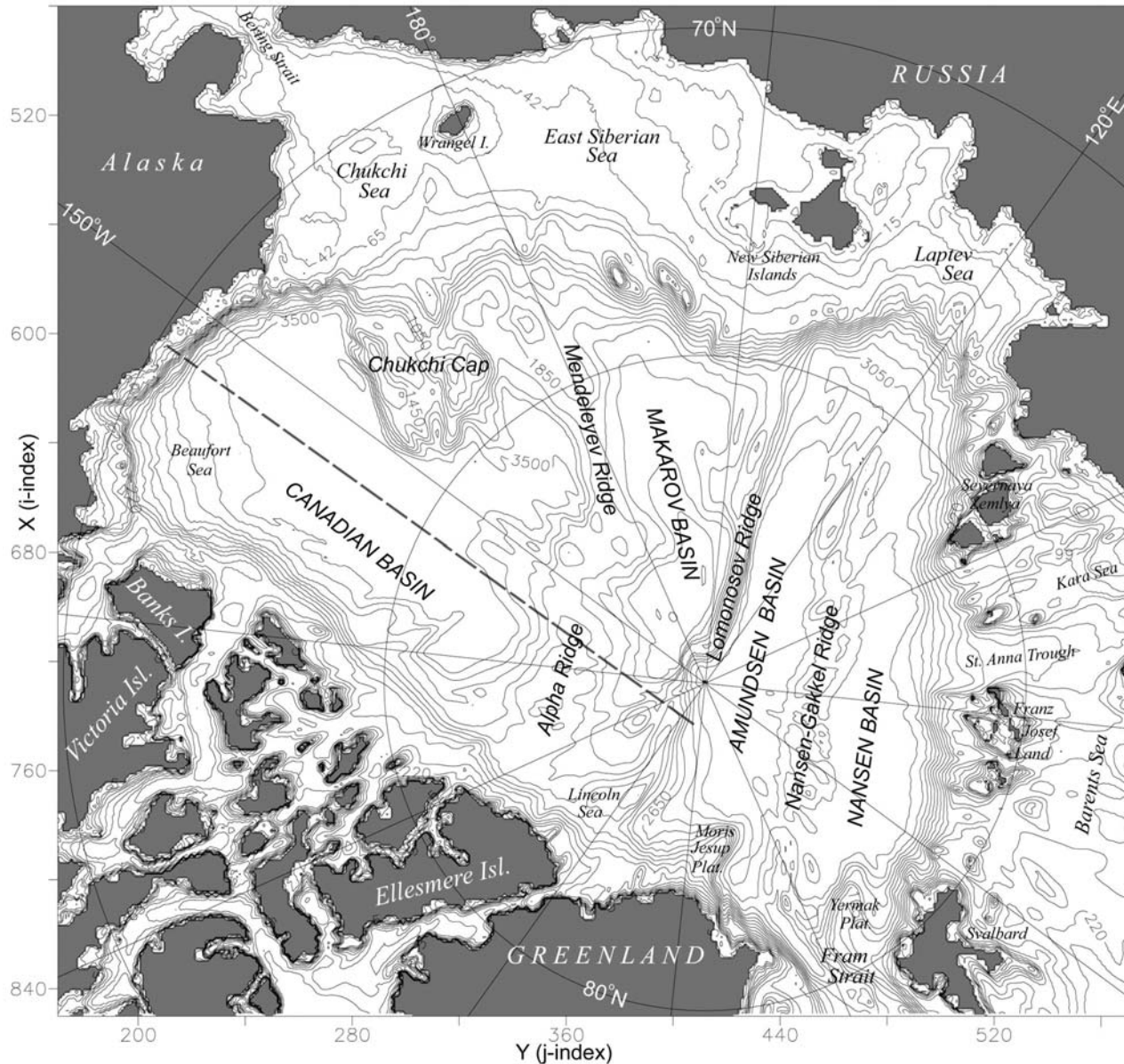


Figure 6.2. Central Arctic Ocean model bathymetry (m). Depth contours are every other model level. Dashed line in the Canadian Basin indicates the model section similar to repeated SCICEX trans-Arctic submarine sections.

In the interest of brevity, the reader is directed to *The Polar Oceans and Their Role in Shaping the Global Environment: The Nansen Centennial Volume*, edited by O. M. Johannessen, R. D. Muench, and J. E. Overland (1994) and *Polar Oceanography, Part A: Physical Science*, edited by W. O. Smith (1990) as excellent compilations of work covering many aspects of the Arctic ice-ocean system and its variability.

B. MODEL PHYSICAL OCEANOGRAPHY

The 1979-1981 three-year mean circulation in the Eurasian Basin of the Arctic Ocean is dominated by the cyclonic boundary current traveling along the shelf break (Figure 6.3). The major components of this flow come from the Barents Sea Branch of Atlantic Water (BSBW), entering the Arctic Ocean mainly through St. Anna Trough, and the Fram Strait Branch of Atlantic Water (FSBW), entering the Arctic Ocean through Fram Strait. These branches meet east of the St Anna Trough, where the BSBW displaces the FSBW to the north, farther off the slope (c.f. Chapter III), and both branches continue to the east along the Laptev Sea shelf. The majority of the flow continues on this eastward trajectory along the shelf break while a fraction turns and travels north along the western side of the Lomonosov Ridge. The separation of the Laptev Sea shelf break current into two branches, a branch continuing along the shelf, crossing the southern end of the Lomonosov Ridge, and a second branch turning north and traveling along the western side of the Lomonosov Ridge was more distinct in a plot

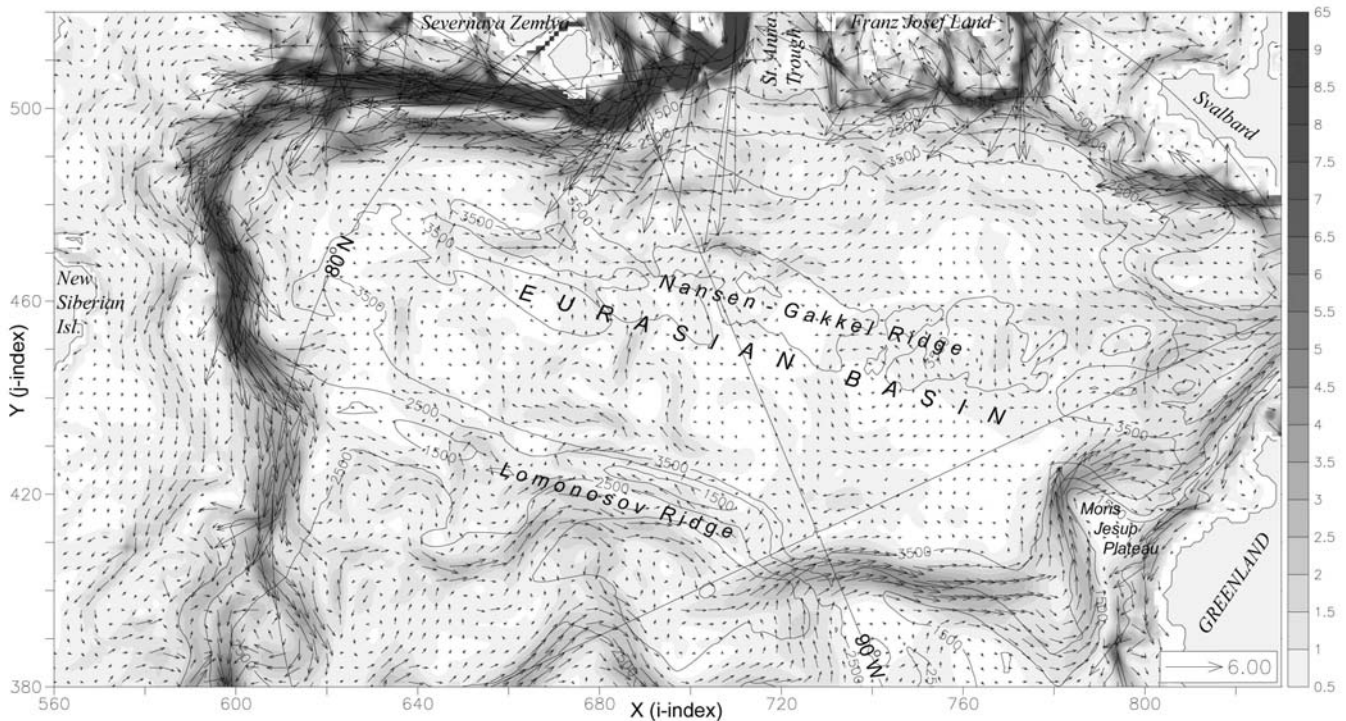


Figure 6.3. Horizontal distribution of three-year mean (1979-1981) 0-226 m (model levels 1-16) mean velocity (cm/s) in the Eurasian Basin. Background shading is 0-226 m mean current speed (scalar). Every third velocity vector is plotted.

of a two year mean circulation from spinup years 17 and 18 (not shown). Analysis of animations of particle trajectories in the spinup year 17 barotropic velocity field, using a model output visualization tool provided by the Major Shared Resource Center (MSRC) Visualization Center at the Naval Oceanographic Office, suggests particles in the BSBW are most likely to follow the southern path across the Lomonosov Ridge. A portion of the particles originally placed in the FSBW, however, tended to turn north and follow the Lomonosov Ridge. It is felt this occurs because the FSBW is farther seaward, over deeper bathymetry than the BSBW, and conservation of vorticity makes the portion of the FSBW in deeper water follow the Lomonosov Ridge. These differences in long term mean circulation suggest that changes in atmospheric forcing influence the seaward, or northward, displacement of the FSBW off of the Barents Sea shelf slope and thus determine the percentage of the Laptev Sea shelf break current that turns north and remains in the Eurasian Basin.

Circulation in the Laptev Sea is dominated by the eastward Kara Sea outflow through Vilkitsky Strait and the strong cyclonic current along the shelf slope in the eastern Eurasian Basin (Figure 6.4). Analysis of animations of Kara Sea outflow reveal that the majority of the Vilkitsky Strait outflow stays on the shelf, in the Laptev Sea. Flow in the central Laptev Sea is to the east, toward the New Siberian Islands. Along the coast, there is indication of a westward flowing coastal current, strongest near the Lena River delta. This coastal flow may change significantly in the vicinity of the Lena and Kotuy Rivers with the inclusion of river inputs to the model

Long term mean circulation within the central Eurasian Basin shows little organization (Figure 6.3). Mean circulation south of the Nansen-Gakkel ridge is weak and predominantly in the direction of Fram Strait. Weak southerly and eastward flow is observed from the east side of the Lomonosov Ridge toward the Nansen-Gakkel Ridge. It is felt that the modeled circulation within the Eurasian Basin is impacted by the quality of the ETOPO5 bathymetry data in the vicinity of the Nansen-Gakkel Ridge and by model resolution. In model bathymetry generated from the ETOPO5 data, the Nansen-Gakkel Ridge is a broad, ill-defined rise whereas with model bathymetry generated from the 2.5 km resolution IBCAO bathymetry data, the ridge is much better represented. It is

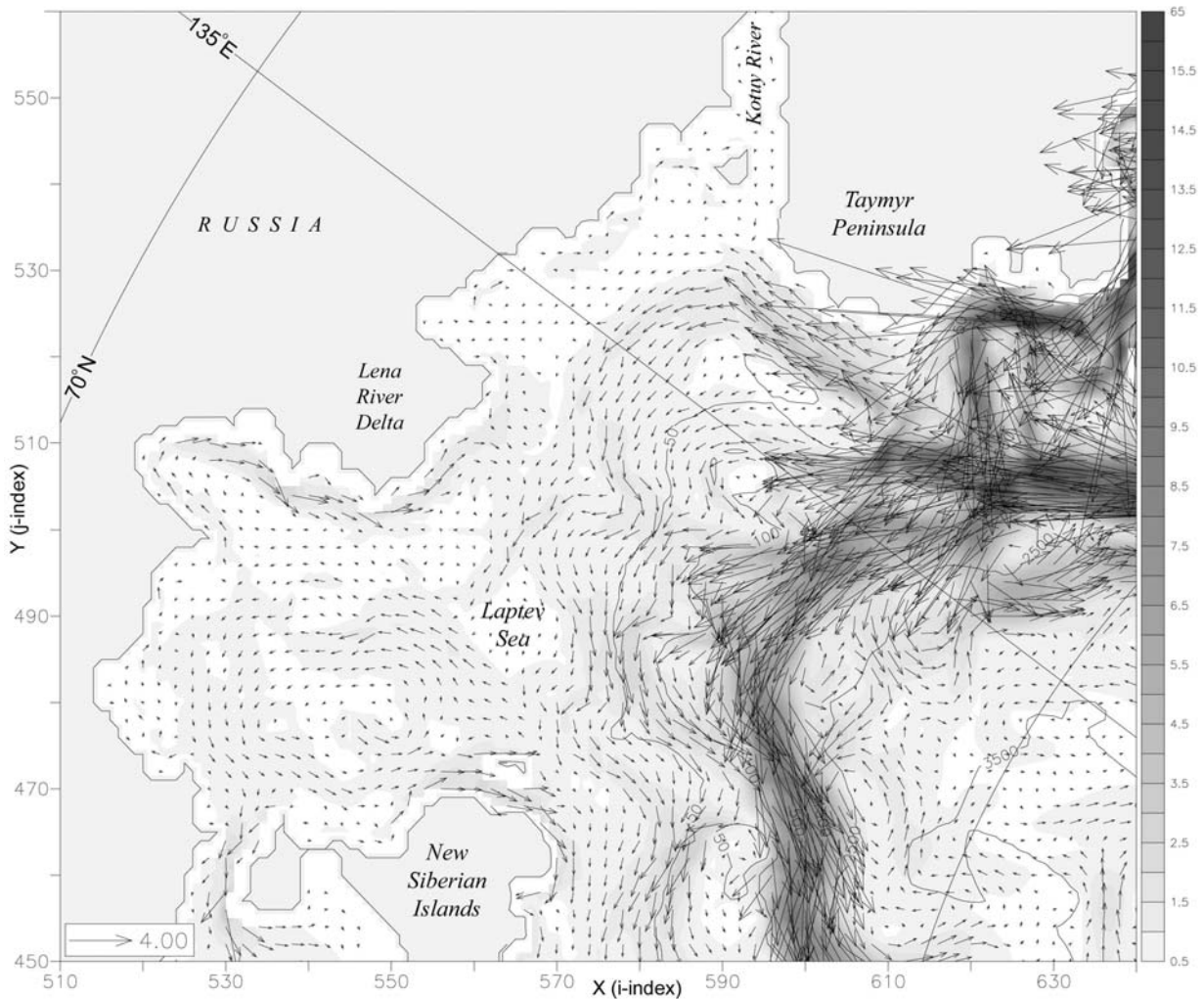


Figure 6.4. Horizontal distribution of three year mean (1979-1981) 0-226 m (model levels 1-16) mean velocity (cm/s) in the Laptev Sea. Background shading is 0-226 m mean current speed (scalar). Every other velocity vector is plotted.

anticipated the central Eurasian Basin circulation will prove more realistic in future model runs. The transpolar drift stream crosses the Lomonosov Ridge near the North Pole at 90° W, heading toward the north coast of Greenland. This circulation follows the bathymetry around the Moris-Jesup Plateau towards Fram Strait. Along the north coast of Greenland, a northwest flowing coastal current travels toward the Lincoln Sea and Nares Strait.

The 1979-1981 0-226 m (model levels 1-16) three year mean flow in the Canadian Basin is dominated by a large anticyclonic Beaufort Gyre and a broad,

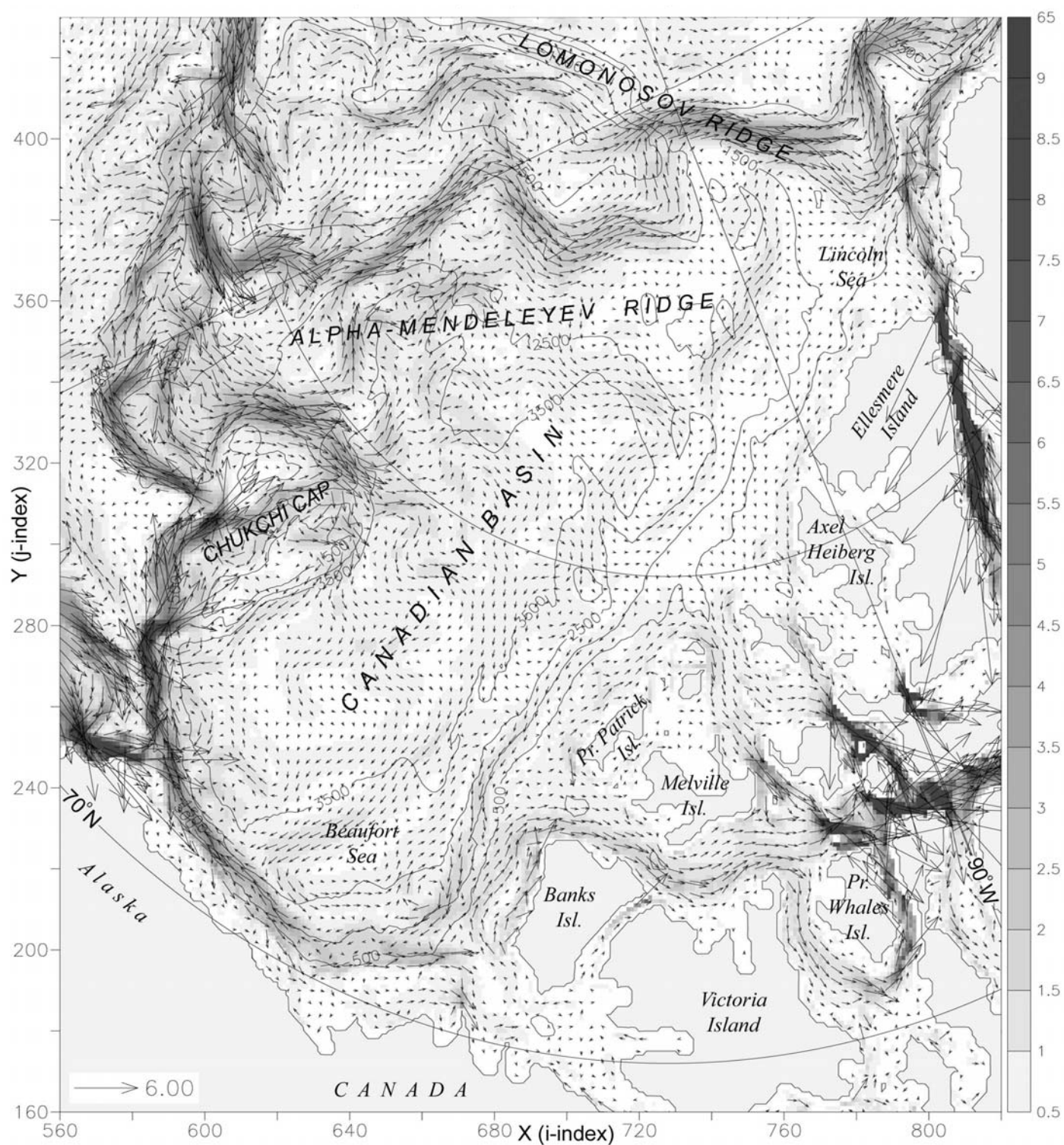


Figure 6.5. Horizontal distribution of 1979-1981 three year mean, 0-226 m (model levels 1-16) mean velocity (cm/s) in the Canadian Basin. Background shading is 0-226 m mean current speed (scalar). Every third velocity vector is plotted.

meandering Transpolar Drift Stream with generally northward flow away from the East Siberian Sea shelf toward the Pole (Figure 6.5). The core of the Transpolar Drift Stream is aligned roughly along the Mendeleyev Ridge, traveling due north toward the Pole roughly along the International Date Line. The eastward flowing cyclonic circulation from the Eurasian Basin meets the westward, or anticyclonic, Canadian Basin circulation west of the Chukchi Cap. It appears the interaction between the two currents causes the eastward flow from the Laptev Sea shelf break to leave the shelf and follow the Mendeleyev Ridge north. A percentage of the anticyclonic circulation, originally from

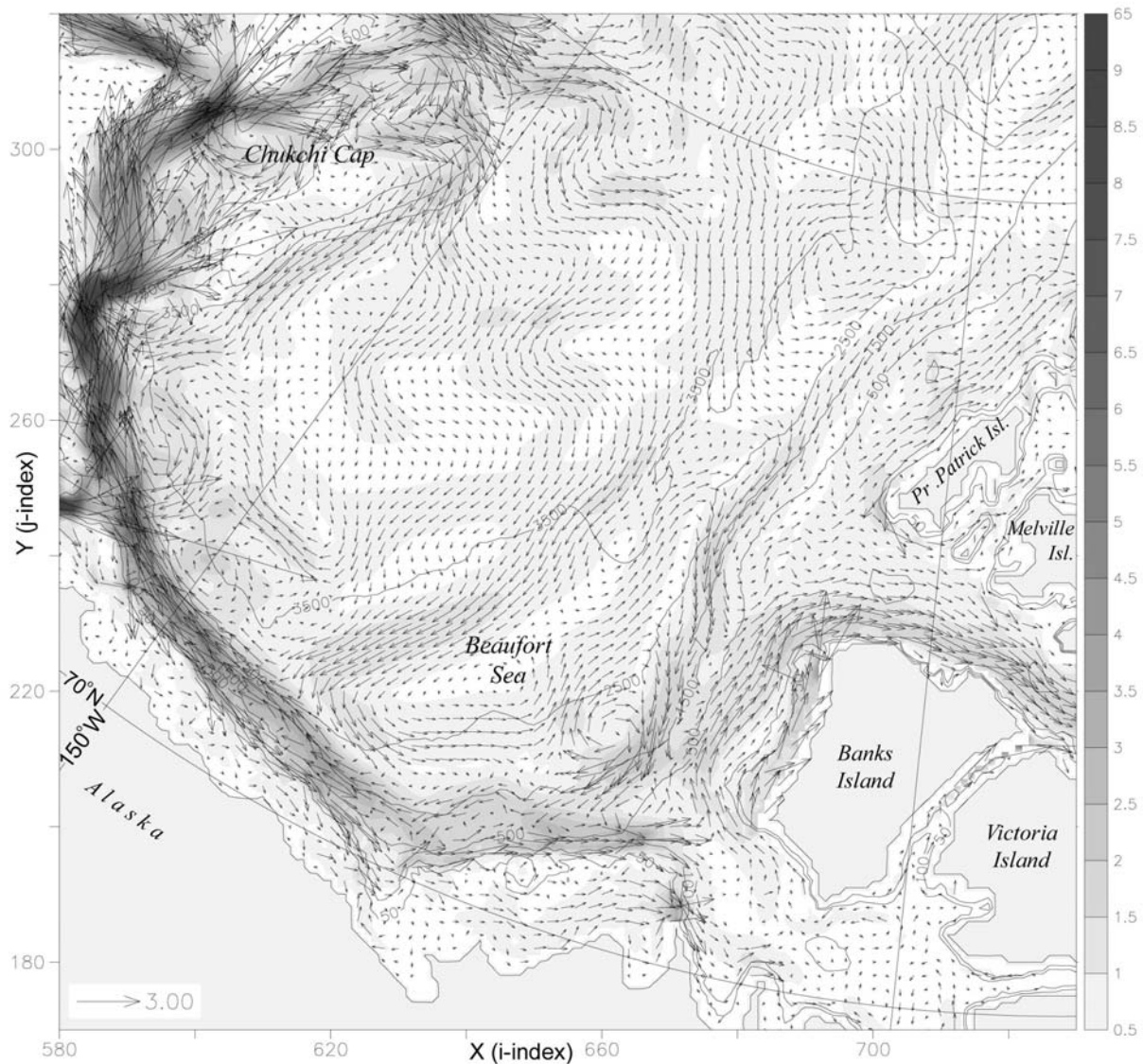


Figure 6.6. Horizontal distribution of 1979-1981 three-year mean, 0-226 m (model levels 1-16) mean velocity (cm/s) in the Beaufort Sea. Background shading is 0-226 m mean current speed (scalar). Every other velocity vector is plotted.

the Beaufort Sea, doubles back and flows around the Chukchi Cap, back toward the Beaufort Sea. The major pathways of Arctic Ocean water entering the Canadian Arctic Archipelago, Nares Strait, Gustav Adolf Sea and McClure Strait are visible as well.

A more detailed examination of the 1979-1981 0-226 m (model levels 1-16) mean circulation in the central Beaufort Sea (Figure 6.6) indicates considerable eastward flow extending from the northern end of the Chukchi Cap toward the central Canadian Basin. A large anticyclonic Beaufort Gyre is represented by southerly circulation along the 3500 m isobath in the eastern Beaufort Sea, which turns east and then north to flow along the 2500 m isobath and primarily anticyclonic circulation between the 2500 and 500 m isobaths in the eastern Beaufort Sea. The Alaskan Coastal Current is well represented by steady eastward circulation between the 500 m isobath and the Alaskan coast and northern Canadian Archipelago islands which appears to originate from the Chukchi Sea via Barrow Canyon and continues east along the Alaskan coast between the 50 and 100 m isobaths.

Long-term mean circulation in the East Siberian Sea is to the east, with a distinct branch along the Siberian coast and another along the model 36 m depth contour, which is the boundary of a shallow plateau in the central East Siberian Sea (Figure 6.7). Currents flow eastward from the Laptev Sea, around the southern New Siberian Islands and into the East Siberian Sea. Circulation northeast of the East Siberian Island group is a complex combination of eastward Laptev Sea outflow and westward flow from the Chukchi Sea as described above in the Beaufort Sea discussion. Circulation in the vicinity of Wrangel Island is controlled by the Bering Strait inflow and travels anticyclonically around the island, north via Herald Canyon and then toward Chukchi Cap, where it meets the strong anticyclonic circulation along the 500 m isobath (Figure 6.5). A broad swath of generally westward flow enters the eastern East Siberian Sea, via a flat 45-50 m deep region. This flow turns north and then east to cross the 50 m isobath and continue north. The flow in the southern third of the East Siberian Sea is discussed in more detail in Chapter V in relation to the Bering Strait outflow.

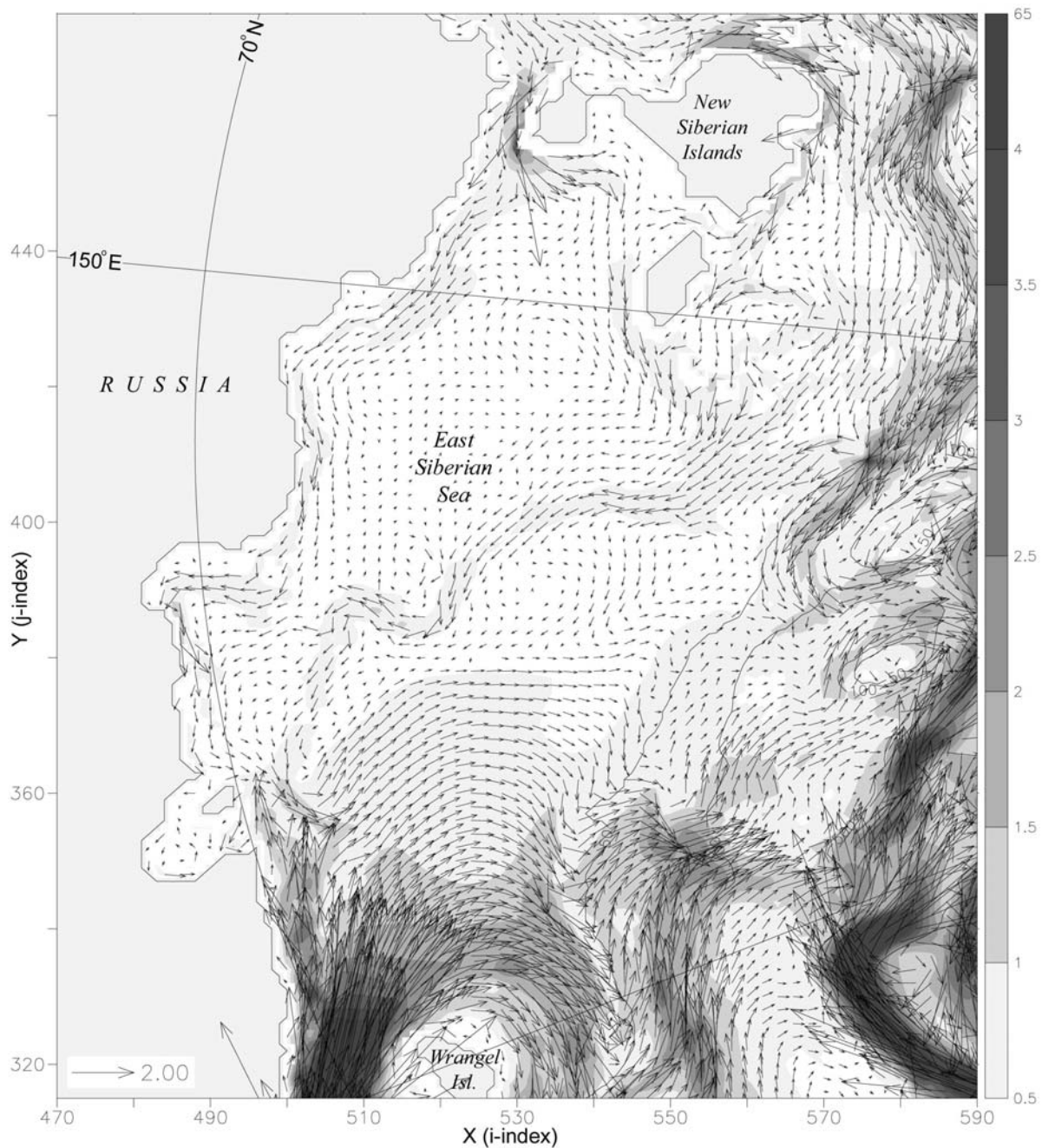


Figure 6.7. Horizontal distribution of three-year mean (1979-1981) 0-226 m (model levels 1-16) mean velocity (cm/s) in the East Siberian Sea. Background shading is 0-226 m mean current speed (scalar). Every other velocity vector is plotted.

The model is able to capture the general characteristics of the distinctive deep water masses in the Arctic Ocean (Figure 6.8(a,b)). This achievement is made more significant when contrasted with the ocean climatology initialization fields (Figure 6.8(c,

d)) which will be discussed later. In the model output, the temperature and salinity differences between colder and fresher Eurasian Basin Deep Water (EBDW) and the warmer and saltier Canadian Basin Deep Water (CBDW) are clearly visible, while the distinction between EBDW and the deep water in the Nordic Seas is less clear, which is acceptable as their observed characteristics are quite similar. The model 1980 mean 3250 m CBDW is 0.17°C colder and just slightly fresher than the -0.5°C and >34.95 classifications of Carmack (1990). In the Eurasian Basin, the 1980 mean 3250 m temperature is $\sim 0.2^{\circ}\text{C}$ colder and ~ 0.02 psu fresher than the -0.7°C and 34.94 psu definitions of EBDW (Carmack, 1990).

The PHC 1.0 3250 m annual mean T/S climatology mapped onto the model (Figure 6.8(c, d)) displays artifacts from interpolation to the model grid. The earliest version of the mapping scheme interpolated ocean climatology values into all surrounding land values to fill the entire model domain, at each level. This was done to fill model ocean points for which there were no climatology values. In cases where a significant gradient existed between regions (e.g., in the vicinity of the Lomonosov ridge), the interpolation routine tended to smooth the gradient and draw values across the boundary. This effect is evident in the cold water on the eastern side of the Lomonosov Ridge in the center of Figure 6.8(c). This bias in the interpolation scheme was first discovered in the northern Baltic Sea as a lens of anomalously high salinity, apparently interpolated from the Norwegian-Atlantic Current values. Regional modifications to the interpolation method have been made and the improved scheme has been used to map the PHC version 2.0 climatology onto the model grid. The Environmental Working Group Arctic Ocean salinity climatology (EWG, 1996, 1997) at the 3000 and 3500 m levels vary over a range of less than 0.5 psu. Thus it is felt that the uniform shape of the higher salinity water in the Canada Basin, plus the apparent disregard for the major bathymetric features, are entirely artifacts of the climatology and the scheme used to interpolate it onto the model grid.

Recalling that deep acceleration was active during spinup years 10 through 20, the deep Arctic Ocean has been effectively integrated for ~ 120 years. The limited benefits, and what appear to be significant drawbacks, of using this numerical method to accelerate

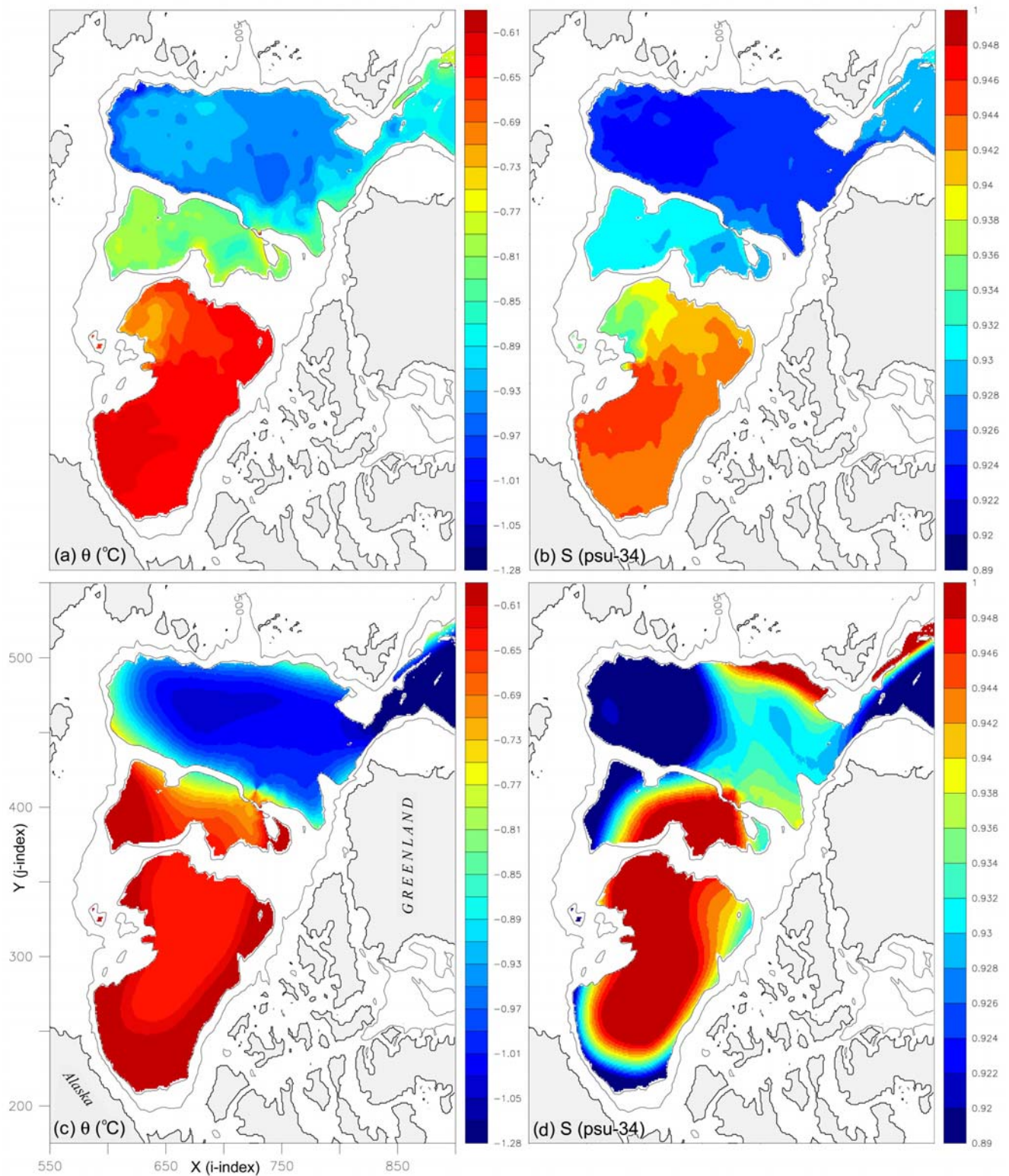


Figure 6.8. Horizontal distribution of 1980 annual mean 3250 m (model level 30) temperature ($^{\circ}\text{C}$) and salinity (psu-34): from (a) and (b) model output; (c) and (d) PHC 1.0 climatology mapped onto the model grid. Model depth contours 500 and 2200 m in black. Note: The 34 psu prefix is omitted from both salinity scales.

spin up in the deep Arctic Ocean will be discussed later. With regard to the temperature and salinity properties of what may be considered the abyssal Arctic Ocean, the use of deep acceleration appears to have allowed the model to overcome deficiencies in the initialization fields. As deep-water residence times in these basins are on the order of centuries, continued integration is necessary to determine the cause of the minor differences from the accepted definitions. Further integration will also determine if there is a continuing trend in either direction or if the 1980 mean values are simply part of an oscillation about these values.

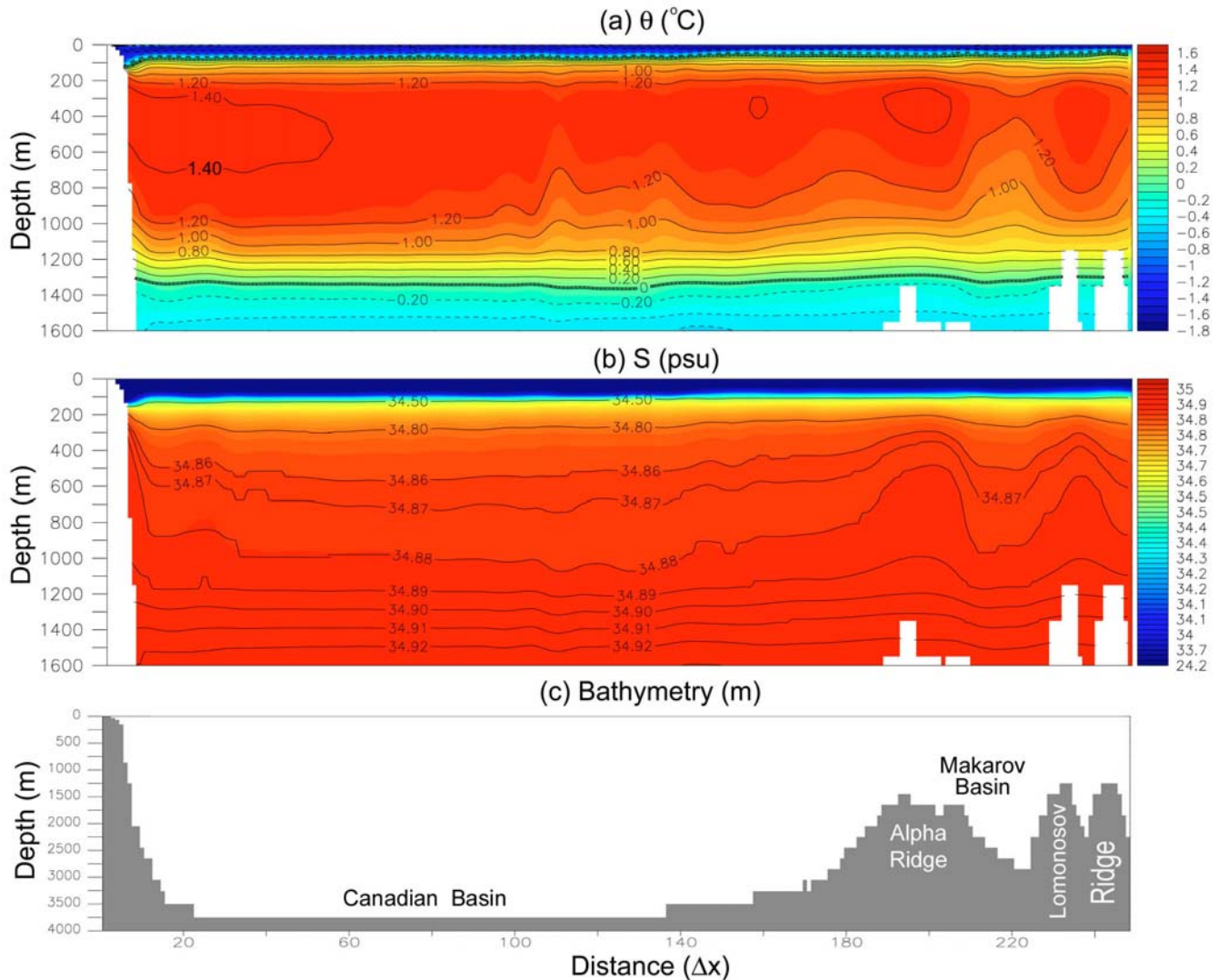


Figure 6.9. Vertical distribution of 1980 Summer (July-August-September) average properties for different seasons in the Canadian Basin: (a) potential temperature; (b) salinity. Note the x-axis is in units of delta-x, or grid spacing. The spacing between tick marks is 20 grid points or ~ 180 km.

Based on the vertical distribution of 1980 summer (July-August-September) average temperature and salinity across the Canadian Basin (Figure 6.9), the model Atlantic Layer is $\sim 1^{\circ}\text{C}$ warmer in the Canadian Basin than temperatures observed during the 1996 USS Pogy SCICEX cruise (Smethie et al., 2000). Additionally, the Atlantic Layer, defined by water $> 0^{\circ}\text{C}$, extends down to $\sim 1300\text{ m}$ vice the observed $\sim 800\text{ m}$ (Aagaard et al., 1985a).

Modeling sensitivity studies performed by Zhang et al. (1998) indicate that the choice of temperature and salinity restoring schemes appears to have a significant impact on the predicted Arctic ice-ocean circulation. Their results show that models with climate restoring particularly stress the importance of convective overturning and vertical and lateral advection to the ice-ocean thermodynamics in the intermediate layers of the Arctic and adjacent oceans. If the simulated mixed layer is excessively fresh all year long, because of strong restoring to the Levitus climatological data or for other reasons, less overturning occurs. This tends to trap more heat in the intermediate layers (Zhang et al., 1998). They go on to discuss how farther advection of heat into the Arctic Ocean, without release through overturning, will cause the intermediate layers to become overly warm.

The above may be a partial explanation for the excessively warm and thick Atlantic Water layer in this model. The model lateral boundaries are restored on a ten-day timescale to the annual mean PHC 1.0 temperature and salinity values, which, at the latitudes of the model boundaries in the Atlantic and Pacific Ocean, are essentially WOA 98 values (Steele et al., 2000). Modifying the lateral boundary restoring to monthly mean PHC 2.0 T/S values and relaxing the restoring timescale may allow proper evolution of the deep temperature and salinity. The application of deep acceleration for diffusion, accelerating the deep ocean T/S evolution by a factor of ten, has most likely compounded the tendency of the intermediate layers to move away from climatology. In a sense, this was fortuitous in helping to identify this shortcoming. After thirty years of integration without deep acceleration, the departure of the intermediate water temperature structure from climatology might not have been as significant as it is after 120 years of integration,

and the current form of the boundary restoring conditions may have been viewed as acceptable.

C. EDDY KINETIC ENERGY

Due to a lack of comparable observational data, preliminary conclusions based on model results are presented here in an effort to develop an understanding of the surface and subsurface eddy kinetic energy distribution in the central Arctic Ocean.

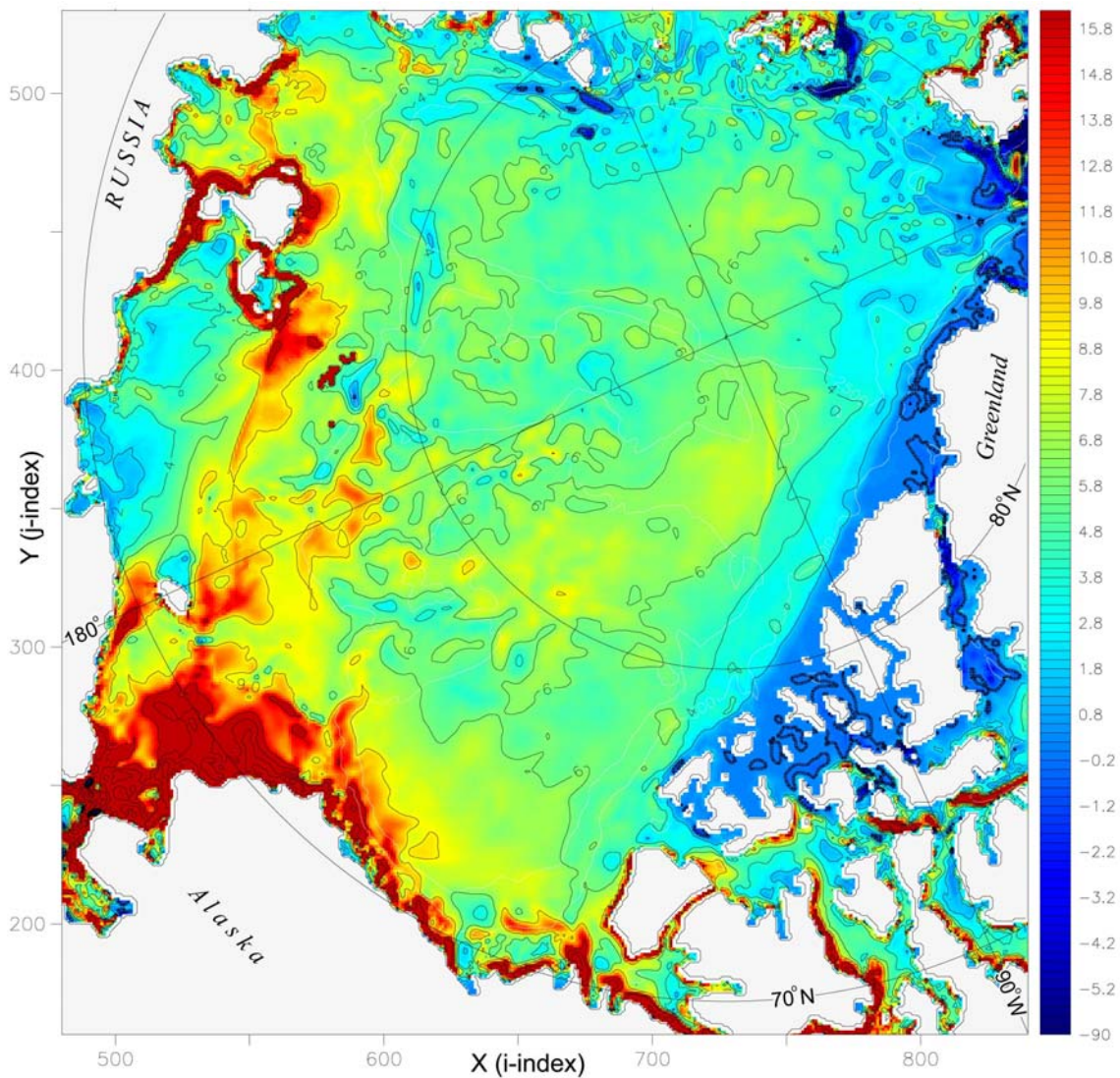


Figure 6.10. Difference field between 1980 summer average (J-A-S) surface (0-5 m, model level 1) eddy kinetic energy (cm^2/s^2) minus winter average (J-F-M) surface EKE.

Examination of seasonal mean fields and daily snapshots of surface (0-5 m, model level 1) EKE (not shown) reveals, as expected, the surface EKE distribution in the central Arctic is damped to near zero by the sea ice cover. Isolated, rapid increases in EKE correspond directly to the appearance of open water, leads and fractures in the sea-ice. These increases in energy, and the corresponding increases in mixing, emphasize the importance of ice-free areas in the transfer of heat and energy between the atmosphere and the ocean, particularly during the winter. A general increase in surface EKE is noted in the summer months, concentrated in the Bering Strait outflow region of the Chukchi Sea and along the shelf break in the Laptev and East Siberian Seas (Figure 6.10). There is a slight EKE increase of $\sim 4\text{-}6\text{ cm}^2/\text{s}^2$ in the central Arctic Ocean which can most likely be attributed to increased divergence and open water in the central ice pack in summer.

Snapshots of daily 60-120 m (model levels 9-12) eddy kinetic energy in March and August of 1980, (Figures 6.10 and 6.11, respectively) highlight the seasonal variability of subsurface Arctic Ocean eddy kinetic energy in the depth zone of the cold halocline layer. Concentrations of high EKE occur in March along most of the Barents Sea shelf break, associated primarily with flow through Fram Strait and suspected increases in density driven outflow from the Barents Sea west of Frans Josef Land and via St Anna Trough (Figure 6.11). The higher levels of EKE toward the central Nansen Basin, north of the 2500 m isobath, are in a region of mean westward flow (Figure 6.3). There are maxima in EKE along the Laptev Sea shelf break, in the central Makarov Basin and aligned with the Mendeleyev Ridge. In the Canadian Basin, high levels of subsurface EKE are located at the base of the Chukchi Cap, along the Chukchi and East Siberian Sea shelf break as well as the northern end of the Chukchi Cap and north of Barrow Canyon. Many of the regions of increased energy appear to be associated with abrupt changes in the bathymetry and regions where shelf break currents cross submarine ridges. In the Lincoln Sea, a narrow region of increased EKE leading toward a definite EKE maximum along the length of Nares Strait is seen. Much of the region in Figure 6.11 is covered with sea ice in late March, with the exception of Fram Strait and portions of the Barents Sea. For this reason and as these depths are below the surface mixed layer, wind influence can be considered minimal. Thus the energy may be attributable to

hydrodynamic instability, changes in density driven flow, strong seasonal changes in the mean currents or the thermohaline flow.

In August 1980, the main concentrations of increased EKE along the shelf break in the Arctic Ocean have shifted to the north coast of Alaska and the Beaufort Sea (Figure 6.12). This is now open water due to the well developed shore lead. Smaller, scattered

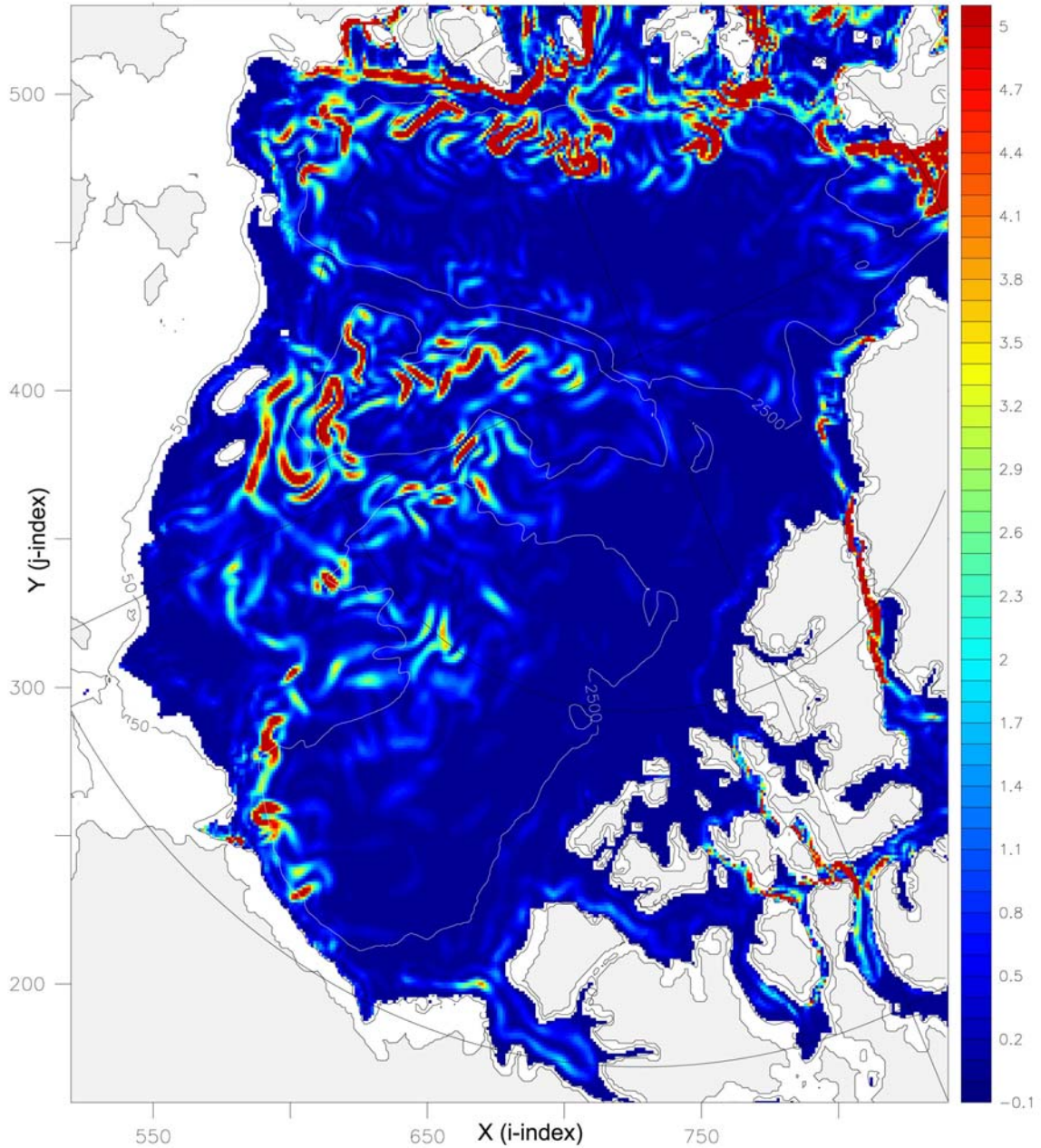


Figure 6.11. Snapshot of March 1980, 60-120 m (model levels 9-12) eddy kinetic energy (cm^2/s^2) in the Arctic Ocean.

regions of increased EKE can still be seen along the Barents and Laptev Sea shelf break as well as in the Nansen Basin. Increased amounts of EKE are noted at the Russian end of the Lomonosov Ridge and in the central Makarov Basin, in contrast with the March snapshot of subsurface EKE. Concentrated regions of increased EKE are seen crossing the southern end of the Mendeleyev Ridge and along the western and northern sides of

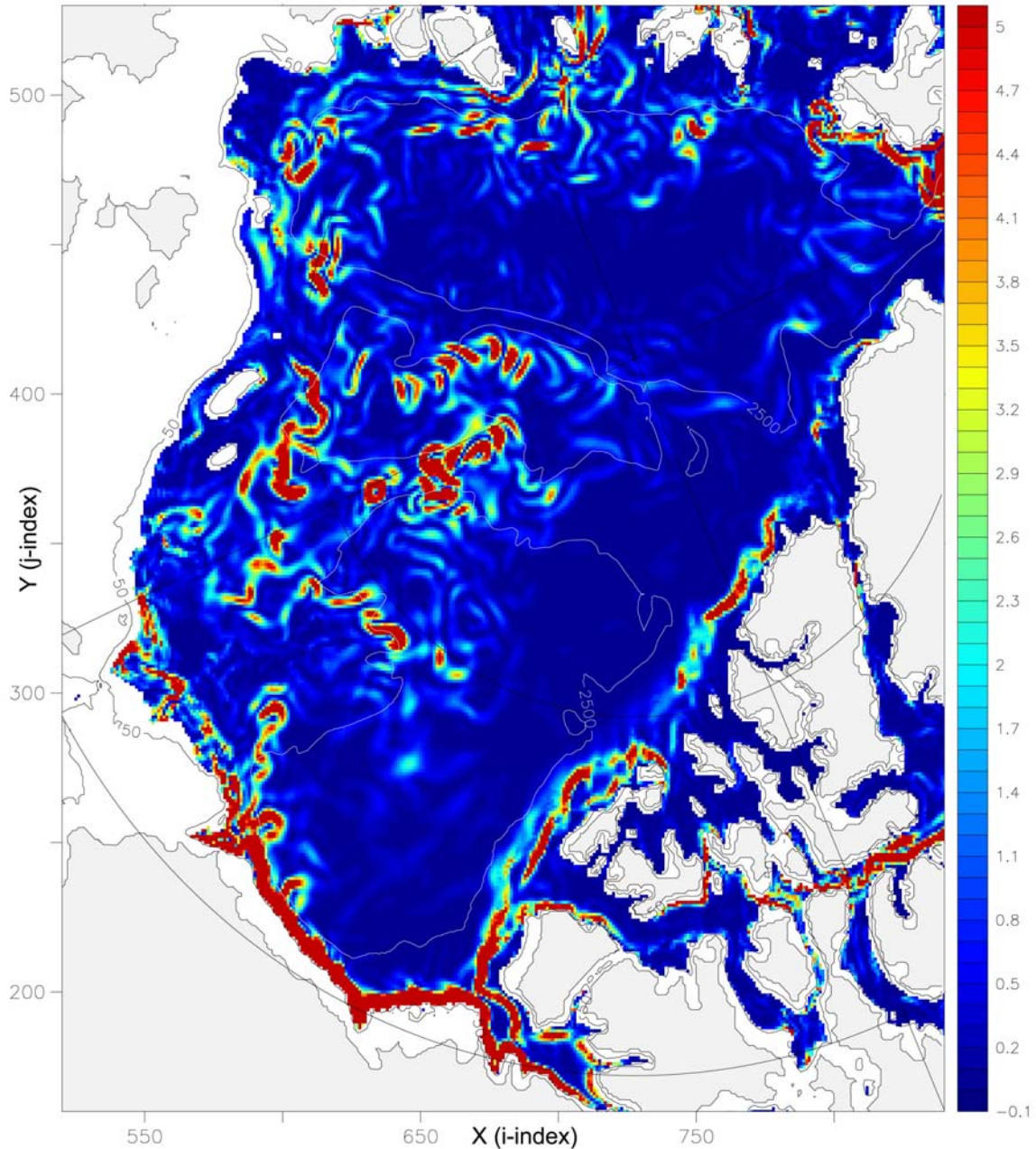


Figure 6.12. Snapshot of August 1980, 60-120 m (model levels 9-12) eddy kinetic energy (cm^2/s^2) in the Arctic Ocean.

the Chukchi Cap. Along the shelf break, east from the international date line to the north coast of Ellesmere Island, there are significantly larger amounts of EKE in August than in March, 1980. The elongated region of EKE through Nares Strait is absent during August and this may be a result of a strengthening of the mean currents through Nares Strait in winter. The large differences in EKE in Amundsen Gulf, in the CAA, may be a result of the seasonal reversal of the mean flow discussed in Chapter IV.

Another feature emphasizing the link between changes in EKE and bathymetry are the increases in EKE following the shape of the Moris Jesup Plateau, north of Greenland, visible in March and August. This also highlights the highly barotropic nature of the shelf break circulation in the Arctic as the minimum depth over the eastern edge of the plateau is ~ 1000 m.

Classifying local increases in EKE as wind induced or thermohaline driven is difficult in August as the sea-ice cover has retreated, thinned and/or diverged over much of the region. Based on comparisons with the March and August 1980 snapshots of sea ice concentration and 60-120 m velocity (not shown) the region of increased EKE in the Makarov Basin appears to be the most isolated from wind effects. The increased levels of EKE in this region may be due to the confluence of the anticyclonic Beaufort Gyre with the cyclonic shelf slope current from the Laptev Sea. The EKE increases along the Alaskan north coast and in the western Canadian Archipelago are most likely a result of the summer sea ice retreat or changes in the mean currents. The elongated regions of increased EKE north of the Canadian Archipelago appear to correspond with a long lead or fracture in the sea ice cover, corresponding to the observed, well established summer shore lead. The southern end of the Mendeleyev Ridge is where, in the model, cyclonic flow leaving the Laptev Sea collides with anticyclonic flow originating in the Beaufort Sea.

Based on an August 1980 snapshot of the vertical distribution of EKE along the SCICEX section in the Canadian Basin (Figure 6.13), the maximum EKE values in the core of the Alaskan Coastal Current, $\sim 200 \text{ cm}^2/\text{s}^2$, are ~ 50 times larger than those in the deep, Atlantic Layer boundary current, $\sim 4 \text{ cm}^2/\text{s}^2$. Increases in EKE are visible above the Alpha and Lomonosov Ridges, which may be indicators of the flow trapped along these

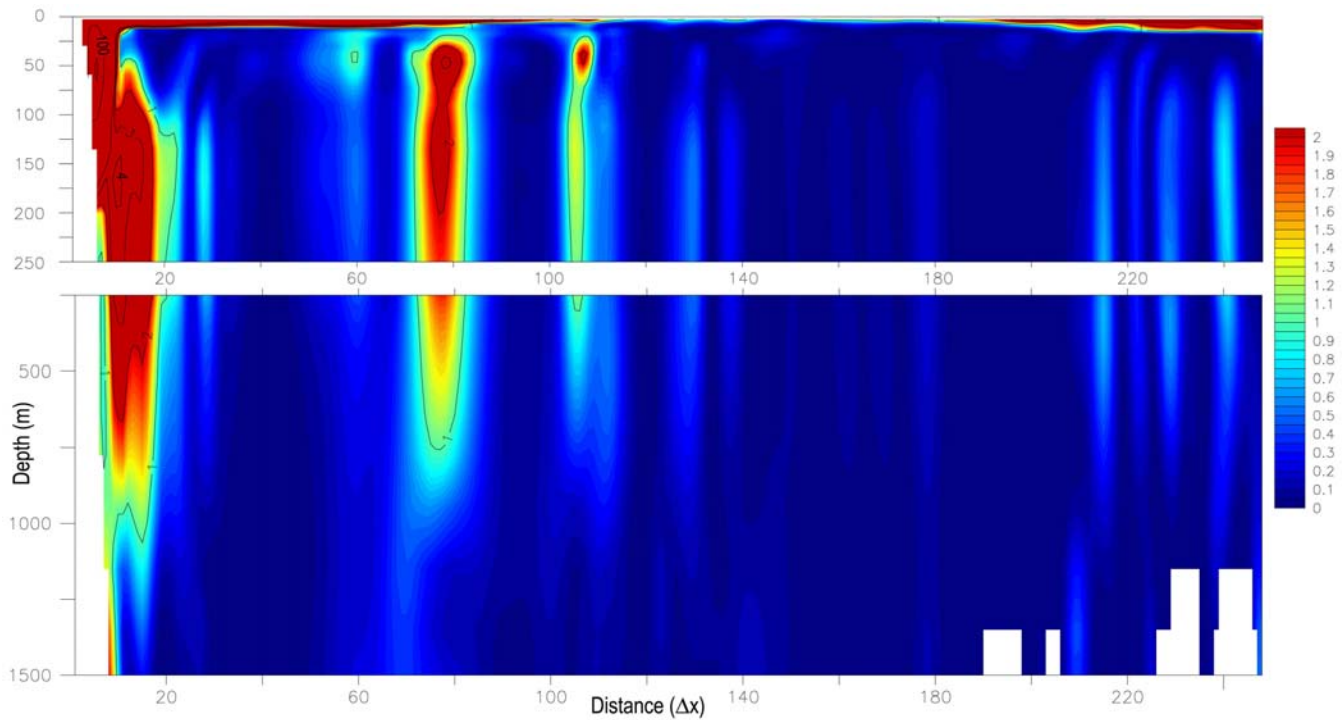


Figure 6.13. Snapshot of the August 1980 vertical distribution of EKE along the SCICEX transect in the Canadian Basin. Note the shading scale is adjusted to highlight lower values of EKE in the center of the basin. Bathymetry profile and x-axis distance scale as in Figure 6.9

ridges. The regions of increased EKE in the central Canadian Basin cannot be attributed to significant changes in the underlying bathymetry. The significant vertical extent of this feature, from ~25 m to 750 m, is too large to be attributed solely to wind influence. Therefore, it is suspected this feature is due to a significant deviation from the annual mean Atlantic Layer flow.

The only definitive conclusion that can be drawn from the snapshots chosen as representative of winter and summer subsurface EKE and the snapshot of the August 1980 vertical EKE distribution is that significant eddy activity exists in the central Arctic Ocean. This is a process long suspected as significant in the variability of the temperature and salinity structure in the central Arctic Ocean (Newton et al., 1974; Aagaard and Carmack, 1994; Rudels et al., 1994). Many of the regions of increased EKE in the central Arctic Ocean are lens shaped or in pairs and their size is on the order of 70-90 km. The elongated regions of increased EKE have a typical width of ~50-60 km.

Conclusions as to the preferred width of Arctic Ocean eddies are difficult to make under the limitations of model resolution versus the ~ 10 km Rossby radius of deformation in the Arctic Ocean. Additionally, it is felt that the model under-represents the Arctic Ocean EKE by, at a minimum, a factor of four, based on comparison of model results with observations in the Labrador Sea (Chapter IV).

D. DISCUSSION

Examination of model skill in simulating the central Arctic Ocean oceanography, though not the main focus of this report, has proven useful in a modeling sense as well as providing what are quite possibly the first estimates of basin-wide eddy kinetic energy below the surface mixed layer.

The model simulates the mean circulation in the upper 200 m of the Central Arctic and shelf seas with considerable skill. It is able to capture the strong boundary currents as well as the more complex and smaller scale circulation patterns in the shelf seas. The addition of riverine temperature and salinity inputs will modify the circulation and T/S distribution in the shelf seas as well as the central Arctic Ocean, altering these results closer towards observations.

The departure of the temperature distribution in the intermediate layers of the model from climatology has helped identify potential solutions in the lateral boundary conditions as well as support the conclusion that the numerical method of deep acceleration for diffusion, as applied in this experiment, was not successful. While this method may have proven helpful in moving model conditions away from deficiencies in the deep initialization fields (Figure 6.8), significant departures from the observed distribution of temperature in the intermediate layers of the Arctic Ocean were introduced. This accumulation of excess heat may have a significant impact on the circulation and the sea ice cover. Adjusting the lateral boundary conditions may indeed improve the representation of Arctic intermediate waters but a period of significant adjustment will be needed as the excess heat is released to the upper layers, possibly thinning the ice cover.

Developing an understanding of the distribution of eddy kinetic energy in the central Arctic Ocean may provide a means of clarifying the transport processes and interactions between the shelf seas and the central basin. The southern Nansen Basin and the southern end of the Mendeleyev Ridge, near the East Siberian Sea, appear to be regions of significant seasonally variable EKE, while the central Makarov Basin, on the eastern side of the Lomonosov Ridge between 84° N and 86° N appears to be a region of elevated EKE year-round. Farther study of longer-term means may prove useful in focusing the efforts of field experiments seeking to measure eddy kinetic energy in the Arctic Ocean.

VII. 9 KM MODEL VERSUS 18 KM MODEL

The primary focus of this chapter is to illustrate the gains realized from doubling model resolution from 18 km to 9 km. The comparison is between two regional coupled ice ocean models with many similar characteristics (Figure 7.1, Table 7.1). The initial question, "Is the 9 km model better at simulating ocean and sea-ice characteristics than the 18 km model?" can be answered with a qualified yes. Yes, in that better representation of the bathymetry has an immediate positive impact on the modeled circulation in several regions of the Arctic Ocean and its adjacent seas, where bathymetry is the controlling factor. Two such regions are the Barents Sea and the Canadian Arctic

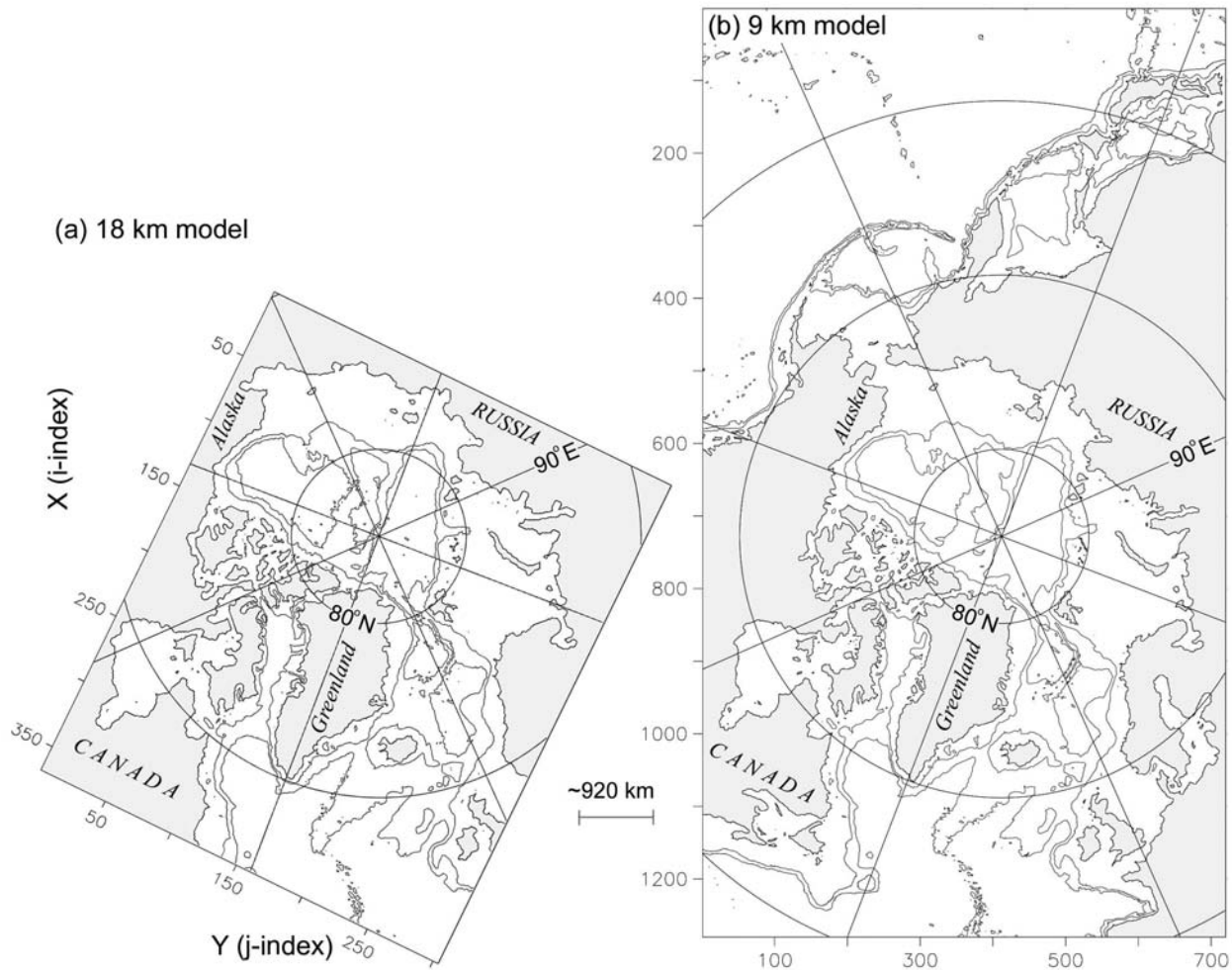


Figure 7.1. 18 km PCAP58 model domain (a) and 9 km PIPS model domain (b). 18 km model image has been rotated 26°. Approximate distance scale is equivalent to 100-9 km model grid points and 50-18 km model grid points. 500 and 2500 m contours in black.

Archipelago. Another yes, in that several narrow boundary currents that were absent or poorly represented in the 18 km model appear or become stronger and well defined in the 9 km model. Examples of this will be shown in the Labrador Sea and along the north coast of Alaska in the Beaufort Sea. Another yes, in that volume transports through Bering Strait, Fram Strait and the Barents Sea are approaching observed values, with the acknowledgement that even at ~9 km resolution, transport through the CAA is under-represented. Finally, the ability of the 9 km model to reasonably represent eddy kinetic energy in the southern Labrador Sea and decrease the gap between modeled and observed values in the northern Labrador Sea from a factor of 10 to a factor of 2 indicates greater skill at simulating observed conditions.

Parameter		18 km model	9 km model
ocean model		LANL POP, free surface	LANL POP, free surface
ice model		Hibler (1979)	Hibler (1979)
horizontal grid		368x304	1280x720
vertical levels		30	45
bathymetry		IBCAO+ETOPO	modified ETOPO
initialization fields		PHC 2.0	PHC 1.0
atmospheric forcing		ECMWF	ECMWF
restoring fields	surface	PHC 2.0 monthly mean	PHC 1.0 monthly mean
	Lat. Bdry	PHC 2.0 annual mean	PHC 1.0 annual mean
restoring timescale	surface	Temp-365 d, Sal-120 d	Temp/Sal-30 d
	Lat. Bdry	30 d	10d
timestep	ocean	20 min	8 min
	ice	120 min	48 min
horizontal diffusion	tracer	-4.00E+18	-5.00E+17
	momentum	-1.00E+19	-1.25E+18
vertical diffusion	bkgd diff.	0.1	0.05
	bkgd visc.	1	0.2
spinup integration completed		10 yr rpt '79-'93 mean, 3x '79-'81 cycle (9yr)	27yr rpt '79-'93 mn, 6yr rpt '79, 3x '79-'81 cycle (9yr)
diagnostic integration completed		1979-1998	planned 1979-2000
approximate integration time		~28 hr/yr on 64 pe, ARSC T3E-900	~168 hr/yr on 128 pe, ARSC T3E-900

Table 7.1. 18 km model (PCAP58) and 9 km model (PIPS) model configurations and key parameters.

Qualifications to the many improvements stem primarily from areas where the newer, high-resolution model deviates from climatological or observed conditions. The representation of certain aspects of Arctic Ocean and sea ice characteristics are significantly improved in the 9 km model when compared with output from a previous 18 km model. However, there are unknowns and shortcomings in the simulation of certain features that the 9 km model shares with the 18 km version, accumulations of thick ice in the Siberian shelf seas, verification of which is made difficult by a lack of observational data, and an overly thick and warm Atlantic Water layer, for example. The majority of these deviations are not necessarily related to model resolution, but rather to choices made in model development, initialization and spinup. Recommendations related to model design and implementation methodology will be discussed in Chapter VIII. The focus in this chapter will be to illustrate how representation of circulation and other features have been improved because of the resolution increase.

The most significant finding the reader should take away from this chapter is that inadequately resolving the basic large scale circulation can adversely impact a model's ability to properly represent water mass distributions and interactions due to advection, which will then impact heat, salt and possibly mass balances. Under-representation of eddies and eddy kinetic energy will also impact the transport and mixing of water mass properties. In essence, improvements gained through perfecting sub-grid-scale parameterizations will not help coarser models as improper representation of the circulation will inhibit or prevent water mass interactions. As shown in Siegel et al. (2001), eddy kinetic energy and the generation of eddies increase with increases in resolution, and at higher resolutions the rate of increase slows somewhat. Their highest resolution experiment, a 1.56 km resolution wind-driven, closed-basin, quasi-geostrophic ocean model, is approximately six times the resolution of the 9 km model discussed in this report. This indicates further increases in resolution will continue to result in improvements in the representation of mesoscale and smaller scale processes in the Arctic Ocean.

A. 18 KM MODEL DESCRIPTION

The 18 km model used in the following analysis is a limited domain, coupled Arctic Ocean and sea-ice general circulation model (Figure 7.2) that has evolved from previous 18 km versions developed at the Naval Postgraduate School (NPS). The reader

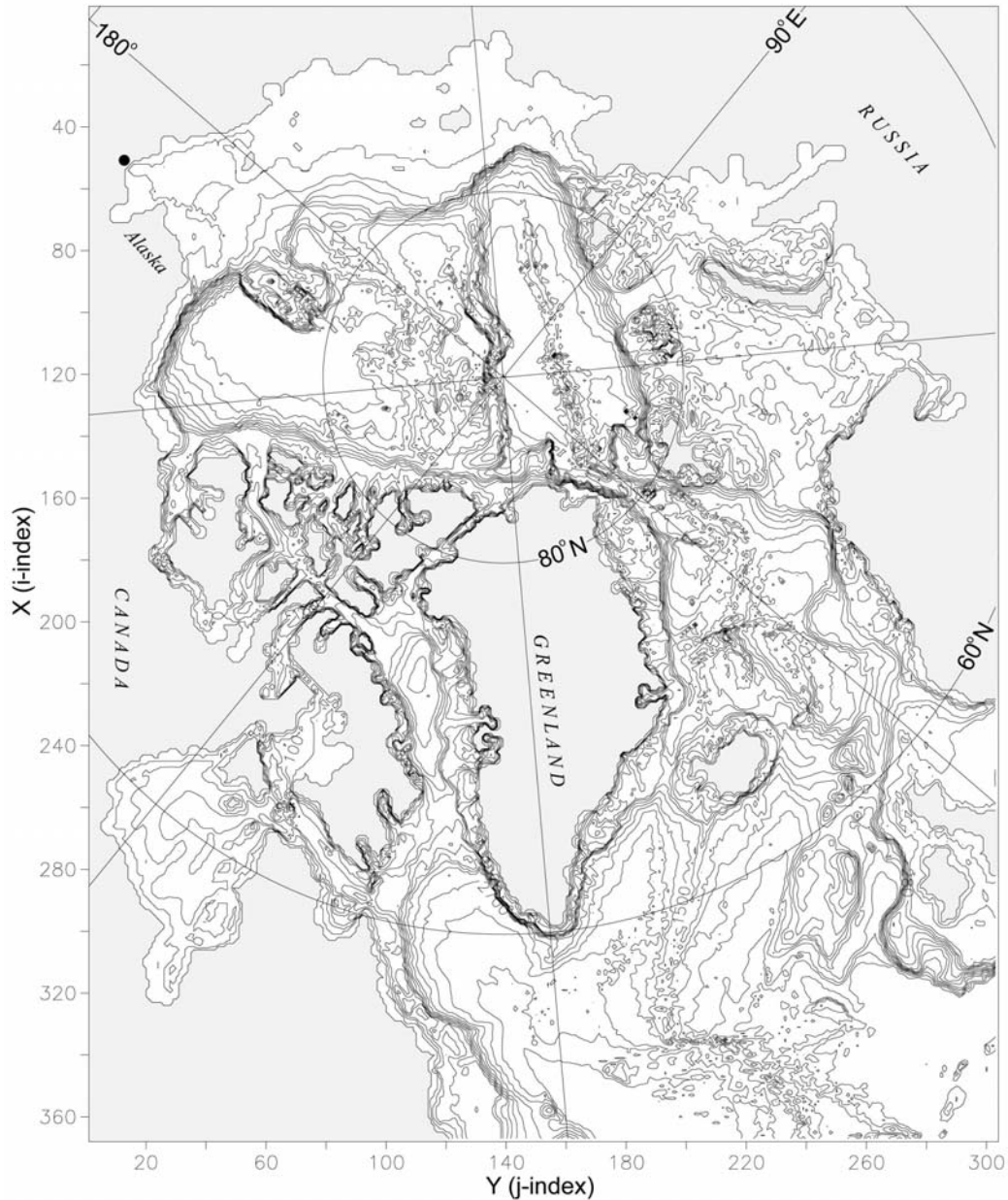


Figure 7.2. PCAP58 18 km coupled ice-ocean model domain and bathymetry (m). Contours are every other model level. Bathymetry north of 64° N derived from IBCAO 2.5 km resolution database. The black dot in the upper left corner denotes the location of the closed Bering Strait.

is referred to Parsons (1995) and Zhang et al. (1999) for details on the development of the original version of the 18 km model and Maslowski et al. (2000) for additional specifics on a modified, massively parallel version of 18 km model. The 9 km model discussed in this report can be considered the third generation of these previous 18 km models. The 9 km model will be referred to as PIPS, for the Navy's Polar Ice Prediction System.

The 18 km model discussed in this report, herein called PCAP58, differs from the Maslowski (2000) 18 km model, known as PCAP38, primarily in the bathymetry dataset used to generate the model grid and the method of spinup. PCAP38 bathymetry was derived from the ETOPO5 database, with significant manual corrections by Parsons and Maslowski using available Office of Naval Research and Russian Hydrological Agency charts. PCAP58 bathymetry was derived from the 2.5 km resolution IBCAO dataset (Jakobsson et al., 2000) north of 64° N and the ETOPO5 database south of 64° N. PCAP38 spinup consisted of 200 years of a repeated 1990-1994 cycle of ECWMF winds, followed by 20 years of repeated 1979 ECMWF atmospheric forcing. Specifics of the PCAP58 spinup period are provided in Table 7.1. The Newfoundland coast has been modified where it meets the 18 km model southern boundary in both PCAP38 and PCAP58 (Figure 7.2).

A brief comparison of PCAP38 and PCAP58 1980 annual mean velocities in the Beaufort Gyre indicated significant differences in the mean circulation of the top 100 m. A detailed analysis of these differences is outside the scope of this report, however it is felt the significantly different spin up periods plays a significant role.

In addition to the size of the domain and the closed Bering Strait in PCAP58, notable differences between PCAP58 and PIPS spinup are the number of years in which the 1979-1993 15-year mean atmospheric forcing was applied (10 years for PCAP58, 27 years for PIPS) and the inclusion of river inputs in PCAP58. Additional differences are the use of deep acceleration in PIPS during the second decade of spinup and later, the application of repeated 1979 forcing in the PIPS spinup.

The 15-year mean forcing was applied to PCAP58 for one decade primarily due to time constraints. Within available time and resource constraints, an effort was made to

match the duration of spinup between PCAP58 and PIPS. Integration of PCAP58 began in mid 2001. Deep acceleration for diffusion was not applied to PCAP58 due to indications from PIPS spinup output that this numerical method, combined with strong lateral boundary restoring to an annual mean climatology, had resulted in a significantly warmer and thicker than observed Atlantic Water layer in the central Arctic Ocean. It is suspected that the PCAP58 deep circulation is still evolving and has not yet reached equilibrium. The choice was made not apply repeated 1979 forcing to PCAP58 based on the tendency for excessive ice growth discovered during PIPS spinup.

One might expect a logical progression of model development, in terms of resolution and bathymetry, to be: (1) 18 km resolution, ETOPO5-based bathymetry; (2) 18 km resolution, IBCAO-based bathymetry; (3) 9 km resolution, ETOPO5-based bathymetry; and (4) 9 km resolution, IBCAO-based bathymetry. The chronological development of these models did not occur in that order, as the high resolution IBCAO bathymetry database had not been released when the 9 km model was ready to begin integration. The decision was made to proceed with the integration using the modified ETOPO5-based bathymetry and attempt to incorporate the improved bathymetry at a later stage. The actual progression of model development has been (1), (3), (2), (4).

The remainder of this chapter will discuss improvements gained through the increase in resolution in the following order: (1) representation of the bathymetry and circulation in regions where bathymetry is the major controlling factor; (2) the representation of shelf break and coastal boundary currents; and (3) the increase in eddies and eddy kinetic energy noted in the 9 km model. In the interests of brevity limited regional examples in each category will be presented. The data used in the comparisons consist primarily of 1980 annual mean fields. This choice was made as the number of years in which realistic daily varying forcing has been applied to PIPS are at this point in time, limited. Every effort has been made to compare equivalent depths and regions. The PIPS model domain is shifted $\sim 26^\circ$ to the west when compared to that of PCAP58. The driving factor behind the design of the PIPS domain was meeting National Ice Center requirements for their upgraded ice forecast system, as opposed to ease of comparison with previous model versions. Therefore, 18 km model images, when placed next to 9

km model images, have been rotated 26° and Latitude and Longitude circles are provided to help orient the reader.

B. BATHYMETRY IMPACTS

It is obvious that increased resolution will result in improved representation of the geography and bathymetry within a model domain. Higher sub-sampling rates along a coastline or a vertical section will capture higher frequency variations in that profile. Some smoothing will occur and many small features will still

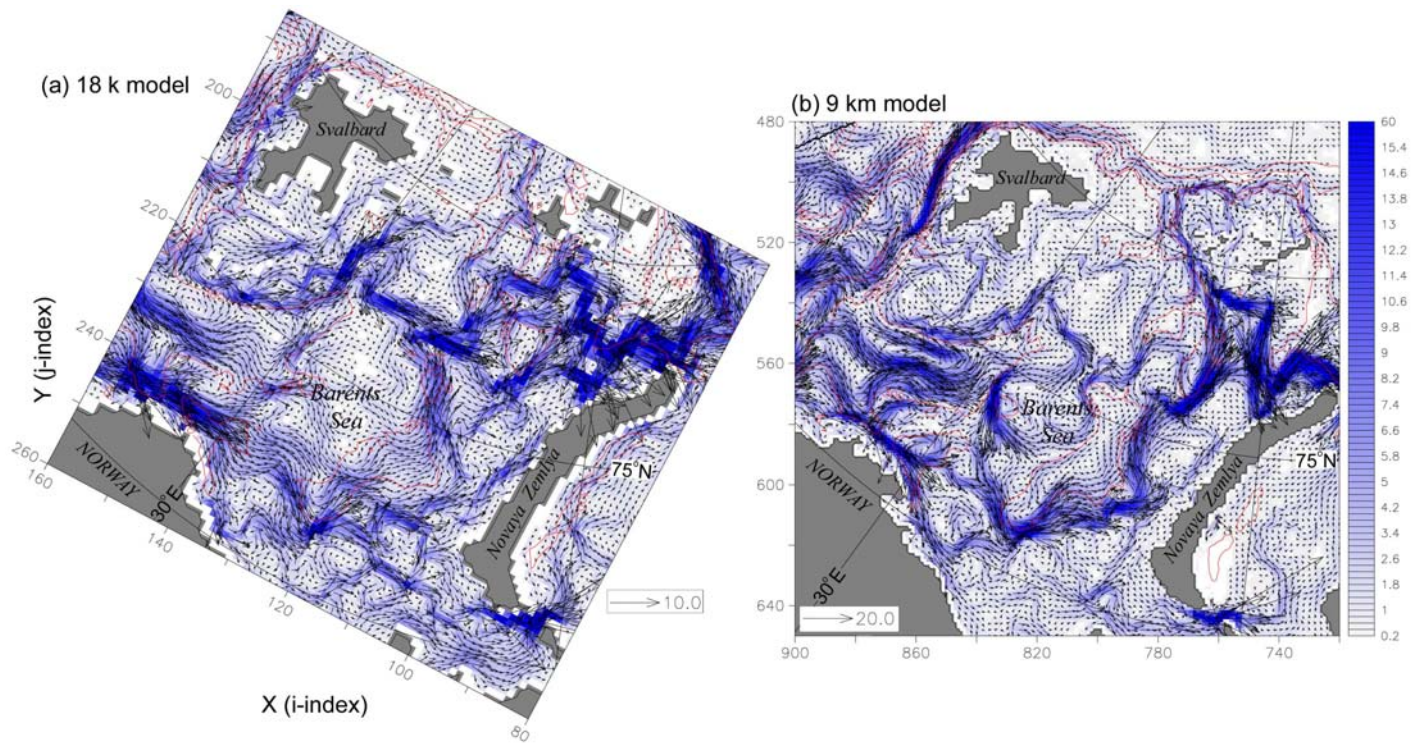


Figure 7.3. Distribution of 1980 annual mean velocity (cm/s) in the Barents Sea. (a) PCAP58, 0-225 m (model levels 1-7), every vector is plotted; (b) PIPS, 0-223 m (model levels 1-15), every other vector is plotted. Background shading is current speed (cm/s) and is the same for both model images. Note the differing vector scales.

be missed but as resolution increases, features attain a more realistic shape. What is less clear is what resolution will ensure enough of the horizontal and vertical variations have been captured to accurately simulate the circulation and mass balances.

As discussed in Chapter III, the 9 km model exhibits considerable skill in representing the mean circulation in the Barents Sea (Figure 3.2), a region where bathymetry is a major controlling factor in the circulation (e.g., Pfirman et al., 1994). Circulation in the PCAP58 Barents Sea (Figure 7.3) exhibits many similar features to the 9 km model. Yet due to poorer vertical resolution and the resultant representation of the bathymetry in the Barents Sea, specifically Great Bank and Central Bank (Figure 3.1), PCAP58 displays pathways that are not in agreement with the observed circulation in the Barents Sea (Ozhigin et al., 2000). There appear to be two paths the warm Atlantic Water can follow through the Barents Sea, with larger velocities and more concentrated currents along the northern path (Figure 7.3(a)). This dynamical difference has significant physical implications in the nature of the water mass transformation that takes place in the Barents Sea, as it places the primary pathway of warm Atlantic Water through the Barents Sea farther to the north, impacting the oceanic frontal structure as well as the ice edge.

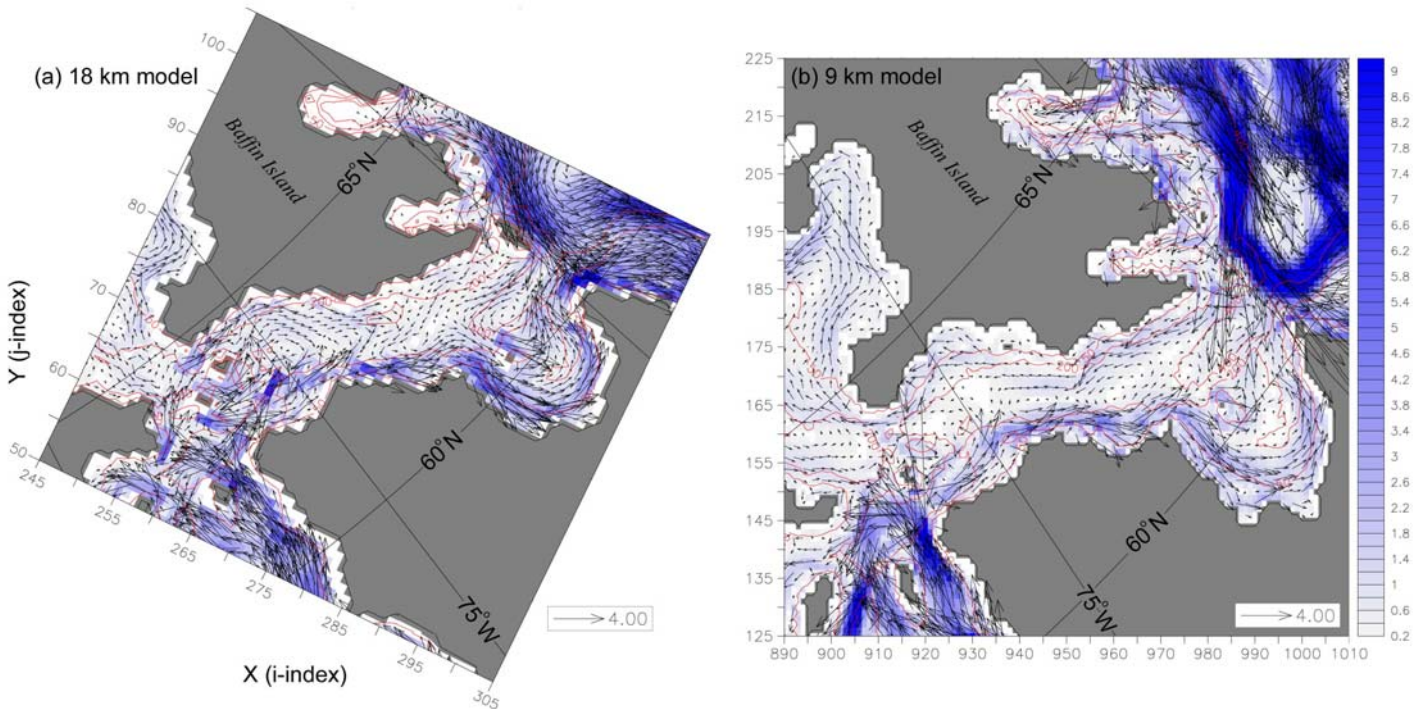


Figure 7.4. Distribution of 1980 annual mean velocity in Hudson Strait. (a) PCAP58, 0-180 m (model levels 1-6), every vector is plotted; (b) PIPS, 0-183 m (model levels 1-14), every other vector is plotted. Background shading as in Figure 7.3.

More islands and narrow channels are resolved in the PIPS Canadian Arctic Archipelago when contrasted with the PCAP58 CAA (Figure 7.1, or Figure 7.2 and Figure 2.1, respectively, for greater detail). The strait between Ellesmere Island and Devon Island, which allows flow out of the Archipelago through Jones Sound, and Prince of Whales Strait, separating Banks Island from Victoria Island (Figure 4.1) are two examples. It appears the main characteristics of Arctic Surface Water outflow through the CAA can be captured by properly resolving the three primary paths: Peary Channel (which includes Viscount Melville Sound and Barrow Strait) to Lancaster Sound; Nares Strait to Smith Sound; and Fury and Hecla Strait to Hudson Strait. However, it was shown that at even 9 km resolution, transports through the Archipelago are possibly under-represented by a factor of two. One possible solution to this is maintaining the current 9 km resolution and artificially modifying the narrowest points of the three major pathways to achieve the proper transport values. The other solution, which will increase the realism of the circulation through the Archipelago and the representation of eddies and eddy kinetic energy, rather than induce artificiality, is an additional increase in model resolution. The inclusion of the CAA as a nested, higher resolution region within the 9 km model is another option, yet it is felt considerable work remains before nested ocean models achieve the realism and reliability seen in atmospheric models.

A comparison of 1980 annual mean circulation in Hudson Strait (Figure 7.4) indicates the increase in resolution allows Baffin Bay outflow to travel the length of Hudson Strait and enter Foxe Basin, as observed (Prinsenberg, 1987). In the 18 km model, eastward flowing Hudson Bay outflow covers the entire western end of the Strait, causing Baffin Bay outflow entering Hudson Strait to recirculate east of $\sim 74^\circ$ N (Figure 7.4(a)). This may have significant impact on the water mass properties in Foxe Basin and Hudson Bay, which will have a subsequent effect on the stratification of the upper layers, sea-ice formation and freshwater export to the south. Dramatic seasonal pulses, or spillovers, of water masses are occasionally observed in animations of 18 km model output and this may be a means of forcing the proper water mass through a constricted opening otherwise blocked by unrealistically wide flow. Despite the resolution increase, it has been shown that without additional physics improvements, such as tidal effects and

river inputs, the seasonal variability in Hudson Bay circulation is not well represented, at even 9 km resolution.

C. BOUNDARY CURRENTS

Boundary currents are crucial in the transport of mass, heat, salt and freshwater throughout the Arctic Ocean and the sub-polar seas (Rudels, 1987; Aagaard, 1989, Rudels et al., 1994). The Labrador Sea plays a key role in the global thermohaline circulation as one of the few deep-water formation regions in the world (Broecker, 1991; Skillingstad et al., 1991). Variations in the transport of cold, fresh Arctic Ocean outflow, as well as sea- ice and icebergs, by boundary currents such as the East and West Greenland Currents, the Baffin Current and the Labrador Current precondition the Greenland Sea and the Labrador Sea for deep convection and deep water formation.

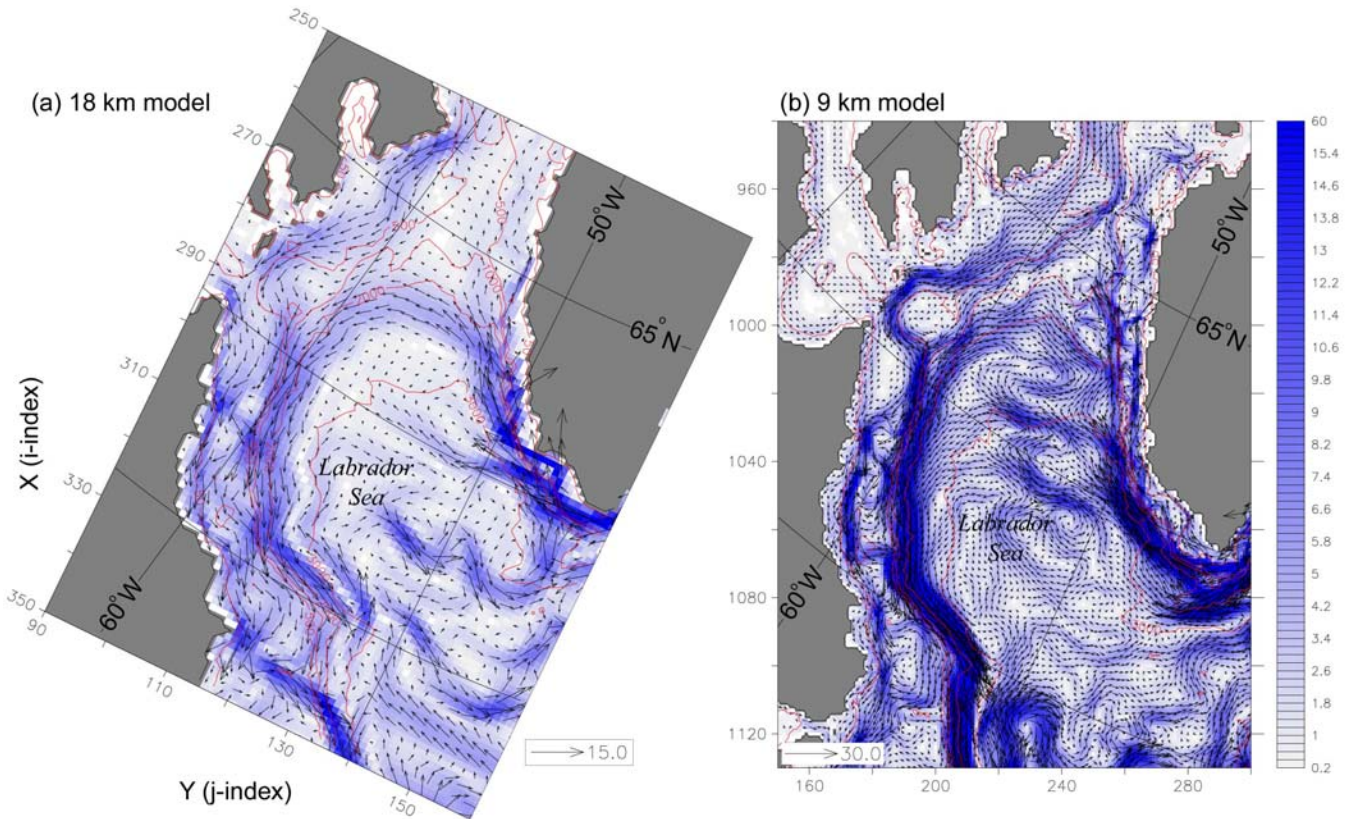


Figure 7.5. Distribution of 1980 annual mean velocity (cm/s) in the Labrador Sea. (a) PCAP58, 0-180 m (model levels 1-6); (b) PIPS, 0-183 m (model levels 1-14). Every other vector is plotted. Background shading as in Figure 7.3. Note the differing vector scales.

Large freshwater outflows can severely reduce or cap deep convection in either area (Dickson et al., 1988, 1996; Visbeck et al., 1995), therefore proper representation of these currents is crucial.

Labrador Sea boundary currents are narrower and stronger in the 9 km model 1980 annual mean velocity in the top 180 m when compared to the 18 km model (Figure 7.5). Improved representation of northward flow through Davis Strait is apparent as well as bathymetric effects on the southerly flowing Baffin Land/Labrador Current. The width of the western branch of the Baffin Land/Labrador Current traveling around the 500 m contour at the mouth of Hudson Strait is ~50 km in the 9 km model versus ~100 km in the 18 km model. The separation of the West Greenland Current into several branches of westward flow across the Labrador Sea (as observed, Cuny et al., 2001) is more distinct, as are the interactions between the current along the Labrador coast and the shelf break current. The proximity of the 18 km model boundary and modifications made to the coastline (Figure 7.2) must be taken into account in the behavior of the coastal current south of 55° N and representation of the northward intrusion of North Atlantic Current meanders into the Labrador Sea (Figure 7.5 (a)).

Boundary currents at several depths along the north coast of Alaska and Canada in the 9 km model Beaufort Sea are faster, more defined and indicate considerably larger horizontal and vertical shear in contrast to the slower and broader 18 km model boundary currents (Figures 7.6, 7.7 and 7.8). The classification of differences due to varying model resolutions is difficult in this region as the lack of realistic Bering Strait volume inputs in PCAP58 (temperature and salinity values are prescribed on an annual cycle) has a dramatic impact on the behavior of the circulation in the upper levels

In the top ~45 m, Chukchi Sea outflow through Barrow Canyon and the eastward flow of Alaskan Coastal Current above the 50 m curve is well represented in the 9 km model, while mean flow is up-canyon in the 18 km model (Figure 7.6 (a)). The 9km model Barrow Canyon outflow bifurcates into an intense cyclonic boundary current and a less intense westward flow across the southern end of Chukchi Cap (Figure 7.6 (b)). These features are absent in the 18 km model.

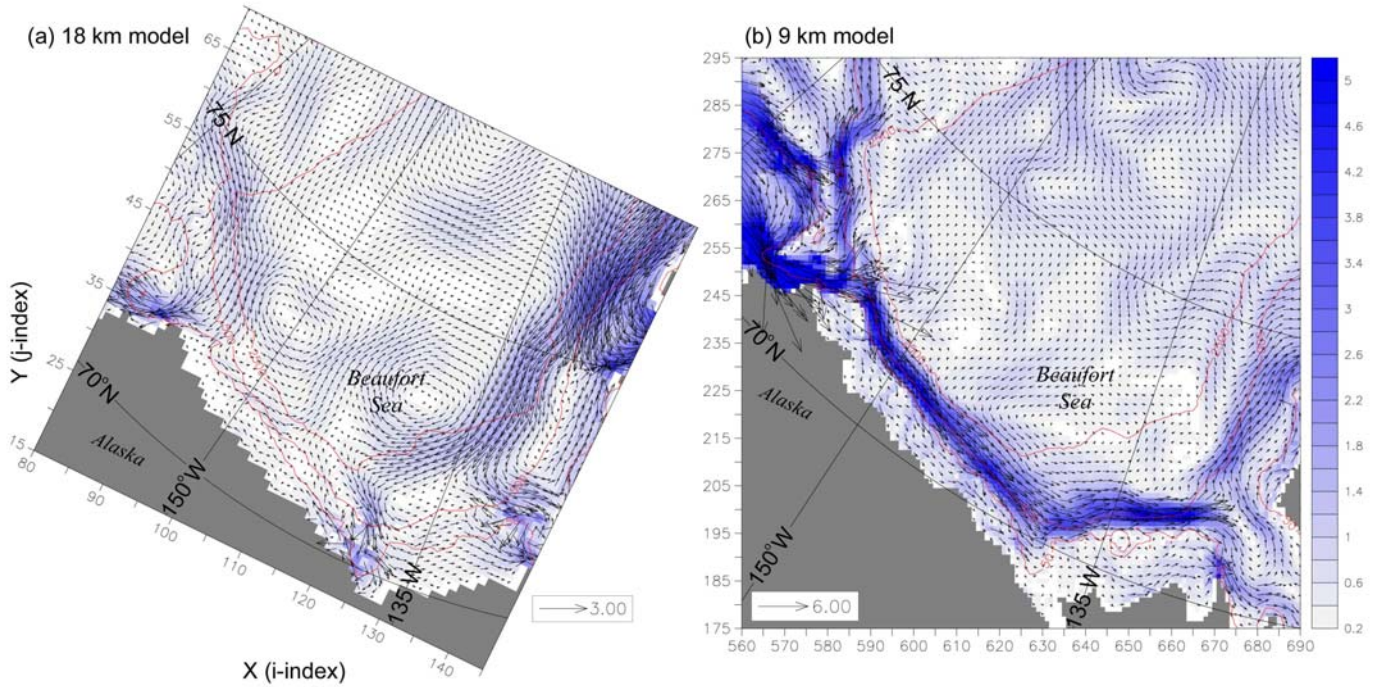


Figure 7.6. Distribution of 1980 annual mean velocity (cm/s) in the surface layer of the Beaufort Sea. (a) PCAP58, 0-45 m (model levels 1-2), every vector is plotted; (b) PIPS, 0-43 m (model levels 1-7), every other vector is plotted. Background shading as in Figure 7.3. Note the differing vector scales.

Between 66-120 m, the Barrow Canyon outflow continues to exert a significant influence on circulation in the 9 km model western Beaufort Sea, with the majority of the outflow joining the anticyclonic flow over the southern end of the Chukchi Cap (Figure 7.7 (b)). The width and intensity of the Alaskan Coastal Current have decreased, by at least a factor of two with depth and more anticyclonic circulation is present. Boundary flow in the 18 km model has taken on a generally anticyclonic nature (Figure 7.7 (a)). In both models, there is southerly flow along the eastern flank of Chukchi Cap. Between 135° W and the Canadian Archipelago (the right edge of each frame, Figure 7.7), a distance of ~300 km, two alternating bands of circulation are visible in the 18 km model, while there are three bands present in the 9 km model, a northward flow between the 2500 m and 500 m isobaths, with southward flow west of the 2500 m isobath and east of the 500 m isobath along the shelf break north of the CAA.

The circulation of the intermediate waters in the Beaufort Sea varies considerably between the two resolutions (Figure 7.8). The 1980 annual mean circulation between 360

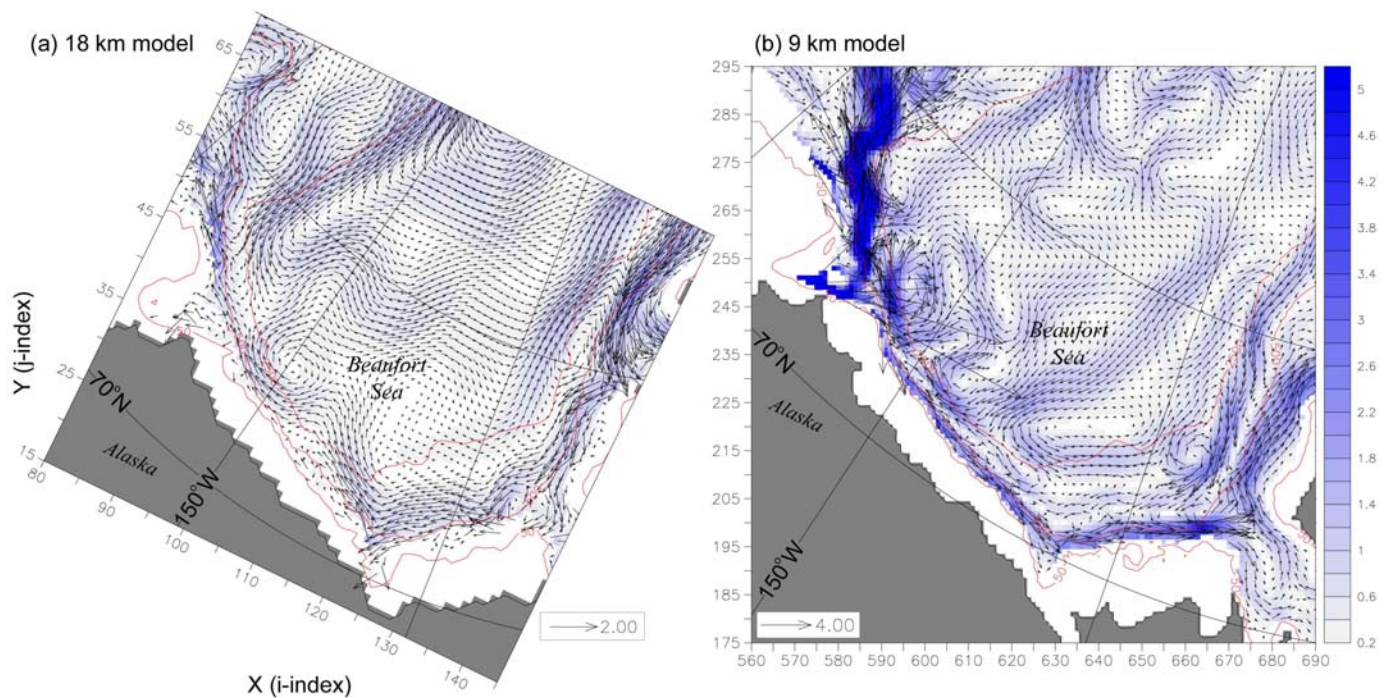


Figure 7.7. Distribution of 1980 annual mean velocity (cm/s) in the halocline of the Beaufort Sea. (a) PCAP58, 71-140 m (model levels 4-5), every vector is plotted; (b) PIPS, 66-120 m (model levels 10-12), every other vector is plotted. Background shading as in Figure 7.3. Note the differing vector scales.

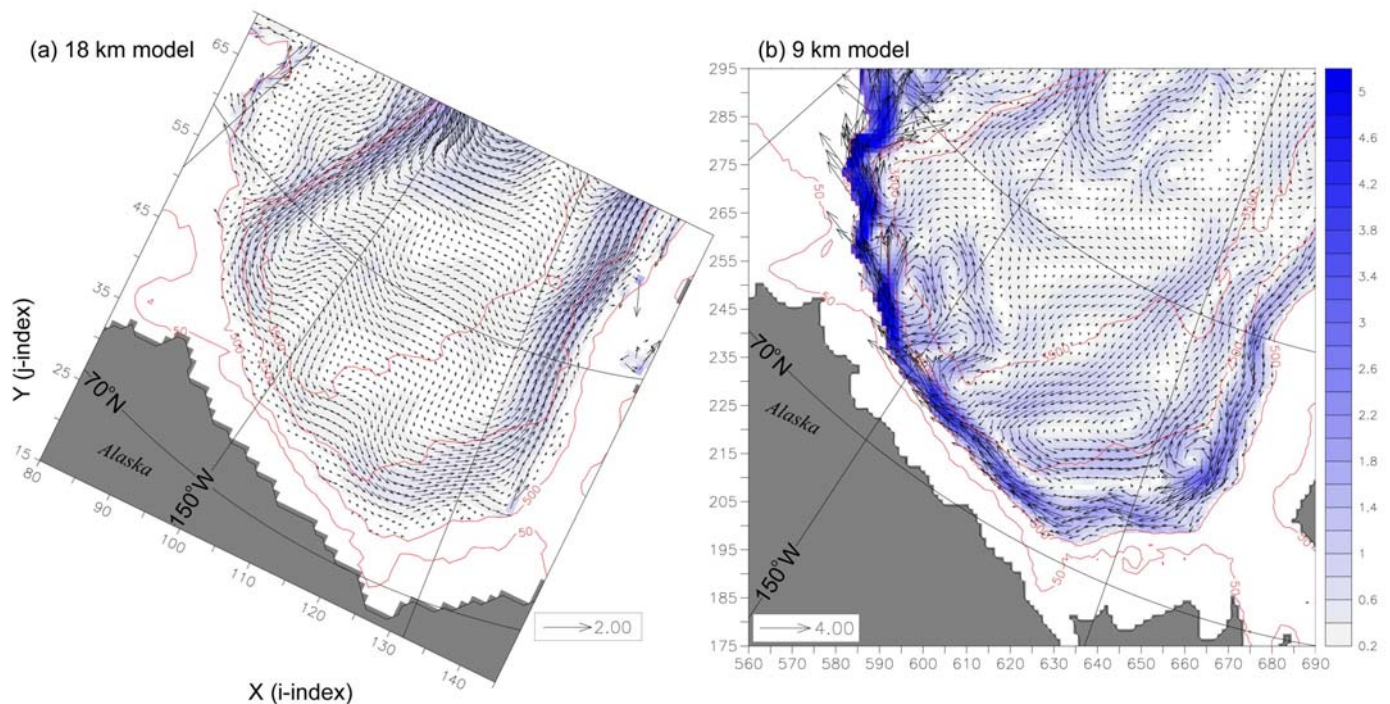


Figure 7.8. Distribution of 1980 annual mean velocity (cm/s) in the Atlantic Layer of the Beaufort Sea. (a) PCAP58, 360-565 m (model levels 10-11), every vector is plotted; (b) PIPS, 398-584 m (model levels 19-20), every other vector is plotted. Background shading as in Figure 7.3. Note the differing vector scales.

and 565 m (levels 10 and 11) in the 18 km model is predominantly cyclonic (Figure 7.8 (a)). The boundary circulation between 398 and 584 m (model levels 19 and 20) in the 9 km model is anticyclonic close to the shelf and generally cyclonic farther toward the interior. A closed, cyclonic circulation is located between the 3500 and 2500 m contours in the southeastern Beaufort Sea (Figure 7.8(b)).

At these levels the influence of Pacific Water flow through Bering Strait can be expected to be minimal. However, the improved representation of the morphology of Barrow Canyon in the 9 km model is suspected as the cause of the significant perturbation in the boundary flow in the vicinity of 72° N, 150° W. Flow along the eastern flank of Chukchi Cap is southerly in both models, and there is considerable southeasterly flow toward the interior of the Beaufort Sea. The cyclonic boundary current in the 18 km model, though between 150-180 km wide, follows the accepted understanding of intermediate water circulation in the Arctic Ocean (Rudels et al., 1994). The strong, steady, ~50-60 km wide anticyclonic boundary current in the 9 km model and the weaker cyclonic circulation to the north merit further investigation but are outside the scope of this report. However, it is difficult to conclude that the circulation represented in 9 km model output is incorrect, as the accepted view of the circulation has often been deduced from observations limited in both time and spatial coverage.

In all, the boundary currents in the 9 km model, approximately twice as narrow in many regions and having velocities 2 to 3 times faster than those in the 18 km model, will have a significant impact on property transports and water mass transformation and may improve estimates of residence times as well.

D. EDDIES AND EDDY KINETIC ENERGY

Eddies play a significant role in oceanic circulation in that they can result in the propagation of significantly different water masses outside of their place of origination (Gent et al., 1995) and their dissipation transfers momentum between length scales and properties between water masses. Proper eddy parameterization in coarser resolution

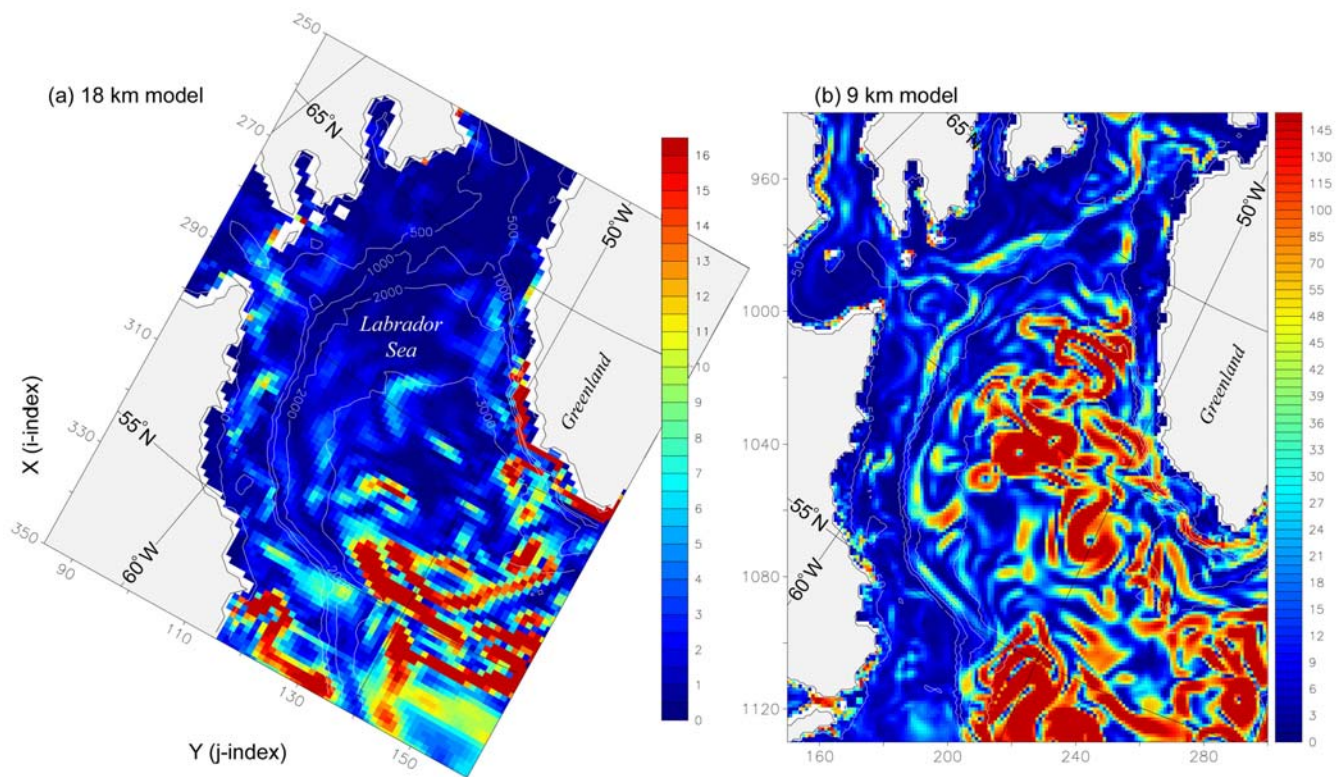


Figure 7.9. August 1980 snapshot of surface layer eddy kinetic energy (cm^2/s^2) in the Labrador Sea: (a) PCAP58, 0-45 m (model levels 1-2); (b) PIPS, 0-43 m (model levels 1-7). Note different shading scales.

models is found to be important insofar as eddy-topography interactions contribute to propelling and sustaining narrow boundary currents (Nazarenko et al., 1997; 1998).

Semtner and Chervin (1992) presented results from the first eddy resolving global ocean circulation model and since then, further improvements in the efficiency of model codes and supercomputer capabilities have allowed continued resolution increases in many applications, which have broadened our view of the intensity and distribution of eddies in the oceans. These resolution increases do come at considerable computational cost (c.f. Table 7.1 for this limited regional example). There is vigorous and continuing discussion about finding the proper balance between resolution increases and parameterizations which will allow long integrations to accurately simulate circulation at multiple length scales and maintain mass and property balances.

Results presented earlier indicated the 9 km model was able to accurately represent the mean levels of EKE observed in the southern Labrador Sea. Whether the

Model	Labrador Sea EKE			Nordic Seas EKE		
	Maximum	Mean	Std Dev	Maximum	Mean	Std Dev
PCAP58	132.50	4.90	9.20	269.40	4.70	13.30
PIPS	3998.00	70.40	203.70	4959.00	43.50	142.70

Table 7.2. Eddy kinetic energy (cm^2/s^2) statistics for the 0-45 m regional snapshots presented in Figures 7.9 and 7.10.

difference between modeled and observed EKE in the northern Labrador Sea is a function of the increased resolution or the significant differences between the atmospheric regime of the early 1980's versus that of the early 1990's adds uncertainty to any conclusions drawn about 9 km model performance in this region. However, comparison of snapshots of EKE in the top ~45 m of the Labrador Sea clearly indicate EKE is significantly under-represented in the 18 km model (Figure 7.9). The southern maximum in EKE in the 18 km model (Figure 7.9(a)) corresponds to energy within a branch of the North Atlantic Current that extends to the north, then east. Geographic distribution of EKE maxima in the 9 km model are in reasonable agreement with the observed means (Figure 4.11(b)). The under-representation of EKE in the 18 km model may cause insufficient mixing of water from the West Greenland Current with surface water in the central Labrador Sea. This would in turn impact the degree of stratification, which would affect overturning and deep-water formation.

Dramatic differences exist in the distribution of 0-45 m eddy kinetic energy in the Nordic Seas between the two models as well (Figure 7.10). When viewed as an aggregate, the concentration of increased EKE in the 9 km model appears to define the path of the North Atlantic Current passing south of Iceland, and the Norwegian Atlantic Current as it travels north, along the west coast of Norway (Figure 7.10(b)). Indication of such a pathway is absent in the distribution of 18 km model EKE (Figure 7.10 (a)). There is an order of magnitude difference in EKE statistics computed for the regional snapshots discussed previously (Table 7.2) as well as in the statistics computed for similar regional annual mean surface (0-20 m, PCAP58 level 1; 0-5 m, PIPS level 1) EKE values (not shown).

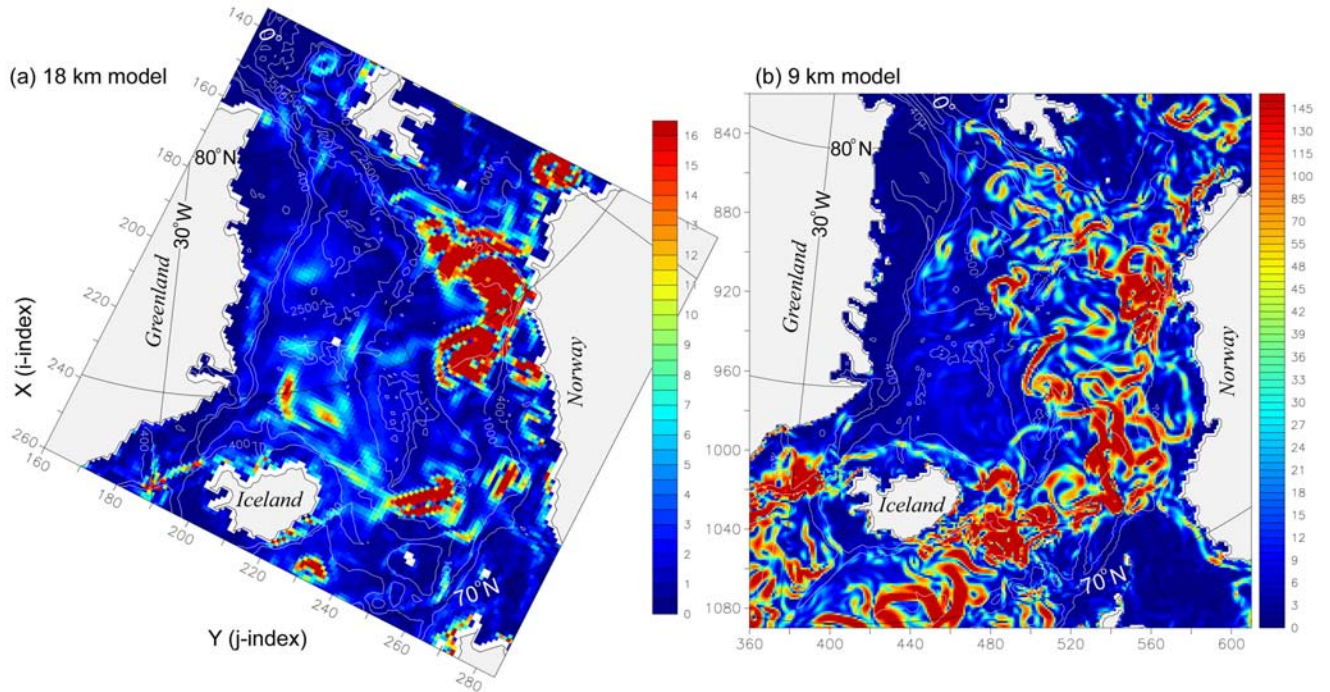


Figure 7.10. August 1980 snapshot of surface layer eddy kinetic energy (cm^2/s^2) in the Nordic (Greenland, Iceland and Norwegian) Seas: (a) PCAP58, 0-45 m (model levels 1-2); (b) PIPS, 0-43 m (model levels 1-7). Note the different shading scales.

E. DISCUSSION

Significant improvements in model skill are realized through a doubling of resolution, from 18 km to 9 km. Increasingly realistic bathymetry improves the simulation of topographically steered flows, which in the case of the Barents Sea and other coastal areas can change the regional distribution and transformation of water masses. The inclusion of smaller channels and islands in model Canadian Arctic Archipelago bathymetry results in less artificiality in the simulated flow. The coarser resolution is shown to actually prevent the proper spatial and temporal distribution of water masses in the case of Hudson Strait. However, mass transports remain under-represented even at the higher resolution, suggesting additional increases in resolution are needed to successfully model this region.

Boundary currents become narrower and stronger at 9 km resolution and the appearance of opposing boundary currents demonstrates a significant increase in horizontal and vertical shear. The representation of circulation within and around the

model Labrador Sea is significantly improved. Better boundary current representation will result in improvements in water mass transport around the perimeter of the Arctic Ocean as well as outflow through the Norwegian and Labrador Seas.

An order of magnitude increase in eddy kinetic energy between the 18 km model and the 9 km model has resulted in simulated values matching observed values in the southern Labrador Sea. The difference between modeled and observed EKE in the northern Labrador Sea is reduced to a factor of two. However, due to the significant differences in the low NAO index atmospheric forcing regime in the early 1980's versus the high NAO regime in the early 1990's (Chapman and Walsh, 1993; Serreze et al., 1997), model EKE values in the northern Labrador Sea may be closer to observed values than thought. Comparison of modeled EKE values with observed values, as the planned 1979-2000 "hindcast" integration progresses through the early 1990's, will provide a clearer determination.

VIII. CONCLUSIONS AND RECOMMENDATIONS

This report has described the successful development, spin-up integration and verification of a high resolution, coupled ice-ocean model of the Arctic Ocean and adjacent sub-polar seas. This project was initiated in part to fulfill an Office of Naval Research (ONR) contract to upgrade the U.S. Navy's Polar Ice Prediction System (PIPS). PIPS output is used by analysts at the National and Naval Ice Center, Suitland, Maryland to produce five day ice forecasts. The author had the privilege to join a team of researchers, primarily from the Naval Postgraduate School, Monterey, California, at the beginning stages of the development of a state of the art ice forecast system for U.S. Navy use.

The new ice-ocean model, PIPS 3.0, has four times the horizontal resolution, ~9 km versus ~36 km, and 3 times the vertical resolution, 45 levels versus 15, of the current system in use, PIPS 2.0. Numerically, based on grid size alone, 1280x720x45 versus 360x360x15, the new model is 21 times larger than its predecessor. A copy of the model code has been provided to scientists at the Navy Research Lab, Stennis Space Center, Mississippi, where it is being modified for transition to operational forecast use. Ultimately, the forecast version of the model will be run at the Fleet Numerical Meteorology and Oceanography Center, Monterey, California. The computational requirements of the increased resolution model are significant and considerations regarding resource allocation, to be able to run the model while meeting operational needs, are well outside the scope of this report.

Through regional analyses of output during the spin up phase of the 9 km model, it is shown that the new model demonstrates significant skill in simulating the mean circulation and water mass properties, and many aspects of the seasonal and annual variability of the Arctic Ocean and its peripheral seas. Some oceanographic features and some regions are not as skillfully represented as others and it is believed the primary cause of these departures from climatology and observations may be traced to model resolution and the spinup method used.

Many of the benefits gained from the higher resolution are immediate and readily seen. Examples are the improved representation of the bathymetry throughout the region, especially in the complex Canadian Arctic Archipelago where the model realistically simulates currents flowing in opposite directions on either side of narrow channels within the CAA. Improvements are also seen in the simulation of boundary currents and other topographically steered flows. Proper representation of topographically steered flows is crucial in the Arctic region due to the barotropic nature of much of the circulation.

Additional benefits from increased resolution are more subtle, yet have significant long term implications toward heat and salt balances. Failure to adequately resolve the large scale circulation, regardless of the accuracy of the sub-grid-scale parameterizations, will impact interactions between water masses and ultimately the distribution of heat and salt throughout the model domain. The need to maintain these balances in a closed boundary regional model may seem trivial, however the locations of geographic concentrations of heat and salt are not. Extending the resolution and balance question to global climate simulations implies that coarser resolution models, attractive due to their fast integration speeds, may encounter serious difficulty in obtaining proper heat and salt balances, especially in the Arctic region.

The unforced, natural variability and the realistic mean transport values in the model Bering Strait are seen as significant successes. The model is one of the first of its kind to realistically simulate Bering Strait circulation without the use of prescribed velocity or transport values in the vicinity of the Strait. The inclusion of the artificial “North American Channel” and the prescribed wind forcing over the channel from the Atlantic Ocean toward the Pacific Ocean are numerical methods used to improve the flow through Bering Strait. However, the model is able to realistically simulate variability in the flow through Bering Strait and the water mass characteristics in the region. It is important to note that most global models have not properly accounted for transports through the Bering Strait. Many either use a latitude circle as a northern boundary condition or prescribe a steady 0.8 Sv northward transport through the Strait. The dramatic observed variability in Bering Strait transport and circulation (Aagaard et al., 2001a; 2001b) indicates application of a steady northward transport will induce

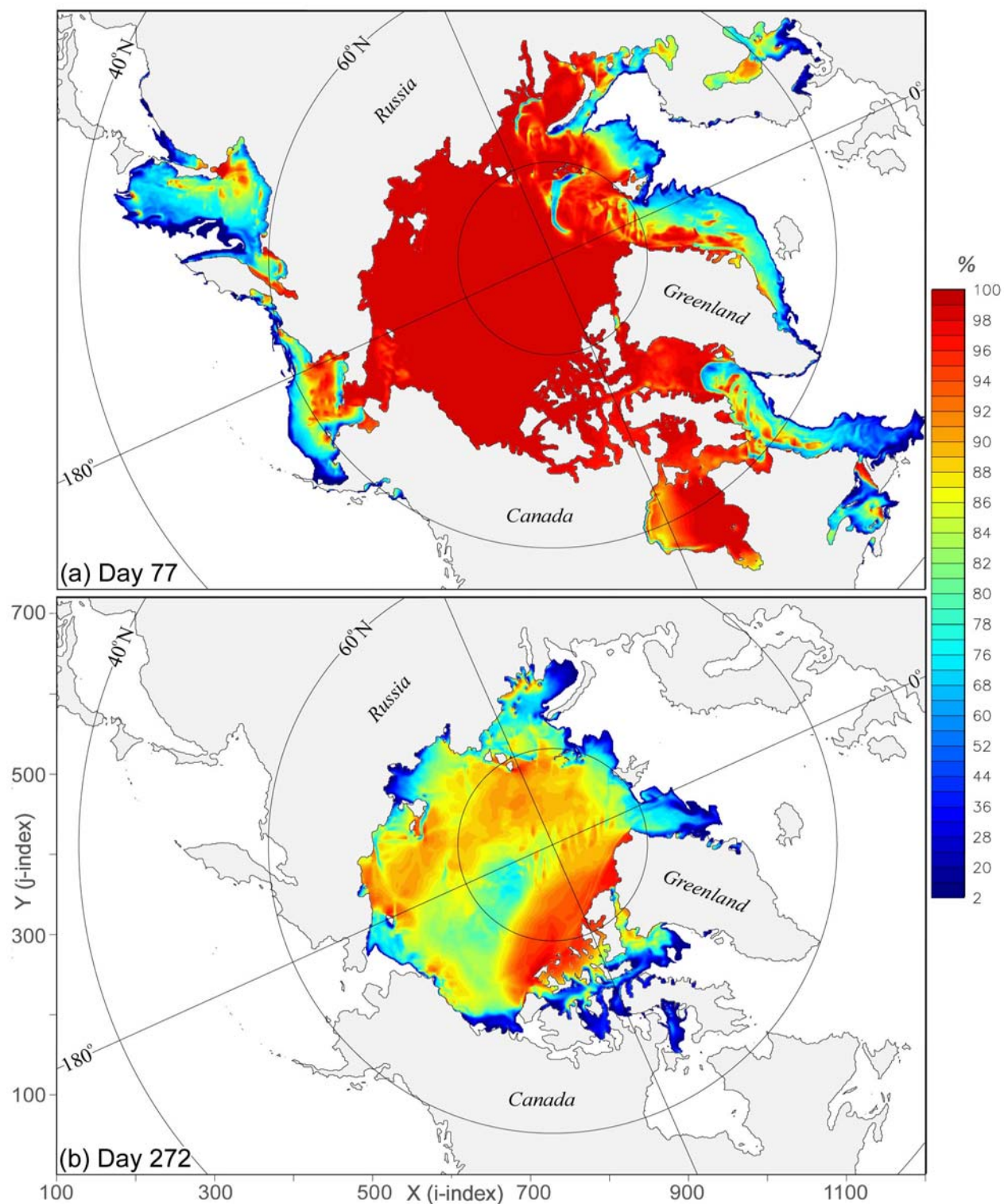


Figure 8.1. 1980 seasonal percent sea-ice concentration snapshots: (a) maximum extent, day 77 (mid March); (b) minimum extent, day 272 (mid September).

significant artificialities in Chukchi Sea and Canadian Basin mass and property balances and circulation.

Considerable seasonal variability is present in the sea-ice concentration and thickness distributions and significant detail in the marginal ice zone (Figure 8.1). The seasonal variability in sea-ice extent is a strong function of seasonal variations in the oceanic surface layer and both are tied to seasonal changes in atmospheric forcing. The detail achieved in the marginal ice zone is tied directly to the ability to resolve properties of the oceanic temperature, salinity and velocity fields in the upper 50 m.

The under-representation of eddies, transports in the CAA and eddy kinetic energy indicate improved sub-grid-scale parameterizations and further resolution increases will result in continued improvement in the simulation of these features. The inclusion of an eddy parameterization scheme, vice an increase in resolution, may prove beneficial in the interactions of eddies with topography and the resultant property

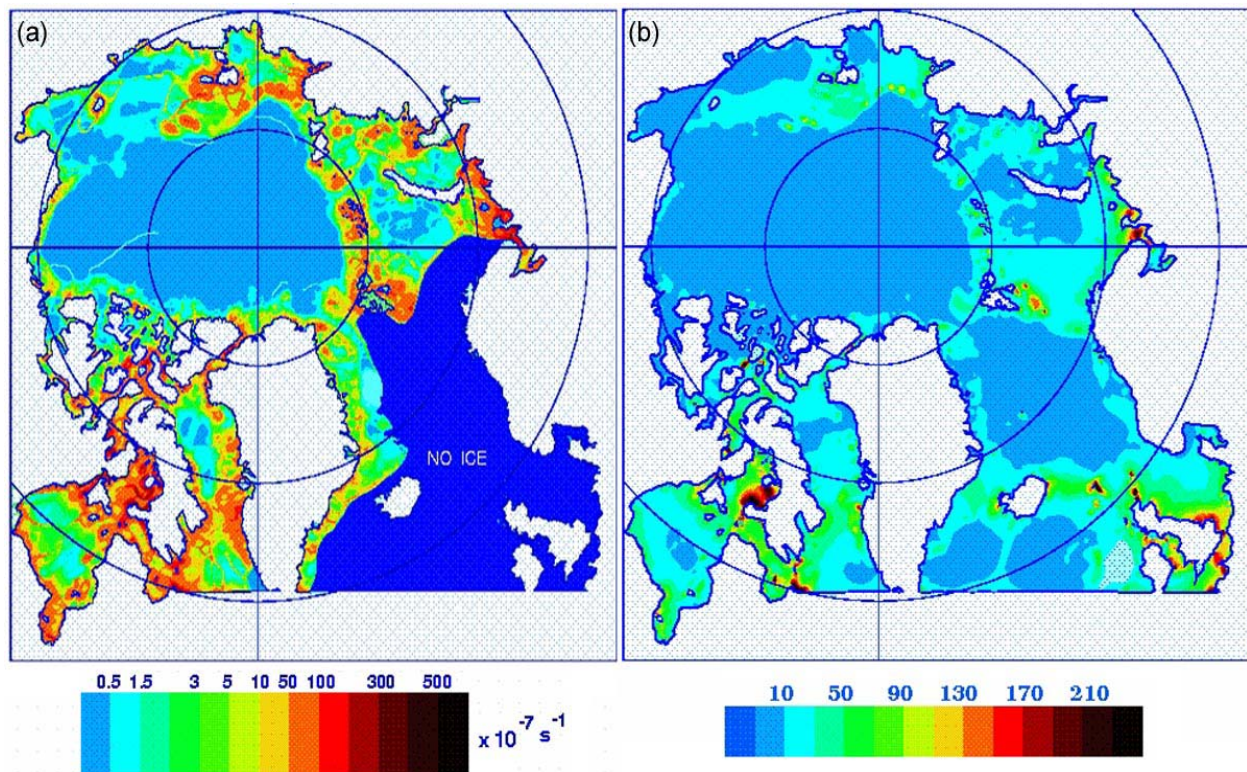


Figure 8.2. Tidal influences on the Arctic Ocean; (a) maximum shear of ice velocity due to M2, S2, K1 and O1 tidal species; (b) maximum tidal currents (cm/s) due to M2, S2, K1 and O1 tidal species (Kowalik and Proshutinsky, 1994).

transports without a significant increase in integration time. This method may not, however, account for many important processes governed by the small deformation radius in the Arctic region. Experiments using a simplified, basin scale wind-driven quasi-geostrophic ocean model indicates dramatic improvements in eddies and eddy kinetic energy will continue to be seen with resolution increases down to ~ 1.5 km (Siegel et al., 2001).

Additional features that may improve simulation of circulation and water mass transformations in the Arctic Ocean, regardless of resolution, are the inclusion of river inputs and a tidal model. In addition to temperature and salinity inputs from the several major rivers draining into Arctic Ocean marginal seas, inputs from the Yukon River south of Bering Strait, Hudson Bay river inputs and freshwater inputs to the Baltic Sea need to be included. Improved vertical and horizontal mixing parameterizations, as discussed previously, may improve representation of Barents Sea water mass transformations and the Arctic Ocean thermocline and halocline. The addition of a mixed layer depth model may improve representation of the thermocline and halocline. Adding a bottom boundary layer parameterization may improve movement of water across the vast Arctic shelves and through shallow channels in the CAA. Each of these improvements will also incur increased computational costs. Due to their significant influence on the circulation and distribution of properties, and their comparatively small computational cost, the addition of river inputs should be given priority as the next major modification to the model.

The work of Kowalik and Proshutinsky (1994), Parsons (1995), and Parsons et al. (1996) highlight the importance of tidal effects on sea ice and Arctic ocean circulation. Large areas of considerable shear in the sea ice and velocity variations attributed to tidal currents will impact sea-ice distribution, formation and melt and the underlying oceanic stratification in those regions (Figure 8.2). Thus, in certain regions, the inclusion of a tidal model will result in potentially significant improvements at much less computational cost than an increase in resolution.

In order to properly resolve oceanic features governed by a Rossby radius of ~ 10 km, and in particular 6 km in the St Anna Trough, model resolution will need to be on the

order of 1-2 km. At ~3 km resolution, a regional model with an equivalent domain as the current 9 km model, will contain ~8.3 million grid points in one horizontal layer. Such a model will never run in an operational forecast mode under the limitations of today's computing power.

The model's ability to reproduce values of eddy kinetic energy in the southern Labrador Sea similar to those observed, within the constraints of comparing 1980 model output with data from the early 1990's, and the order of magnitude increase in EKE between the 18 km model and the 9 km model, are significant improvements realized directly from the increase in resolution. It is felt that additional increases in resolution are needed in order to accurately simulate Arctic Ocean circulation. The current 9 km model simulates much of the large scale and intermediate sized features in the circulation with considerable skill but cannot simulate eddy-scale motion

It must be emphasized that choices made in the method of spin up and the nature of the atmospheric forcing that will be applied during spin up can dramatically influence the long term horizontal and vertical distribution of water mass properties as well as sea-ice concentration and thickness distribution, and ultimately the success of the simulation. It is felt that a combination of strong restoring of the oceanic boundaries to annual mean temperature and salinity climatology, using the numerical method of deep acceleration for diffusion, and multi-decadal application of slightly "cold-biased" atmospheric forcing appear to have resulted in excessive accumulations of sea-ice and deviations of intermediate and upper layer salinity and temperature distributions from observed and climatological values. It appears corrections to these deviations will either have to take the form of (1) restarting the model and spinning it up using different atmospheric forcing; (2) application of a correction factor to a model restart file, or to the model during integration, to bring T and S distributions more in line with climatological values; or (3) continued integration with realistic daily varying forcing in the hopes that natural processes accounted for in the model will move the T and S distribution in the intermediate and upper layers more towards those observed. The computational expense of option (1), in that it would ignore integration up to this point, and the uncertainty involved in option (3), make option (2) seem the most attractive. Changes in T and S

distribution will also impact the velocity fields so any adjustment factor would need to be applied incrementally to avoid creating instability in the model. Modifying the vertical coordinate system from z-coordinates to isopycnal coordinates or increasing the order of the diffusion equations, from second order to fourth order, may also improve the representation of upper and intermediate layer salinity and temperature distribution. As discussed in Chapter II, vertical levels in isopycnal coordinate models are based on density surfaces, which will avoid some of the excessive-mixing that occurs in z-coordinate models as water masses attempt to move between fixed z-levels. Higher order differential equations will result in less numerical diffusion. Both of these methods are significant changes in nature of the model and if implemented, will require restarting the model from rest.

A difficulty encountered during the verification phase of this effort was the limited availability of comparable observational data for model verification. Satellite and radar data are the only observational methods with comparable spatial and temporal coverage, and until the late '80s and early '90s and the increase in trans-Arctic oceanographic sections (Figure 1.2), much of the observational data was limited to point samples and sections from short duration cruises. Thus it was necessary in certain cases to compare monthly and annual mean model output with point data, limited duration time series, or even data collected in different decades, during considerably different atmospheric regimes. As the integration progresses into the late 1980's and the 1990's, it is felt verification will become easier as the density of available observational data increases.

Along these lines, it is recommended that every means possible be explored to continue the cooperative Scientific Ice Experiments (SCICEX) using U. S. Navy submarines as Arctic science platforms. Although not used extensively in this report, data gathered during this series of six cruises has resulted in huge advances in our understanding of the oceanography and the geology of the Arctic region. Additionally, continued annual or semi-annual occupation of the SCICEX transect from the Alaskan Coast toward the North Pole will provide an excellent means of detecting any trends in

Arctic Ocean temperature, salinity and sea-ice thickness and concentration distributions induced by global warming or climate change.

Alternative data collection methods such as autonomous underwater vehicles or high endurance subsurface drifters need to be developed to augment data collected through surface ship cruises. The development of a coordinated long term observing system in the Arctic Ocean, consisting of placement of moorings and sensors in the key inflow and outflow areas, would be a vital asset to oceanographers and an ideal means of gathering data to aid in model verification. At a minimum, extended monitoring should take place in Fram Strait, Bering Strait, Hudson Strait, Davis Strait and in the Barents Sea between Svalbard and Norway to obtain a detailed understanding of Arctic Ocean inflow and outflow. These limited locations do not begin to address processes within the Arctic Ocean, which are equally as important. However, the harsh environmental conditions present daunting technological challenges in the area of automated data collection and will continue to make data collection in the Arctic difficult and expensive as well.

Tremendous opportunity for continued oceanographic research with this model still exists. Out of necessity, choices were made to limit the scope of this report to provide a detailed analysis of the inflow and outflow regions of the Arctic Ocean. The high resolution also allows examination of many processes within the Arctic Ocean, such as thermocline and halocline maintenance, St. Anna Trough and Barrow Canyon outflows, the interior circulation of the Canadian and Eurasian Basins, and the impact of improved Lomonosov Ridge bathymetry on the exchange of intermediate and deep water between the Amundsen and Makarov Basins to name a few. All of these processes remain the source of considerable debate within the Arctic science community. Model output can be used for analysis of each of the included sub-polar seas as well.

In terms of numerical modeling, significant work remains on the implementation of river and tidal influences, possible modifications to the boundary conditions and continued analysis and verification as integration into the 1990's progresses.

In all, development and integration of the 9 km coupled ice-ocean model described here has helped improve understanding of circulation and property transports in

the major inflow and outflow regions of the Arctic Ocean, validated the need for continued increases in model resolution in this region and produced some valuable insights on model development and spin up.

THIS PAGE INTENTIONALLY LEFT BLANK

BIBLIOGRAPHY

Aagaard, K., and P. Greisman, Toward new mass and heat budgets for the Arctic Ocean, *J. Geophys. Res.*, 80 (27), 3821-3827, 1975.

Aagaard, K., L.K. Coachman, and E. Carmack, On the halocline of the Arctic Ocean, *Deep-Sea Res.*, 28A (6), 529-545, 1981.

Aagaard, K., J. H. Swift, and E. C. Carmack, Thermohaline circulation in the Arctic Mediterranean seas, *J. Geophys. Res.* 90, 4833-4846, 1985a.

Aagaard, K., A. T. Roach, and J. D. Schumacher, On the wind driven variability of the flow through Bering Strait, *J. Geophys. Res.*, 90, 7213-7221, 1985b.

Aagaard, K., A synthesis of the Arctic Ocean circulation, in *Reun. Cons. Int. Explor. Mer.*, edited by P.-V. Rapp, pp. 11-22, 1989.

Aagaard, K., and E.C. Carmack, The Arctic Ocean and climate: A perspective, in *The Polar Oceans and Their Role in Shaping the Global Environment: The Nansen Centennial Volume*, edited by O.M. Johannesen, R.D. Muench, and J.E. Overland, pp. 5-20, AGU, Washington, D.C., 1994.

Aagaard, K., T. Weingartner, J. Grebmeier, E. C. Carmack, and R. Moritz, Bering Strait: A Vital Ocean and Ecosystem Connection. A. Variability of Flow and Water Properties, <http://www.cifar.uaf.edu/ari00/aagaard.html>, Cooperative Institute for Arctic Research, 2001a.

Aagaard, K., R. Woodgate, and T. Weingartner, Bering Strait: Pacific gateway to the Arctic, <http://psc.apl.washington.edu/HLD/Bstrait/bstrait.html>, University of Washington, Polar Science Center, Seattle Washington, 2001b.

Aukrust, T., and J. M. Oberhuber, Modeling of the Greenland, Iceland, and Norwegian Seas with a coupled sea ice-mixed layer-isopycnal model, *J. Geophys. Res.*, 100, 4771-4789, 1995.

Anderson, L.G., G. Bjork, O. Holby, E.P. Jones, G. Kattner, K.P. Koltermann, B. Liljeblat, R. Lindgren, B. Rudels, and S. J., Water masses and circulation in the Eurasian Basin: Results from the Oden 91 expedition, *J. Geophys. Res.*, 99 (C2), 3273-3283, 1994.

Antonov, J. I., S. Levitus, T. P. Boyer, M. E. Conkright, T. D. O'Brien, and C. Stephens: World Ocean Atlas 1998 Vol. 1: Temperature of the Atlantic Ocean, *NOAA Atlas NESDIS 27*, U.S. Government Printing Office, Washington, D.C, 1998.

Battisti, D.S., C.M. Bitz, and R.E. Moritz, Do general circulation models underestimate the natural variability in the Arctic climate?, *J. Clim.*, 10, 1909-1920, 1997.

Belkin, I.M., S. Levitus, J.I. Antonov, and S.-A. Mamlberg, "Great Salinity Anomalies" in the North Atlantic, *Progr. Oceanogr.*, 41, 1-68, 1998.

Bitz, C.M., W. H. Lipscomb, An energy conserving thermodynamic model of sea ice, *J. Geophys. Res.*, 104 (C7), 15,669-15,677, 1999.

Blindheim, J., Cascading of Barents Sea bottom water into the Norwegian Sea. *Rapp. P.-v. Reun. Cons. int. Explor. Mer*, 188, 49-58, 1989.

Bourke, R. H., Currents, fronts and fine structure in the marginal ice zone of the Chukchi Sea, *Polar Record*, 21 (135), 569-575, 1983.

Bourke, R. H., and R. P. Garrett, Sea ice thickness distribution in the Arctic Ocean, *Cold Regions Sci. Technol.*, 13, 259-280, 1987.

Bourke, R. H., M. D. Tunnicliffe, J. L. Newton, R. G. Paquette, and T. O. Manley, Eddy near the Molloy Deep revisited, *J. Geophys. Res.*, 92, 6773-6776, 1987.

Bourke, R. H., A. M. Weigel, and R. G. Paquette, The Westward turning branch of the West Spitsbergen Current, *J. Geophys. Res.*, 93 (C11), 14065-14078, 1988.

Bourke, R. H., V. G. Addison, and R. G. Paquette, Oceanography of Nares Strait and northern Baffin Bay in 1986 with emphasis on deep and bottom water formation, *J. Geophys. Res.*, 94 (C6), 8289-8302, 1989.

Bourke, R. H., and R. G. Paquette, Formation of Baffin Bay Bottom and Deep Waters, in *Deep Convection and Deep Water Formation in the Oceans*, edited by P.C. Chu, and J.C. Gascard, Elsevier, New York, 1991.

Bourke, R. H., and A. S. McClaren, Contour mapping of Arctic basin ice draft and roughness parameters, *J. Geophys. Res.*, 97 (C11), 17715-17728, 1992.

Boyer, T. P., S. Levitus, J. I. Antonov, M. E. Conkright, T. D. O'Brien, and C. Stephens: World Ocean Atlas 1998 Vol. 4: Salinity of the Atlantic Ocean, *NOAA Atlas NESDIS 30*, U.S. Government Printing Office, Washington, D.C, 1998.

Broecker, W.S., The great ocean conveyor, *Oceanogr.*, 4 (2), 79-89, 1991.

Brooks, D.A., A model study of the buoyancy driven circulation in the Gulf of Maine, *J. Phys. Oceanogr.*, 24, 2387-2412, 1994.

Bryan, K., A numerical method for the study of the circulation of the world ocean, *J. Comput. Phys.*, 4, 347-376, 1969.

Bryan, K., and M. Cox, An approximate equation of state for numerical models of ocean circulation, *J. Phys. Oceanogr.*, 2, 510-514, 1972.

Carmack, E. C., Large-scale physical oceanography of polar oceans. In *Polar Oceanography, Part A: Physical Science*, W. O. Walker, Jr., Ed., Academic Press, San Diego, CA, 171-221 pp, 1990.

Carmack, E. C., R. W. Macdonald, R. G. Perkin, F. A. McLaughlin, and R. J. Pearson, Evidence for warming of Atlantic Water in the Southern Canadian Basin of the Arctic Ocean: Results from the Larsen-93 Expedition, *Geophys. Res. Lett.*, 22, 1061-1064, 1995.

Carmack, E. C., K. Aagaard, J. H. Swift, R. W. Macdonald, F. A. McLaughlin, E. P. Jones, R. G. Perkin, J. M. Smith, K. M. Ellis, and L. R. Killius, Changes in temperature and tracer distributions within the Arctic Ocean: Results from the 1994 Arctic Ocean section, *Deep Sea Res., Part II*, 44 (8), 1487-1502, 1997.

Chapman, W.L., and J.E. Walsh, Recent variations of sea ice and air temperature in high latitudes, *Bull. American Meteorological Soc.*, 74 (1), 33-47, 1993.

Coachman, L. K., and K. Aagaard, Transports through the Bering Strait: Annual and interannual variability, *J. Geophys. Res.*, 93, 15535-15539, 1988

Colbourne, E.B., and G. Mertz, Spatial and temporal variability of ocean temperature over the Labrador Shelf, *Atmos.-Ocean*, 36 (4), 299-317, 1998.

Cuny, J., P. Rhines, P. Niiler, and S. Bacon, Labrador Sea boundary Currents and the fate of the Irminger Sea Water, submitted *J. Phys. Oceanogr.* 2001.

Dickson, R.R., J. Meincke, S.-A. Malmberg, and A.J. Lee, The "Great Salinity Anomaly" in the northern North Atlantic 1968-1982, *Progr. Oceanogr.*, 20, 103-151, 1988.

Dickson, R.R., J. Lazier, J. Meincke, P. Rhines, and J. Swift, Long-term coordinated changes in the convective activity of the North Atlantic, *Progr. Oceanogr.*, 38, 241-295, 1996.

Dickson, R.R., J. Meincke, I. Vassie, J. Jungclauss, and S. Osterhus, Is variability of the Denmark Strait overflow predictable?, , 1998.

Dickson, R.R., All change in the Arctic, in *Nature*, pp. 389-391, 1999.

Dickson, R. R., T. J. Osborn, J. W. Hurrell, J. Meincke, J. Blindheim, B. Adlandsvik, T. Vinje, G. Alekseev, and W. Maslowski, The Arctic Ocean response to the North Atlantic Oscillation, *J. Clim.*, 13 (15), 2671-2696, 2000.

Drange, H., and K. Simonsen, Formulation and spin up of the ESOP2 version of MICOM, Technical Report 117, Nansen Environmental and Remote Sensing Center, Bergen, Norway, 1997.

Dukowicz, J. K., and R. D. Smith, Implicit free-surface method for the Bryan-Cox-Semtner ocean model, *J. Geophys. Res.*, 99 (C4), 7991-8014, 1994.

Endoh, M.C., C. N. K. Mooers, W. R. Johnson, A coastal upwelling circulation model with eddy viscosity depending upon Richardson number, in *Coastal Upwelling, Coastal and Estuarine Sciences*, edited by F.A. Richards, pp. 203-208, AGU, Washington, D. C., 1981.

Environmental Working Group (EWG): Joint U.S.-Russian Atlas of the Arctic Ocean for the Winter Period [CD-ROM], *Natl. Snow and ice Data Cent.*, Boulder, Colorado, 1997.

Environmental Working Group (EWG): Joint U.S.-Russian Atlas of the Arctic Ocean for the Summer Period [CD-ROM], *Natl. Snow and ice Data Cent.*, Boulder, Colorado, 1998.

Ekwurzel, B., P. Schlosser, R. A. Mortlock, and R. G. Fairbanks, River runoff, sea ice meltwater, and Pacific water distribution and mean residence times in the Arctic Ocean, *J. Geophys. Res.*, 106 (C5), 9075-9092, 2001.

Fahrbach, E., J. Meincke, S. Osterhus, G. Rohardt, U. Schauer, V. Tverberg, and J. Verduin, Direct measurements of volume transports through Fram Strait, *in press Polar Sci.*, 2001

Falkingham, J. C., Sea ice in the Canadian Arctic in the 21st Century, Canadian Ice Service Report, 5 pp, 2000.

Fissel, D. B., J. R. Birch, H. Melling and R. A. Lake, Non-tidal flows in the Northwest Passage, Canadian Technical Report of Hydrography and Ocean Sciences No. 98, 143 pp, 1988.

Fleming, G.H., and A.J. Semtner, A numerical study of interannual ocean forcing on Arctic ice, *J. Geophys. Res.*, 96, 4589-4603, 1991.

Foffonof, P., Physical properties of seawater, in *The Sea*, pp. 864, Interscience, New York, 1962.

Galt, J.A., A numerical investigation of Arctic Ocean dynamics, *J. Phys. Oceanogr.*, **3**, 379-396, 1973.

Gent, P. R., and J. C. McWilliams, Isopycnal mixing in ocean circulation models. *J. Phys. Oceanogr.*, **20**, 150-155, 1990.

Gent, P. R., J. Willebrand, T. McDougall, and J. C. McWilliams, Parameterizing eddy-induced tracer transports in ocean circulation models. *J. Phys. Oceanogr.*, **25**, 463-474, 1995.

Gerdes, R., and U. Schauer, Large-scale circulation and water mass distribution in the Arctic Ocean from model results and observations, *J. Geophys. Res.*, **102** (C4), 8467-8483, 1997.

Gerdes, R., M. Karcher, J. Brauch, C. Koeberle, and B. Fritzsche, Propagation of Atlantic Water into the Nordic Seas and the Arctic Ocean in high resolution, coupled sea ice-ocean simulations, (manuscript in preparation), 1999.

Gibson, J. K., P. Kallberg, S. Uppala, A. Hernandez, A. Nomura, E. Serrano, ERA-15 Description (Version 2-January 1999), ECMWF Re-Analysis Project Report Series, European Centre for Medium-Range Weather Forecasts, 1999.

Gloersen, P., W. J. Campbell, D. J. Cavalieri, J. C. Comiso, C. L. Parkinson, and H. J. Zwally, Arctic and Antarctic sea ice 1978-1987: satellite passive-microwave observations and analysis, NASA SP-511, 1992.

Goosse H., and T. Fichefet, Importance of ice-ocean interactions for the global ocean circulation: a model study. *J. Geophys. Res.* **104**(C10), 23337-23355, 1999.

Grotefendt, K., K. Logemann, D. Quadfasel and S. Ronski, Is the Arctic Ocean warming? *Geophys. Res. Lett.*, Vol. 103, No. C12, 27679-27687, 1998.

Hakkinen, S., Models and their applications in polar oceanography, in *Polar Oceanography, Part A: Physical Science*, edited by W.O. Smith, Academic Press, Inc., 1990.

Hakkinen, S., and G. L. Mellor, Modeling the seasonal variability of the coupled Arctic ice-ocean system, *J. Geophys. Res.*, **97**, 20,285-20,304, 1992.

Harms, I.H., Water mass transformation in the Barents Sea - application of the Hamburg Shelf Ocean Model (HamSOM), *J. Mar. Sci.*, **54**, 351-365, 1997.

Harms, I.H., and M. J. Karcher, Modeling the seasonal variability of hydrography and circulation in the Kara Sea, *J. Geophys. Res.*, **104** (C6), 13431-13448, 1999.

Hibler, W. D. III, A dynamic thermodynamic sea ice model, *J. Phys. Oceanogr.*, 9, 815-846, 1979.

Hibler, W.D.III., and K. Bryan, Oceanic circulation: Its effect on seasonal sea ice simulations, *Science*, pp. 489-492, 1984.

Hibler, W.D.III., and K. Bryan, A diagnostic sea ice model, *J. Phys. Oceanogr.*, 17, 17, 987-18,015, 1987.

Holland, D. M., L. A. Mysak, and J. M. Oberhuber, An investigation of the general circulation of the Arctic Ocean using an isopycnal model, *Tellus, Ser. A*, 48, 138-157, 1996.

Hunke, E. C., and J. K. Dukowicz, An elastic-viscous-plastic model for sea ice dynamics, *J. Phys. Oceanogr.*, 27, 1849-1867, 1997.

Hunke, E. C., and Y. Zhang, A comparison of sea ice dynamics models at high resolution, *Mon. Wea. Rev.*, 127, 396-408, 1999.

Ingram, R. G., and S. Prinsenbergh, Coastal oceanography of Hudson Bay and surrounding eastern Canadian Arctic waters, in The Sea, Volume II, J. Wiley & Sons, Inc., pp 835-861, 1998.

Ingvaldsen, R., H. Loeng, and L. Asplin, Variability in the Atlantic inflow to the Barents Sea based on a one-year time series from moored current meters, *subm. Cont. Shelf Res*, 2000.

Jakobsson, M., N.Z. Cherkis, J. Woodward, R. Macnab, and B. Coakley. New grid of Arctic bathymetry aids scientists and mapmakers; *Eos, Transactions*, American Geophysical Union, volume 81, number 9, February 29, 2000.

Johnson, D.R., T.A. McClimans, S. King, and O. Grennes, Fresh water masses in the Kara Sea during summer, *J. Mar. Sys.*, 12, 127-145, 1997.

Johnson, M. A., A. Y. Proshutinsky, and I. V. Polyakov, Atmospheric patterns forcing two regimes of Arctic circulation: A return to anticyclonic conditions? *Geophys. Res. Lett.*, 26 (11), 1621-1624, 1999.

Killworth, P. D., D. Stainforth, D. J. Webb, and S. M. Patterson, The development of a free surface Bryan-Cox-Semtner ocean model, *J. Phys. Oceanogr.*, 21, 1333-1348, 1991.

Kowalik, Z., and A. Y. Proshutinsky, The Arctic Ocean tides, in *The Polar Oceans and Their Role in Shaping the Global Environment: The Nansen Centennial Volume*, edited by O.M. Johannessen, R.D. Muench, and J.E. Overland, pp. 137-158, AGU, Washington, D.C., 1994.

Large, W.G., J. C. McWilliams, and S. C. Doney, Oceanic vertical mixing: A review and a model with a nonlocal boundary layer parameterization, *Rev. Geophys.* (32), 363-403, 1994.

LeBlond, P. H., On the surface circulation in some channels of the Canadian Arctic Archipelago, *Arctic*, 33 (1), 189-197, 1980.

Levitus, S., Climatological atlas of the world ocean, NOAA Professional Paper, 13, Washington, D. C., 1982.

Levitus, S., R. Burgett, and T. Boyer, World Ocean Atlas, 1994, Volume 3, Salinity, NOAA Atlas NESDIS 3, NOAA, Washington, DC, 1994.

Levitus, S., and T. Boyer, World Ocean Atlas, 1994, Volume 4, Temperature, NOAA Atlas NESDIS 3, NOAA, Washington, DC, 1994.

Loeng, H., Features of the physical oceanographic conditions of the Barents Sea, *Polar Res.*, 10, 5-18, 1991.

Loeng, H., Ozhigin, V., Adlandsvik, B., and H. Sagen, Current measurements in the northeastern Barents Sea, *ICES Statutory Meeting*, 22p, 1993.

Loeng, H., Ozhigin, V., and B. Adlandsvik, Water fluxes through the Barents Sea, *ICES J. Mar. Sci.*, 54, 310-317, 1997.

Loeng, H., Measuring the Barents Sea throughflow, in *H. U. Sverdrup Symposium. Towards and Arctic-Subarctic Ocean Flux array (ASOF)*, Tromso, Norway, 2000.

Manley, T. O., R. H. Bourke, and K. L. Hunkins, Near-surface circulation over the Yermak Plateau in northern Fram Strait, *J. Mar. Sys.*, 3, 107-125, 1992.

Martin, S., and R. Drucker, The effect of possible Taylor columns on the summer ice retreat in the Chukchi Sea, *J. Geophys. Res.*, 102, (C5), 10,473-10,482, 1997.

Maslanik, J., and J. Dunn, On the role of sea-ice transport in modifying Arctic responses to global climate change, *Annals Glac.*, 25, 102-106, 1997.

Maslowksi, W., Advanced modeling of the Arctic Ocean and sea ice in support of global climate studies, *Workshop on Polar Processes in Global Climate*, American Meteorology Society, Cancun, Mexico, November, 1996.

Maslowksi, W., J. McClean, B. Newton, P. Schlosser, Y. Zhang, A. J. Semtner, and D. Martinson, Modeling interannual variability of the Arctic Ocean and sea ice circulation, Supp. to *EOS Transactions*, AGU Volume 79, 45, 1998.

Maslowksi, W., B. Newton, P. Schlosser, A. J. Semtner, and D. Martinson, Modeling recent climate variability in the Arctic Ocean, *Geophys. Res. Lett.*, 27 (22), 3743-3746, 2000.

Maslowksi, W., D. C. Marble, W. Walczowski and A. J. Semtner, On large scale shifts in the Arctic Ocean and sea ice conditions during 1979-1998, in press *Annals Glac.*, 2001.

Matishov, G., A. Zhev, V. Golubev, N. Adrov, V. Slobodin, S. Levitus, and I. Smolyar, Climatic Atlas of the Barents Sea 1998: Temperature, Salinity and Oxygen, *NOAA Atlas NESDIS 26*, Washington, D. C, 1998.

Mauritzen, C., and S. Hakkinen, Influence of sea ice on the Meridional Overturning Cell in the North Atlantic, in *AACP Notes*, pp. 6-10, 1997.

McClean, J., W. Maslowksi, R. Tokmakian, A. Semtner, A high resolution fully global ocean model forced with daily ECMWF wind stresses, heat and freshwater fluxes for 1979-1997, Supp. to *EOS Transactions*, AGU Volume 79, 45, 1998.

McPhee, M.G., T.P. Stanton, J.H. Morison, and D.G. Martinson, Freshening of the upper ocean in the Arctic: Is perennial sea ice disappearing?, *Geophys. Res. Lett.*, 25 (10), 1729-1732, 1998.

Melling H., R. A. Lake, D. Topham and D. Fissel, Oceanic thermal structure in the western Canadian Arctic, *Cont. Shelf Res.*, 3, 223-258, 1984.

Melling, H., Hydrographic changes in the Canada Basin of the Arctic Ocean, 1979-1996, *J. Geophys. Res.*, 103 (C4), 7637-7645, 1998.

Mellor, G. L., S. Hakkinen, T. Ezer, and S. Pazan, A generalization of a sigma coordinate ocean model and an intercomparison of model vertical grids, submitted to *Ocean Forecasting: Theory and practice*, Springer Pub., N. Pinardi (Ed.), 1999.

Mesinger, F., A. Arakawa, Numerical methods used in atmospheric models, pp. 64, WMO-ICSU Joint Organizing Committee, 1976.

Miller, J.R., and G. L. Russell, Investigating the interactions among river flow, salinity and sea ice using a global coupled atmosphere-ocean-ice model, *Annals Glac.*, 25, 121-126, 1997.

Mirsky, J., To the Arctic! The story of northern exploration from earliest times, University of Chicago Press, Chicago, 334 pp, 1934.

Morison, J., K. Aagaard, and M. Steele, Report on the study of the Arctic change workshop, in *Study of the Arctic Change Workshop*, Polar Science Center, Applied Physics Laboratory, University of Washington, Seattle Washington, 1997.

Muench, R. D., The physical oceanography of the northern Baffin Bay region, Baffin Bay – North Water project, Scientific Report No. 1, Arctic Institute of North America, Washington, D.C., 150 pp, 1971.

Munchow, A., and E.C. Carmack, Synoptic flow and density observations near an Arctic shelf break, *J. Phys. Oceanogr.*, 27, 1402-1419, 1997.

Munk, W.H., and E. R. Anderson, Notes on a theory of a thermocline, *J. Mar. Res.*, 7, 276-295, 1948.

Mysak, L.A., D. K. Manak, and R. F. Marsden, Sea ice anomalies observed in the Greenland and Labrador Seas during 1901-1984 and their relation to an interdecadal Arctic climate cycle, *Clim. Dyn.*, 5, 111-133, 1990.

Mysak, L.A., and S.A. Venegas, Decadal climate oscillations in the Arctic: A new feedback loop for atmospheric-ice-ocean interactions, *Geophys. Res. Ltrs*, 25, 3607-3610, 1998.

Nansen, F.e., The oceanography of the north polar basin., in *The Norwegian North Polar Expedition, 1893-1896, Scientific Results*, pp. 422, Longmans, Green and Co., 1902.

Nansen, F., Northern water: Captain Roald Amundsen's oceanographic observations in the Arctic Seas in 1901. Videnskabs-Selskabets Skrifter, I, Matematisk-Naturv. Klasse, 1906, 3, pp. 145, 1906.

Nazarenko, L., T. Sou, M. Eby, and G. Holloway, The Arctic ocean-ice system studied by contamination modelling, *Annals Glac.*, 25, 17-21, 1997.

Nazarenko, L., G. Holloway, and N. Tausnev, Dynamics of transport of "Atlantic signature" in the Arctic Ocean, *J. Geophys. Res.*, 103 (C13), 31,003-31,015, 1998.

Newton, J. L., K. Aagaard, and L. K. Coachman, Baroclinic eddies in the Arctic Ocean, *Deep Sea Res.*, 21, 707-719, 1974.

Oberhuber, J. M., Simulation of the Atlantic circulation with a coupled sea ice-mixed layer-isopycnic general circulation model, *J. Phys. Oceanogr.*, 23, 808-829, 1993.

Ozhigin, V.K., A. G. Trofimov, and V. A. Ivshin, The Eastern Basin Water and currents in the Barents Sea, in *ICES Annual Science Conference 2000*, 2000.

Parkinson, C. L., and W. M. Washington, A large-scale numerical model of sea ice, *J. Geophys. Res.*, 84, 311-337, 1979.

Parsons, A.R., On the Barents Sea Polar Front in summer and interpretations of the associated regional oceanography using an Arctic Ocean general circulation model, Ph.D. dissertation, Naval Postgraduate School, Monterey, 1995.

Parsons, A.R., Bourke, R. D., Muench, R. D., Chiu, C. C., Lynch, J. F., Miller, J. H., Pluedemann, A. J., and R. Pawlowicz, The Barents Sea polar front in summer, *J. Geophys. Res.*, 101 (C6), 14201-14221, 1996.

Paquette, R. G., and R. H. Bourke, Observations on the coastal current of Arctic Alaska, *J. Mar. Res.*, 32 (2), 195-207, 1974.

Paquette, R. G., and R. H. Bourke, Ocean circulation and fronts as related to ice melt-back in the Chukchi Sea, *J. Geophys. Res.*, 86 (C5), 4215-4230, 1981.

Pfirman, S.L., D. Bauch, and T. Gammelsrod, The Northern Barents Sea: Water Mass Distribution and Modification, in *The Polar Oceans and Their Role in Shaping the Global Environment: The Nansen Centennial Volume*, edited by O.M. Johannessen, R.D. Muench, and J.E. Overland, pp. 77-94, American Geophysical Union, 1994.

Preller, R. H., and P. Posey, The Polar Ice Prediction System – a sea ice forecasting system, NORDA Report 212, Naval Research Laboratory, Stennis Space Center, MS, 1989.

Prinsenbergh, S. J., Seasonal current variations observed in western Hudson Bay, *J. Geophys. Res.*, 92 (C10), 10756-10766, 1987.

Prinsenbergh, S. J., and E. B. Bennet, Mixing and transports in Barrow Strait, the central part of the Northwest Passage, *Cont. Shelf Res.*, 7 (8), 913-935, 1987.

Prinsenbergh, S. J., and E. B. Bennet, Transport between Peel Sound and Barrow Strait in the Canadian Arctic, *Cont. Shelf Res.*, 9 (5), 427-444, 1989.

Prinsenbergh, S. J., Volume, heat and freshwater fluxes through the Canadian Arctic Archipelago: Present understanding and future research plans, in Polar Processes and Global Climate (ACSYS) Proceedings Part II, pp 200-202, 1997.

Prinsenbergh, S. J., and Q. Yao, The seasonal evolution of sea ice cover off eastern Canada as simulated by a coupled ice-ocean model for 1991/92 and expected 2xCO₂ atmospheric conditions, unpublished manuscript, 1999.

Proshutinsky, A., and M. Johnson, Two circulation regimes of the wind-driven Arctic Ocean, *J. Geophys. Res.*, *102*, 12493-12514, 1997.

Rigor, I.G., and R.L. Colony, Monthly ice motion and atmospheric pressure in the Arctic basin, 1979 - 1993, Applied Physics Laboratory, University of Washington, Seattle, Washington, 1994.

Rigor, I.G., and A. Heiberg, International Arctic Buoy Program data report 1 January 1995 - 31 December 1995, Applied Physics Laboratory, University of Washington, Seattle, Washington, 1996.

Rigor, I.G., and A. Heiberg, International Arctic Buoy Program data report 1 January 1996 - 31 December 1996, Applied Physics Laboratory, University of Washington, Seattle, Washington, 1997.

Roach, A.T., K. Aagaard, C.H. Pease, S.A. Salo, T.J. Weingartner, P. V., and M. Kulakov, Direct measurements of transport and water properties through the Bering Strait, *J. Geophys. Res.*, *100* (C9), 18433-18457, 1995.

Roberts, M. J., R. Marsh, A. L. New, and R. A. Wood, An intercomparison of a Bryan-Cox type model and an isopycnic ocean model, Part 1: The subpolar and high-latitude processes, *J. Phys. Oceanogr.*, *26*, 1495-1527, 1996.

Rudels, B., The outflow of polar water through the Arctic archipelago and the oceanographic conditions in Baffin Bay, *Polar Res.*, *4*, 161-180, 1986.

Rudels, B., On the mass balance of the Polar Ocean, with special emphasis on the Fram Strait, *Nor. Polarinst. Skr.*, *188*, 53 pp, 1987.

Rudels, B., The formation of Polar Surface Water, the ice export and the exchanges through the Fram Strait, *Progr. in Oceanogr.*, *22*, 205-248, 1989.

Rudels, B., E.P. Jones, L.G. Anderson, and G. Kattner, On the intermediate depth waters of the Arctic Ocean, in *The Polar Oceans and Their Role in Shaping the Global Environment: The Nansen Centennial Volume*, edited by O.M. Johannessen, R.D. Muench, and J.E. Overland, pp. 33-46, AGU, Washington, D.C, 1994.

Rudels, B., R. D. Muench, J. Gunn, U. Schauer, and H. J. Friedrich, Evolution of the Arctic Ocean boundary current north of the Siberian shelves, *J. Mar. Sys.*, *25*, 77-99, 2000.

Rudels, B., and H. J. Friedrich, The transformation of Atlantic Water in the Arctic Ocean and their significance for the freshwater budget, in *The Freshwater Budget of the Arctic Ocean*, edited by E. L. Lewis et al., pp. 503-532, Kluwer Academic Publishers, Netherlands, 2000.

Rudels, B., R. Meyer, E. Fahrbach, V. V. Ivanov, S. Osterhus, D. Quadfasel, U. Schauer, V. Tverberg, and R. A. Woodgate, Water mass distribution in Fram Strait and over the Yermak Plateau in summer 1997, *Ann. Geophysicae*, 18, 687-705, 2000.

Schauer, U., R.D. Muench, B. Rudels, and L. Timokhov, Impact of eastern Arctic Shelf waters on the Nansen Basin halocline, *J. Geophys. Res.*, 102 (C2), 3371-3382, 1997.

Schauer, U., B. Rudels, E. P. Jones, L. G. Anderson, R.D. Muench, G. Bjork, J. H. Swift, V. Ivanov, and A-M. Larsson, Confluence and redistribution of Atlantic Water in the Nansen, Amundsen and Makarov basins, *subm. Ann. Geophys*, 2000.

Schneider, W., and G. Budeus, On the generation of the NEW Polynya, *J. Geophys. Res.*, 100 (C3), 4269-4286, 1995.

Seigel, A., J. B. Weiss, J. Toomre, J. C. McWilliams, P. S. Berloff, and I Yavneh, Eddies and vortices in ocean basin dynamics, *Geophys Res Lett.*, 28 (16), 3183, 3186, 2001.

Semtner, A.J., A numerical investigation of Arctic Ocean circulation, Ph.D. dissertation, Princeton University, Princeton, 1973.

Semtner, A.J., Numerical simulation of the Arctic Ocean circulation, *J. Phys. Oceanogr.*, 6, 409-425, 1976a.

Semtner, A.J., A model for the thermodynamic growth of sea ice in numerical investigations of climate, *J. Phys. Oceanogr.*, 6, 379-389, 1976b.

Semtner, A.J., On modelling the seasonal thermodynamic cycle of sea ice in studies of climatic change, *Clim. Change*, 6, 27-37, 1984.

Semtner, A.J., A numerical study of sea ice and ocean circulation in the Arctic, *J. Phys. Oceanogr.*, 17, 1077-1099, 1987.

Semtner, A. J., and R. M. Chervin, Ocean circulation from a global eddy-resolving model, *J. Geophys. Res.*, 97, 5493-5550, 1992.

Semtner, A.J., Modeling ocean circulation, *Science*, 269, 1379-1385, 1995.

Serreze, M.C., F. Carse, R. G. Barry, and J. C. Rogers, Icelandic low cyclone activity: climatological features, linkages with the NAO, and relationships with recent changes in the Northern Hemisphere circulation, *J. Climate*, 10, 453-464, 1997.

Simonsen, K., and P. M. Haugan, Heat budgets of the Arctic Mediterranean and sea surface heat flux parameterizations for the Nordic Seas, *J. Geophys. Res.*, 101 (C3), 6553-6576, 1996.

Skyllingstad, E.D., D.W. Denbo, and J. Downing, Convection in the Labrador Sea: Community Modeling Effort (CME) results, in *Deep Convection and Deep Water Formation in the Oceans*, edited by P.C. Chu, and J.C. Gascard, Elsevier, New York, 1991.

Smedsrud, L. H. and T. Furevik, Towards an ice free Arctic?, *Cicerone* 2000(2), 19-23, 2000.

Smethie, W. M., P. Schlosser, and G. Bonisch, Renewal and circulation of intermediate waters in the Canadian Basin observed on the SCICEX '96 cruise, *J. Geophys. Res.*, 105 (C1), 1105-1121, 2000.

Steele, M., R. Morley, and W. Ermold, Polar Science Center Hydrographic Climatology (PHC) A Global Ocean Hydrography with a High Quality Arctic Ocean, *in press J. Clim.*, 2000.

Steele, M., W. Ermold, G. Holloway, S. Hakkinen, D. Holland, M. Karcher, F. Kauker, W. Maslowski, N. Steiner, and J. Zhang, Adrift in the Beaufort Sea: A model intercomparison, *Geophys. Res. Lett.*, 28 (15), 2935-2938, 2001.

Stigebrandt, A., The North Pacific: A global scale estuary, *J. Phys. Ocean.*, 14, 464-470, 1984.

Swift, J. H., E. P. Jones, K. Aagaard, E. C. Carmack, M. Hingstrom, R. W. MacDonald, F. A. McLaughlin, and R. G. Perkin, Waters of the Makarov and Canada Basins, *Deep Sea Res, Part II*, 44 (8), 1503-1529, 1997.

Thompson, D.W., and J. M. Wallace, The Arctic Oscillation signature in the wintertime geopotential height and temperature fields., *Geophys. Res. Lett.*, 25, 1297-1300, 1998.

UNESCO, Tenth report of the joint panel on oceanographic tables and standards, pp. 25, UNESCO, Paris, 1981.

U. S. Arctic Research Commission, The Arctic Ocean and climate change: A scenario for the U.S. Navy, Washington, D.C., November, 2000.

U. S. Arctic Research Commission, Report on goals and objectives for Arctic Research, Washington, D.C., 2001.

U. S. Navy Symposium: Naval operations in an ice free Arctic Ocean, sponsored by the Oceanographer of the Navy, Washington, D.C., 17-18 April, 2001.

Visbeck, M., J. Fischer, and F. Schott, Preconditioning the Greenland Sea for deep convection: Ice formation and ice drift, *J. Geophys. Res.*, *100* (C9), 18,489-18,502, 1995.

Wadhams, P., and J. C. Comiso, Two modes of appearance of the Odden ice tongue in the Greenland Sea, *Geophys. Res. Lett.*, *26* (16), 2497-2500, 1999.

Wang, J., L. A. Mysak, and R. G. Ingram, A three-dimensional numerical simulation of summer ocean circulation in Hudson Bay, *J. Phys. Oceanogr.*, *24*, 2496-2514, 1994.

Washington, W.M., J.W. Weatherly, A.J. Semtner, T.W. Bettge, A.P. Craig, W.G. Strand, V.B. Wayland, R. James, G.A. Meehl, and Y. Zhang: A DOE coupled Parallel Climate Model (PCM) with high resolution ocean and sea ice: an update, 1998.

Washington, W. M. et al: Parallel Climate Model (PCM): Control and Transient Simulations. Accepted to *Climate Dynamics*, 2000.

Weatherly, J. W., Greenhouse warming in an Arctic ice-ocean model, In: *Modeling the Arctic system: A workshop report on the state of modeling in the Arctic System Science Program. The Arctic Research Consortium of the U.S.*, Fairbanks, Alaska, 141 p., Feb. 1997.

Weatherly, J.W. and Y. Zhang: The response of the polar climate to increasing CO₂ in a global climate model with elastic-viscous-plastic sea ice. Accepted to *Journal of Climate*, 2000.

Yao, Q., and S. J. Prinsenberg, Sensitivity tests of a 2-category Hibler ice model and comparison to a 10 category Hibler ice mode both coupled to a Cox-Bryan ocean model, *Can Tech Rep. Hydrogr. Ocean Sci.* *201*: xii+108pp, 1999.

Yao, T., C. L. Tang, and I. K. Peterson, Modeling the seasonal variation of sea ice in the Labrador Sea with a coupled multicategory ice model and the Princeton ocean model, *J. Geophys. Res.*, *105*, (C1), 1153-1165, 2000.

Zhang, J., and W. Hibler, On an efficient numerical method for modeling sea ice dynamics, *J. Geophys. Res.*, *102*, 8691-8702, 1997.

Zhang, J., W.D. Hibler III, M. Steele, and D.A. Rothrock, Arctic ice ocean modeling with and without climate restoring, *J. Phys. Oceanogr.*, *28*, 191-217, 1998a.

Zhang, J., D.A. Rothrock, and M. Steele, Warming of the Arctic Ocean by a strengthened Atlantic inflow: Model results, *Geophys. Res. Ltrs*, 25 (10), 1745-1748, 1998b.

Zhang, J., D.A. Rothrock, and M. Steele, Recent changes in Arctic sea ice: the interplay between ice dynamics and thermodynamics, *J. Clim*, 13, 3099-3114, 2000.

Zhang, Y., W. Maslowski, and A.J. Semtner, Impact of mesoscale ocean currents on sea ice in high-resolution Arctic ice and ocean simulations, *J. Geophys. Res.*, 104, (C8), 18,409-18,430, 1999.

Zhang, Y., and E.C. Hunke, Recent Arctic change simulated with a coupled ice-ocean model, *J Geophys. Res.*, 106 (C3), 4369-4390, 2001.

THIS PAGE INTENTIONALLY LEFT BLANK

INITIAL DISTRIBUTION LIST

1. Defense Technical Information Center
Fort. Belvoir, Virginia
2. Dudley Knox Library
Naval Postgraduate School
Monterey, California
3. Goldthwait Polar Library
Byrd Polar Research Center
Columbus, Ohio
lay.1@osu.edu
4. Albert J. Semtner
Oceanography Dept., Naval Postgraduate School
Monterey, California
sbert@ucar.edu
5. Wieslaw Maslowski
Oceanography Dept., Naval Postgraduate School
Monterey, California
maslowsk@ucar.edu
6. Robert Bourke
Oceanography Dept., Naval Postgraduate School
Monterey, California
bourke@oc.nps.navy.mil
7. Roland W. Garwood, Jr
Oceanography Dep., Naval Postgraduate School
Monterey, California
garwood@nps.navy.mil
8. Peter S. Guest
Meteorology Dept., Naval Postgraduate School
Monterey, California
pguest@nps.navy.mil
9. Ursula Schauer
Alfred Wegener Institute
Bremerhaven, Germany
uschauer@AWI-Bremerhaven.DE

10. Michael Steele
Applied Physics Laboratory, University of Washington
Seattle, Washington
mas@apl.washington.edu
11. Duane F. Marble
Center for Mapping, Ohio State University
Columbus, Ohio
marble.1@osu.edu
12. Douglas C. Marble
Fleet Numerical Meteorology and Oceanography Center
Monterey, California
dcmarble@compuserve.com
13. CDR Rost Parsons
Oceanography Dept., Naval Postgraduate School
Monterey, California
arparson@nps.navy.mil
14. Julie McClean
Oceanography Dept., Naval Postgraduate School
Monterey, California
mcclean@oc.nps.navy.mil
15. Donald Stark
Oceanography Dept., Naval Postgraduate School
Monterey, California
stark@oc.nps.navy.mil
16. Waldemar Walczowski
Oceanography Dept., Naval Postgraduate School
Monterey, California
waldek@oc.nps.navy.mil
17. Simon Prinsenbergs
Bedford Institute of Oceanography
Dartmouth, Nova Scotia
prinsenbergs@mar.dfo-mpo.gc.ca
18. Harald Loeng
Institute of Marine Research
Bergen, Norway
harald.loeng@imr.no

19. Bob Newton
Lamont Dougherty Earth Observatory, Columbia University
New York, New York
bnewton@ldeo.columbia.edu